Numerical modelling of deformation and recrystallisation mechanics in ice and ice-air aggregates

Dissertation

der Mathematisch-Naturwissenschaftlichen Fakultät
der Eberhard Karls Universität Tübingen
zur Erlangung des Grades eines
Doktors der Naturwissenschaften
(Dr. rer. nat.)

vorgelegt von
Florian Steinbach
aus Alsfeld

Tübingen
2017

Tag der mündlichen Qualifikation:	12. Mai 2017
Dekan:	Prof. Dr. Wolfgang Rosenstiel
1. Berichterstatter:	Jun.-Prof. Dr. Ilka Weikusat
2. Berichterstatter:	Prof. Dr. Paul D. Bons

Erklärung

Ich erkläre hiermit, dass ich die zur Promotion eingereichte Arbeit selbständig verfasst, nur die angegebenen Quellen und Hilfsmittel benutzt und wörtlich oder inhaltlich übernommene Stellen als solche gekennzeichnet habe. Ich erkläre, dass die Richtlinien zur Sicherung guter wissenschaftlicher Praxis der Universität Tübingen (Beschluss des Senats vom 25.5.2000) beachtet wurden. Ich versichere an Eides statt, dass diese Angaben wahr sind und dass ich nichts verschwiegen habe. Mir ist bekannt, dass die falsche Abgabe einer Versicherung an Eides statt mit Freiheitsstrafe bis zu drei Jahren oder mit Geldstrafe bestraft wird.

Tübingen, 30. März 2017

THOSE WHO CANNOT UNDERSTAND HOW TO PUT THEIR THOUGHTS ON ICE SHOULD NOT ENTER INTO THE HEAT OF DEBATE

Friedrich Nietzsche

Abstract

Ice sheets and glaciers flow under their own weight and their flow of ice is a major contributor to both global sea-level and climate changes. The macroscopic flow of ice is affected by the properties of the microstructure, which is formed by a small aggregate of individual ice crystals. The deformation of ice is accompanied by recrystallisation, a term which describes mechanisms causing re-orientations of the crystalline lattice, the formation of new crystals or the migration of their boundaries. The ice crystal is marked by a significant viscoplastic anisotropy, which causes a distinctly higher resistance to flow, if the crystalline lattice is unfavourably oriented. With deformation, the ice grains align and develop a crystallographic-preferred orientation within the ice-aggregate, which induces a macroscopic anisotropy. A knowledge of the micro-dynamic deformation and recrystallisation mechanisms and how they affect the properties of the ice aggregate is a key to understand ice sheet dynamics.

The objective of this thesis to investigate the deformation and recrystallisation mechanisms in ice and the involved changes in the microstructures of ice- and ice-air aggregates. This is done by means of two-dimensional numerical simulations using the modelling platform Elle, which optimised for modelling interacting micro-dynamic processes. The simulations couple a numerical model for viscoplastic deformation of anisotropic polycrystalline aggregates to implementations of recrystallisation mechanisms in Elle. In particular, an explicit numerical approach to consider secondary phases such as air inclusions in the numerical setup is developed, implemented and used in this thesis for the first time. Additionally, the new approach allows grain-size-reducing mechanisms, which allows the achievement of stable-state microstructures with deformation. In each scientific publication presented in the thesis, qualitative comparisons to natural polar ice accompany the numerical simulations.

The results of this thesis show that the deformation and microstructures of ice are generally more heterogeneous than previously thought. Strain localisation is common in ice and related to viscoplastic anisotropy and intensified by the presence of air inclusions.

Probably, strain localisation is occurring over a range of scales and has implications for the large-scale flow of ice. The thesis further demonstrates that deformation-induced recrystallisation mechanisms are common in ice and discusses their relation to strain localisation. In particular, the study points out the importance of the dissection of grains by migrating grain boundaries as an additional grain-size-reducing process in polar ice, which was not studied previously. This thesis confirms that the activation of deformation and recrystallisation mechanisms is a function of the deformation conditions such as strain rate, temperature and likely the load of impurities and dust particles. The steady-state numerical-microstructures reflect the prescribed deformation conditions, but appear largely independent from the initial microstructures. These results of this study indicate a high rate of change in crystallographic-preferred orientation and other microstructural properties. Furthermore, the thesis confirms that the development of crystallographic-preferred orientation is a function of strain rather than time or stress.

Zusammenfassung

Eisschilde und Gletscher fließen unter ihrem eigenen Gewicht und ihr Fluss hat einen großen Einfluss sowohl auf globale Meeresspiegel- als auch Klimaveränderungen. Das makroskopische Fließverhalten von Eis wird von den Eigenschaften der Mikrostruktur, die sich aus kleinen Gefügen von einzelnen Eiskristallen zusammensetzt, beeinflusst. Die Deformation des Eises geht mit Rekristallisation einher, ein Begriff, der Mechanismen beschreibt, die eine Neuorientierung des Kristallgitters, das Entstehen neuer Kristalle oder die Bewegung der Kristallgrenzen verursachen. Der Eiskristall ist durch eine deutliche mechanische Anisotropy gekennzeichnet, was einen deutlich höhren Widerstand gegen Deformation bedeutet, wenn das Kristallgitter ungünstig orientiert ist. Mit der Deformation richten sich Eiskristalle innhalb des Gefüges entlang einer kristallographisch bevorzugten Richtung aus, was auch makroskopisch eine Anisotropie erzeugt. Kenntnisse über die mikrodynamischen Deformations- und Rekristallisationsmechanismen und deren Einlfuss auf die Eigenschaften der Eismikrostruktur sind grundlegend für ein verbessertes Verständnis der Eisschilddynamik.

Das Anliegen dieser Arbeit ist eine Untersuchung der Deformations- und Rekristallisationsmechanismen in Eis und der damit einhergehenden mikrostrukturellen Veränderung in reinem Eis und Eis mit Lufteinschlüssen. Dafür sieht die Arbeit zweidimensionale numerische Simulationen mit Hilfe der Modellierplattform Elle, die für die Modellierung von interagierenden mikrodynamischen Prozessen optimiert ist, vor. Die Simulationen koppeln ein numerisches Modell für viskoplastische Deformation unter Beachtung der Kristallanisotropie mit Implementierungen von Rekristallisationsmechanismen in Elle. Insbesondere beschäftigt sich die Arbeit erstmalig mit der Entwicklung, Implementierung und Anwednung eines numerischen Ansatzes, der weitere Phasen wie Lufteinschlüsse einbezieht. Zusätzlich erlaubt der neue Ansatz korngrößenverkleindernde Prozesse, wodurch die simulierten Mikrostrukturen mit Deformation einen Gleichgewichtszustand erreichen können. Jede wissenschaftliche

Veröffentlichung in dieser Arbeit, nimmt außerdem qualitative Vergleiche von natürlichem polarem Eis mit numerischen Simulationen vor.

Die Ergebnisse dieser Arbeit zeigen generell eine höhere Heterogenität in Eisdeformation und Mikrostruktur als bislang angenommen. Verformungslokalisation ist verbreitet in Eis, steht in Verbindung mit der Kristallanisotropie und wird durch Lusteinschlüsse verstärkt. Wahrscheinlich kann eine Verformungslokalisation über verschiedene Größenordnungen auftreten und hat eine Bedeutung für das großmaßstäbliche Eisfließen. Desweiteren zeigt die Arbeit, dass deformationsinduzierte Rekristallisationsmechanismen in Eis verbreitet sind und diskutiert deren Verhältnis zur Verformungslokalisation. Insbesondere zeigt die Arbeit, dass die Zerteilung von Körnern durch Korngrenzmigration ein wichtiger, jedoch bislang nicht untersuchter, korngrößenverkleindernder Prozess in polarem Eis ist. Die Arbeit bestätigt außerdem, dass die Aktivierung von Deformations- und Rekristallisations-mechanismen von Deformationsbedingungen wie Verformungsrate, Temperatur und wahrscheinlich dem Anteil von Verunreinigungen abhängt. Im Gleichgewichtszustand spiegeln die simulierten Mikrostrukturen die vorgegebenen Deformationsbedingungen wider, aber sind größtenteils unabhängig von der Ausgangsmikrostruktur. Diese Ergebnisse deuten darauf hin, dass die Rate der mikrostrukturellen Änderungen in beispielsweise kristallographisch bevorzugten Richtungen oder Korngrößen in Eis hoch ist. Außerdem bestätigt die Arbeit, dass die Entwicklung einer kristallographisch bevorzugten Richtung von der aufgebauten Verformung abhängt, nicht aber vom Zeit oder Spannungs-zustand.

Table of contents

Introduction

1 Background

1.1 The flow of ice

Ice is one of the most abundant minerals on the Earth's surface and occupies vast areas in mountain glaciers and ice sheets. The Greenland and Antarctic ice sheets are the largest fresh-water reservoirs on Earth and store water equivalent to more than 65 m of sea-level rise (IPCC, 2013; Vaughan et al., 2013). The mass of ice in the Greenland and Antarctic ice sheet decreased over the last two decades and the rate of ice loss continuously accelerates (IPCC, 2013; Vaughan et al., 2013). An uncertainty in the mass balance of the significantly larger Antarctic ice sheet remains. While East Antarctica gained mass, ice loss has been observed for West Antarctica and the Antarctic Peninsula (e.g. Shepherd et al., 2012; Helm et al., 2014). In particular, in Antarctica significant mass loss is achieved by ice sheets flowing towards ice shelves and outlet glaciers, where the ice is discharged into the ocean. This causes land-ice flow to be a main contributor to sea-level changes (IPCC, 2013; Church et al., 2013). Additionally, although ice-sheets are known as valuable paleo-climate archives, ice flow disrupts the climate signal questioning the integrity of the paleo-climate record (e.g. Faria et al., 2010).

Describing the flow of ice is essential to understand the role of ice sheets for global climate, sea-level and environmental changes. To date, ice flow models (Huybrechts 2007; Greve and Blatter 2009) are based on the experimentally derived "Glen's law" (Glen, 1952; 1955). This empirical power-law describes the strain rate ($\dot{\varepsilon}$) as a function of stress (σ), stress exponent (n) and an Arrhenius-type term, which depends on temperature (T), the universal gas constant (R) and an activation energy (Q). The parameter A is scaled for material properties such as grain size, density, impurity content or mechanical anisotropy (see section 1.2 for information on mechanical anisotropy in ice).

$$\dot{\varepsilon} = A \cdot e^{\left(-Q/RT\right)} \cdot \sigma^n \tag{1}$$

Bore hole deformation, remote sensing ice velocity measurements and laboratory experiments suggest values for the stress exponent ranging from about one to five (Glen, 1952; 1955; Hooke, 1981; Goldsby and Kohlstedt, 2001; Gillet-Chaulet et al., 2011). Glen's law was obtained from the secondary stage of ice flow or *creep* (0.5 to 2% strain, Budd and Jacka, 1989), where strain evolution over time was thought to be steady. However, creep experiments to strain higher than approximately 10% yield a three staged evolution of strain over time (Steinemann, 1954; Budd and Jacka, 1989; Treverrow et al., 2012).

The creep behaviour can be inferred from laboratory experiments subjecting ice samples to a constant load, a review on deformation experiments is provided by Budd and Jacka (1989), Treverrow et al. (2012) or Faria et al. (2014b). All experiments describe three creep stages, which are common to many polycrystalline materials known from geology or metallurgy. The creep of ice is characterised by an initial instantaneous elastic strain. This is followed by primary or transient creep. A significant part of primary creep strain is recovered hours after the experiment load is removed (Duval, 1978). Primary creep is characterised by a rapid decrease in strain rate until approximately 1% strain, where a minimum in strain rate is reached independent of stress or temperature (Budd and Jacka, 1989). Deceleration during primary creep is followed by secondary creep, during which strain rates transiently remain constant and strain accumulates linearly over time indicating a steady-state. However, continuing the deformation experiment unveils that secondary creep is essentially only a transitional zone between 0.5 to 2% strain (Faria et al., 2014b) connecting decelerating primary creep and accelerating tertiary creep with a characteristic strain rate minimum at 1% strain. Acceleration continues until approximately 10% strain, where steady-state tertiary creep is reached marked by constant strain rates and linear strain accumulation over time.

The transition from the secondary minimum to accelerating tertiary creep is associated with the onset of recrystallisation mechanisms causing softening and accelerating strain rates as internal deformation energy decreases with recrystallisation (Poirier, 1985; Montagnat et al., 2009; Cuffey and Paterson, 2010; Faria et al., 2014b). In addition, accelerating tertiary creep is accompanied by progressive development of crystallographic preferred orientations (CPO) (Steinemann, 1954; Budd, 1972; Kamb, 1972) with the crystals' c-axes aligning with the maximum finite-shortening direction (Azuma and Higashi, 1985). Therefore, the transient secondary creep stage is not observed if deformation experiments on samples with initially aligned c-axes are performed (Gao and Jacka, 1987; Budd and Jacka, 1989; Treverrow et al., 2012). Experimental work by Jacka and Li (1994) suggests that the development of steady-state strain rates and CPOs is accompanied by the development of an equilibrium grain size depending on the stresses at which the experiment is performed. These observations are supported by polar ice core studies showing the development of stable CPO and grain size (Li et al., 1998; Montagnat et al., 2012; 2014a; Weikusat et al., 2017a).

Although successfully applied in modelling ice dynamics (Huybrechts, 2007; Pattyn et al., 2008; Greve and Blatter, 2009), currently the empirical Glen's law does not sufficiently take into account the micro-dynamic mechanisms that affect flow properties. For instance, the CPO development has an important mechanical meaning for ice dynamics: Hexagonal ice (space group Ih) is the only stable ice-polymorph on Earth (Schulson and Duval, 2009). It exhibits significant mechanical anisotropy with deformation significantly easier perpendicular to the c-axes (see details in section 1.2.1; Duval et al., 1983). This induces a mechanical anisotropy to the polycrystalline ice-aggregate (Steinemann, 1954; Gao and Jacka,

1987; Budd and Jacka, 1989; Treverrow 2012) that Glen's law cannot account for. Still, approaches towards including anisotropy in ice flow models are suggest by various studies (e.g. Azuma and Goto-Azuma, 1996; Gillet-Chaulet et al., 2005; Seddick et al., 2008), their combination and integration of CPO heterogeneity remains challenging (Gagliardini et al., 2009). The same holds for dynamic recrystallisation mechanisms altering CPO and grain size development and hence affecting the flow of ice (Duval and Castelnau, 1995; Castelnau et al., 1996; Duval et al., 2000). Furthermore, although particularly Antarctic ice is very pure, air bubbles are a common "impurity" in the upper hundreds to thousand meters of ice. It is suspected that bubbles influence deformation and recrystallisation dynamics (cf. section 1.3; PAPER I; Arena et al., 1997; Azuma et al., 2012; Roessiger et al., 2014), but this effect is too poorly understood to be represented in a mechanistic ice flow-law. Understanding the effect of other soluble and insoluble impurities is even more challenging as they are observed to change strain rates, CPO and grain sizes (Paterson, 1991; Cuffey et al., 2000). Their micro-dynamic effects are still under discussion in recent contributions (Eichler, et al., 2017).

1.2 Micro-dynamic processes during the flow of ice

1.2.1 Deformation mechanisms

Ice on Earth experiences very high temperatures relative to its pressure melting point, which is expressed in high homologous temperatures (T_{actual} / $T_{meltpoint}$). Owing to this characteristic, it behaves similarly to metamorphic minerals in Earth's crust at comparable homologous temperatures and has been used as an analogue for rock-forming minerals (e.g. Wilson, 1981; 1983). In nature, ice sheets and glaciers creep under gravitational forces (Petrenko and Whitworth, 1999), their macroscopic flow is affected by the properties of the aggregate individual ice crystals. On Earth, only the hexagonal ice polymorph Ih is stable (Schulson and Duval, 2009). The main agents of deformation in ice are dislocations, intracrystalline lattice defects gliding and climbing through the crystal lattice allowing the accommodation of strain, which is known as *dislocation creep* (Shoji and Higashi, 1978; Pimienta and Duval, 1987).

The glide of dislocations is possible only on distinct slip systems or planes. Principle slip planes are the basal plane (perpendicular to the c-axis) and the prismatic and pyramidal planes (Hirth and Lothe, 1991; Hondoh, 2000; Hondoh, 2009; Faria et al., 2014b). The ice Ih crystal has a strong mechanical anisotropy, meaning the critical resolved shear stress is about 60 to 80 times higher on the hard non-basal planes relative to the soft basal plane (Duval et al., 1983). The critical resolved shear stress should not be understood as a yield stress necessary to initiate gliding, rather it can be imagined as a viscosity or glide resistance factor. As mentioned in section 1.1, the c-axes align with the direction of maximum finite shortening during deformation (Azuma and Higashi, 1985) causing the development of a macroscopic

mechanical anisotropy for the whole polycrystalline ice aggregate (Steinemann, 1954; Gao and Jacka, 1987; Budd and Jacka, 1989; Treverrow 2012).

Although dislocation glide on basal planes is almost two orders of magnitude easier, the activation of non-basal planes remains necessary to compensate for strain incompatibilities. In some stress configurations, the shear stresses resolved on non-basal relative to basal planes may be high, which makes it energetically favourable to accommodate strain by non-basal glide. The strain rate decrease during primary creep is attributed to the activation of non-basal planes and increasing strain heterogeneities (Wilson, 1986; Petrenko and Whitworth, 1999; Schulson and Duval, 2009). The activation of non-basal glide could also be demonstrated in deep ice-core samples by Weikusat et al. (2009a; 2011a,b; 2017b).

Other deformation mechanisms that contribute to the flow of polycrystalline ice are *diffusion creep* and *grain boundary sliding*. Diffusion creep describes the diffusion of matter around or through the ice lattice, whereas grain boundary sliding is the mere motion of grains past each other, which causes incompatibilities that diffusion creep, but also dislocation activities can accommodate (Raj and Ashby, 1972; Shoji and Higashi, 1978). The glide of dislocations is faster than diffusion, but requires sufficient stresses to be efficient (Goodman et al., 1981). Therefore, diffusion creep and grain boundary sliding become strain rate controlling at low stresses, high temperatures and low grain sizes (Goldsby and Kohlstedt, 1997; 2001; Pettit and Waddington, 2003). Micro-shear zones on the grain- to subgrain-scale are related to diffusion creep and grain boundary sliding (Bons and Jessell, 1999). The onset of micro-shearing was suggested to explain soft layers and microstructural peculiarities in EDML (European Project for Ice Coring in Antarctica, Dronning Maud Land) ice core by Faria et al. (2006). Another significant contributor to ice sheet motion is sliding over bedrock or glacial till (Alley et al., 1987; Engelhardt and Kamb, 1998).

1.2.2 Recrystallisation mechanisms

Deformation of ice is accompanied by recrystallisation. Since recrystallisation mechanisms are temperature dependant following an Arrhenius-term (e.g. Humphreys and Hatherly, 2004), they are efficient in high homologous temperature materials such as ice. Recrystallisation is defined as “any reorientation of the lattice caused by grain boundary migration and/or formation of new grain boundaries” (Faria et al., 2014b). This underlines its importance as recrystallisation modulates the microstructural properties affecting deformation mechanisms in ice. Differences in nomenclature for recrystallisation processes exist. Metallurgy or related disciplines tend to refer to recrystallisation as continuous or discontinuous in the sense of temporal continuity (Gottstein and Mecking, 1985; Drury and Urai, 1990). However, this thesis employs recent terminology from geology and glaciology referring to recrystallisation as static or dynamic (Passchier and Trouw, 2005; Faria et al., 2014b). By distorting

the crystalline lattice, dislocations induce an additional elastic or potential energy, which is described as strain energy. The qualifier static refers to microstructural modifications not related to deformation or strain energies, while dynamic denotes all processes driven by the minimisation of strain-induced energies.

Static recrystallisation is essentially *normal* or *static grain-growth*, which is the increase of the mean grain area driven by surface energy reduction (Smith, 1964; Weaire and Rivier, 1984; Alley et al., 1986a,b; Evans et al., 2001). This mode of grain boundary migration leads to equidimensional grains with only slightly-curved grain boundaries and 120° angles at grain boundary triple junctions (denoted *foam texture*). According to Humphreys and Hatherly (2004, pp. 334-335), the resulting grain diameter distribution is log-normal.

Contrary to static grain-growth, *strain-induced grain boundary migration* (SIBM) is a feature of dynamic recrystallisation. It is driven by the reduction of strain energies, which manifests in characteristic bulge-shaped grain boundaries migrating into a high dislocation density area, leaving behind a region free of strain energies and dislocations (Passchier and Trouw, 2005, pp. 42-43; Humphreys and Hatherly, 2004, pp. 251-253). Therefore, SIBM is marked by irregular grain boundaries. Surface-energy-driven static grain-growth together with SIBM are denoted *dynamic grain-growth* (Faria et al., 2014a,b). However, SIBM does not always increase grain size as it may be accompanied by nucleation of small grains (Faria et al., 2014b) or lead to *grain dissection* by strong bulging (Urai et al., 1986; Means, 1989). Whether this process is relevant for ice is discussed in PAPER II of this thesis.

The grain boundary velocity is a function of the temperature-dependant grain boundary mobility and the driving force for migration (Humphreys and Hatherly, 2004, pp. 123-124; Nasello et al., 2005; Becker et al., 2008). Migrating grain boundaries can potentially drag along and redistribute impurities in the material (Olgaard and Evans, 1986; 1988). Impurities or micro-inclusions themselves are suspected to reduce the mobility (Alley and Woods, 1996; Durand et al., 2006) or cause pinning of the grain boundary (*Zener pinning*; Olgaard and Evans, 1986; Weygand et al., 1999), leading to a deceleration of grain boundary migration and effectively smaller grain sizes. However, the relevance of pinning by solid micro-particles in natural polar ice is under discussion (Eichler, et al., 2017)

The grain size in ice is not solely determined by the interplay of dynamic grain-growth and deceleration by impurities or pinning micro-particles, but other grain-size- decreasing processes. The common grain-size-reducing process suggested for ice is rotation recrystallisation or *polygonisation* (Urai et al., 1986; Alley et al., 1995; De La Chapelle et al., 1998), which includes both a recovery process and the subsequent development of new grain boundaries. During *recovery*, dislocations re-arrange into lower energy configurations know as dislocation walls (White, 1977; Urai et al. 1986; Borthwick et al. 2014) accompanied by re-orientation of the crystalline lattice. With ongoing recovery, dislocation walls gradually transform into subgrain boundaries, which manifest as distinct planes of low lattice

misorientation (also called low-angle grain boundary) (Weikusat et al., 2017b). Eventually, a new high-angle grain boundary develops if the lattice misorientation exceeds a critical angle of about 3° to 5° for ice (Weikusat et al., 2011a,b). This process effectively reduces grain sizes as existing grains are split in two or more parts. The *spontaneous nucleation* of new grains or grain-embryos could also efficiently reduce grain sizes. However, this is thought to be very unlikely in the absence of strong chemical driving forces, as is the case for ice (Drury and Urai, 1990; Humphreys and Hatherly, 2004; Faria et al., 2014b).

The grain size results from a combination of grain growth and grain size reduction by polygonisation (Alley et al., 1995; De La Chapelle et al., 1998; Montagnat and Duval, 2000; Mathiesen et al., 2004; Roessiger et al., 2011), but potentially grain dissection is an additional grain-size-reducing process in ice as discussed in PAPER III. In various deep ice cores, after a stage of grain size increase, a stabilisation in grain size is observed with increasing depth (Li et al. 1998; Montagnat et al. 2012; Fitzpatrick et al. 2014; Weikusat et al. 2017a; Faria et al. 2014a and references therein). This implies a stronger relative contribution of grain-size-reducing mechanisms, once stable grain sizes are achieved. Previously, depth was used to describe regimes of dominating recrystallisation mechanisms (Alley et al., 2005; De La Chapelle et al., 1998). However, physical variables such as temperature and strain rate are likely to have a first-order control on the dominating mechanisms, which is expressed in the recrystallisation diagram (Faria et al. 2014b, section 5.3 therein). This diagram illustrates the contribution of recrystallisation mechanisms with respect to grain size evolution. It describes an attractor surface in the 3D space of the three dependent variables strain rate, temperature and grain size. If two variables are kept constant (such as temperature and strain rate) the third (grain size) will evolve towards this surface, where equilibrium is achieved.

1.3 Air bubbles in ice

1.3.1 Evolution of air in ice with depth

Ice sheets contain significant numbers of air bubbles as second phases in their upper approximately thousand meters and air hydrates below. This illustrates the importance of investigating the micro-dynamic effects of air bubbles. In the uppermost layers of the ice column, snow particles re-arrange and merge to firn by compaction and sintering processes (Wilkinson and Ashby, 1975; Colbeck, 1983; Blackford, 2007). This is accompanied by porosity reduction and described by various firn densification models (Herron and Langway, 1980; Barnola et al., 1991; Freitag et al., 2013). In the permeable firn, the pore spaces are connected to each other and the atmosphere, whereas below the firn-ice transition individual air bubbles are sealed off (Schwandner and Stauffer, 1984; Stauffer et al., 1985). According to Maeno and Ebinuma (1983), the firn ice transition is reached at a critical density of about 820 kg/m^3. However, several studies suggest high variability in critical densities as a function of the firn and snow

types that result from different climatic conditions (Alley et al., 1982; Johnson, 1998; Freitag et al., 2004; 2103).

Below the firn-ice transition, the bubble sizes decrease as a function of overburden pressure and surface tension counter-acting the inner bubble pressure. This process is accommodated by evaporation, diffusion and precipitation of matter through the gas phase, which maintains spherical bubble shapes depending on strain rate and temperature (Alley and Fitzpatrick, 1999). In ice sheets, this continues until a transition zone where air bubbles transform in hydrates (Miller, 1969; Shoji and Langway, 1982) at about 600 to 1300 m (Lipenkov, 2000; Ohno et al., 2004; Hondoh, 2009; Uchida et al., 2014). The "brittle zone" is found closely above this transformation. Ice samples from this zone are marked by crack formation and decreasing quality soon after they are released from surrounding pressures in the ice column (Uchida, et al., 1994). Crack formation and brittle sample behaviour is a result of over-pressure of air bubbles after extraction of the ice core section.

1.3.2 Mechanistic effects of air bubbles in ice

The mechanisms causing firn densification have implications on several other processes. For examples, air bubbles provide a unique record of the paleo-atmosphere (Fischer et al., 2008; 2010; Lüthi et al., 2008; Schmitt et al., 2012). As air bubbles are in exchange with the atmosphere until the firn-ice transition, firn densification models are important to understand the incorporation of this record once pores are closed off. These models also improve ice sheet mass balances. Remote sensing is typically used for large-scale ice-sheet mass balances (e.g. Rignot et al., 2008), but the surface elevation can be modulated by accumulation, melting and firn densification (Arthern and Wingham, 1998; Zwally and Li, 2000), which is discussed with recent densification models (Ligtenberg et al., 2011). An understanding of the mechanisms involved in firn densification is important for the refinement of densification models.

At shallow depths in firn, apart from compaction of the pore space, grain boundary sliding is assumed to be a main deformation agent (Alley, 1987). With ongoing densification, a transition from grain boundary sliding to dislocation creep at a critical density of 550 kg/m³ is suggested by Maeno and Ebinuma (1983). This is used as a characteristic for the progress of densification in some densification models (e.g. Arnaud et al., 2000). However, recent studies imply an even shallower onset of dislocation creep (Freitag et al., 2008; Faria et al., 2014b, appendix B therein) or even the absence of grain boundary sliding (Theile et al., 2011). This is consistent with observations of dynamic recrystallisation in shallow ice and firn (Kipfstuhl et al., 2009), which indicate strain energies as driving forces that imply the activation of dislocation creep. The occurrence of dynamic recrystallisation is further discussed in PAPER I. In addition, an understanding of processes active within firn is important as microstructural properties such as grain size or CPO may be inherited from firn in deeper levels of the ice sheet (Kennedy

et al., 2013; Riche et al., 2013; Calonne et al., 2017). However, whether such inheritance is possible is questionable as numerical simulations by Llorens et al. (2016a,b) and simulations presented in this thesis (PAPER I-III) indicate that these properties are rapidly overprinted during deformation and recrystallisation.

The study of the ice-air aggregate has implications beyond understanding processes in firn and in the firn-ice transition. Air bubbles are stable until the air-hydrate transformation and form an abundant second phase, suggesting that the inclusion of their micro-dynamic effects is important for the development of a mechanistic ice flow-law. The presence of air bubbles is observed to decrease the rate of grain growth (Levi and Ceppi, 1982; Nasello et al., 1992). This is related to grain boundary migration being affected by air bubbles, which are either dragged along with the grain boundary causing a significant decrease in grain boundary mobility or cause pinning of grain boundaries (Arena et al., 1997; Azuma et al., 2012).

Numerical modelling of surface-energy-driven grain growth by Roessiger et al. (2014) identified three regimes of grain growth in the ice-air aggregate: In regime 1, the bubble spacing is significantly larger than the grain diameter, which allows relatively unhindered growth of grains independent of bubbles. The grain growth rate is the same or similar to single-phase ice. Regime 2 is a transitional regime, where grain diameters decrease towards the value of bubble spacing. This is accompanied by a decrease in grain growth rate until the third regime is reached. In regime 3, a steady-state growth is achieved as the bubble spacing and grain diameter remain similar and bubbles are mainly found in grain boundary triple junctions. This regime is again characterised by a constant grain-growth rate, which is now significantly lower than in regime 1. Therefore, the achievement of the third regime depends on the number and size of air bubbles.

The abundance and size of air bubbles is suggested to depend on temperature and accumulation rate and hence, on the conditions prevailing during snow deposition (Lipenkov, 2000). The study by Bendel et al. (2013) supports this assumption by showing a correlation between the abundance of bubbles and climate proxies such as oxygen isotopes and dust concentration. A lower abundance of bubbles is observed in Holocene relative to glacial ice. Furthermore, Bendel et al. (2013) explain that low numbers of bubbles correlate with large air bubbles and, in turn, where large numbers of bubbles are observed, small bubbles predominate. Bendel et al. (2013) observe small-scale and sub-seasonal variations of bubble number densities and explain these with stronger firn layering in glacial times compared to recent firn. Whether ice-flow has an effect on number and distribution of air bubbles remains questionable, numerical techniques developed in the course of this thesis (PAPER I) help to investigate this effect.

Strain markers help to assess the integrity of the paleo-climate signal, which may be disrupted by ice-flow (section 1.1; Faria et al., 2010). Such markers are typically faint as strong deformation of pure polycrystalline ice is usually masked by extensive deformation (Llorens et al., 2016a,b). Apart from

folding of visible dust layers or "cloudy bands", as observed in deep ice cores (Alley et al., 1997; Samyn et al., 2011; Fitzpatrick et al., 2014; PAPER IV), elongated bubbles may indicate the local strain. Elongated bubbles shapes are observed in samples of highly-deformed ice-sheet ice (Russel-Head and Budd, 1979; Alley and Bentley, 1986; Fitzpatrick, 1994). The elongation of an air bubble is a function of the relative effectiveness of deformation elongating the bubble and diffusive (evaporation and precipitation) processes, which promote spherical bubble shapes (Alley and Fitzpatrick, 1999; Redenbach et al., 2009). Accordingly, elongated bubbles are favoured at high strain rates and low temperatures, that is, if the relative time for diffusive or surface-energy equilibrating processes is lower than for deformation causing the elongated shapes. The study by Alley and Fitzpatrick (1999) proposes that the use of air bubbles as strain markers is only valid relative to the effectiveness of the diffusive processes. The latter depend on the size of air bubbles, which explains the tendency for small bubbles to be less elongate.

2 Motivation and objectives of this thesis

Section 1 highlights the necessity for further investigation into the micro-dynamic processes in ice, which forms the precursor for a new mechanistic ice flow-law. Laboratory experiments are useful, but cannot achieve natural strain rates of the order of 10^{-13} to 10^{-12} s^{-1} (Montagnat et al., 2012; Weikusat et al., 2017a) and therefore need extrapolation from field observations. On the contrary, records of natural microstructures usually represent only a depth-series along an ice core and cannot resolve the microstructural development over time or strain. With increasing computer power, numerical modelling has become a useful tool to support experiments and ice core studies (see also review by Montagnat et al., 2014b). Numerical modelling at prescribed deformation conditions, provides a time-resolved microstructural evolution and insights into strain energy and strain distribution, which are usually hardly visible in natural ice (Llorens et al., 2016a,b). In this thesis, these processes are investigated by means of multi-process numerical microstructure-models based on the modelling framework Elle (Bons et al., 2008). Five general objectives of this thesis can be identified:

- **[Microstructure and rheology]** A general objective of this thesis is to investigate the dynamic behaviour of deformation and recrystallisation mechanisms with respect to microstructural properties (CPO, grain size, etc.). With knowledge of how these mechanisms affect microstructure evolution, microstructures obtained from ice cores can be used as an indicator for prevailing deformation conditions and rheology in the ice column. For the first time, grain-size-reducing mechanisms are included in the numerical procedure. This is expected to allow the development of a microstructural steady-state that reflects the prescribed numerical deformation conditions. The thesis aims to (1) investigate how the deformation conditions affect the activity of micro-dynamic mechanisms and (2) to obtain information how the mechanisms affect microstructural properties.

This supports the development of conceptual models on how the microstructure reflects rheology, which is required for a physically-based ice flow-law.

- **[The ice-air aggregate]** Another major objective of the thesis is to investigate the abovementioned micro-dynamic mechanisms in the ice-air aggregate. The thesis investigates the effect of air bubbles on deformation and assesses the importance of dynamic recrystallisation in the shallow levels of ice sheets. Special attention is drawn to strain distribution in the ice-air aggregate and its implications on microstructural properties such as grain sizes, grain shapes and CPO.
- **[From micro- to macro-dynamics]** The goal of this research is to demonstrate that the small-scale interaction of microstructural properties, deformation and recrystallisation mechanisms has implications for the larger scale. This is relevant for disciplines such as paleo-climate research or ice-sheet dynamics.
- **[Link with natural samples]** In addition to the abovementioned objectives, the thesis intends to present the first comparisons of results from this numerical approach with natural ice. This puts the numerical results into perspective, helps to reassess the numerical approach and suggests future scientific and methodological objectives.
- **[Developing the numerical procedure]** A central objective and requirement of this project is the development, implementation and validation of new methods in the numerical approach. This is necessary to enable the scientific studies proposed above. Specifically, this work aims to provide the first explicit numerical approach that combines polyphase and polycrystalline deformation by dislocation creep and dynamic recrystallisation during microstructure evolution. Furthermore, the new approach should consider grain-size-reducing mechanisms. Section 3 provides an overview on methodological achievements.

3 Numerical microstructure-modelling

3.1 Basics of the numerical procedure

The current numerical procedure is not only applicable to ice, but any polyphase polycrystalline aggregate. For instance, the study of Ran et al. (in prep.) uses the numerical approach for simulations on the deformation of pebbles in isotropic and anisotropic matrices. Table 1 summarises the most significant updates. Figure 1 illustrates the numerical procedure, highlighting the new developments (Fig. 1, red-framed boxes red labels). A detailed summary of methodological developments is provided in the appendix of this thesis (appendix A.1). The basics of the numerical approach are outlined below. For more detail, the reader is referred to section 3.2, the cited literature and to the methodological descriptions in PAPER I-IV.

Table 1: Summary of the updates in the numerical procedure made during this thesis. Changes were made in about 10 standalone process-codes, ranging from minor bug-fixes to extensive re-programming. More than 15 new process-codes were created. All changes were accompanied by debugging, testing and documentation of the code. Additional MATLAB and bash-scripts were created along with the C/C++ Elle codes.

Type of code	Purpose	Changes for this study
Polyphase grain boundary migration	• grain boundary migration for polyphase, polycrystalline aggregates, driven by surface- and strain-energies	• update of any part of the code to consider more phases • store *bnode* driving forces • extensive debugging, sensitivity studies and comparison with analytical solution
Recovery	• rearranging the intracrystalline lattice orientations, annihilate dislocations	• extensive debugging and commenting in the code • exclusion of phases such as air
Grain size reduction by polygonisation	• allow insertion of new high-angle grain boundaries between *unode* clusters of misorientation exceeding a critical value	• code provided by A. Griera • incorporation in the multi-process procedure • debugging and sensitivity studies • exclusion of phases such as air
VPFFT output to Elle	• conversion of VPFFT output to Elle microstructure • update of *bnode* and passive marker positions according to local strain fields • update of CPO and dislocation density in *unodes*	• debugging and improvement of passive marker grid calculation • extensive update of the whole algorithm to compute deformation tensors and allow finite-strain analysis
Topology checks	• perform all pre-existing topology checks within one process-code • allow merge of non-neighbouring *bnodes* and deletion of small grains below resolution threshold	• development of algorithms for new topology checks • programming of entire C++ code
Control program	• control the multi-process simulation in an user-friendly way • read input and store results perform basic post-processing	• programming of the entire bash script
Various post-processing tools	• determine mean grain sizes, shape parameters (perimeter ratio) • process slip system activities, stress tensors, driving forces for grain boundary migration • quantification of strain localisation • visualisation (passive marker grids, maximum stretching directions, etc.)	• development of new post-processing analyses • programming a suite of about 10 C++ codes and additional MATLAB scripts, some based on MTEX (Bachmann et al., 2010)

Table 1: continued.

Type of code	Purpose	Changes for this study
Strain-energy-driven recovery	• scale the amount of lattice re-orientation by recovery to the numerical time-step • allow strain energy minimisation as driving force and a new dislocation density model based on lattice-misorientations	• development of the new algorithm • implementation based on the recovery code and change of governing equations
Grain boundary sliding	• assume grain boundary sliding by adding a soft "boundary phase" for VPFFT	• development of the technique to allow a boundary phase • programming of two new C++ codes
3D grain growth model	• 3D grain growth simulations, which can provide an input for 3D VPFFT	• development of algorithm • programming of the new C++ (not based on Elle)

The numerical modelling platform Elle (Jessell et al., 2001; Bons et al., 2008; Piazolo et al., 2010) was employed and further developed in the course of this thesis. Elle simulates the dynamic interaction of multiple physical deformation and recrystallisation processes. Each of these processes is programmed in a discrete process-code or module. Successively running each module over a short numerical time-step, approximates natural conditions, where the processes operate concurrently. The schematic numerical setup is illustrated in Fig. 1A. For the simulations in this thesis, each increment of deformation by VPFFT (full-field crystal viscoplasticity code) was followed by a recrystallisation loop successively running grain boundary migration, recovery and polygonisation (PAPER I-III, appendix A.2.1). The numerical strain rate resulted from the strain increment predicted by the dimensionless VPFFT code and the total numerical time over which the recrystallisation loop was performed (see PAPER I-II).

The Elle platform provided the data structure necessary to create a numerical microstructure. In Elle, two-dimensional microstructure is discretised in a set of contiguous polygons called *flynns* in a cell with fully wrapping and periodic boundaries. The *flynns* are defined by straight boundaries joining boundary nodes (*bnodes*) in either double- or triple junctions. The *bnodes* are successively moved to achieve grain boundary migration and apply the local strain after an increment of VPFFT. To store intracrystalline properties such as CPO, dislocation density or local strain rate, a regular grid of unconnected nodes (*unodes*) is superimposed on the *flynn* network. As VPFFT requires re-meshing of *unodes* into a regular grid after each simulation step, the deformation was applied to another set of *unodes*, which served as passive markers.

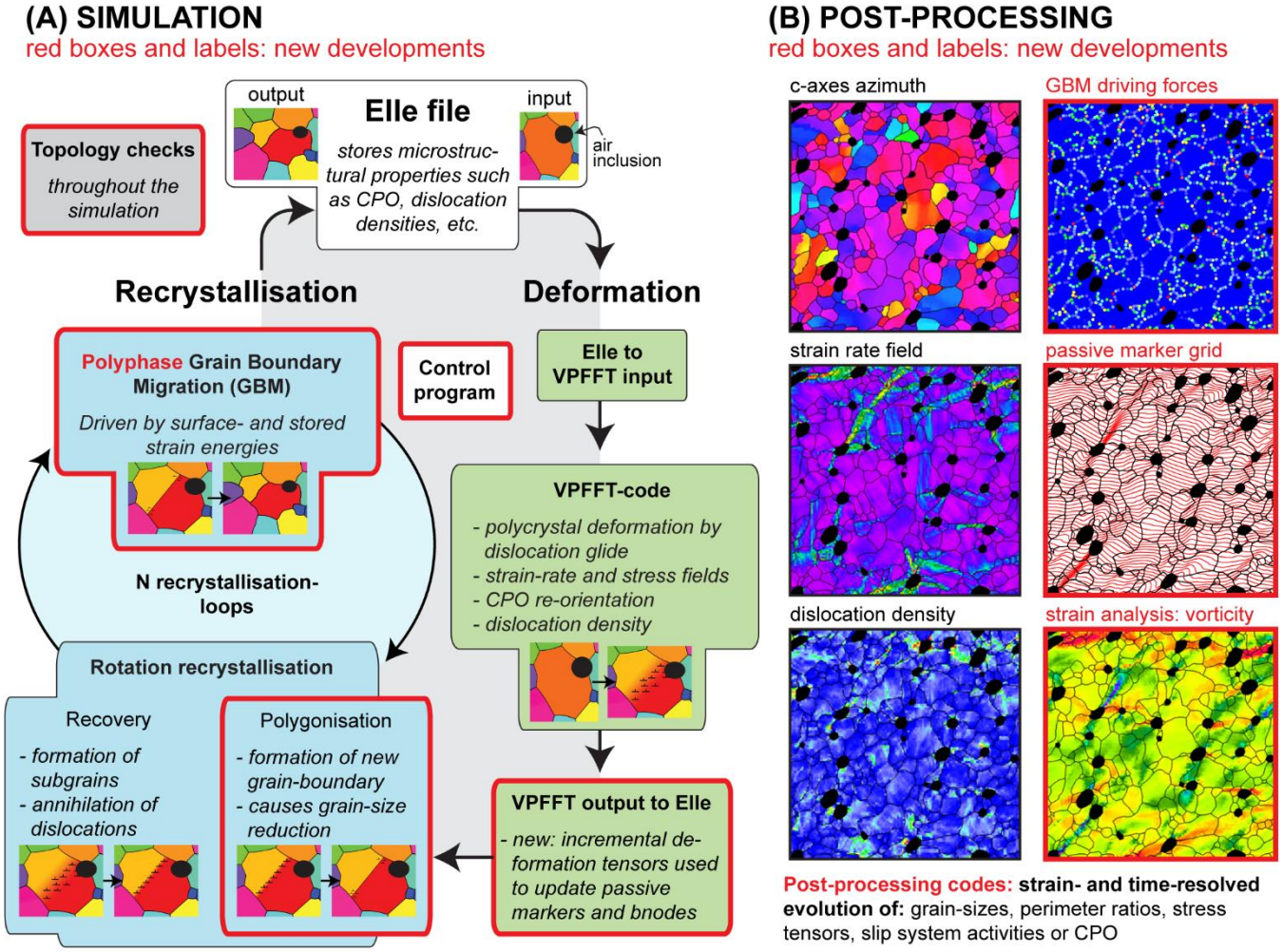

Figure 1: Overview on the complete numerical procedure for modelling deformation and recrystallisation in the ice- and ice-air aggregate. New developments are highlighted as red boxes and red labels. (A) Schematic flow-chart of the multi-process simulation setup consisting of several standalone process-codes for deformation and recrystallisation (edited after PAPER I). (B) Schematic summary of available post-processing tools using a low-resolution, dextral simple-shear simulation on the ice-air aggregate. The numerical strain rate was set to $4 \cdot 10^{-11}$ s^{-1} at a temperature of -30°C, results shown for a shear strain of $\gamma = 1$, equivalent to ≈ 40% of vertical shortening. Further post-processing tools are mentioned below, they allow calculation and visualisation of the evolution of microstructural parameters over strain- or time.

The numerical approach used in this thesis was developed based on the methods used for previous studies (Lebensohn, 2001; Becker et al., 2008; Griera et al., 2011; 2013; Roessiger et al., 2011; 2014; Llorens et al., 2016a,b). Roessiger et al. (2011) use Elle to model the competition between normal grain-growth and grain size reduction. Roessiger et al. (2014) present a polyphase grain boundary migration code based on Becker et al. (2008) and apply it to normal grain-growth in the ice-air aggregate. This approach only assumes surface-energy-driven grain boundary migration and is not coupled to deformation. Based on preliminary model setups shown in the review by Montagnat et al. (2014b), the study by Llorens et al. (2016a) presents simulations coupling numerical approaches to simulate viscoplastic deformation (VPFFT) and recrystallisation in ice systematically. They assume strain-energy minimisation as an additional driving force for grain boundary migration (i.e. SIBM) and apply an

approach to simulation recovery (Borthwick et al., 2014). However, the approach by Llorens et al. (2016a,b) does not take into account grain-size-reducing mechanisms or second phases such as air.

To accomplish the scientific objectives of this thesis, thorough programming work was an essential part of the study as the necessary simulation codes had to be developed or required extensive changes (see Table 1, Figure 1). The thesis involves the development, implementation and testing of an updated numerical approach. In particular, the new approach considers additional phases such as air-inclusions, and assumes grain size reduction by polygonisation. Along with the new numerical modelling techniques, new post-processing analyses and new topological routines were developed and implemented. The topological routines identify and resolve problems in the discretisation of the microstructure changing under deformation and recrystallisation. This increases the robustness of simulations and allows more complex and realistic grain topologies, more closely replicating those found in natural microstructures during dynamic recrystallisation. Extensive validation, debugging and the comprehensive documentation of the new developments complemented any change in the numerical procedure. All codes used and developed in the course of this thesis, are provided in a digital appendix.

3.2 Numerical modelling approaches for deformation and recrystallisation

3.2.1 Full-field crystal viscoplasticity

To include deformation, the VPFFT by Lebensohn (2001) is coupled to Elle by Griera et al. (2013). VPFFT assumes deformation by dislocation glide including the full, mechanically-anisotropic crystallography and uses a non-linear viscous rate-dependent law. VPFFT is based on calculating the mechanical fields from a kinematically admissible velocity field that minimises the average local work-rate under compatibility and equilibrium constraints (Lebensohn, 2001; Lebensohn et al., 2009; Griera et al., 2013). The constitutive equation (Eq. 2) predicts the strain rate $\dot{\varepsilon}_{ij}(\boldsymbol{x})$ at each *unode* position in the grid $\boldsymbol{x}$ as a function of the deviatoric stress (σ'_{ij}), a reference shear rate ($\dot{\gamma}_0$) and the sum of the shear strain rates ($\dot{\gamma}^s$) on N individual slip systems.

$$\dot{\varepsilon}_{ij}(\boldsymbol{x}) = \sum_{s=1}^{N} m_{ij}^{s}(\boldsymbol{x})\dot{\gamma}^{s}(\boldsymbol{x}) = \dot{\gamma}_0 \sum_{s=1}^{N} m_{ij}^{s}(\boldsymbol{x}) \left(\frac{m_{ij}^{s}(\boldsymbol{x})\sigma'_{ij}(\boldsymbol{x})}{\tau^{s}(\boldsymbol{x})} \right)^{3} \tag{2}$$

In VPFFT, each individual slip system s is defined by a glide resistance or critical resolved shear-stress (τ^s) and its orientation stored in the symmetric Schmidt tensor (m_{ij}^s). As the stress- and strain rate fields are initially unknown, an iterative solver based on Fast Fourier Transformation is implemented. In addition to the mechanical fields, VPFFT predicts lattice re-orientation and dislocation densities following the model by Brinckmann et al. (2006). In the Elle file, the *bnode* and passive maker positions were updated according to the local strain field after every deformation step by VPFFT. For this thesis,

the theoretically infinitely soft air phase was numerically described as a mechanically isotropic ice Ih crystal with equal critical-resolved shear stresses 5000-times lower than on the ice-basal plane. The resulting numerical error is minor, as discussed in PAPER I. Alternatively, future studies could use an approach that assumes vanishing stresses for *undoes* belonging to the air phase (Lebensohn et al., 2011; 2013). The handling of VPFFT and related codes is outlined in appendix A.2.2.

3.2.2 Numerical modelling of dynamic recrystallisation

A major requirement for the study in PAPER I is the update of the grain boundary migration routine to take into account a second phase such as air. To consider strain-induced energies in the polyphase approach by Roessiger et al. (2014), the algorithms of existing codes (Montagnat et al., 2014b, Llorens et al., 2016a) are adopted. The front-tracking approach for grain boundary migration was based on an energy-minimisation system first presented by Becker et al. (2008). The grain boundary velocity is determined by the minimum in the energy-field around each *bnode*. In addition to surface-energies (Becker et al., 2008) and an area energy achieving conservation of mass in polyphase aggregates (Roessiger et al., 2014), strain-induced energies are added to the total energy field. The incremental displacement of a *bnode* (Δx) is a function of the driving force (S), the numerical time-step (Δt) and the grain boundary mobility (M), which itself is a function of an intrinsic mobility (M_0) and temperature (T) (Eq. 3).

$$\Delta x = SM(\, M_0, T(°C)\,)\Delta t \tag{3}$$

The driving force (S) is obtained using four small orthogonal trial displacements of that *bnode*. For each trial displacement, the total change in free energy is determined, defined as the sum of the change of the individual energies (surface- and strain energy). Accordingly, each *bnode* is moved in the direction of maximum free-energy reduction.

At phase-boundaries and intra-phase boundaries, the approach is adjusted to allow scaling the contribution of strain-energy from 0 (do not consider strain-energy for this boundary-type) to 1 (consider 100% of the strain-energy). This allows modelling of purely surface-energy-driven migration of ice-air boundaries and air-air boundaries, which exist for numerical reasons. The dislocation density model used by VPFFT only assumes ice basal-plane dislocations, but non-basal dislocations exhibit strain energies up to four times higher than basal dislocations (Hondoh, 2000). Therefore, a scaling of strain-energies to the non-basal activity predicted by VPFFT is included in the new grain boundary migration code (application in PAPER II).

Intracrystalline recovery is modelled using the approach described in Llorens et al. (2016a). Similar to the grain boundary migration code, an energy minimisation system is used. Each *unode* is regarded as a small crystallite characterised by a lattice misorientation (θ) with respect to its first-order neighbours. Misorientation is the difference in lattice orientation between two *unodes*, which increases the total free

energy of the local system. A change in misorientation ($d\theta$) leads to a change in free energy ($d\gamma(\theta)$). Small trial rotations are used to determine which lattice rotation would result in the maximum decrease in local energy. The amount of lattice rotation in the *unode* (ω) was calculated according to the energy decrease for this trial rotation and a "mobility" term (M) (Eq. 4, see Borthwick et al. (2014) and Llorens et al. (2016a) for details).

$$\omega = M \frac{d\gamma(\theta)}{d\theta} \tag{4}$$

For this thesis, a polygonisation routine programmed by Albert Griera is incorporated in the numerical setup, which allows grain size reduction during the simulations. The approach finds *unode* clusters characterised by misorientations to other clusters below a critical angle (in the models set to 5°), which defines high-angle grain boundaries. The new grain boundaries (defined by *bnodes*) are inserted at *unode*-cluster boundaries. In order to use the approach during the numerical setup, the new code was tested and debugged for this thesis. The polygonisation routine is associated with the recovery code, which models the progressive transformation of dislocation walls to subgrain boundaries. The polygonisation together with the recovery code simulate the process of "rotation recrystallisation" (Fig. 1A). To consider the presence of air inclusions during rotation recrystallisation, the option to exclude phases from the calculation is implemented. The handling of all recrystallisation codes is outlined in appendix A.2.3.

3.3 Further developments in the numerical approach

Apart from the update of the process codes for deformation and recrystallisation, more developments in the Elle/VPFFT approach were achieved during this thesis and are listed below. The implementation of the updated approach, including polyphase grain boundary migration, recovery, polygonisation and VPFFT, required **(A) extensive testing, debugging and development of new topological routines**. To be compatible with the updated numerical approach, new post-processing utilities were developed and implemented and are now available for Elle/VPFFT (A.2.4, A.4). In particular, **(B) a post-processing routine for finite-strain analyses** was developed and implemented (A.4.4). Furthermore, other process-codes were developed and implemented in Elle in the course of this thesis, but are not yet applied to scientific questions raised by the thesis. However, these codes provide the base for ongoing and future studies. A detailed summary of these developments is provided in appendix (A.4). The most significant of these developments are the implementation of **(C) an updated recovery code** (A.4.1), an algorithm to assume **(D) grain boundary sliding** (A.4.2) and **(E) a suite of tools to prepare and run the simulation**. All codes are found in the digital appendix to this thesis.

(A) The comparison of the grain boundary migration code to an analytical solution shows low numerical errors if numerical time-steps are low (A.5). Further sensitivity tests for the simulations in this thesis

revealed the necessity for updated and more sophisticated topological checks throughout the simulations (A.2.4). A new, comprehensive "topology-check" module was programmed for Elle, which solves both existing and new topological issues. In particular, the new topological routine grain dissection during SIBM (see PAPER II for details) and deletes *flynns* below the resolution threshold.

(B) The simulations provide information on the instantaneous strain rate. However, structures such as elongated grains in ice and other rocks are the result of accumulated finite strain. In particular, in natural ice these structures are overprinted by efficient recrystallisation (Llorens et al., 2016a,b). The new finite strain-analysis utility computes finite strain information for the microstructure (appendix A.4.4). For the new utility, an updated approach for finding the new positions of *bnodes* and passive markers after an increment of deformation was created (cf. "VPFFT output to Elle", Fig.1A), which is based on calculating incremental deformation tensors for each *unode*. In a post-processing step, the tensors are used to calculate further information such as maximum finite strain, strain-ellipse ratio, vorticity and maximum stretching direction (see vorticity in Fig. 1B). The strain-analysis code is applied in a numerical study on the deformation of pebbles by Ran et al. (in prep.).

(C) The new strain-energy-driven recovery code is developed and implemented (appendix A.4.1), but not yet applied within the multi-process numerical setup. The new approach determines the angular velocity of lattice re-orientation ($\dot{\omega}$) as a function of the change of strain-energy (dE_ε) with a change in lattice-misorientation ($d\theta$) (Eq. 5). A rotation resistance parameter is implemented (A), but proper adjustment of this parameter to temperature or similar properties remains part of future research.

$$\dot{\omega} = A\left(\frac{dE_\varepsilon}{d\theta}\right)^3 \tag{5}$$

Similar to grain boundary migration, the updated recovery approach is based on minimising the strain-energy stored in a *unode*. Hence, the amount of lattice rotation in the new approach is determined by the multiplication of the velocity with the numerical time-step, which is not implemented in the "old" approach. To determine the strain-energy as a function of lattice misorientation, the new approach requires the use of an updated dislocation density model.

(D) The development and implementation of a possibility to consider grain boundary sliding during VPFFT is another achievement of this project (appendix A.4.2). Grain boundary sliding is assumed by assigning "boundary properties" to *unodes* that are very close to *bnodes*. Similar to the description of air in VPFFT in PAPER I, the boundary phase is described as an isotropic crystal. Therefore, a lattice re-orientation and dislocation density is predicted that needs to be removed from the boundary *unodes* in subsequent step. The grain boundary sliding approach requires further testing and development to achieve high strains and couple it to recrystallisation processes.

(E) Apart from the aforementioned developments, new bash-script to control the multi-process simulation is available together with bash-scripts for post-processing and several MATLAB routines. Additionally, to generate a 3D foam texture that serves as a simulation input for 3D VPFFT simulations, a 3D Potts model for grain growth was developed and programmed (A.4.3).

4 Synthesis and main outcome of the thesis

This thesis investigates the dynamics of deformation and recrystallisation mechanisms with respect to microstructure evolution in pure polycrystalline ice as well as in ice-air aggregates. The results have implications for small scale-dynamics, which affect the rheology of ice sheets and glaciers on the large scale. The most important conclusions (1-5) are listed below, followed by a more detailed description.

1) The simulations in this thesis allow the development of a steady-state not only in CPO, but also in grain size and stress, which is achieved by considering grain size reduction. With this, the simulations are for the first time capable of approximating steady-state tertiary creep conditions. The thesis shows that in addition to polygonisation, grain dissection is an efficient grain-size-reducing process in ice.

2) By using a more complete suite of micro-dynamic mechanisms, the new numerical approach confirms that which mechanism is dominant is controlled by deformation conditions. Strain rate, temperature and, likely, impurity content control how the microstructure evolves.

3) The rate of microstructural changes (CPO, grain size) in ice is very high. Once a steady-state is achieved, microstructural properties are likely independent from the initial microstructure. Natural ice microstructures likely reflect the in-situ deformation conditions whereas the inheritance and preservation of CPO during the flow of ice appears unlikely.

4) Strain localisation is common in ice and ice deformation is generally more heterogeneous than previously thought. Air bubbles intensify strain localisation enabling a shallow onset of dislocation creep and dynamic recrystallisation.

5) Microstructural properties are likely important on a large range of scales. For instance, strain localisation can lead to the amplification of inhomogeneities and cause folding. The numerical methods of the thesis contributed to developing a conceptual model for folding in ice, which is based on mechanical anisotropy and applies to multiple scales.

1) Simulations reach steady state and approximate tertiary creep

The studies by Llorens et al. (2016a,b) simulated microstructure evolution during dislocation creep and concurrent dynamic recrystallisation in pure (Llorens et al., 2016a) and simple shear (Llorens et al., 2016b). This thesis adds a comparison of the two deformation modes and includes grain-size-reducing mechanisms. In both deformation modes, CPO evolves towards a stable pattern where c-axes are aligned with the maximum finite shortening direction (PAPER III). This CPO development is expected from natural polar ice and deformation experiments (Azuma and Higashi, 1985). PAPER III indicates only a minor influence of the amount of dynamic recrystallisation on CPO development, which is also consistent with observations from creep experiments (Budd and Jacka, 1989; Treverrow et al., 2012).

For the first time, this thesis implements grain size reduction by polygonisation in the numerical procedure (PAPER I-III). In addition to polygonisation, grain dissection can provide an effective grain-size-reducing mechanism in ice, which has not been considered before (PAPER II). While the activation of grain-size-reducing mechanisms has only a minor effect on CPO development (PAPER III), it allows the development of a steady-state microstructure by counteracting dynamic grain-growth and allowing a stable grain size to develop (PAPER II-III). This is consistent with the recrystallisation diagram by Faria et al. (2014b) predicting an equilibrium in grain size at stable deformation conditions. The development of a stable grain size is accompanied by reduced strain hardening and the development towards steady-state stresses (PAPER III). During creep experiments, the development of a steady-state in strain rate and stress is interpreted as a result of recrystallisation and seen as characteristic for tertiary creep, which is usually achieved after about 10% strain in laboratory experiments (Budd and Jacka, 1989; Treverrow et al., 2012; Faria et al., 2014b). Therefore, natural ice is usually assumed to deform in tertiary creep, which the numerical approach in this thesis can now approximate by assuming grain-size-reducing processes.

2) The deformation conditions control microstructure evolution

As mentioned in section 1.2, the occurrence of micro-dynamic mechanisms, and thus microstructural properties, is a function of deformation conditions instead of depth, which only has an indirect control (Faria et al., 2014b). This is supported by the simulation results presented in this thesis (Paper I-III). The results show steady-state microstructures that are independent of the initial microstructure, but depend on the prescribed strain rate (see also conclusion (4) and PAPER I-III). Furthermore, the simulations confirm that the development of CPO is a function of accumulated strain rather than time or stress (PAPER I-III). The study by Kerch (2016) revealed a CPO and grain size evolution in an alpine ice core from Colle Gnifetti glacier (Switzerland) that is comparable to the one repeatedly observed in polar ice cores down to their base (see review by Faria et al., 2014a and references therein). This supports the conclusion that the microstructural development is a function of deformation conditions as alpine ice cores are about an order of magnitude shorter than polar ice cores.

3) Microstructures reflect in situ conditions

After an initial stage of grain size increase, stable grain sizes in ice cores are typically observed within Holocene ice (Li et al., 1998; Montagnat et al., 2012; Fitzpatrick et al, 2014). However, comparatively distinct microstructural changes are evident where drill cores penetrate climate transitions (Durand et al., 2009; Weikusat et al., 2017a; Faria et al., 2014a,b and references therein). All pure shear simulations in this thesis (PAPER I-IV) predict significant microstructural changes in CPO or grain size to achieve a steady-state over comparatively low amounts of finite vertical shortening of approximately 30% or less (e.g. PAPER II). Contrary, finite vertical shorteningings ice sheets easily approach 100% at high homologous temperatures (Huybrechts et al., 2007; Kennedy et al., 2013; Rasmussen et al., 2013). Therefore, the simulations imply that the rate of CPO and microstructural change may be very high in natural ice. This implies that ice microstructures rapidly adapt to changes in deformation conditions and are likely to reflect the in-situ deformation conditions. The numerical simulations in PAPER I show that a decrease in rate of CPO development can be achieved by the presence of air inclusions. However, a significant change in CPO is still evident after applying 50% shortening, particularly where strain localisation is observed. Therefore, preservation and inheritance of CPO from firn and shallow to deeper levels, as suggested by several studies (Kennedy et al., 2013; Riche et al., 2013; Calonne et al., 2017), appears unlikely. The main inheritance is probably in impurity load, which influences the microstructure evolution (section 1.2).

4) Strain localisation is common in ice

Strain and strain-rate localisation is observed in all simulations presented in this thesis (PAPER I-IV), which in combination with other studies (Montagnat et al., 2011; 2014b, Llorens et al., 2016a,b; Weikusat et al., 2017a) shows that strain localisation is the rule rather than the exception in ice. However, strain localisation is difficult to observe in polar ice microstructures as grain shapes cannot easily mark deformation due to efficient recrystallisation at low strain rates (Llorens et al., 2016a,b; PAPER I). Numerical simulations store the actual accumulated strain in passive marker grids and thus can visualise strains heterogeneities and allow an examination of causes and evolution of strain localisation. In pure polycrystalline ice, strain localisation is related to viscoplastic anisotropy. Grains, or clusters of grains with initially suitable orientations for basal slip accommodate strain more efficiently and initiate strain localisation. With progressive strain, these localisation zones strengthen as the basal planes align or are deactivated in favour of other, more favourably oriented localisation zones. Deactivation occurs when either the orientation of the internal lattice or the localisation zone becomes less suitable to accommodate strain. Once deactivated, localised zones only rotate and move passively with the bulk deformation.

In addition to CPO, the presence of air bubbles controls strain localisation. Even if only minor fractions of air bubbles are present, strain localisation is intensified and localisation zones develop between

bubbles (PAPER I). Simulations on the ice-air aggregate imply that in the shallow ice and firn, dynamic recrystallisation can be expected (PAPER I). The occurrence of dynamic recrystallisation is consistent with evidence from natural firn microstructures presented by Kipfstuhl et al. (2009) and with the aforementioned conclusion (2) as the deformation conditions can vary significantly on the grain-aggregate scale due to strain localisation. Furthermore, dynamic recrystallisation implies dislocation creep as the predominant deformation mechanism. A shallow onset of dislocation creep independent of depth in ice is consistent with the findings of Freitag et al. (2008) and Theile et al. (2011) in natural polar firn and simulations.

5) Larger scale implications of microstructural properties

As the utilised VPFFT approach that predicts strain localisation is dimensionless, strain localisation may occur on a large range of scales. Therefore, the thesis demonstrates implications of microstructural properties and strain localisation on larger scales (PAPER IV). Visual stratigraphy unveils 10-centimeter scale folding of stratigraphic bands in the NEEM (North Greenland Eemian Ice Drilling) ice core (Samyn et al., 2011). Simulations in PAPER IV indicate that the observed folding is a result of the formation of fabric stripes or bands of CPO deviating from the bulk single maximum CPO (Alley et al., 1997). The formation of these kink-bands, also called "tilted-lattice bands" (PAPER IV) requires a highly anisotropic material and a well-developed single-maximum CPO. Local variations in CPO provide seeds for tilted-lattice bands, which allow strains to localise, lead to amplification of slight inhomogeneities, and cause folding. This folding mechanism is consistent with amplification of inhomogeneities proposed by Azuma and Goto-Azuma (1996) and shows how the microstructure and CPO can cause the development of larger-scale structures.

High-quality ice-penetrating radar images show large-scale folding and overturned folds (NEEM community members, 2013; Wolovick et al., 2014; MacGregor et al., 2014). The folds are interpreted to result from bedrock topography, melting and refreezing of ice close to bedrock or "slippery patches" of meltwater that allow subglacial slip and create disturbances on the scale of the observed folds (Bell, et al., 2014; MacGregor et al., 2014; Wolovick et al., 2014). The recent study by Bons et al. (2016) investigates the effect of converging flow and viscoplastic anisotropy on large scale folding at the onset of Petermann Glacier, North Greenland. Based on the methods developed for this thesis, the dimensionless VPFFT approach is applied to the large-scale by Bons et al. (2016) to show that folds form by lateral compression of mechanically anisotropic ice. A general assumption made in this thesis is that the large-scale flow of ice is affected by the properties of individual ice-crystals, which is supported by the study of Bons et al. (2016).

5 Future perspectives

Any contribution to scientific publications in the course of this thesis, compared the simulation results to natural polar (micro-)structures. The comparisons yield information on potential future research topics or reveal the shortcomings of the actual modelling approach. To solve these shortcomings, further improvements of the numerical procedure should focus on **(i)** the incorporation of a compressible air phase, **(ii)** the simulations predicting too high grain sizes and **(iii)** an observed mismatch in numerically predicted and natural CPO development during pure shear. Furthermore, to improve our understanding of how micro-dynamic mechanisms, microstructures and rheology are linked, **(iv)** comparison with polar and alpine ice microstructures from various deformation conditions are necessary.

i. The simulations in PAPER I assume an incompressible air-phase, whereas in natural firn, significant vertical shortening is achieved by compression of the pore space. The implemented area energy (Roessiger et al., 2014; PAPER I) allows compressibility, but needs scaling to parameters such as inclusion size and overburden pressure. Due to the conservation of mass requirement, the area fraction of ice and air should remain constant during the simulations. The decreasing amount of air due to compression could be counter-balanced by decreasing the size of the model box according to properties such as the composite Poisson's ratio of the ice-air aggregate, which can be calculated following Roberts and Garboczi (2000).

ii. Comparison with natural samples revealed unexpectedly large numerical grain sizes when applying natural strain rates in the simulations (PAPER I-II). The mismatch in predicted grain sizes may be solved by considering additional mechanisms such as grain boundary sliding or the effects of impurities. In particular, future research should question the employed parameters such as experimentally-derived mobilities and activation energies. The activation energies are shown to increase in the presence of air bubbles (Azuma et al., 2012), which efficiently reduces the grain boundary mobility according to Arrhenius-term that is typically employed for temperature dependent processes (e.g. Nasello et al., 2005). Benchmarks with natural samples could provide the base for such studies. In addition, the relative effectiveness of grain-size-reducing mechanisms such as polygonisation could be too low. This may be improved by integrating a time-dependant recovery approach (appendix A.4.1) and lowering the critical angles for high-angle grain boundary formation (was 5° for PAPER I-III, details in A.2.3), which would be consistent with Weikusat et al. (2011a,b), who suggested critical angles between 3° and 5°.

iii. The simulations presented in the thesis unveiled unexpected behaviour in numerical CPO development in comparison to natural ice. During pure shear simulations, the c-axes develop sub-parallel to the finite shortening direction. More precisely, the development of two single

maxima still being close to each other is observed (particularly PAPER III), which is consistent with natural samples (Budd and Jacka, 1989). These maxima are situated in plane, which is sub-parallel to the maximum shortening direction, but *perpendicular* to the maximum stretching direction (PAPER III). However, natural samples show c-axes tending to align in a plane *parallel* to both the maximum shortening and stretching directions (e.g. see Budd and Jacka, 1989, Figure 3 therein, Amery Ice Shelf). It is possible that the mismatch is due to the simulations lacking an important mechanism such as grain boundary sliding, which is suggested to affect CPO development (Fliervoet et al., 2011). Alternatively, the difference may be related to stereological issues. The 2D simulations cannot employ various natural stress fields such as converging flow at the onset of Petermann Glacier, North Greenland (Bons et al., 2016). Therefore, future research should envisage 3D VPFFT simulations. In the controlled setup, these simulations can cover the full suite of stress fields relative to CPO and provide an important contribution towards integrating mechanical anisotropy into ice flow-laws.

iv. Cooperation with ice-core drilling projects from a large range of deformation conditions are beneficial to benchmark models and parameterise micro-dynamic mechanisms. For instance, alpine ice typically deforms at higher strain rates than polar ice, whereas microstructure evolution in alpine and polar ice is potentially very similar (Kerch, 2016). Additionally, a new international ice-core drilling campaign in east Greenland aims to retrieve ice core samples from the Northeast Greenland Ice Stream (NEGIS). NEGIS represents a rapidly moving major drainage system of the Greenland ice-sheet and can be regarded as a large-scale example of strain localisation. The East Greenland Ice-core Project (EastGRIP, www.eastgrip.org) represents the first ice-coring project motivated by ice-dynamics research instead of paleo-climate reconstruction. EastGRIP will deliver samples from NEGIS that are deformed under higher strain rates than any other sample available from deep ice cores. In particular, the mechanical reasons for activation or deactivation of ice flow localising in NEGIS and other ice streams should form part of future research. A prediction of future localisation of ice flow would be a significant scientific progress towards a prediction of how ice sheets influence sea-level and climate changes.

Contributions to scientific publications

PAPER I

Steinbach, Florian, Bons, P. D., Griera, A., Jansen, D., Llorens, M.-G., Roessiger, J. and Weikusat, I.: *Strain localization and dynamic recrystallization in the ice–air aggregate: a numerical study*. Published in The Cryosphere, 10(6), 3071–3089. doi:10.5194/tc-10-3071-2016 (2016)

Scientific ideas	Data generation	Analysis and interpretation	Paper writing
Full development of the scientific idea of strain localisation in ice-air aggregate and relation to dynamic recrystallisation. Initial idea for models on ice-air aggregate by JR, IW and PDB	Generation of all data presented in the paper, apart from natural microstructure image. Previously, substantial work on program code together with AG, JR and MGL	All analysis and Interpretation with minor contribution of all co-authors	All paper writing. Proof-reading and comments by all co-authors

PAPER II

Steinbach, Florian, Kuiper, E. N., Eichler, J., Bons, P.D., Drury, M.R., Griera, A., Pennock, G.M. and Weikusat, I.: *Grain dissection: A new process for grain-size reduction in polar ice cores and numerical models*. Submitted to Frontiers in Earth Science, Cryospheric Sciences (2017)

Scientific ideas	Data generation	Analysis and interpretation	Paper writing
Initial development of the scientific ideas on grain dissection together with ENK. All ideas related to numerical modelling.	Generation of all numerical modelling data presented in the paper, including substantial work on program code together with AG. EBSD data by ENK, MRD and GMP. Fabric Analyser images by JE and IW	All analysis and interpretation of numerical modelling data in the paper. Further analysis and interpretation together with ENK and JE	All paper writing, apart from: ENK provided text for EBSD data, JE provided text for Fabric Analyser data. Proof-reading and comments by all co-authors

PAPER III

Llorens, M.-G., Griera, A., **Steinbach, Florian**, Bons, P. D., Gomez-Rivas, E., Jansen, D., Roessiger, J., Lebensohn, R. A. and Weikusat, I.: *Dynamic recrystallization during deformation of polycrystalline ice: insights from numerical simulations*. Published in Philosophical Transactions of the Royal Society of London A: Mathematical, Physical and Engineering Sciences, 375(2086). doi:10.1098/rsta.2015.0346 (2017)

Scientific ideas	Data generation	Analysis and interpretation	Paper writing
Support for MGL, who provided most scientific ideas. Contributing ideas on polygonisation	Generation of all data related to models with polygonisation. Remaining data generation by MGL	Supported analysis and interpretation, mainly on simulations with polygonisation	Most paper writing by MGL. Contribution of text on polygonisation, proof-reading and comments

PAPER IV

Jansen, D., Llorens, M.-G., Westhoff, J., **Steinbach, Florian**, Kipfstuhl, S., Bons, P. D., Griera, A. and Weikusat, I.: *Small-scale disturbances in the stratigraphy of the NEEM ice core: observations and numerical model simulations*. Published in The Cryosphere, 10(1), 359–370. doi:10.5194/tc-10-359-2016. (2016)

Scientific ideas	Data generation	Analysis and interpretation	Paper writing
Discussions with DJ, MGL and other co-authors on *their* ideas. Apart from this, no significant contribution.	No significant contribution. Numerical simulations performed by MGL	Interpretation of the numerical modelling results together with DJ and MGL. Assisting DJ in processing numerical modelling results	Most paper writing by DJ. Contribution to paper writing in form of proof-reading and commenting the text for further improvement

PAPER I

Strain localisation and dynamic recrystallisation in the ice–air aggregate: a numerical study

Florian Steinbach[1,2], Paul D. Bons[1], Albert Griera[3], Daniela Jansen[2], Maria-Gema Llorens[1], Jens Roessiger[1], and IlkaWeikusat[1,2]

1. Department of Geosciences, Eberhard Karls University Tübingen, 72074 Tübingen, Germany
2. Alfred Wegener Institute Helmholtz Centre for Polar and Marine Research, 27568 Bremerhaven, Germany
3. Departament de Geologia, Universitat Autònoma de Barcelona, 08193 Bellaterra (Barcelona), Spain

Published in *The Cryosphere*, 21 December 2016.

Abstract

We performed numerical simulations on the microdynamics of ice with air inclusions as a second phase. Our aim was to investigate the rheological effects of air inclusions and explain the onset of dynamic recrystallisation in the permeable firn. The simulations employ a full-field-theory crystal plasticity code coupled to codes simulating dynamic recrystallisation processes and predict time resolved microstructure evolution in terms of lattice orientations, strain distribution, grain sizes and grain-boundary network. Results show heterogeneous deformation throughout the simulations and indicate the importance of strain localisation controlled by air inclusions. This strain localisation gives rise to locally increased energies that drive dynamic recrystallisation and induce heterogeneous microstructures that are coherent with natural firn microstructures from EPICA Dronning Maud Land ice coring site in Antarctica- We conclude that although overall strains and stresses in firn are low, strain localisation associated with locally increased strain energies can explain the occurrence of dynamic recrystallisation.

1 Introduction

The ice sheets on Greenland and Antarctica are composed of snow layers, originally containing a large proportion of air, which are transformed into solid ice due to compaction and sintering processes (Herron and Langway, 1980; Colbeck, 1983). At the firn–ice transition, the air is sealed off in bubbles as the pores are no longer connected and do not allow exchange with air from other layers or the atmosphere (Schwandner and Stauffer, 1984; Stauffer et al., 1985). For this reason, the ice sheets are considered as valuable archives of the palaeoatmosphere (Luethi et al., 2008; Fischer et al., 2008). However, ice sheets are not static but rather flow under their own weight, which can potentially cause the palaeoclimatic record to lose its integrity (Faria et al., 2010). For the interpretation of these records it is essential to understand not only the deformation dynamics of polycrystalline ice but also the implications of a second phase in the form of air bubbles. For consistency, we use the expression "air bubbles" whenever referring to the natural material and air inclusion only for numerical models, where the individual units of air are neither interconnected nor communicating.

Compared to other abundant minerals on the surface, ice on Earth is always at high homologous temperatures ($T_h = T_{actual}/T_{meltpoint}$), close to its pressure melting point and therefore creeping under gravitational forces (Petrenko and Whitworth, 1999; Faria et al., 2014a). The macroscopic behaviour of the ice aggregate results from the local response of individual ice crystals and the distribution of second phases within the polycrystalline aggregate.

Deformation in the ice crystal is mainly accommodated by dislocations, meaning intracrystalline lattice defects gliding and climbing through the crystal lattice, which is known as dislocation creep (Shoji and Higashi, 1978; Schulson and Duval, 2009; Faria et al., 2014b). Ice Ih is the ice polymorph that occurs on Earth. It has a hexagonal symmetry and dislocation glide is primarily on planes perpendicular to the c axes (i.e. basal planes) or on pyramidal or prismatic planes. Dislocation glide in ice Ih is characterised by a strong viscoplastic anisotropy, with resistance to glide on basal planes at least 60 times smaller than on other planes (Duval et al., 1983). The strong preference for basal glide usually leads to an approximately single maximum crystallographic preferred orientation (CPO) with the c axes mostly aligned with the direction of maximum finite shortening (Azuma and Higashi, 1985). Early experimental studies by Steinemann (1954) show that such a single maximum CPO causes a mechanical anisotropy of a deformed aggregate of ice grains. This is supported by experiments by Gao and Jacka (1987), the review by Budd and Jacka (1989) and more recent studies by Treverrow et al. (2012).

Viscoplastic deformation of ice is accompanied by recrystallisation (Duval, 1979; Jacka and Li, 1994; Faria et al., 2014b), as is common in minerals at high homologous temperatures. Recrystallisation processes have direct implications on creep behaviour as they affect fabric development and hence the flow of ice (Duval and Castelnau, 1995; Castelnau et al., 1996; Duval et al., 2000). The nomenclature

to describe recrystallisation and microstructure varies among glaciology, geology and material science. For consistency, in this paper we employ the terminology proposed by Faria et al. (2014b).

Under static conditions and non-deformation-related normal grain growth (NGG) or static grain-boundary migration driven by surface-energy minimisation (Stephenson, 1967; Gow, 1969; Duval, 1985) leads to a microstructure with only slightly curved grain boundaries and 120° angles at grain triple junctions (foam texture). The resulting grain size distribution is log-normal according to Humphreys and Hatherly (2004, pp. 334–335). In contrast, strain-induced boundary migration (SIBM) as described by Duval et al. (1983) or Humphreys and Hatherly (2004, pp. 251–253) minimizes stored strain energy by migrating boundaries towards less strained neighbouring grains. Intracrystalline annihilation of dislocations by lattice reorientation into lower energy configurations, known as recovery (White, 1977; Urai et al., 1986; Borthwick et al., 2014), additionally lowers stored strain energies. Recovery accompanied by gradual formation of subgrain boundaries and ultimately new high-angle grain boundaries (e.g. polygonisation; Alley et al., 1995) is termed "rotation recrystallisation" (Passchier and Trouw, 2005). These recrystallisation phenomena operating during deformation are summarised by the term "dynamic recrystallisation" (DRX).

Recrystallisation processes operate concurrently, but the proportion of contribution of each mechanism varies. The DRX diagram by Faria et al. (2014b) describes the relative contributions as a function of strain rate and temperature, as was done before for quartz (Hirth and Tullis, 1992). According to these models, rotation recrystallisation is more dominant with higher strain rates, whereas strain-induced boundary migration dominates at higher temperatures.

In very shallow firn, at mass densities below 550 kg m^{-3}, compaction by displacement, rearrangement and shape change of snow particles is attributed to grain-boundary sliding (Alley, 1987), neck growth between grains by isothermal sintering (Blackford, 2007) and temperature gradient metamorphism (Riche et al., 2013). Once the critical density is exceeded, the dominating mechanism becomes plastic deformation by intracrystalline creep (Anderson and Benson, 1963; Faria et al., 2014b). For the EPICA Dronning Maud Land (EDML) ice core, this critical density is reached at around 20m depth (Kipfstuhl et al., 2009). However, more recent tomographic analyses on EDML samples by Freitag et al. (2008) provide evidence for an early onset of plastic deformation at shallow depths of 10 m. Simulations by Theile et al. (2011) suggest an even shallower onset of plastic deformation and the absence of grain-boundary sliding.

One way to determine which deformation mechanisms are operating is to study the microstructure of the deformed material (Passchier and Trouw, 2005; Kipfstuhl et al., 2009; Faria et al., 2014a, b). Apart from experiments, numerical simulations are increasingly used as a tool to establish the link between deformation mechanisms, boundary conditions and resulting microstructures (see review of Montagnat et al., 2014b). Unfortunately, most studies on ice deformation only considered pure ice without air

bubbles. Some exceptions are the experimental studies of Arena et al. (1997) and Azuma et al. (2012) and the numerical simulations of Roessiger et al. (2014) on grain growth of ice in the presence of air inclusions. Recent numerical modelling by Cyprych et al. (2016) indicates the importance of strain localisation in polyphase materials but does not include a description of microstructure evolution during recrystallisation. Systematic numerical studies of the effect of a second phase, in this case air, on plastic deformation and concurrent microstructure evolution during DRX are still lacking.

In this contribution we investigate the implications of air inclusions on deformation and recrystallisation to assess the importance of DRX at shallow levels of ice sheets. For that purpose, we for the first time employ an explicit numerical approach combining both polyphase crystal plasticity and recrystallisation. Particular focus is given to two microdynamical aspects, which are (1) the strain distribution in the polyphase and polycrystalline ice–air aggregate and (2) its relation to (deformation-induced) DRX.

2 Methods

2.1 Multi-process modelling with Elle

We used the open-source numerical modelling platform Elle (Bons et al., 2008; Jessell et al., 2001; Piazolo et al., 2010), as this code is very suitable to model the interaction of multiple processes that act on a microstructure. So far, Elle has been applied to a range of microdynamical processes, such as strain localisation and porphyroclast rotation (Griera et al., 2011, 2013), deformation of polyphase materials (Jessell et al., 2009) or folding (Llorens et al., 2013a, b). Recent applications of Elle codes utilised and updated for this study are on DRX in pure ice (Llorens et al., 2016a, b), grain growth (Roessiger et al., 2011, 2014), and folding in ice sheets in relation to mechanical anisotropy, both on the small (Jansen et al., 2016) and large scale (Bons et al., 2016). To simulate viscoplastic deformation of the polyphase and polycrystalline aggregate with concurrent recrystallisation, the full-field crystal viscoplasticity code VPFFT by Lebensohn (2001) was coupled to implementations of recrystallisation processes in Elle using the approach described in Llorens et al. (2016a, b). Here we only briefly explain the essentials of the modelling technique. The reader is referred to Jessell et al. (2001) and Bons et al. (2008) for the general principles of Elle. Details of the algorithms for grain-boundary migration can be found in Becker et al. (2008) and Roessiger et al. (2011; 2014), and for coupled VPFFT and recrystallisation in Llorens et al. (2016a, b).

2.2 Discretisation of the microstructure

The two-dimensional microstructure of ice and air inclusions is discretised in a contiguous set of polygons with fully wrapping and periodic boundaries (Fig. 1a; Llorens et al., 2016a, b; Bons et al., 2008). In the set-up used here, the polygons (termed *flynns*) are either ice crystals or air inclusions.

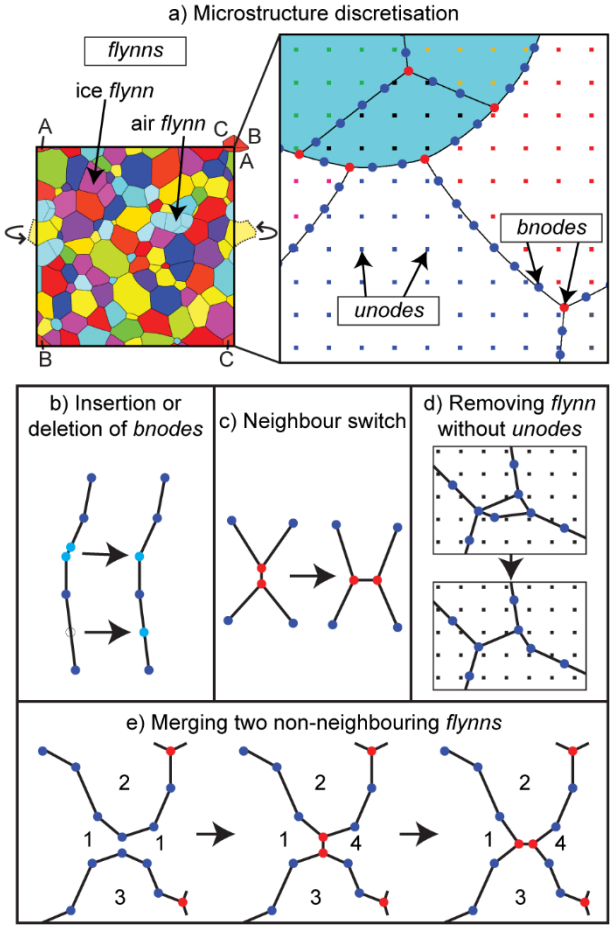

Figure 1: Microstructure discretization in Elle. (a) A contiguous set of polygons (*flynns*) is composed of boundary nodes (*bnodes*) and has periodic boundaries. An additional grid of unconnected nodes (*unodes*) is superimposed on *flynns* and *bnodes* to store intracrystalline properties, state variables and track deformation. (b–e) Topological checks performed to keeping topological restrictions in Elle. Checks (b), (c) and (e) are based on minimum and maximum *bnode* separations. Check (d) removes extremely small *flynns* that contain no undoes or have areas smaller than the area enclosed by four neighbouring *unodes* by merging them to a neighbour of the same phase.

Island grains such as a grain inside another grain are not allowed in Elle, for topological reasons. *Flynns* are delimited by straight segments that join boundary nodes (*bnodes*) in either double or triple junctions. Quadruple or higher-order junctions are also not allowed in Elle. Additionally, we superimpose a regular grid of unconnected nodes (*unodes*) on the set of *flynns*. *Unodes* store local state variables such as stress, normalised von Mises strain rate or dislocation density. Crystallographic orientations at *unodes* are defined by Euler triplet angles, following the Bunge convention. After each deformation increment, all state variables are mapped back to a regular, rectangular *unode* grid, as this is required by the VPFFT code. To track the finite deformation, a second set of *unodes*, on an initially regular square grid, represent material points or passive markers that are displaced each deformation step. Topology checks are carried out at all times during a simulation to ensure compliance with topology restrictions and to maintain the set resolution. These include keeping *bnode* distances between a minimum and maximum separation by either deleting or inserting *bnodes* (Fig. 1b), and removing *flynns* that are smaller than a set minimum area or contain no *unodes* (Fig. 1c). To avoid the formation of a quadruple junction, a neighbour switch

is performed between triple junctions closer than the minimum separation distance (Fig. 1c). When two sides of a *flynn* approach each other to below a set minimum distance, the *flynn* is split into two (Fig. 1e). This allows bulging grain boundaries to sweep across entire grains without causing overlapping *flynns*.

2.3 Viscoplastic deformation using full-field approach

The full-field crystal viscoplasticity code (VPFFT) by Lebensohn (2001) was coupled to the Elle numerical modelling platform following the approach by Griera et al. (2013) and Llorens et al. (2016a). The approach is based on calculating the mechanical field (i.e. stress, strain rate) from a kinematically admissible velocity field that minimizes the average local work-rate under the compatibility and equilibrium constraints (Lebensohn, 2001; Lebensohn et al., 2009; Griera et al., 2013).

In this approach, intracrystalline deformation is assumed to be accommodated by dislocation glide on predefined slip systems, using a non-linear, viscous, rate-dependent law. The strain rate $\dot{\varepsilon}_{ij}(\boldsymbol{x})$ at each position $\boldsymbol{x}$ (*unode* position) in the grid is essentially the sum of the shear strain rates on all *N* slip systems (Eq. 1):

$$\dot{\varepsilon}_{ij}(\boldsymbol{x}) = \sum_{s=1}^{N} m_{ij}^{s}(\boldsymbol{x})\dot{\gamma}^{s}(\boldsymbol{x}) = \dot{\gamma}_0 \sum_{s=1}^{N} m_{ij}^{s}(\boldsymbol{x}) \left(\frac{m_{ij}^{s}(\boldsymbol{x})\sigma'_{ij}(\boldsymbol{x})}{\tau^{s}(\boldsymbol{x})} \right)^{3} \quad (1)$$

The constitutive equation relates the shear rate $\dot{\gamma}^{s}$ on each slip system (*s*), relative to a reference shear rate $\dot{\gamma}_0$, to the deviatoric stress σ'_{ij} and the orientation of the slip system that is defined by the symmetric Schmidt tensor m_{ij}^{s} (the dyadic product of a vector normal to the slip plane and slip direction). The effective viscosity or "ease of slip" of each slip system is defined by the slip-system-dependent critical resolved shear stress τ^{s}. Here we use a stress exponent of three, assuming Glen's law (Glen, 1958).

Since the strain rate and stress fields are initially unknown, an iterative scheme is implemented with a spectral solver using a fast Fourier transformation. The VPFFT code provides the full velocity field, which is integrated to the displacement field for a small time step, assuming velocities remain constant. The displacement field is applied to the passive marker grid and to all *bnodes* to apply the deformation to the grains and air inclusions. Lattice orientations are updated and remapped onto the rectangular *unode* grid. Furthermore, geometrically necessary dislocation densities are calculated using the plastic strain gradient following Brinckmann et al. (2006) and assuming constant Burgers vectors for all slip systems.

2.4 Recrystallisation

2.4.1 Polyphase grain-boundary migration

Polyphase grain-boundary migration is modelled using a front-tracking approach, which is explained in detail by Becker et al. (2008) and Llorens et al. (2016a). Grain-boundary migration is achieved by moving individual *bnodes*. In general, the movement $\Delta \boldsymbol{x}$ of a *bnode* is calculated from its mobility M and driving force S over a small numerical time step Δt:

$$\Delta x = SM(\, M_0, T(°C)\,)\Delta t \tag{2}$$

where the mobility M is a function of temperature T and intrinsic mobility M_0 (Nasello et al. 2005). The intrinsic mobility M_0 varies for different phase boundaries. The driving force S is calculated from the change in local free energy (dE) resulting from a change in position ($d\boldsymbol{x}$) of the *bnode* under consideration. dE is a function of the change in boundary length and, hence, total local grain-boundary surface energy (Becker et al. 2008) and the change in stored strain energy (Llorens et al. 2016a). A *bnode* is moved (using Eq. 2) in the direction of maximum free-energy reduction, which is determined from four small orthogonal trial displacements of that *bnode*. For the movement of ice-air boundaries, the stored strain energy was not taken into account.

In a polyphase aggregate, the conservation of mass requirement influences boundary migration. In theory, any local movement of a boundary needs to conserve the cross-sectional area of its host grain. This restriction would inhibit most ice-air interface movements, prohibiting any geometrical changes of air inclusions. Therefore, an additional energy term (E_{area}) is introduced to counteract that the surface energy (E_{surf}) would drive an ice-air boundary inwards and let air inclusions shrink (Roessiger et al., 2014). For ice-air boundaries, the total local energy (E_{total}) at a given trial position j only depends on the surface energy change and the relative area change resulting from a theoretical movement of the boundary node to this position:

$$E_{total}(j) = E_{surf}(j) + E_{area}(j) \tag{3}$$

$$E_{area}(j) = c\left(\frac{A(j) - A_0}{A_0}\right)^2 \tag{4}$$

where A_j is the area of the air inclusion when the *bnode* is at trial position j and A_0 is the initial inclusion area. Decreasing c essentially increases the accepted violation of the conservation of mass requirement, allowing a stronger change in cross-sectional area. For the polyphase aggregate of ice and air, the pre-factor c can be regarded as a compressibility factor: Theoretically, surface energy drives the bubble surface inward, compressing the enclosed air and increasing the air pressure in the bubble. This pressure would counteract the surface movement until an equilibrium between surface tension and inner bubble

pressure is reached, leading to a stable bubble cross-sectional area. The factor c controls how quickly this equilibrium is reached.

To fulfil the conservation of mass requirement, any movement of the interface that is not mass conserving should be inhibited. However, this would cause a locking of the ice-air interface and inhibit any changes in inclusion shape. Therefore, we allow movements that conserve the overall fraction of air but allow for sufficient shape changes of the bubbles. Preparatory tests yielded $c = 0.1$ as a compromise achieving this equilibrium. This assumption will inhibit almost all porosity changes during the simulation, causing our approach to assume an incompressible air inclusion, which does not allow us to quantitatively compare the modelled inclusion shapes or sizes with natural samples that experienced compaction. This limitation is further discussed in section 4.5.

We chose to use most input parameters from published literature to allow comparability of the results to previous modelling. Following the experimental results of Nasello et al. (2005), the intrinsic mobility $M_{ice\text{-}ice}$ of ice-ice boundaries was set to 0.023 $m^4\ J^{-1}\ s^{-1}$, which Nasello et al. (2005) determined for slow movement and is consistent with previous modelling by Llorens et al. (2016a,b). A slower movement is more suitable for our simulations as a higher mobility would cause numerical errors when using the same time step. Furthermore, it mitigates the effect of large numerical grain sizes (section 4.5). The grain-boundary mobility was determined as a function of temperature and intrinsic mobility according to Nasello et al. (2005). To be consistent with previous modelling, the surface energy $\gamma_{ice\text{-}ice}$ of ice-ice boundaries was set to 0.065 J m^{-2}, as commonly used in the literature (Ketcham and Hobbs, 1969; Nasello et al., 2005; Roessiger et al., 2014; Llorens et al. 2016a,b). Based on Roessiger et al. (2014), the mobility ratio of ice-ice and ice-air boundaries $M_{ice\text{-}ice}/M_{ice\text{-}air}$ was set to 10, which in their study provided results in compliance with the experimentally derived grain growth rates of Arena et al. (1997). The surface energy $\gamma_{ice\text{-}air}$ for ice-air boundaries was set to 0.52 J m^{-2}, which as a function of ice-ice surface energies ($\gamma_{ice\text{-}ice}$) results in dihedral angles of 173° and almost circular air inclusions (Roessiger et al., 2014).

In a two-phase model, such as ice with air inclusions, three boundary types are possible: ice-ice, air-ice and air-air boundaries. Air-air boundaries can occur in the model, for example when two air inclusions merge into one. These boundaries are purely numerical and have no physical meaning. They are therefore excluded them from any modelling processes or post-processing analyses.

During the simulation, all *bnodes* are selected in a random order and moved according to Eq. (3.2) one at a time. After each movement, topological checks are performed in keeping with the topological restrictions of Elle and to avoid impossible topologies such as *bnodes* sweeping across other grain-boundary segments. Once a *unode* is swept by a moving boundary and thus changes its host grain, its dislocation density is set to zero and its lattice orientation to the value of the nearest neighbour *unode* in the new host grain.

2.4.2 Rotation recrystallisation

The process of rotation recrystallisation is modelled in two separate steps during the multi-process simulation: (1) recovery by rearranging the intracrystalline lattice orientations into lower energy configurations such as subgrain boundaries, which is the predecessor for (2) the creation of new grains defined by high-angle boundaries, which here implies inserting new boundary nodes and splitting an existing *flynn*.

In analogy to the grain-boundary migration code, an energy minimisation system is used. Each *unode* is regarded as a small crystallite characterised by a lattice misorientation with respect to its first-order neighbours. Misorientation is the difference in lattice orientation between two *unodes*, which increases the total free energy of the local system. Small trial rotations are used to determine which lattice rotation would result in the maximum decrease in local free energy. The lattice in the *unode* is then rotated according to this decrease and a "mobility" term, as described in detail in Borthwick et al. (2014) and Llorens et al. (2016a).

Both the viscoplastic deformation and the above recovery process lead to polygonisation, i.e. the formation of new high-angle grain boundaries defined by a lattice misorientation between neighbouring

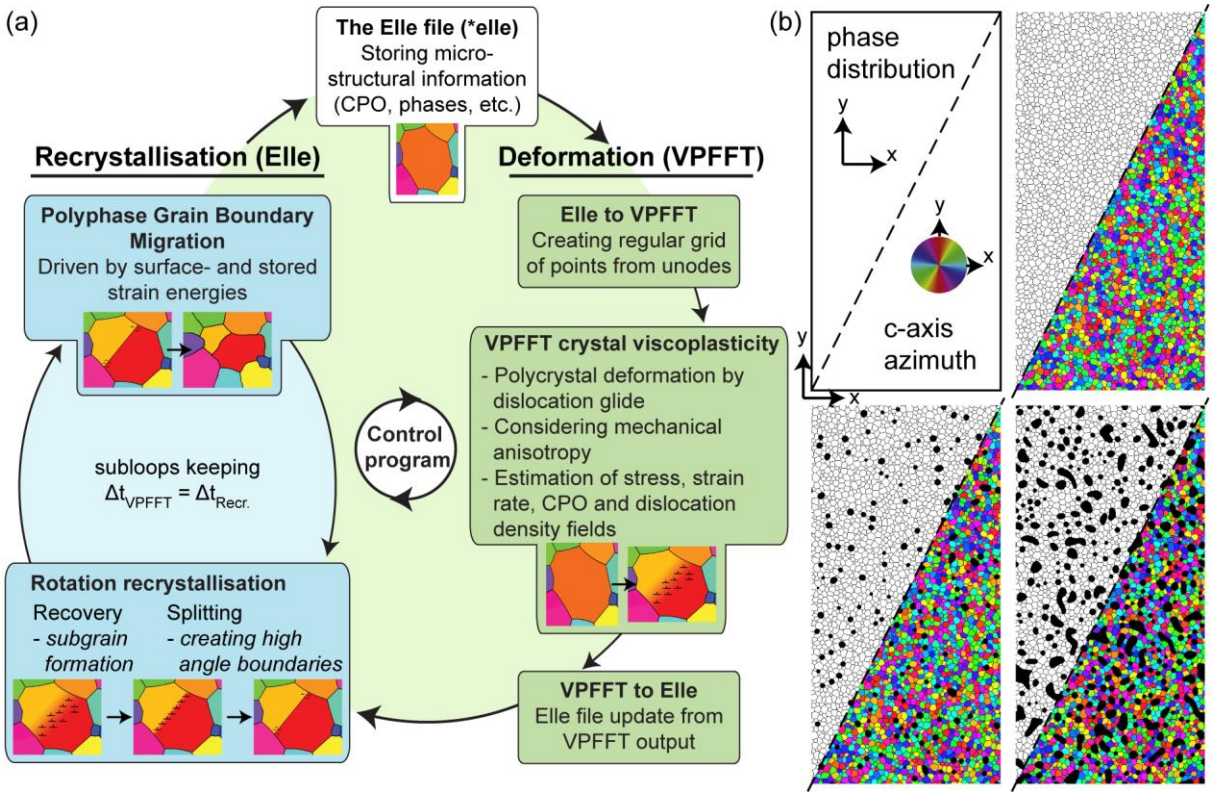

Figure 2: (a) Multi-process modelling by operator splitting is achieved by successively running individual process modules. One step of deformation by VPFFT code is followed by five subloops (with shorter time steps) of recrystallisation, each comprising four steps of recovery and grain-boundary migration, to keep a constant time step for all combined processes. (b) Initial 1020 cm microstructures with foam textures containing 0, 5 and 20% of air and with an initially random crystallographic fabric. Upper left half shows grain-boundary network and lower right the lattice orientations.

unodes that exceeds a critical angle α_{hagb}. Such new grain boundaries are initially not defined by *bnodes* and are thus numerically excluded from grain-boundary migration (Sect. 2.4.1). Polygonisation requires the creation of new high-angle grain boundaries by splitting an existing *flynn* and inserting new boundary nodes. When intragranular misorientations that exceed α_{hagb} are detected, grain splitting is activated. This is achieved by finding clusters of *unodes* with common lattice orientations, separated by high-angle boundaries. The positions of the new boundary nodes are found using a Voronoi decomposition of the *unode* clusters, storing the Voronoi points surrounding the cluster as new *bnodes*. The critical angle α_{hagb} has been suggested to be 3 to 5° for ice Ih, based on experiments that combine grain-boundary properties and high-angular resolution measurements (Weikusat et al., 2011a, b). Here we use α_{hagb}= 5° as a conservative estimate. Lower angles would lead to smaller grain sizes, which potentially cause more topological problems.

2.5 Process coupling

Multi-process modelling of polyphase deformation and recrystallisation is achieved by operator splitting. In Elle, the specific physical processes that contribute to microstructure evolution are programmed as stand-alone modules. These are coupled by a control program, successively running them in isolation, each for a short numerical time step (Fig. 2a). The numerical set-up takes into account the viscoplastic deformation (Sect. 2.3) and dynamic recrystallisation (Sect. 2.4), which here covers grain-boundary migration, recovery and polygonisation.

The recrystallisation modules are computationally less expensive but require short numerical time steps. To reduce numerical errors, the time step for recrystallisation processes is set 20 times smaller than for deformation (VPFFT). In accordance with the smaller time step, one simulation step comprises one VPFFT step and five subloops that run the recrystallisation codes four times per subloop. This adds up to 20 times more recrystallisation steps than VPFFT steps but an equal time step for all physical processes. Systematic studies showed that the order of the processes as illustrated in Fig. 2a has no significant influence on the results using the properties described above.

2.6 Set-up of simulations

Three starting microstructures were used to investigate the effect of viscoplastic deformation and DRX at different area fractions of air inclusions of 0, 5 and 20% air phase, termed F00, F05 and F20, respectively (Fig. 2b). In general, we refrain from relating our air fractions to specific depth or porosity ranges in firn or ice as our approach is limited and assumes an incompressible air phase. We chose to use these settings to represent only approximate ice–air aggregates as found in firn (F20) and well below the firn–ice transition (F05) and used simulation F00 for reference. With this, we do not limit our study to firn, but to ice–air aggregate in general. All initial microstructures were created from the same 10x20

cm² foam texture with 3267 grains. With this, the initial mean grain sizes of our modelling were larger than typical firn mean grain sizes as presented in e.g. Kipfstuhl et al. (2009) but consistent with previous simulations by Llorens et al. (2016a, b). Lattice orientations were mapped onto a regular grid of 256x256 *unodes* with a random initial lattice orientation assigned to each grain. Air inclusions were introduced by setting air properties to the desired area percentage of grains, followed by running solely surface-energy-based (static) polyphase grain-boundary migration until air inclusion sizes equilibrated in area and shape. For consistency, for this static grain-boundary migration, the same area energy factor $c = 0.1$ (Eq. 4) as for the actual dynamic recrystallisation and deformation simulations was used. Section 4.5 discusses the use of this factor in more detail.

The three starting microstructures were deformed in pure shear with a constant incremental strain of 1% vertical shortening over 75 simulation steps. Each simulation step comprised 20 recrystallisation steps per VPFFT step and equalled 10^8s = 3.16 yrs, resulting in a vertical strain rate of 10^{-10} s^{-1} and deformation up to 53% vertical shortening. We remark that the modelled strain rate is about an order of magnitude faster than assumed for firn at the EDML site (Faria et al., 2014b) and that modelling a slower strain rate is possible, yet currently too numerically expensive. From a technical point of few, fast strain rates have the advantage that the time steps for recrystallisation routines can be small. To achieve slower strain rates, the number of recrystallisation steps per deformation step would need to be increased at a significant expense of computation time.

Dislocation glide was assumed for ice Ih crystallography with slip on basal, pyramidal and prismatic planes, using a ratio of basal to non-basal critical resolved shear stresses of $\tau_{basal}/\tau_{non\text{-}basal} = 20$. Air was modelled as an incompressible crystalline material with the same crystallography and slip systems as for ice, but with $\tau_{s\text{-}air}$ set 5000 times smaller than τ_{basal} of ice. Hence, as for ice Ih, deformation in the air phase was also resolved on basal, pyramidal and prismatic planes which were characterised by equally small critical resolved shear stresses. This leaves the air phase slightly anisotropic as the deformation is restricted to these defined slip planes. However, this approximation does not significantly affect the results (section 4.5 and supplementary figure S2). With this treatment of the air phase, the stress in points belonging to pores can be considered to nearly vanish compared to stresses reached in the solid grains, which is coherent with results from modelling of void growth using a dilatational viscoplastic full-field-theory-based formulation (Lebensohn et al, 2013). The simplification of assuming incompressibility allowed us to exclude the effect of compaction during microstructure evolution and is further discussed in section 4.5.

Temperature throughout the simulations was assumed constant at -30 °C. A detailed summary of all input properties can be found in Table 1. Where not indicated differently, we employed input parameters as used by Llorens et al. (2016a, Table 1).

For comparison of grain-size statistics, we additionally performed three NGG simulations using solely

Table 1: Input properties for the simulations F00, F05 and F20. Remaining input properties according to Llorens et al. (2016, Table 1). A more detailed description of the parameters is provided in Sects. 2.4 and 2.6 and Llorens et al. (2016a, b).

Symbol	Explanation	Input value
	Minimum *bnode* separation	2.5 x 10^{-4} m
	Maximum *bnode* separation	5.5 x 10^{-4} m
	Time step per simulation step	10^{8} s
	Ratio of time step between VPFFT and recrystallisation codes	20
	Number of recrystallisation subloops per one step of VPFFT within one simulation step	20
	Incremental strain per simulation step	0.01
$\tau_{basal} / \tau_{non\text{-}basal}$	Ice Ih: Ratio non-basal / basal glide resistance	20
$\tau_{basal} / \tau_{s\text{-}air}$	Air: Ratio ice Ih basal resistance/air flow stress	5000
$M_{ice\text{-}ice}$	Intrinsic mobility of ice-ice boundaries (Nasello et al., 2005)	0.023 m^4 J^{-1} s^{-1}
$M_{ice\text{-}air}$	Intrinsic mobility of ice-air boundaries (Roessiger et al., 2014)	0.0023 m^4 J^{-1} s^{-1}
$\gamma_{ice\text{-}ice}$	Ice-ice interface surface energy (Ketcham and Hobbs, 1969)	0.065 J m^{-2}
$\gamma_{ice\text{-}air}$	Ice-air interface surface energy (Roessiger et al., 2014)	0.52 J m^{-2}
	Resulting dihedral angle at ice air triple junctions (Roessiger et al., 2014)	173 °
α_{hagb}	Critical misorientation: ice high angle boundary (Weikusat et al., 2010; 2011)	5 °
c	Area energy or compressibility factor (10 times the value of Roessiger et al., 2014)	0.1

surface-energy-driven grain-boundary migration and no deformation. The NGG simulations used the three microstructures for F00, F05 and F20 as presented in Fig. 2b and the numerical time step was kept the same as in the deformation simulations.

2.7 Post-processing

2.7.1 Strain rate and strain localisation quantification

In order to visualise and explain the simulations, some post-processing steps were necessary. Strain-rate tensor fields predicted by VPFFT were transformed in von Mises equivalent strain rates normalizing the von Mises strain rate for each *unode* to the bulk value of the whole model. The von Mises strain rate $\dot{\varepsilon}_{vM}$ provides a scalar measure of strain-rate intensity and was calculated as a function of the symmetric strain-rate tensor:

$$\dot{\varepsilon}_{vM} = \sqrt{\frac{2}{3}\dot{\varepsilon}_{ij}\dot{\varepsilon}_{ij}} \tag{5}$$

In addition, we quantified strain localisation at each step during the simulation. Analogous to Sornette et al. (1993) and Davy et al. (1995), the degree of localisation *F* was calculated with

$$F = 1 - \frac{1}{N_u}\frac{(\sum \dot{\varepsilon}_{vM})^2}{\sum \dot{\varepsilon}_{vM}^{\,2}} \tag{6}$$

where N_u is the total number of *unodes* within ice grains and $\dot{\varepsilon}_{vM}$ the von Mises equivalent strain rate of each *unode*. The localisation factor *F* ranges from 0 to 1, such that 0 represents completely homogeneous deformation and 1-1/ N_u maximum localisation, where all strain is accommodated by a single *unode*. Note that Sornette et al. (1993) and Davy et al. (1995) used a slightly different localisation factor *f*=1-*F*, where 1 represents homogeneous deformation.

2.7.2 Driving forces and crystallographic orientations

For each step of grain-boundary migration, the driving forces for migration were stored in *bnode* attributes differentiating between surface and stored strain energy driving forces. Details about the driving force calculation can be found in Llorens et al. (2016a, equations 10-12). By normalizing the local stored strain energy to *bnode* mean surface energy, we obtained a quantitative measure of how much grain-boundary migration is induced by strain energy. For each simulation step, the *bnodes* only stored the driving forces for the last grain-boundary migration step. This allowed to capture the correct driving forces at the end of the simulation step after a time increment during which strain energy was induced by deformation and reduced by recrystallisation processes. Hence, we determined a minimum estimate for strain energies, which may have been higher in an intermediate stage of the simulation step.

Crystallographic preferred orientations were stored and updated during the simulations. Pole figures and eigenvalues were extracted using the texture analysis software MTEX (Bachmann et al., 2010; Mainprice et al., 2011) based on the orientation distribution function. The projection plane was chosen to be parallel to the x-y plane of the numerical model and c-axis orientation was expressed using the angles of azimuth and dip in this plane.

3 Results

Table 2 and Fig. 3 provide an overview of the results obtained from simulating pure shear deformation with ongoing recrystallisation for three different amounts of air inclusions. Selected movies illustrating the full microstructure evolution can be found as supplementary material in the AV Portal of TIB Hannover (av.tib.eu). The resulting microstructures are characterised by heterogeneous grain size distributions and a slight increase in average grain sizes compared to the initial one. Most grains have smoothly curved boundaries and are usually equidimensional to slightly elongate in the *x*-direction. Coalescence of air inclusions (Roessiger et al., 2014) led to a number of large inclusions in simulation F20. The largest air inclusions show a marked elongation, mostly oblique to the shortening direction. Small inclusions remained circular.

The strain and strain rate distribution is difficult to discern from the final air inclusion and grain shapes only, as these are constantly reworked by DRX (Llorens et al., 2016b). Instantaneous strain rate maps and finite strain passive marker grids provide better insight in deformation heterogeneity (Fig. 3), which is also visible in movies that show the whole deformation history (AV Portal of TIB Hannover, av.tib.eu). Strain localisation is observed in all simulations independent of the presence of air inclusions.

While instantaneous strain rate maps (Fig. 3b) can only show localisation at the current time step, passive marker grids reflect the accumulated strain throughout the microstructure evolution (Fig. 3a-b). Figure 3b shows that zones with high strain rates are oriented at ≤45° to the shortening direction. Zones with a high finite strain, or shear bands, are visible in the finite-strain pattern. These zones of accumulated shear strain initially formed at ca. 45° and subsequently rotated away from the shortening direction, especially in air-free ice (F00). High strain (-rate) zones form bridges between air inclusions when these are present. Regions between the high strain zones are characterised by both low strain rates and low accumulated finite strains.

Using the localisation factor *F*, it is possible to quantify the degree of strain localisation in our simulations. Figure 4 shows the evolution of this factor with strain for all simulations. In accordance with strain rate maps and passive marker grids, non-zero ($F \geq 0.3$) values are observed throughout the simulations, indicating strain localisation in all cases. *F* increases up to about 40% vertical shortening,

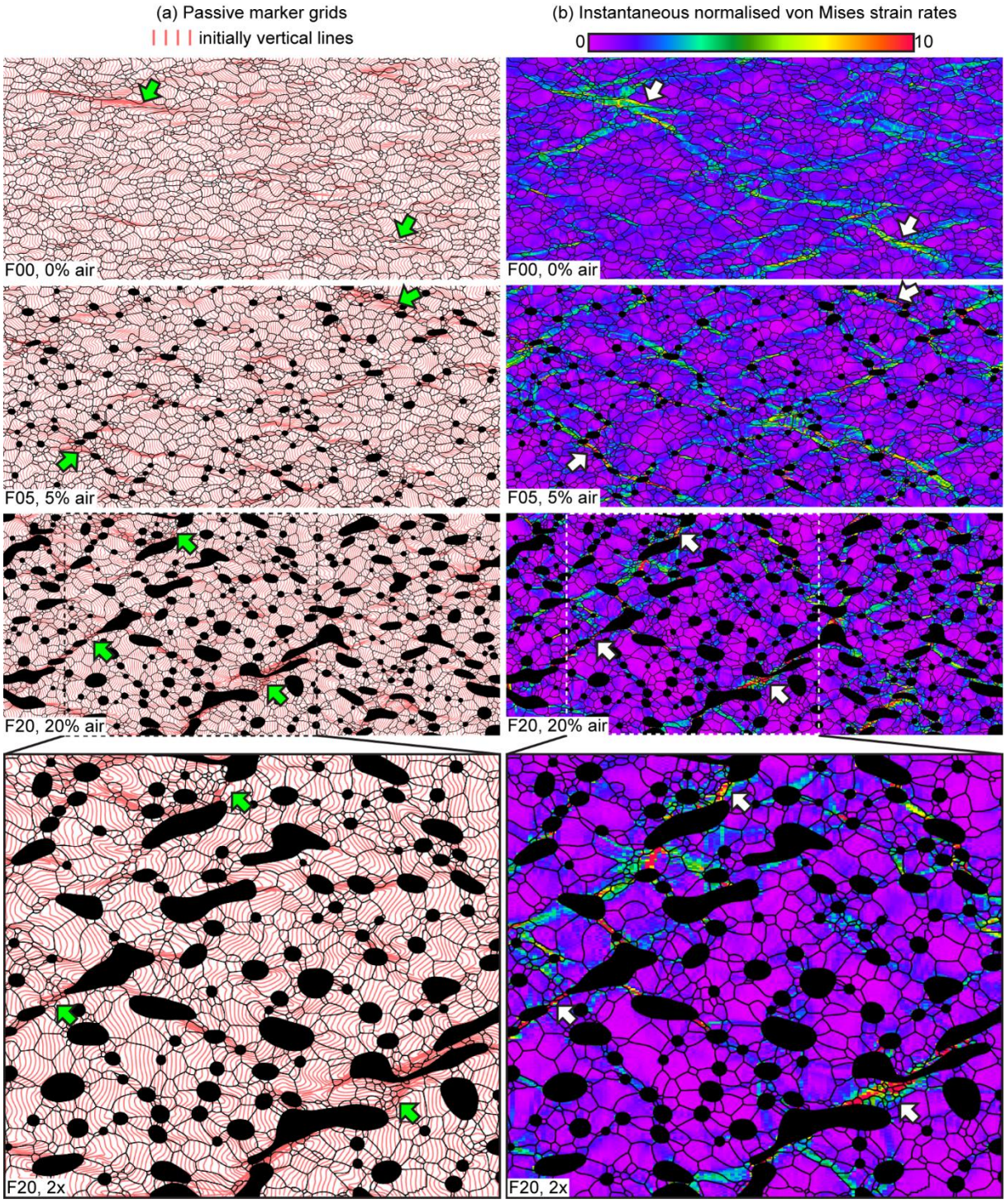

Figure 3: Overview of modelling results at last time step at 53%vertical shortening under pure shear conditions. (a) Grain-boundary network superimposed on passive marker grid of initially vertical parallel lines to show the finite strain distribution. (b) The same microstructures superimposed on the map of instantaneous strain rates expressed as von Mises strain rates normalised to the bulk value. Arrows in both images indicate zones of marked strain localisation. Air inclusions are displayed in black.

Table 2 Overview on numerical simulations using crystal viscoplasticity and dynamic recrystallisation (DRX) and only normal grain growth (NGG) simulations. NGG simulations used the same initial microstructures than DRX simulations.

	Area fraction of air	**Initial number of ice grains**	**Final number of ice grains DRX (*NGG*)**	**Initial mean ice grain area and (*standard deviation*)**	**DRX: Final mean ice grain area and (*standard deviation*)**	**NGG: Final mean ice grain area and (*standard deviation*)**	**Final and (*initial*) first eigen-value of CPO**
F00	0 %	3267	1631 (*1093*)	6.12 mm² (*3.50 mm²*)	12.17 mm² (*12.26 mm²*)	18.30 mm² (*13.25 mm²*)	0.7603 (*0.3393*)
F05	5 %	3128	1994 (*1155*)	6.07 mm² (*3.43 mm²*)	9.44 mm² (*10.87 mm²*)	16.43 mm² (*12.34 mm²*)	0.6975 (*0.3390*)
F20	20 %	2654	1891 (*1265*)	5.96 mm² (*3.33 mm²*)	8.30 mm² (*9.80 mm²*)	12.53 mm² (*10.52 mm²*)	0.5665 (*0.3468*)

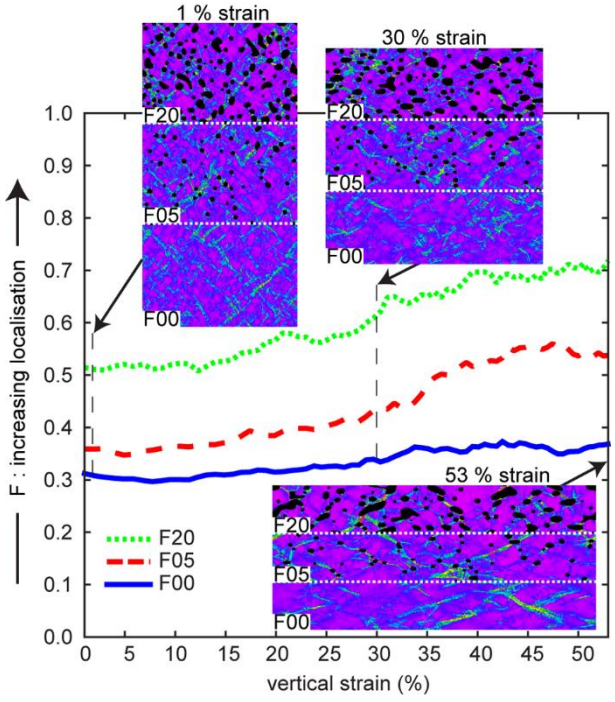

Figure 4: Evolution of localisation factors (*F*) with strain quantifying strain localisation in the microstructures for all simulations. A factor of 0 represents homogeneous deformation; the factor increases towards one with increased strain-rate heterogeneity and localisation. The normalized von Mises strain-rate maps at 1, 30 and 53% vertical strain are shown for reference. The maps are subdivided to show results of simulation F20 in the upper third, F05 in the middle and F00 in the lower third part of the model box. They illustrate strain localisation at different stages of the simulation.

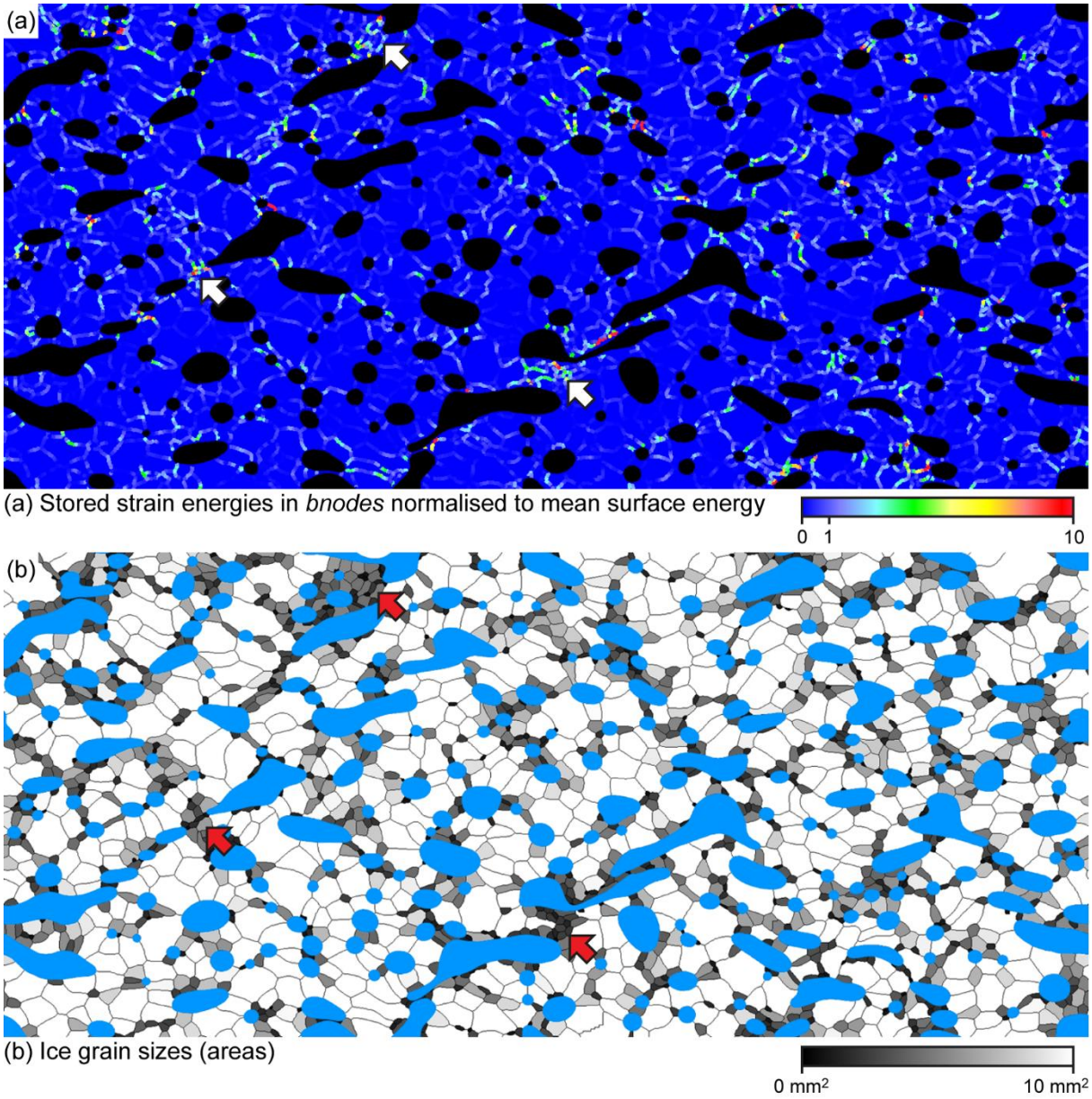

Figure 5: Details of results of simulation F20 at 53% vertical shortening. (a) Boundary nodes colour-coded according to the proportion of strain-induced boundary migration. Air inclusions are plotted in black since they do not contribute to strain-induced boundary migration. (b) Microstructure colour-coded according to the areas of ice grains, with air inclusions displayed in blue. Smallest grains appear grey to black. Arrows in both images indicate zones of marked strain localisation.

after which the rate of increase is lower. Localisation increases with the amount of air inclusions, with $F \approx 0.5\text{-}07$ in simulation F20 about double that for pure ice ($F \approx 0.3\text{-}0.35$).

To investigate the competition between surface and stored strain energies in grain-boundary migration, the strain energy driving forces for simulation F20 were normalised to mean surface energies and plotted for each *bnode* (Fig. 5a). The colour scale is adjusted to plot *bnodes* without a contribution of strain-induced energies in the background colour (blue). Boundaries with a significant contribution of stored strain energies are indicated by green to red colours. A comparison with Fig. 3 shows that grain-

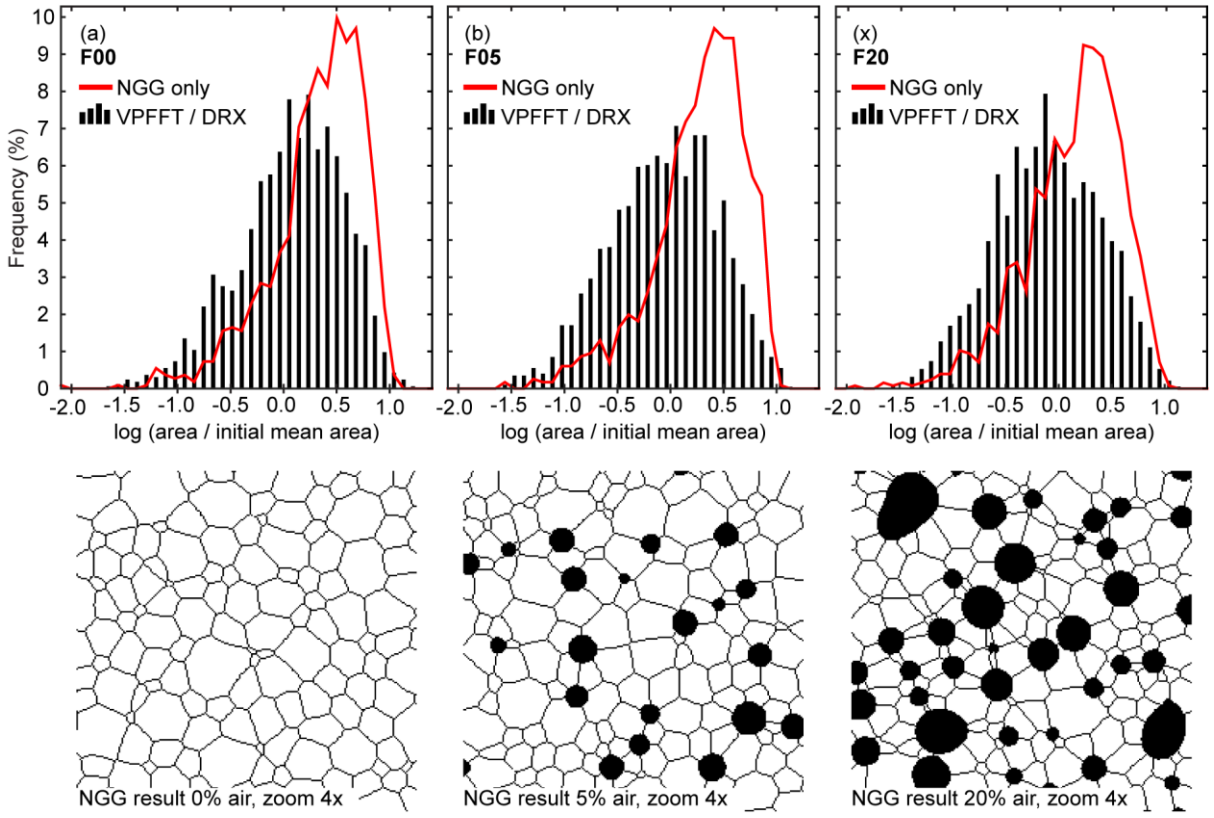

Figure 6: Comparison of ice grain area histograms of the last simulation step of simulations (a) F00, (b) F05 and (c) F20. Normal grain growth (NGG) simulations using F00, F05 and F20 input models are displayed with the respective deformation and dynamic recrystallisation (VPFFT/DRX) simulation results. Areas were normalised to initial mean values that plot at a value of 0.0 on x axis. For reference, a fourfold zoom in the resulting microstructures from NGG simulations is displayed below the histograms.

boundary migration that is driven mostly by strain energy (bright colours) is predominantly located in high strain (-rate) zones. Examples are indicated by large arrows in Fig. 5a and between three elongated and large air inclusions in the lower middle region of the final microstructure of F20. Conversely, the contributions of surface and strain energy to grain-boundary migration are about equal in less strained areas.

Qualitatively, microstructure images show a heterogeneous grain size distribution (Fig. 3). To further visualise the spatial distribution of grain sizes, the microstructure in Fig. 5b shows ice grains coloured according to their area. Analogous to the driving force distribution for grain-boundary migration, we observe the smallest grains between air inclusions coinciding with zones of marked strain localisation.

Figure 6 depicts ice grain size statistics for the final microstructures. To visualise the influence of dynamic recrystallisation, grain size histograms are compared with NGG simulation results. All simulations show an increase of average grain areas with respect to the initial mean grain sizes (Fig. 6, Table 1). However, DRX simulations resulted in a grain size distribution skewed towards smaller grain sizes than for NGG simulations. Furthermore, the distribution of grain sizes is broadened when DRX

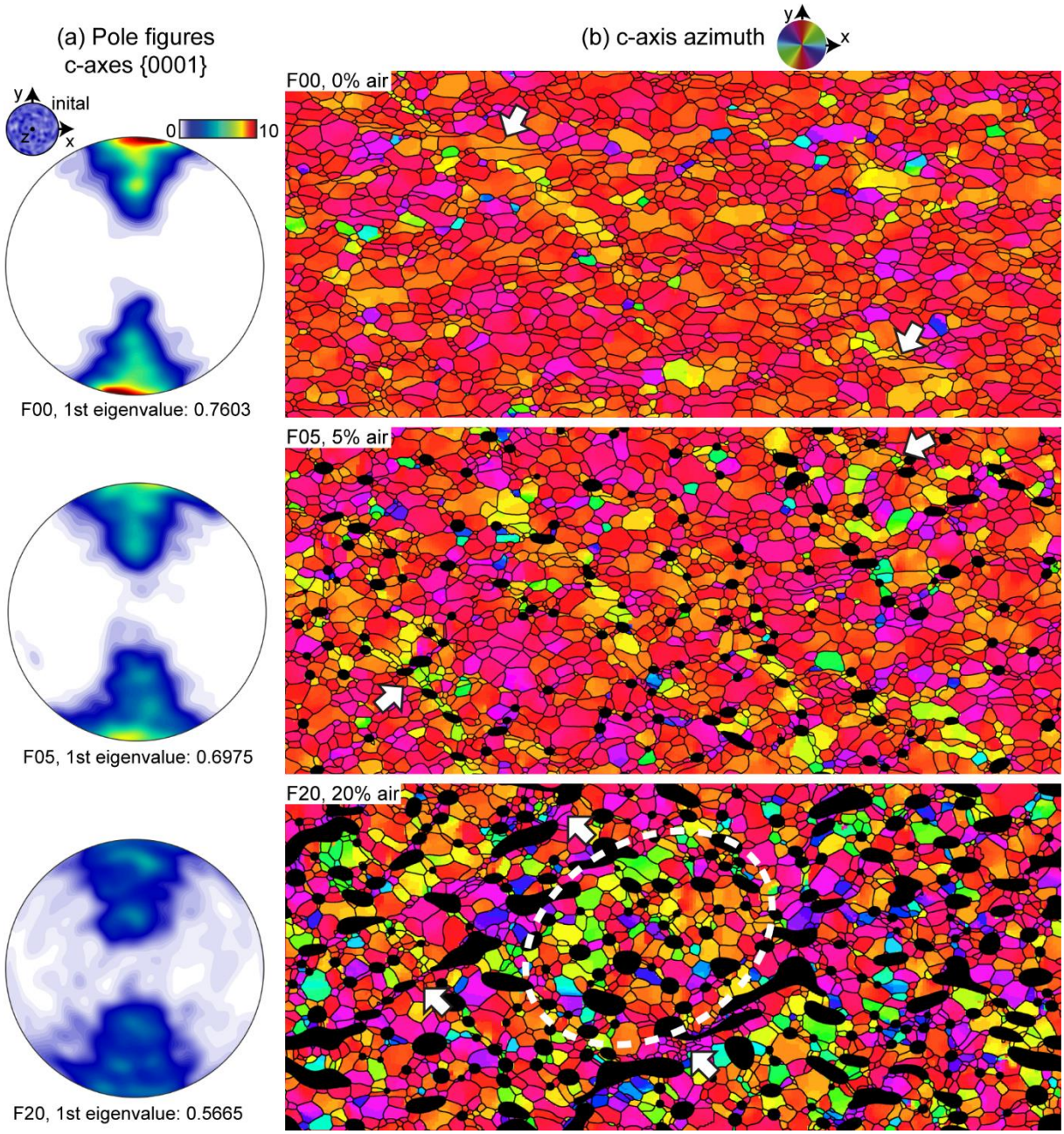

Figure 7: Overview of c axis orientations at 53% vertical shortening for all simulations. (a) Pole figures with the projection plane parallel to the x-y plane of the 2-D model. (b) Maps of c axis azimuth distributions. Air inclusions are shown in black. White arrows in both images indicate zones of marked strain localisation. Dotted white line indicates zone of low strain where more random crystallographic orientations are preserved.

was active. With increasing amount of air in simulations F05 and F20, the average grain-size increase compared to the initial state is lower for both DRX and NGG results.

Crystallographic preferred orientations in simulations are visualised using pole figures and maps of c axis azimuths (Fig. 7). The evolution of orientations is also illustrated in movies to be found in the AV Portal of TIB Hannover (av.tib.eu). After 53%of vertical shortening, the initially random fabric is rearranged with c axes preferentially oriented parallel to the vertical shortening direction (Fig. 7a). This

maximum becomes less pronounced with increasing amount of air as reflected in pole figures and quantified by a decrease in first eigenvalues of the orientation distribution from 0.80 (F00) to 0.69 (F20). This trend is also visible in c axis orientation maps (Fig. 7b), which shows a more heterogeneous distribution of well-aligned and random fabrics with increasing air content. Most grains in simulation F00 have c axes azimuths parallel to the y axis. Grains within high strain bands are marked by a slight tilt of the c axes to the left or right, depending on the orientation of the shear bands. In contrast, simulation F05 and, even more, F20 show areas of small grains with c axes strongly aligned perpendicular to high strain bands (white arrows in Fig. 7b). This means that the basal planes are aligned parallel to these bands. In low strain areas, such as the middle part of the F20 model, a much more random c axis distribution is observed (white circle in Fig. 7b) compared to simulation F00.

4 Discussion

4.1 Strain localisation

Our simulations indicate a distinct strain localisation in both pure ice and ice with bubbles. Strain localisation is not a transient effect, but it actually increases, at least up to about 40% of strain (Fig. 4). Strain localisation in pure ice (F00) is related to the plastic anisotropy of the ice crystal. Grains, or clusters of grains, with initially suitable orientations for slip accommodate strain more efficiently and thus initiate the first regions of strain-rate localisation. With progressive strain these localisation zones may strengthen as the basal planes align themselves with the local shear plane, or they are deactivated when either the internal lattice orientations or the orientation of the localisation zones become less suitable for further localisation. Once deactivated, the localised zones only rotate and move passively with the bulk deformation and may remain visible as shear bands in the finite strain grid. Our observation of strain localisation in a polyphase aggregate is consistent with numerical models by Cyprych et al. (2016), who predict strain localisation as an important mechanism in polyphase materials, such as ice with soft or hard inclusions.

In the presence of air inclusions, localisation zones are forming at bridges between the inclusions where stresses are highest. Even in the absence of plastic anisotropy this leads to the formation of localisation zones, especially in power law materials (Jessell et al., 2009). With increasing air fraction, the arrangement and geometry of air inclusions become the main controllers of strain localisation in the ice–air aggregates and crystallographic orientations exert only a secondary control. The additional localisation mechanism causes stronger localisation in ice with air than without air.

The localisation zones enclose lozenge-shaped areas of low strain rate, which we term microlithons, in keeping with terminology used in geology (e.g. Passchier and Trouw, 2005 p. 78). In pure ice, the CPO within the microlithons is strong and trends towards a single maximum fabric. With air inclusions

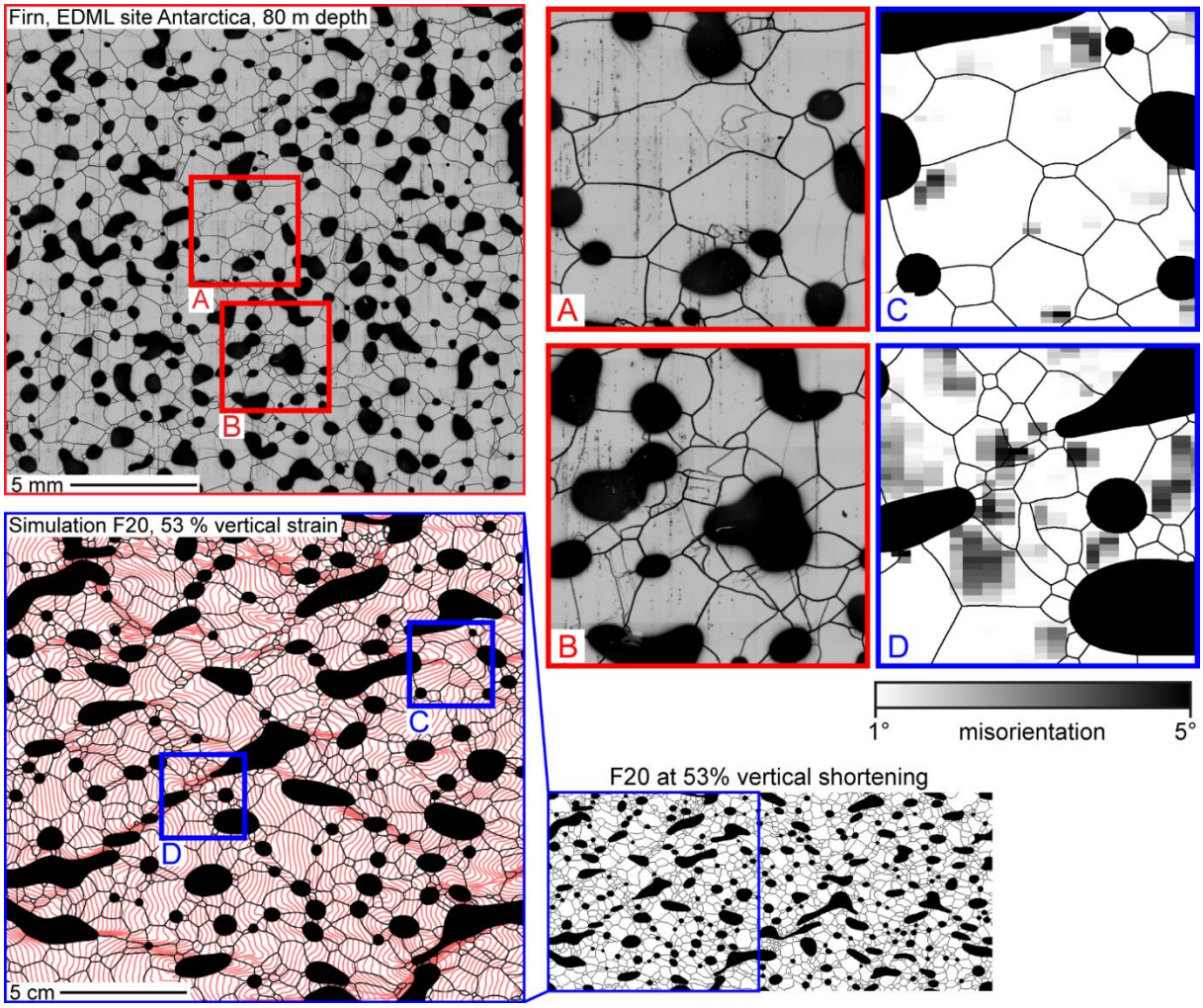

Figure 8: Comparison of simulation results of F20 at 53% vertical shortening with firn microstructure mapping images from the EDML ice core site at 80m depth (courtesy of Sepp Kipfstuhl). The detail areas A–D illustrate different microstructures occurring in relation to strain localisation. Grain boundaries stand out as black lines and subgrain boundaries are visible as fainter grey lines. Vertical stripes appearing in the overview image are related to the sample polishing technique and not reflecting any microstructural property. Greyscales C and D indicate local average misorientations as stored in *unodes* and therefore appear blurred due to the strong magnification. Note, however, that strain paths of the natural microstructure (compaction) and the simulation (pure shear) are not identical and the comparison is restricted to the microstructural similarities and inferred localisation and recrystallisation processes.

causing intensified strain localisation, the CPO is expected to be more heterogeneous with differences between high and low strain-rate zones. Within localisation zones, the basal planes rotate towards the local shear plane, causing a divergence of the c axes azimuths away from the vertical compression direction. This is in contrast to the microlithons, in which CPO development is slower because of the relatively low strain rate. The weaker bulk single maximum fabric with increasing amount of air is thus an effect of air inclusions causing distinctly localised zones that accommodate most of the deformation and less deformed microlithons that preserve the initial fabric. Our results are an illustrative example of the role of second phases on CPO development. If the weak phase is the secondary phase and the strong

phase is load bearing, as in our simulations, strain localisation controlled by the distribution of second-phase inclusions. This produces a locally weaker CPO in the microlithons as well as in the bulk material.

Grain-boundary sliding is assumed to be an explanation for a weaker CPO in polyphase materials (e.g. Fliervoet et al., 1997). However, a weaker CPO with increasing content of the second phase is found in our simulations, in the complete absence of grain-boundary sliding. Therefore, a weaker CPO alone should not be regarded as unambiguous evidence for grain-boundary sliding. This supports studies indicating a very shallow onset of plastic deformation in the ice sheets (Freitag et al., 2008) and absence of grain-boundary sliding (Theile et al., 2011).

4.2 Natural firn microstructures and numerical simulations

For comparison with natural ice and firn core samples, a microstructure image from 80m depth from the EDML site is used (Fig. 8). For this image, a 2-D sample was vertically cut from the firn core and processed for microstructure mapping as described in Kipfstuhl et al. (2006, 2009) using a large area scan macroscope (Krischke et al., 2015). Here, we refrain from any detailed or quantitative comparison of our numerical simulations with respect to grain sizes, bubble size, shape or distribution. Such comparisons are hindered by model assumptions such as assuming an incompressible air phase or area conserving pure shear deformation (Sect. 4.5). We observed air inclusions coalescing during our simulations. This is expected from static polyphase grain-growth simulations by Roessiger et al. (2014) but may be suppressed in firn as simultaneous shrinkage of bubbles may hinder them from touching and merging.

The F20 and EDML microstructure show qualitative similarities (Fig. 8), in particular in the heterogeneity in grain shape and relative grain size distribution. As an estimate for numerical subgrain boundary density, average misorientation between *unodes* was plotted together with the grain-boundary network. In case of natural firn, detail area A (Fig. 8) contains larger grains, with more 120° angles at triple junctions and a lower density of subgrain boundaries than area B, which is characterised by a higher density of bubbles. Visually, similar areas can be found in simulation F20. Area C has large grains with straight grain boundaries and 120° angles at triple junctions and lower misorientations (qualitatively comparable to A), and area D is characterised by small grains relative to C. Triple junction angles in D differ from 120° and D has higher internal misorientations (qualitatively comparable to B). The grain sizes can only be compared relatively, as mean grain size in simulation and sample differ. Besides, this natural sample is a 2-D slice through a 3-D body, but the simulations are purely 2-D. For more rigorous comparisons, corrections for stereologic issues are required.

With respect to the limitations of the modelling approach (Sect. 4.5), we cannot quantitatively compare the simulations to natural firn. However, as detail D (Fig. 8) is marked by higher finite strains related to strain localisation and is indicates more influence of DRX as presented by Kipfstuhl et al. (2009), similar

processes may have controlled the natural microstructure in detail image B (Fig. 8). In contrast, the natural ice in detail A probably experienced lower finite strains, as suggested from a comparison with the numerically modelled detail image C (Fig. 8). As strain localisation and the resulting heterogeneity in finite deformation pattern can be masked by grain-boundary migration in natural ice (Llorens et al., 2016b), our numerical simulations can help to visualise the actual heterogeneity within the structure, leading to an improved understanding of how DRX is distributed within the ice–air aggregate.

4.3 Implications of strain localisation for the occurrence of dynamic recrystallisation

According to published deformation mechanism maps (Shoji and Higashi, 1978; Goldsby, 2006), dislocation creep is to be expected for the average grain size, strain rate and temperature of our simulations. Also, the effective density of the simulation F20 (approximately 750 kg m^{-3} is above the critical density of 550 kg m^{-3} where plastic deformation via dislocation creep is classically supposed to dominate (Maeno and Ebinuma, 1983). Therefore, we assume that our model assumption of deformation accommodated by dislocation creep only is sufficient to draw conclusions on mechanisms acting at comparable densities and depth in nature.

With the assumption of dislocation glide as the only strain accommodating mechanism, the dislocation density is expected to increase unless recovery reduces densities by rearrangement of misorientations in lower energy configurations. A localisation in strain results in higher strain gradients at the localisation zone margins and hence locally higher strain energies. It is therefore associated with locally enhanced strain-induced boundary migration, as can be seen in Fig. 5a. This is in accordance with Weikusat et al. (2009) stating that strain-induced boundary migration occurs localised and the driving forces have to be considered locally. Duval (1985) argued that the strain energy in firn should be small in comparison with surface energies and Duval and Castelnau (1995) conclude that strain-induced boundary migration is most dominant for temperatures of -10°C or higher. This led to the assumption by De la Chapelle et al. (1998) that DRX is essentially restricted to the basal part of ice sheets and therefore an improbable process in firn.

Faria et al. (2014b, p. 45) theoretically discuss the relation of strain localisation to localised DRX in firn. They state that although the overall stresses and strains in firn are low, it is "characterised by large strain variability" and locally highly increased stresses and strains depending on the geometry of the air bubble network. They further conclude that stored strain energy could be very high in particular regions of the ice skeleton causing DRX to start in shallow levels. Our simulations are coherent with this statement and confirm the theoretical predictions by Faria et al. (2014b).

Since improving microstructural imaging methods by Kipfstuhl et al. (2006) gave further insight in firn microstructures, studies by Weikusat et al. (2009) and Kipfstuhl et al. (2009) gave microstructural

evidence for DRX in shallow parts of the ice column and firn. In contrast to assumptions by for instance De la Chapelle et al. (1998), it therefore seems probable that DRX already takes place at very shallow levels in the ice sheet, at least in localised zones. Our simulations at -30°C as well as observations of natural firn microstructures at EDML ice coring site (Kipfstuhl et al., 2009) with approximately -45°C annual mean temperature (Oerter et al., 2009) indicate that even at low temperatures deformation provides enough energy to allow for strain-induced grain-boundary migration. The relative dominance of this process is also a function of strain rate, since locally high strain rates and stress concentrations at bridges between the air inclusions induce high driving forces. This is in accordance with the recrystallisation diagram by Faria et al. (2014b), in which the occurrence of recrystallisation mechanisms is essentially a function of temperature and strain rate (i.e. work rate, which is the product of stress and strain rate) rather than depth.

According to the DRX diagram by Faria et al. (2014b), a lower strain rate would decrease the contribution of rotation recrystallisation and increase that of strain-induced grain-boundary migration to the final microstructure. This would reduce the difference in grain size between high and low strain zones. A difference variation in grain size is, however, still observable in the EDML sample, indicating that grain-boundary migration was not able to obliterate the effects of rotation recrystallisation in these suspected high strain zones, even at the lower natural strain rate.

Because of DRX, grain shapes are mostly equidimensional, even in the highest-strain bands. Recrystallisation thus masks the localisation in the microstructure (Llorens et al., 2016b), making it difficult to discern strain localisation in natural samples. Subtle indications of localisation may, however, be zones with a deviating lattice orientation (Fig. 7) (Jansen et al., 2016) or zones with a smaller grain size (Fig. 5b). In single-phase ice, where localisation zones shift through the material, only the youngest localisation zones may be visible, as the microstructure is reset in extinct localisation bands (compare simulation F00 in Figs. 3 and 7) (Jansen et al., 2016). Since bubbles fix the locations of shear localisation, their presence may be more obvious in natural samples, such as the one from the EDML (Fig. 8). In general, bubbles may only be useful to discern localisation zones (as in F20), if the bubbles are large and strain rates are high enough, which will cause elongated bubble shapes.

4.4 Grain size analysis

We refrain from a detailed comparison of our grain-size data and those observed in nature as a discussion of the stereologic issues related to our 2-D model and sections through 3-D natural samples would be beyond the scope of this paper. Furthermore, the limitations of the current modelling approach, such as the large initial grain size, requirement of fast strain rates and incompressibility of air inclusions, do not allow for such a detailed quantitative study. Still, the grain size statistics of the simulation results provide

a comparison between the distribution for the non-deformation-related NGG and deformation-induced DRX with varying amounts of air.

An increase in grain size is observed in all simulations, but less for DRX and also less with an increasing amount of air inclusions. The observation of a lower final grain sizes for higher amounts of air is related to the growth regimes presented by Roessiger et al. (2014) based on numerical simulations on NGG in ice–air aggregates. (1) The first regime is characterised by ice grain sizes less than bubble spacing, where most grains can grow unhindered by bubbles as in single-phase polycrystalline ice. The growth rate is constant. (2) The second regime is a transitional regime, where bubble spacing is close to the grain diameter and the growth rate decreases. (3) In the third regime, all grains are in contact with bubbles. A slow, but steady growth rate is reached again, controlled by the coalescence rate of bubbles that increases their spacing. In our case, NGG in the simulations with air inclusions is slowed down, indicating regime (2) growth with a small, but significant, fraction of the grains in contact with inclusions, and thus hindered in their growth (Fig. 6).

In comparison with NGG simulations, our VPFFT simulations with DRX show smaller final grain sizes and broader distributions. The broadening reflects the microstructural heterogeneity induced by dynamic recrystallisation (in particular grain splitting during rotation recrystallisation) and strain localisation. Locally, grains size has remained small due to rotation recrystallisation, whereas in other, low strain rate regions, grain sizes have increased. Here surface energy constituted a significant, if not dominant, proportion of the driving force for grain-boundary migration. These results are consistent with the observed broadening of the grain size distribution with depth in firn from the EDML site (Kipfstuhl et al., 2009), accompanied by an increasing number of deformation-related substructures such as subgrain boundaries and irregular boundary shapes. Our modelling confirms the interpretation by Kipfstuhl et al. (2009) that this trend is related to the onset of DRX.

4.5 Limitations of the modelling approach

In our polyphase simulations, air inclusions are modelled as an incompressible material. By imposing pure shear, we assume a deformation mode that conserves the total area and in turn the mass of both phases. However, in natural firn, most of the vertical thinning is achieved compaction. Compaction is a function of the surface energy driving movement of the ice–air interface and the counteracting inner bubble pressure that depends on overburden pressure and bubble size and shape. Our model assumes equilibrium between those pressures leading to a stable fraction of air. This is controlled by the area energy that is incorporated in the pre-factor c. The lower this factor is, the more influence of surface energy is allowed and the more the conservation of mass requirement is violated as more inward movement of the ice–air interface is allowed. The pre-factor constant c (Eq. 4) was adjusted to allow slight changes in cross-sectional area that keep the overall amount of air in the model constant but

compensate shape changes due to deformation to maintain an approximately circular bubble shape and allow bubbles to merge. Preparatory tests yielded c = 0.1 as a suitable value to achieve this compromise. More detailed research is necessary to study the effect of a varying c or scale it to natural ice.

We refrain from any study of depth evolution of porosity, inclusion shape or distribution. In fact, the numerical microstructure evolution cannot be regarded as an evolution with depth like in natural firn and ice. However, the model can be used to study the behaviour of firn or bubbly ice, independent of the history that led to the particular microstructure. At all times during the simulation, we observe strain localisation controlled by air inclusions. This is even observed for small accumulated strains at low air contents (F05, Fig. 4). In addition, trial simulations showed that localisation also occurs at very different distributions of air inclusions at the same air fractions (see Supplement Fig. S1). There is no reason to expect that the strain localisation and elevated strain energies that drive DRX that we observe for area conservative pure shear would not occur during compaction.

Another approximation in the VPFFT approach is the treatment of the air phase. In the current model, air is treated as an ice Ih symmetry crystal with equal basal, pyramidal and prismatic critical resolved shear stresses that are all 5000 times lower than for ice basal slip. This leaves the air phase slightly anisotropic. However, this assumption does not significantly affect the results since the effective contrast in slip resistance is significantly higher with a stress exponent of three (Eq. 1). To further investigate any effects on the results, we compared our approach with an updated VPFFT code that avoids any crystallography in the air phase by imposing zero stiffness to air *unodes*, thus causing their stresses to vanish (Lebensohn et al., 2011, 2013). This was done by applying both our and the updated VPFFT approach to the initial set-up of F20 for an increment of 1% vertical shortening to compute the instantaneous strain rate and stress distributions. The results are essentially the same for both set-ups (see Supplement Fig. S2) and show that the predictions of our simulations are not significantly affected by how we treat the air phase. Future simulations should include the optimized VPFFT approach imposing zero stiffness to air *unodes*.

Initial and final numerical grain sizes are larger than in natural firn, in particular with respect to the relatively high numerical strain rate. We chose to use initial grain sizes comparable to previous numerical simulations by Llorens et al. (2016a, b) and not to natural firn as other model assumptions would still hinder quantitative comparisons to natural samples. Adopting different grain-boundary mobilities can significantly alter the resulting grain size. Therefore, we chose to use accepted literature values for grain-boundary mobility as experimentally derived by Nasello et al. (2005) and used for previous numerical simulations by Roessiger et al. (2014), Llorens et al. (2016a, b) and Jansen et al. (2016). Although the use of lower mobilities would decrease the predicted grain sizes, the use of accepted literature values is more justified with respect to the scope of the study. Atomistic processes driving recrystallisation may be decelerated in nature due to the presence of impurities and pinning

microparticles, which our simulation approach does not take into account. Any future comparison of simulations with natural ice may necessitate unexpectedly low or high values for material parameters, such as an adapted lower grain-boundary mobility, to achieve a more realistic grain size. Investigating a more suitable numerical mobility remains part of future developments.

While the model scale affects the Elle recrystallisation processes and in turn grain sizes, the VPFFT approach is dimensionless and scale independent. The strain localisation bands and associated balance of recrystallisation driving forces is predicted by the VPFFT routine. This implies that the main observations and interpretations drawn in this paper in relation to strain localisation remain valid independently of the numerical grain sizes.

5 Conclusions

We used polyphase numerical models of deformation and recrystallisation to investigate the occurrence of dynamic recrystallisation in an air–ice composite such as polar ice and firn. To our knowledge this provides the first full-field numerical simulation results on dynamic recrystallisation in polyphase crystalline aggregates in glaciology. We show that strain and strain-rate localisation is to be expected during ice deformation, forming shear bands that accommodate significant amounts of strain. Dynamic recrystallisation can occur at relatively shallow levels of the ice sheet where it is related to strain localisation and stress concentrations between the air inclusions. This results in an increased heterogeneity in ice sheet deformation and more dynamic recrystallisation activity than previously assumed. In fact, strain localisation is probably not the exception, but the rule in ice sheets and glaciers. Wherever present, second phases such as air bubbles provide an effective mechanism for strain localisation in addition to mechanical anisotropy. Due to strain localisation, the rate of fabric change can be high locally, which is of special importance in firn, where bubbles are most abundant. The effects of localisation and heterogeneity in distribution of firn recrystallisation and deformation could be considered in future firn densification models. Furthermore, as the utilised VPFFT approach is dimensionless, future research could investigate the probably large range of scales at which strain localisation may occur in glaciers and ice sheets.

Data availability

The video supplement related to this article is available online from the AV Portal of TIB Hannover (av.tib.eu):

Simulation F00:
doi:10.5446/19279 – grain boundaries
doi:10.5446/19281 – passive marker grid
doi:10.5446/19280 – orientations of c axes
doi:10.5446/19282 – strain rates
Simulation F05:
doi:10.5446/19283 – grain boundaries
doi:10.5446/19285 – passive marker grid
doi:10.5446/19284 – orientations of c axes
doi:10.5446/19286 – strain rates
Simulation F20:
doi:10.5446/19287 – grain boundaries
doi:10.5446/19289 – passive marker grid
doi:10.5446/19288 – orientations of c axes
doi:10.5446/19290 – strain rates

The Supplement related to this article is available online at doi:10.5194/tc-10-3071-2016-supplement.

Acknowledgements

We are thankful for support and helpful discussions with the members of the Elle community. We thank Till Sachau, Sepp Kipfstuhl and Johannes Freitag for their input to improve the manuscript as well as the helpful comments by two anonymous reviewers. This study was funded by the DFG (SPP 1158) grant BO 1776/12-1. Furthermore, we acknowledge funding by the Helmholtz Junior Research group "The effect of deformation mechanisms for ice sheet dynamics" (VH-NG-802) and travelling funds for presenting and improving this study by the EPICA Descartes travel price, the ESF research networking programme on the microdynamics of ice (MicroDICE) and the Helmholtz Graduate School for Polar and Marine Research (POLMAR).

PAPER II

Grain dissection: A new process for grain size reduction in polar ice cores and numerical models

Florian Steinbach[1,2], Ernst N. Kuiper[3,2], Jan Eichler[2,1], Paul D. Bons[1], Martyn R. Drury[3], Albert Griera[4], Gill M. Pennock[3] and Ilka Weikusat[1,2]

1. Department of Geosciences, Eberhard Karls University Tübingen, 72074 Tübingen, Germany
2. Alfred Wegener Institute Helmholtz Centre for Polar and Marine Research, 27568 Bremerhaven, Germany
3. Department of Geosciences, Utrecht University, 3508 TA Utrecht, Netherlands
4. Departament de Geologia, Universitat Autònoma de Barcelona, 08193 Bellaterra (Barcelona), Spain

Submitted to *Frontiers in Earth Science, Cryospheric Sciences*, 28 March 2017.

Abstract

The flow of ice depends on the properties of the aggregate of individual ice crystals, such as grain size or lattice orientation distributions. Therefore, an understanding of the processes controlling ice micro-dynamics is needed to ultimately develop a physically based macroscopic ice flow-law. We investigated the relevance of the process of grain dissection as a grain-size-modifying process in natural ice. For that purpose, we performed numerical multi-process microstructure-modelling and analysed microstructure and crystallographic orientation maps from natural deep ice-core samples from the North Greenland Eemian Ice Drilling (NEEM) project. Full crystallographic orientations measured by electron backscatter diffraction (EBSD) have been used together with c-axis orientations using an optical technique (Fabric Analyser). During grain dissection, grain boundaries bulge into a neighbouring grain in an area of high dislocation energy and merge with the opposite grain boundary. This splits the high dislocation-energy grain into two parts, effectively decreasing the local grain size. Currently, grain size reduction in ice is thought to be only achieved by the progressive transformation from dislocation walls into new high-angle grain boundaries, called subgrain rotation or polygonisation. Both our time-resolved numerical modelling and NEEM ice core samples show that grain dissection is a common mechanism during ice deformation and can provide an efficient process in addition to polygonisation to reduce grain sizes and counter-act dynamic grain-growth. Thus, our results show that strain-induced boundary

migration can have a grain-size-decreasing character in polar ice, in particular if strain energy gradients are high. We describe the microstructural characteristics that can be used to identify grain dissection in natural microstructures.

Keywords: ice microstructure modelling, cryo-EBSD, fabric analyser, ice deformation, dynamic recrystallisation, grain size evolution, grain dissection, NEEM ice core

1 Introduction

Knowledge of the properties and processes controlling the flow of ice is essential to understand ice sheet dynamics. Ice sheets creep under gravitational forces (Petrenko and Whitworth, 1999) and their macroscopic flow is affected by properties of individual ice crystals, such as crystallographic preferred orientation (CPO) and grain size (Steinemann, 1954; Budd and Jacka, 1989; Van der Veen and Whillans, 1990; Mangeney et al., 1997; Ng and Jacka, 2014). Ice crystals in ice sheets are thought to mainly accommodate deformation by viscoplastic glide and climb of intracrystalline lattice defects, which is known as *dislocation creep* (Shoji and Higashi, 1978; Pimienta and Duval, 1987). On Earth, the only stable ice polymorph is hexagonal ice Ih, which has a significant viscoplastic anisotropy. The glide resistance on the basal plane, which is perpendicular to the c-axis, is at least 60 times lower than that on the prismatic and pyramidal glide planes (Duval et al., 1983). With deformation, c-axes align in the direction of maximum finite shortening (Azuma and Higashi, 1985) causing a macroscopic mechanical anisotropy of the polycrystalline aggregate (Gao and Jacka, 1987; Budd and Jacka, 1989).

Dislocation creep depends on the CPO and is grain size insensitive. However, other deformation mechanisms such as *grain boundary sliding* or *diffusion creep* are known to depend on grain sizes (Raj and Ashby, 1972; Shoji and Higashi, 1978) and may be strain rate controlling at low stresses (Goldsby and Kohlstedt, 1997; 2001; Pettit and Waddington, 2003). An understanding of grain size evolution in ice sheets including all relevant processes and proposed models (Ng and Jacka, 2014; Durand et al., 2006) is essential to include the full suite of deformation mechanisms into ice flow modelling.

In various deep ice cores, grain size is observed to increase with depth until a stable value is reached (Li et al., 1998; Montagnat et al. 2012; Fitzpatrick et al., 2014). Where drill cores penetrate the glacial to Holocene transition, a distinct decrease in grain size and increase in CPO strength is found (Montagnat et al. 2014a; Weikusat et al., 2017a; Faria et al., 2014a and references therein). In the North Greenland Eemian Ice Drilling (NEEM) ice core a relatively stable grain size of about 10 to 12 mm² is observed below a depth of ca. 400m., but the CPO progressively strengthens further down. (Kipfstuhl, 2010a; Weikusat and Kipfstuhl, 2010; Montagnat et al., 2014a; Binder, 2014). A distinct change towards

strongly aligned c-axes that form an elongated, vertical single maximum is observed at the transition from Holocene to glacial ice at 1400 m depth (Montagnat et al., 2014a; Binder et al., 2014). In the glacial ice, the grain sizes are smaller and more variable than in Holocene ice. This is observed to correlate with higher impurity load in glacial ice. However, the relation of grain size and CPO with impurities is still under discussion (Eichler et al., 2017).

The grain size in ice results from a combination of grain growth and grain-size-reducing mechanisms. The downward increase in grain size in shallow ice towards stable grain sizes implies a stronger relative contribution grain-size-reducing mechanisms when stable grain sizes are achieved. As ice in ice sheets mostly deforms at temperatures close to its pressure melting point, recrystallisation is expected to accompany viscoplastic deformation (Duval, 1979; Jacka and Li, 1994; Kipfstuhl et al., 2009). Recrystallisation includes rotation of crystal lattices, as well as grain boundary migration and/or formation of new grain boundaries (Faria et al., 2014b).

The migration of grain boundaries during *normal grain-growth* (NGG) is driven by surface energy minimisation (Smith, 1964; Weaire and Rivier, 1984; Alley et al., 1986a,b; Duval, 1985; De La Chapelle et al., 1998). NGG leads to an increase of mean grain area with time and equidimensional grains with slightly curved grain boundaries forming 120° angles at grain boundary triple junctions. *Strain-induced boundary migration* (SIBM), however, is driven by strain energies that result from the elastic lattice distortion caused by dislocations (Humphreys and Hatherly, 2004, pp. 251-253). During SIBM, grain boundaries migrate towards highly strained areas in adjacent grains and leave behind dislocation-free regions. This usually causes irregular grain boundaries and bulges towards high energy regions (Means, 1981). SIBM in ice is assumed to cause increasing grain sizes (Duval and Castelnau, 1995) and has been termed *dynamic grain-growth* when combined with NGG (Faria et al., 2014a,b).

During *recovery*, dislocations arrange in lower energy configurations (White, 1977; Urai et al. 1986). This leads to the gradual transformation of low-angle dislocation walls into subgrain boundaries (Weikusat et al., 2017b) and eventually into new high-angle grain boundaries. This process of rotational recrystallisation or *polygonisation* leads to a grain size reduction (Alley et al., 1995; Roessiger et al., 2011). The formation of new grains by *nucleation* is a further mechanism of grain-size reduction, but is thought to be very unlikely in the absence of strong chemical driving forces, as is the case for ice (Drury and Urai, 1990; Humphreys and Hatherly, 2004; Faria et al., 2014b). The deformation-induced recrystallisation mechanisms (SIBM, polygonisation and nucleation) are together termed *dynamic recrystallisation*. Of these mechanisms, SIBM and polygonisation are thought to be dominant in glaciers and ice sheets.

Although SIBM in isolation is in glaciology generally assumed to result in a grain-size increase, it has been observed to decrease grain size in deformation experiments on rock analogues by Means (1983, cf. Figure 4 therein) and Urai (1983, cf. Figure 14 therein). Both studies observed SIBM with rapidly

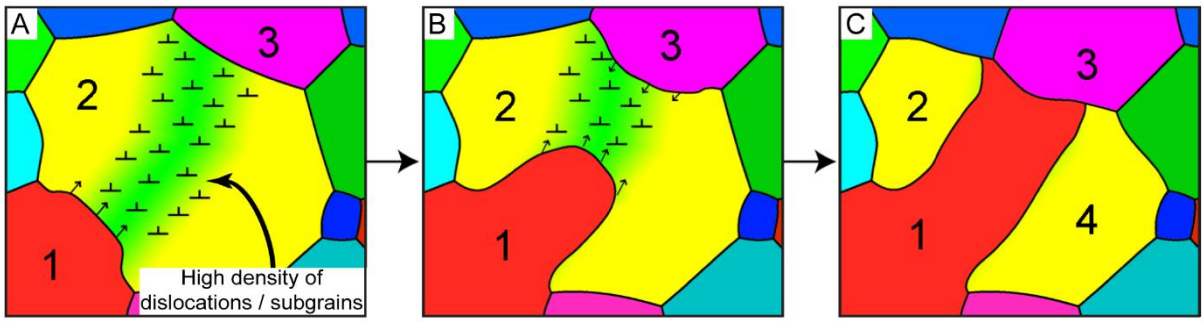

Figure 1: Schematic illustration of the grain dissection process according to Means (1983) and Urai (1983). (A) A bulge of grain 1 is migrating into a high dislocation-density area to reduce locally high strain energies in grain 2. (B) The bulge of grain 1 is migrating further through the high strain-energy area of grain 2. (C) The bulge ultimately reaches grain 3, dividing grain 2 into two grains. Bulging stops due to low energy gradients and driving forces between grain 1 and 3. The new grain 4 and grain 2 are characterised by a similar lattice orientation; an orientation family.

migrating bulges, eventually migrating through a grain and splitting it into two parts when reaching an opposite grain boundary. This causes an effective mean grain-size reduction by forming two "new" grains with similar CPO. Resulting groups of grains with similar orientation were called "orientation families" by Urai (1983). This process was termed *grain dissection* by Urai et al. (1986; 1987) and is known as *geometric dynamic recrystallisation* in metallurgy (Humphreys and Hatherly, 2004, pp. 461-465; de Meer et al., 2002) (Figure 1). Grain dissection is only effective when the grain size is similar to the size of grain-boundary bulges. At larger grain sizes, bulges cannot reach the other side of a grain and polygonisation would dominate. At smaller grain sizes, bulges sweep over a whole grain and thus remove it, which leads to a mean grain-size increase. It follows that grain dissection is most effective at a stable grain size, when polygonisation and grain dissection operate in conjunction.

Grain dissection has not yet been described in natural ice microstructures. Breton et al. (2016) report grain dissection in deformation experiments on laboratory-prepared ice and suspect a grain-size-reducing character. So far, it is assumed that stable grain sizes in ice are achieved by an interplay of dynamic grain-growth and polygonisation only (Alley et al., 1995; De La Chapelle et al., 1998; Montagnat and Duval, 2000; Mathiesen et al., 2004; Roessiger et al., 2011). However, in rock analogues, grain dissection is observed as an effective grain-size-reducing process, in particular at steady-state grain sizes (Jessell, 1986; Urai, 1987).

In this study we will consider the role of grain dissection in the grain size evolution in glacier/ice sheet ice and assess under which conditions it can potentially be an efficient grain-size-reducing mechanism other than polygonisation. We use two approaches: (1) micro-dynamical modelling using the Elle microstructure-modelling platform coupled to a full-field crystal viscoplasticity code (VPFFT) and (2) microstructure and crystallographic orientation maps of ice sampled from the NEEM ice core.

2 Methods

2.1 Microstructural modelling

2.1.1 The Elle modelling platform

The open-source numerical modelling platform Elle (Jessell et al., 2001; Bons et al., 2008; Piazolo et al., 2010) is optimised to model coupled or interacting microstructural processes. Elle was applied in various studies on ice microstructures, such as single and polyphase grain-growth (Roessiger et al., 2011; 2014). The full-field crystal viscoplasticity code (VPFFT) by Lebensohn (2001) coupled to Elle was used to simulate strain localisation, dynamic recrystallisation and folding in ice with and without air bubbles (Llorens et al., 2016a,b; 2017; Steinbach et al., 2016; Jansen et al., 2016; Bons et al., 2016).

Here, only the essentials of the modelling approaches for deformation and recrystallisation are summarised. For more detail on the principles of Elle, the reader is referred to Jessell et al. (2001) and Bons et al. (2008), for the VPFFT code to Lebensohn et al. (2001), and for the coupling of both codes to Griera et al. (2013). Details on the grain boundary migration and recovery codes are presented in Becker et al. (2008) and Borthwick et al. (2014), respectively. The Elle/VPFFT algorithms to model dynamic recrystallisation can be found in Llorens et al. (2016a) and Steinbach et al. (2016). If not indicated differently, we used previously published input parameters for our numerical models (see Llorens et al., 2016a,b; Steinbach et al., 2016).

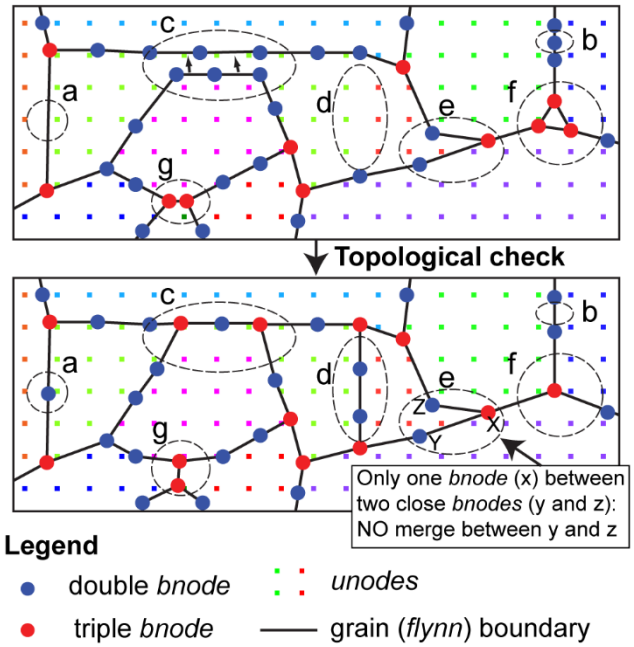

Figure 2: Microstructure discretisation and topological events necessary if *bnodes* move due to deformation or grain boundary migration. Insertion (a) and deletion (b) of a *bnode* to keep a constant resolution (c) Merging two non-neighbouring *bnodes*, this numerically defines grain dissection (d) Insertion of new grain boundary by polygonisation between *unode* clusters above a critical misorientation (e) No merging of two non-neighbouring *bnodes* as number of other *bnodes* between the two close *bnodes* is < 3 (f) Deletion of small *flynn* containing no *unodes* (g) Neighbour switch in triple *bnodes*.

2.1.2 Microstructure discretisation

In Elle, the two-dimensional microstructure of polycrystalline ice is discretised in a set of contiguous polygons, called *flynns*, in a cell with fully wrapping and periodic boundaries. The *flynns* are defined by straight boundaries than link boundary nodes (*bnodes*) in either double- or triple junctions. The *bnodes* are successively moved to achieve grain boundary migration. During grain boundary migration, the development of quadruple or higher-order *bnode* junctions is not allowed, as well as island *flynns* with only one surrounding neighbour *flynn*. To store intracrystalline properties, such as crystal orientation, local stresses, strain rates or dislocation densities, a set of unconnected nodes (*unodes*) is superimposed on the *flynn* network. For our simulations, the *unodes* are arranged in a regular grid of 256x256 *unodes*, which is a requirement of VPFFT. Crystal orientations are mapped onto *unodes* using Euler triplet angles following the Bunge convention (Bunge, 1982).

Topology checks are carried out at all times during the simulations to ensure compliance with topological restrictions (see Figure 2). The topology checks maintain the resolution defined by the set minimum (0.5 mm) and maximum (1.1 mm) *bnode* separation. A new topological check allows for grain dissection: Two unconnected (non-neighbouring) double-junction *bnodes* are merged if they approach closer than the set minimum separation (Figure 2, (c)). This effectively splits the *flynn* adjacent to both *bnodes*, into two daughter *flynns*, which constitutes a grain dissection event. A dissection is not performed if less than three *bnodes* are between the two non-neighbouring *bnodes*, as this would lead to an unviable daughter *flynn* (Figure 2, (d)). The number of dissection events is tracked throughout the simulation.

2.1.3 Modelling crystal viscoplasticity and dynamic recrystallisation

The full-field crystal viscoplasticity code (VPFFT) is based on calculating the stress field from kinematically admissible velocity fields that minimises the average local work-rate under compatibility and equilibrium constraints (Lebensohn, 2001; Lebensohn et al., 2009; Griera et al., 2013). VPFFT assumes intracrystalline deformation in ice Ih accommodated by dislocation glide on basal, pyramidal and prismatic slip systems. The non-basal slip resistance is set 20 times higher than for basal slip as a compromise between accuracy and computational efficiency (Llorens et al., 2016a,b; Steinbach et al., 2016). The non-linear viscous, rate-dependent flow law predicts the strain rate and stress at each point in the computational grid defined by *unodes*.

Since the strain rate and stress fields are initially unknown, VPFFT uses an iterative spectral solver based on the Fast Fourier Transformation. VPFFT computes the viscoplastic response for a short time-step during which velocities are assumed constant. The updated lattice orientations are remapped onto the rectangular *unode* grid and the displacement field is applied to all *bnodes*. Furthermore, geometrically necessary dislocation-densities are calculated by means of the plastic-strain gradient

following Brinckmann et al. (2006). The strain energy at a given position is a function of the dislocation density ρ and the dislocation line energy E_D, which is proportional to square of the Burgers' vector length of the respective dislocation type (Humphreys and Hatherly, 2004, pp. 17-18). In ice Ih, the Burgers' vector of non-basal dislocations is approximately two times longer compared to basal ones (Hondoh, 2000). Hence, non-basal dislocations can provide about four times higher strain energies. Previous numerical models by Llorens et al. (2016a,b) and Steinbach et al. (2016) assume all dislocations are on basal planes and at constant Burgers' vector length, which underestimates strain energies. Here, we use an updated approach that scales the strain energies to the non-basal activity in each *unode* which is predicted by VPFFT to allow up to about four times higher strain energies due to the presence of non-basal dislocations.

Following each VPFFT step, recrystallisation is modelled using Elle. Each recrystallisation step comprises successive steps of discrete implementations of grain boundary migration, recovery and polygonisation. Each mechanism is modelled using a fixed numerical time step and temperature (see section 2.1.4 for input parameters). For numerical stability reasons, the order in which the discrete implementations are performed on the numerical microstructure is first polygonisation, followed by grain boundary migration and recovery. This loop is repeated until the numerical time for the recrystallisation processes equals the one envisaged for one deformation increment by VPFFT, which determines the numerical strain rate (see Steinbach et al., 2016 and Figure 2 therein). As the numerical time steps and the resulting microstructural changes per step are low, we assume that the effective microstructural response is not significantly different from conditions during which the mechanisms operate concurrently.

Grain boundary migration is modelled using a front-tracking approach moving individual *bnodes* towards lower energy positions (cf. Becker et al., 2008; Llorens et al., 2016a). In this energy-minimisation approach, the *bnode* velocity is proportional to a driving force calculated from the change in local surface- and strain-energy that result from a change in position of that *bnode*. These energy fields are determined with four trial positions close to the actual *bnode* position. The change in surface energy is due to a change in length of the grain-boundary segments to neighbouring *bnodes*. The change in strain energy results from reducing the strain energy to zero in the area swept by the *bnode* and its adjoining boundary segments.

For the recovery mechanism, an energy minimisation system is used that is analogous to the grain-boundary migration approach. It is based on decreasing the lattice misorientation between two *unodes* towards a lower energy configuration (see Borthwick et al. (2014) and Llorens et al. (2016a) for details). Recovery reduces the local dislocation density proportional to the decrease in lattice misorientation and allows the development of subgrains. The subgrains are defined as *unode* clusters and are characterised by a certain misorientation with neighbouring clusters. The polygonisation routine detects these clusters

and adds new high-angle grain boundaries defined by *bnodes*, if the cluster misorientation is above a critical angle. This is done by Voronoi decomposition of the *unode* clusters using the Voronoi points surrounding the cluster as new *bnodes* (Steinbach et al., 2016). To be consistent with Steinbach et al. (2016), we use a critical angle of 5°, comparable to the 3-5° reported for ice Ih (Weikusat et al., 2011a,b).

2.1.4 Simulation setup

The simulation setup comprises two numerical strain rates applied to eight model setups with different initial mean grain-areas (Table 1). Each initial microstructure was discretised in a 14.14 x 7.07 cm box (ratio height/width = 2) and deformed under pure shear conditions to approximately 50% vertical shortening at incremental strains of 0.5% over 140 time-steps. Different strain rates were achieved by varying the number of recrystallisation loops per strain increment. Two or 20 recrystallisation loops, per $1.25 \cdot 10^{7}$s time, per a VPFFT strain increment of 0.5%, achieved strain rates of $2 \cdot 10^{-10} s^{-1}$ or $2 \cdot 10^{-11} s^{-1}$, respectively. These values are higher than reported for the NEEM ice core, where the estimated mean vertical strain rate is $3.2 \cdot 10^{-12}$ s^{-1} (Montagnat et al., 2014a). Therefore, the numerical strain rates are only qualitatively comparable with natural strain rates (Steinbach et al., 2016). The temperature in the simulations was set to -30°C, which is comparable to Holocene ice conditions in NEEM ice core (Sheldon, et al., 2014). The initial grain sizes were set by varying the initial number of grains in a foam texture (Table 1). The initial c-axis orientations were adjusted to be similar to measured second-order orientation tensor eigenvalues from NEEM ice core at approximately 700m depth, defining a weak single maximum CPO which is realistic for many ice cores (see review by Faria et al., 2014a). As summarised in Table 1, the simulations are labelled using a terminology that indicates their mean initial grain area in mm² (G) and the order of magnitude in strain rate (R). Hence, for instance the simulation starting with a grain area of 20 mm² at a strain rate of $2 \cdot 10^{-11}$ s^{-1} is named G20R11.

During the simulations, the numbers of split events by grain dissection and polygonisation is automatically counted for each time-step. As outlined in section 2.1.2, a grain dissection event during the simulation is defined as a topological event during which two non-neighbouring *bnodes* are merged into one. This way, the number of grain dissection and polygonisation events is slightly overestimated. Technically, it is not a grain dissection event when two *bnodes* or grain boundaries close without splitting a grain. The same holds for polygonisation, where all events are counted, including those where a resulting grain is too small and is immediately deleted. Nevertheless, counting split events remains the most reproducible way to estimate the efficiency of grain dissection compared to polygonisation.

To improve statistics, each of the 16 simulations indicated in Table 1 was repeated three times. For each repetition the initial CPO was slightly varied to allow for some variation between the simulations. The numbers of both polygonisation and grain dissection events for each step were normalised to the actual number of grains at this simulation step. The resulting value can be regarded as the number of events

Table 1: Overview of the settings of the numerical simulations. Each simulation is labelled with the initial mean grain-area in mm² (G) and with the strain rate with R10 and R11 standing for $2 \cdot 10^{-10}$ and $2 \cdot 10^{-11}$ s^{-1}, respectively. All simulations were repeated three times to average the number of grain dissection and polygonisation events

Simulation name	Initial number of grains	Initial mean grain area (mm^2)	Numerical strain rate (s^{-1})
G05R10	2003	4.99	$2 \cdot 10^{-10}$
G10R10	1000	10.00	$2 \cdot 10^{-10}$
G15R10	667	14.99	$2 \cdot 10^{-10}$
G20R10	500	20.00	$2 \cdot 10^{-10}$
G30R10	333	30.03	$2 \cdot 10^{-10}$
G40R10	250	40.00	$2 \cdot 10^{-10}$
G60R10	167	59.88	$2 \cdot 10^{-10}$
G80R10	125	80.00	$2 \cdot 10^{-10}$
G05R11	2003	4.99	$2 \cdot 10^{-11}$
G10R11	1000	10.00	$2 \cdot 10^{-11}$
G15R11	667	14.99	$2 \cdot 10^{-11}$
G20R11	500	20.00	$2 \cdot 10^{-11}$
G30R11	333	30.03	$2 \cdot 10^{-11}$
G40R11	250	40.00	$2 \cdot 10^{-11}$
G60R11	167	59.88	$2 \cdot 10^{-11}$
G80R11	125	80.00	$2 \cdot 10^{-11}$

per grain in the respective time-step of the simulation.

2.2 Microstructure characterisation of NEEM ice core samples

Microstructure and crystallographic-orientation mapping for this study is performed using both EBSD (electron backscatter diffraction) and the automated Fabric Analyser. Using cryo-EBSD, we study three ice core sections from Holocene ice at 442.7 m, 718.8 m and 889.3 m depth and four ice core sections from the glacial ice at 1737.7 m, 1937.7 m, 1993.8 m and 2103.8 m depth.

Each ice core section of approximately 90x55 mm was cut into 10 to 15 EBSD samples using the method of Weikusat et al. (2011a). The samples were imaged by optical microscopy at the Alfred Wegener Institute (AWI) in Bremerhaven before being transported to Utrecht University. All ice core sections, except the ice core section at 442.7 m depth, were mapped using the Nova Nanolab equipped with an EBSD detector (Oxford Instruments HKL Technology, Abingdon, UK) and a cryo-stage (Quorum

Technologies Ltd. Ringmer, UK). These EBSD patterns were acquired, processed and indexed using the Channel 5 software of OI-HKL Technology. The ice core section at 442.7 m depth was mapped using a FEI Helios NanoLab G3 UC equipped with the same EBSD detector and cryo-stage. The EBSD patterns of this ice core section were indexed using the Aztec software (Oxford Instruments, High Wycombe, UK). The reader is referred to Weikusat et al. (2011a) for an extensive description of the EBSD sample preparation, sample transfer and the EBSD mapping conditions we used.

A total number of 216 EBSD maps is used for this study, 91 in the Holocene ice and 125 maps in the glacial ice. Depending on the grain size and the area of interest, the EBSD maps vary in area from 0.5 mm^2 to 6 mm^2. Each of these EBSD maps was visually checked for signs of grain dissection according to the schematic descriptions of grain dissection by Means (1983), Urai (1983) and Figure 1. The number of grain dissection events was counted with the area of the EBSD map and its mean grain area. This counting is intended as a qualitative estimate of the frequency of grain dissection in the NEEM ice core. The area of the EBSD map was divided by the observed number of grain dissection events in this map. This provides a measure for the average area necessary to observe one grain dissection event. Afterwards, the average grain size of the EBSD map was divided by this measure resulting in a corrected value. Essentially, this procedure is similar to simply dividing the number of dissection events by the number of grains, but allows correcting for the difference in average grain size, EBSD-map area and for the low number of grains in an EBSD map. We counted completed grain dissection in EBSD maps, which implies that the dissection itself may have occurred in the past and adds a “memory effect” that increases the relative occurrence values. Therefore, the resulting unit is “number of grain dissection events per grain” and can be regarded as the relative chance of a grain being dissected or having been dissected based on the EBSD dataset.

The automated Fabric Analyser (G50 by Russell-Head Instruments) provides high-resolution c-axis-orientation maps of ice thin sections (Wilson et al., 2003). The obtained "c-axis maps" are an essential addition, as they provide better statistics by covering a larger area and, thus, more grains than EBSD maps. Furthermore, more samples per depth can be analysed (Weikusat and Kipfstuhl, 2010).

For our study, 13 c-axis maps (total area 1.15 m^2 and 8392 grains) from the Holocene part of the NEEM ice core were reviewed to detect grain dissection. C-axis maps from the glacial part are not suitable for the search for grain dissection events as c-axis misorientations are too low to identify high-angle boundaries. Therefore, the comparison between Holocene and glacial ice can only be based on the EBSD data.

In contrast to the EBSD, which measures the full crystallographic orientation, the Fabric Analyser provides only orientations of the c-axes. This limitation has a crucial effect on the identification of grain dissection events in c-axis maps. When two second-neighbouring grains share the same crystallographic orientation, there is a high probability for them being a product of grain dissection. However, if the full

orientation information is missing, such a conclusion may be erroneous. Thus, we add a grain-connectedness criterion and searched c-axis maps only for grains where grain dissection appeared imminent, but has not yet been completed. For each c-axis map, the number of imminent grain dissection events was counted and divided by the number of grains. Effectively, the result is the same statistical parameter that is derived from EBSD maps, but only for imminent grain dissection events, which results in lower values obtained from c-axis maps than from EBSD maps. The results are therefore only qualitatively comparable.

Grain dissection observed in EBSD maps or c-axis maps can potentially be a sectioning effect of a 3D sample. Both methods only show a snapshot of a continuously evolving microstructure, hence an uncertainty remains whether a bulge would have completed the dissection in the third dimension. However, this stereological issue is unproblematic with respect to grain size evolution as grain sizes in ice are also determined from two-dimensional sections (see methods of Binder, 2014).

3 Results

3.1 Numerical simulation results

An overview of selected microstructures after 50 % of vertical shortening is shown in Figure 3. The final microstructure is marked by curved grain boundaries and only a few equidimensional grains. The c-axes are mainly aligned towards a single maximum CPO as shown by stereographic projections and by common red colours in c-axis azimuth maps. Microstructural similarities are only observed between simulations with common strain rates, independent of initial grain area. As expected, the high strain-rate simulations show smaller final grain areas, whereas the low strain-rate simulations show larger final grain areas. Dislocation densities are higher and more homogeneously distributed at a high strain rate than at a low strain rate.

The circles in Figure 3 represent regions where a splitting of a grain by polygonisation appears imminent. In particular, the grain indicated by circle A in the final microstructure of simulation G10R11 contains two distinct regions with different c-axis azimuth. This grain is expected to split into two grains by polygonisation in the following numerical time-step. Red squares in Figure 3 indicate regions where grain dissection appears either completed (square E) or imminent (squares C and D). Especially square D provides information on the driving force for bulging. Here, two bulges migrate into an area of a grain that exhibits the highest dislocation densities in the microstructure. Close examination of the centre of square D reveals high dislocation densities distributed in stripes. The dislocation densities vary strongly locally, also within regions with overall high dislocation densities.

All 16 numerical simulations show situations, during which strongly-bulging grain boundaries migrate through a grain and either merge with the opposite grain boundary or with another bulge (cf. supplementary material). Both situations cause splitting of a grain into two parts in the sense of grain dissection. Figure 4 illustrates several examples of grain dissection during the simulations. For example, simulation G15R10 shows a grain boundary bulging into an area of high variation in lattice orientation from step 74 to 84. Ultimately, this bulge migrates through the grain and merges with the opposite boundary. A similar situation is observed results from simulation G60R10, where a rapidly migrating bulge merges with the opposite boundary, which dissects a grain into two parts. The example from G20R11 illustrates both an event of grain dissection and polygonisation. The bulge indicated by the square migrates towards- and finally merges with the opposite grain boundaries. This dissects the former grain into three parts. The small new grain in the upper left of the bulge shrinks and disappears within the following simulation steps. Furthermore, the bulging grain itself is dissected between simulation step 76 and 80, as visible on the right hand edge of the images. The white ellipse marks a subgrain boundary that develops into a high-angle grain boundary by polygonisation (Figure 4C). All bulges move towards high dislocation-density areas, leaving behind an area free of dislocations. The local dislocation-density field shows highly heterogeneous distributions of dislocations.

Both the low and the high strain-rate simulations with initial grain areas up to 15 mm² are marked by mean grain-area increase (Figure 5A). Mean grain-area decrease is observed in high strain rate simulations with initial grain areas higher than 20 mm². The mean grain-area evolutions can be classified in two stages. The first stage up to 30% of vertical shortening is characterised by a regular change in grain area, which either increases or decreases. In the following second stage, an approximate stable mean grain area of 17±0.5 mm² and 80±2.1 mm² is reached in the high and low strain-rate simulations, respectively. Some simulations appear not to have reached a steady state, even at 50% shortening (G80R10 and G60R10; dotted lines in Figure 5). Grain-area histograms (Figure 5B) show that the grain size distribution broadens with strain from the initial near log-normal distribution.

The number of polygonisation and grain dissection events (Figure 6) for each of the eight initial grain-sizes and two strain rates was averaged over the two stages observed in mean grain-area evolution (Figure 5). The first stage was taken from step one to 74 (0 to 31% of vertical shortening) and the second one from step 74 to 140 (31 to 50% of vertical shortening). The highest frequencies of both grain dissection and polygonisation events per grain are observed at the low strain rate (left y-axis, black and red symbols in Figure 6). Hence, a comparison of their relative frequency is necessary, which is illustrated in the blue curve of Figure 6 (right y-axis) that shows the percentage of mean grain dissection events from the total mean number of both grain dissection and polygonisation events per grain. Large errors (standard deviation) for the low strain-rate simulations are a result of the large grain sizes and, therefore small number of grains. In general, the highest fractions of grain dissection events are

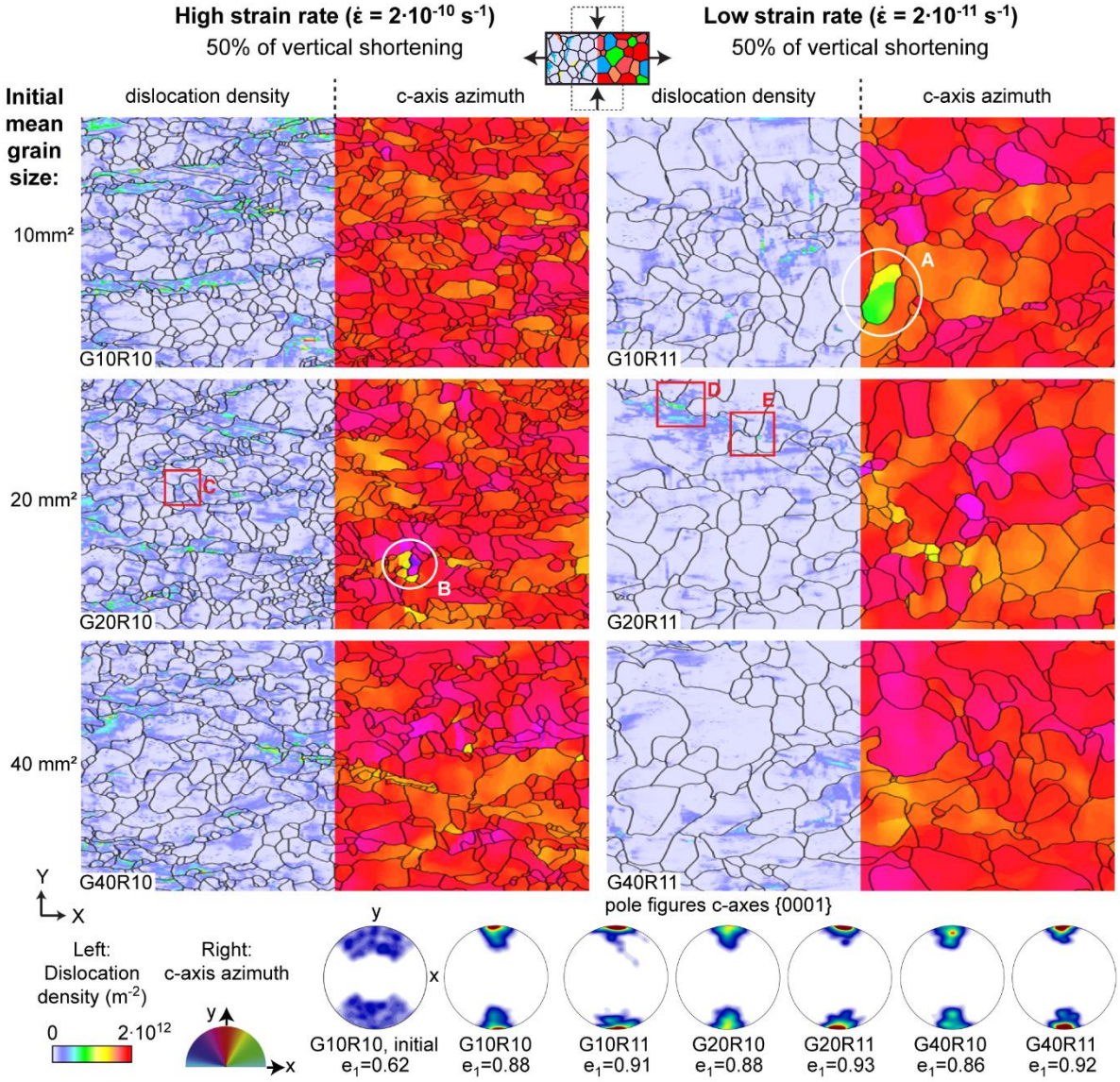

Figure 3: Overview of numerical microstructures after 50% of vertical shortening (i.e. final simulation step) with grain boundary networks (black lines) for the whole deformation box. The box is subdivided in the colour code for dislocation density (left) and for the c-axes azimuths (right), where red colours indicate vertically oriented c-axes. The corresponding pole figures and first eigenvalues of the second order orientation tensor (e_1) are shown below. The initial pole figure and first eigenvalue of G10R10 are provided as an example of the starting configuration. The squares indicate regions where grain dissection has either occurred or is imminent, while the circles show subgrain boundaries likely to develop into new high-angle grain boundaries by polygonisation.

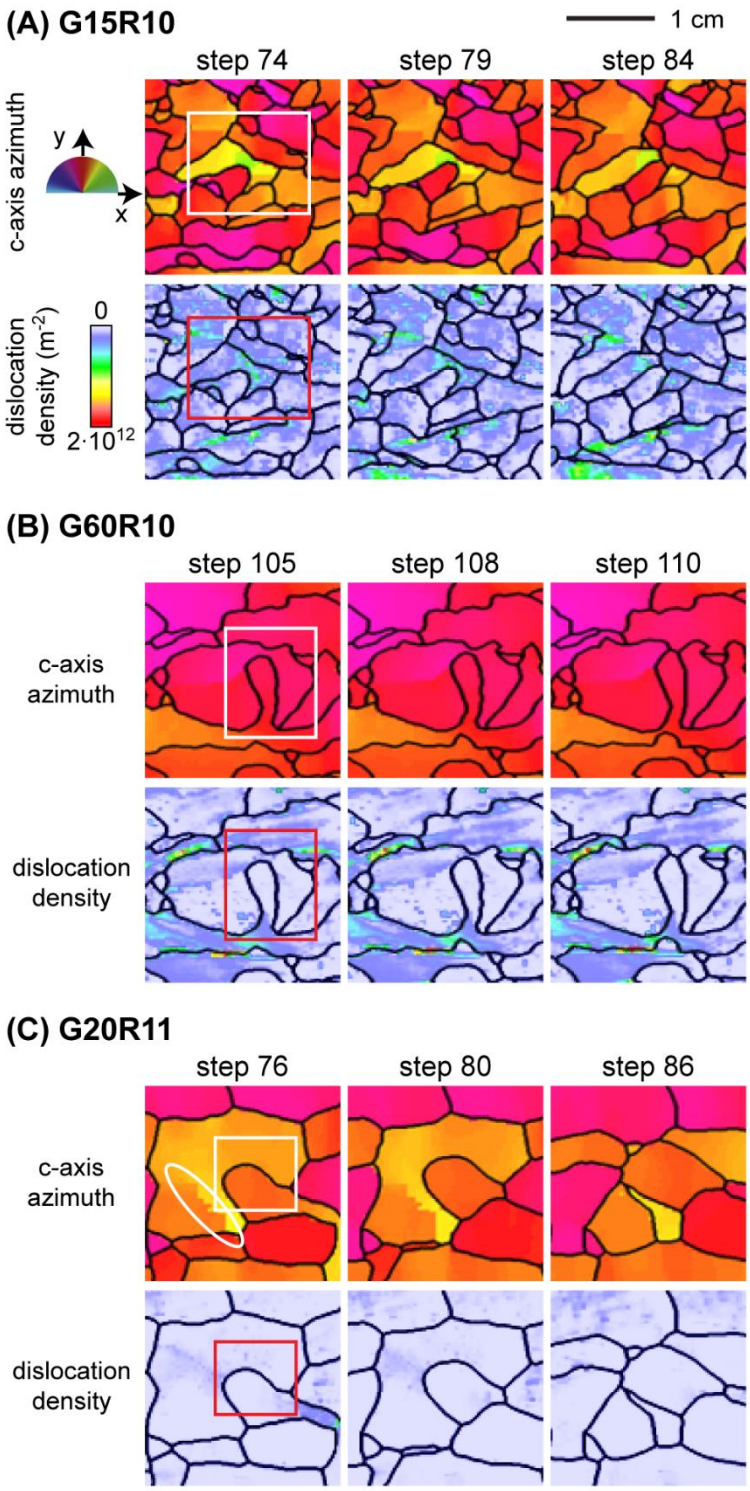

Figure 4: Detail of several examples of grain dissection events observed in the numerical simulations. The images are 1 by 1 cm snapshots and are colour coded for c-axis azimuth and dislocation density. The squares indicate rapidly-migrating bulges merging with an opposite grain boundary (grain dissection). The white ellipse shows where a subgrain boundary develops into a high-angle grain boundary by polygonisation.

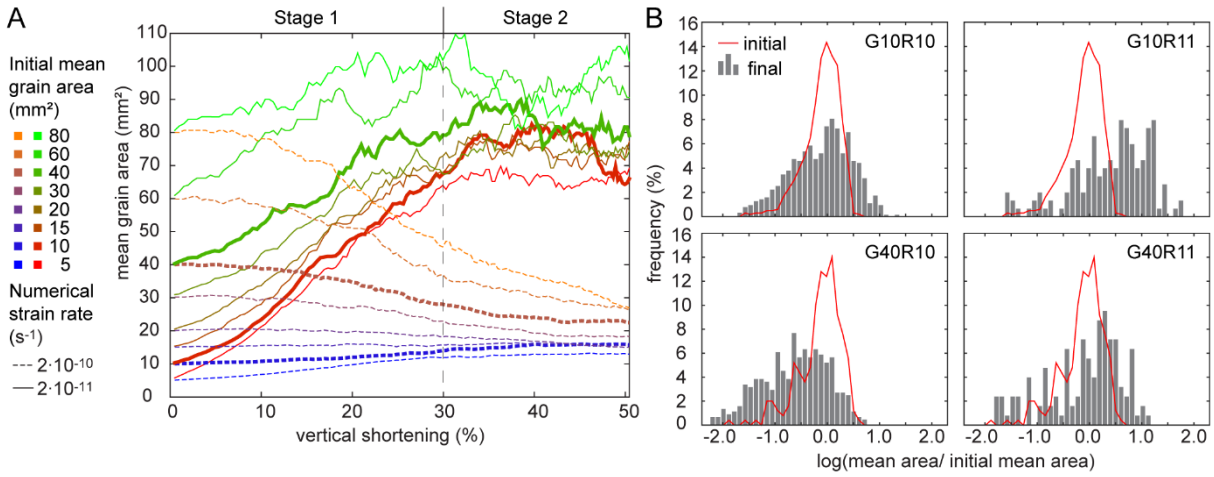

Figure 5: Overview of grain-area evolution in the numerical simulations. (A) Mean grain-area as a function of vertical shortening. In a first stage until approximately 30% shortening, mean grain areas either increase or decrease, which is followed by a second stage of more stable grain areas. Simulation results shown in detail in (B) (10 mm² and 40 mm²) are highlighted as bold lines. (B) Grain area histograms of selected simulations at initial and final simulation step. Areas were normalised to initial mean values.

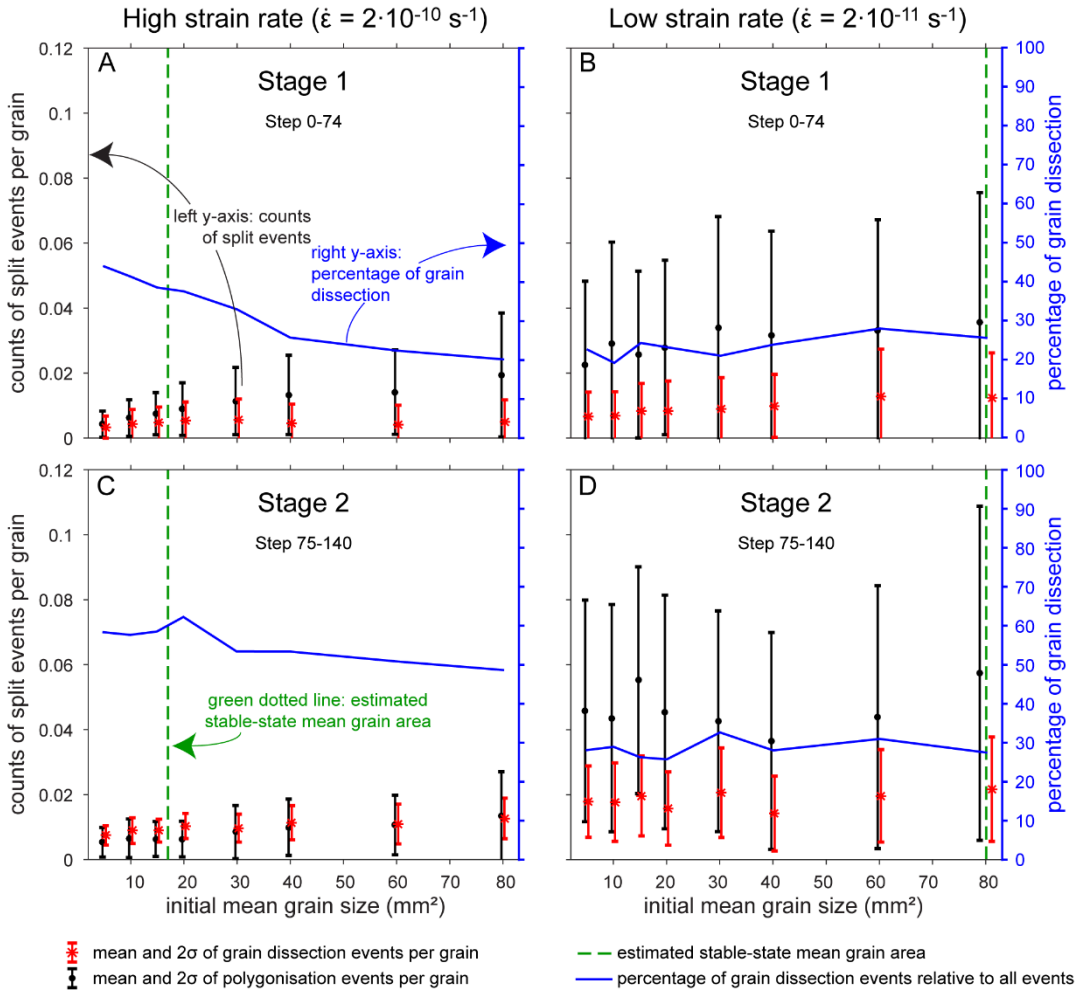

Figure 6: Statistics of grain-dissection and polygonisation events per grain. Data is sorted for the (A,B) first and (B,D) second stage of grain size evolution and (A,C) high and (B,D) low strain rate. The first stage was taken from step 0 to 74 (0-31% shortening) and the second one step from 75 to 140 (from 31% shortening). Error bars indicate two standard deviations (2σ) of the counting statistics. The dotted green line indicates approximate stable mean grain areas for the high and low strain-rate simulations. The blue line and right y-axis show the mean percentage of grain-dissection events per grain from the total number of splitting events by grain dissection and polygonisation.

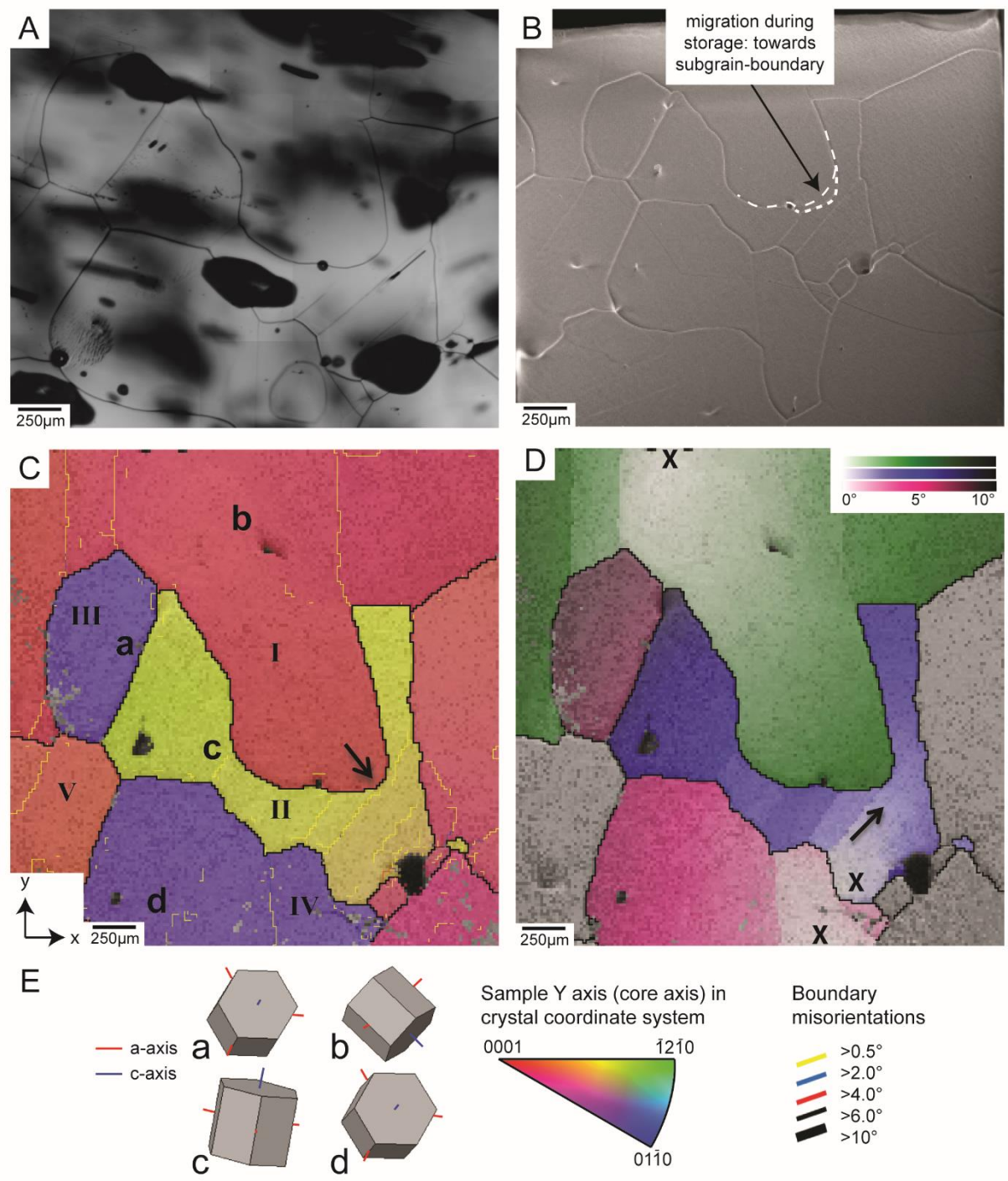

Figure 7: Optical-microscopy, SEM and EBSD maps of an ice core sample at 718.8m depth in the NEEM ice core. (A) Part of the optical-microscopy image taken just after sample preparation. (B) SEM image of the mapped part of the EBSD sample with the edge of the EBSD sample in the upper part of the image. (C) EBSD map, with the y-axis parallel to the (vertical) core axis. (D) Map showing the orientation difference of up to 10° relative to the three spots marked with 'X'. (E) Schematic illustration of measured full CPO (c- and a-axes) at positions (a-d), and colour codes for CPO and boundary misorientation.

observed at the high strain rate, although polygonisation generally dominates over grain dissection. However, dissection events dominate when the grain size is close to equilibrium (green dotted lines in Figure 06SplitStatsElle) in the high strain rate experiments. This is observed for small initial mean grain-size simulations already from stage 1 and also for large initial mean grain-size simulations during stage 2. Here, we observe 50% or more split events by grain dissection.

3.2 EBSD and Fabric Analyser results from NEEM ice core

Figure 7 shows an example of grain dissection in the NEEM core at 718.8m depth. The black spots in the optical microscopy image of Figure 7A are air bubbles at or just below the surface (Kipfstuhl et al. 2006). The comparison of this image with the SEM image (Figure 7B) shows that the bulge of grain I migrated slightly into grain II during the nine days of sample transport and storage. The map in Figure 7D shows a strong orientation gradient of approximately 10° in grain II. Most of this orientation gradient is accommodated by four parallel low-angle (< 2°) subgrain boundaries in grain II. The orientation gradient map indicates a comparatively low misorientation of about 2 to 3° between grain III and IV, which is also visible in the schematic illustrations of CPO at positions (a) and (d) in Figure 7E.

Figure 8 shows another example of grain dissection in Holocene ice at 442.7m depth in the NEEM ice core. The comparison of the optical microscopy image with the SEM image (Figure 8B), which was taken eleven days after sample preparation, shows that the surface changed very little during transport and storage at Utrecht University. The EBSD map in Figure 8C shows a strong bulge in grain I between grains II and III. Grain II and III differ by about 3° in 3D crystallographic orientation (Figure 8D) showing that grain II and III have a very similar CPO (Figure 8E). Grain III shows a very low orientation gradient, except for the part close to the bulge of grain II as indicated by the arrow. This low orientation gradient is also reflected in the low misorientations along subgrain boundaries of about 0.5° in this area (Figure 8C).

The c-axis maps obtained using the Fabric Analyser were processed manually to detect potential grain dissection events. As described in section 2.2, we selected only events where grain dissection appears imminent and the future fragments are still connected through a thin bridge. Figure 9 shows a 7 x 9 cm thin section from the NEEM ice core at 1211.7 m depth, grain dissection events are marked by white rectangles. As shown in Figure 9C, dissected grains often develop subgrain boundaries across the connecting bridge. This is in agreement with the EBSD data showing high orientation gradients and formation of subgrain boundaries within the dissected grains.

The frequencies of grain dissection events as a function of depth across the Holocene-glacial ice transition are shown in Figure 10. There appears a downward trend towards more dissection events, counted in EBSD images, in the Holocene ice, but with only three samples, this trend may not be significant (Figure 10A). There is, however, a significant decrease in dissection frequencies in the

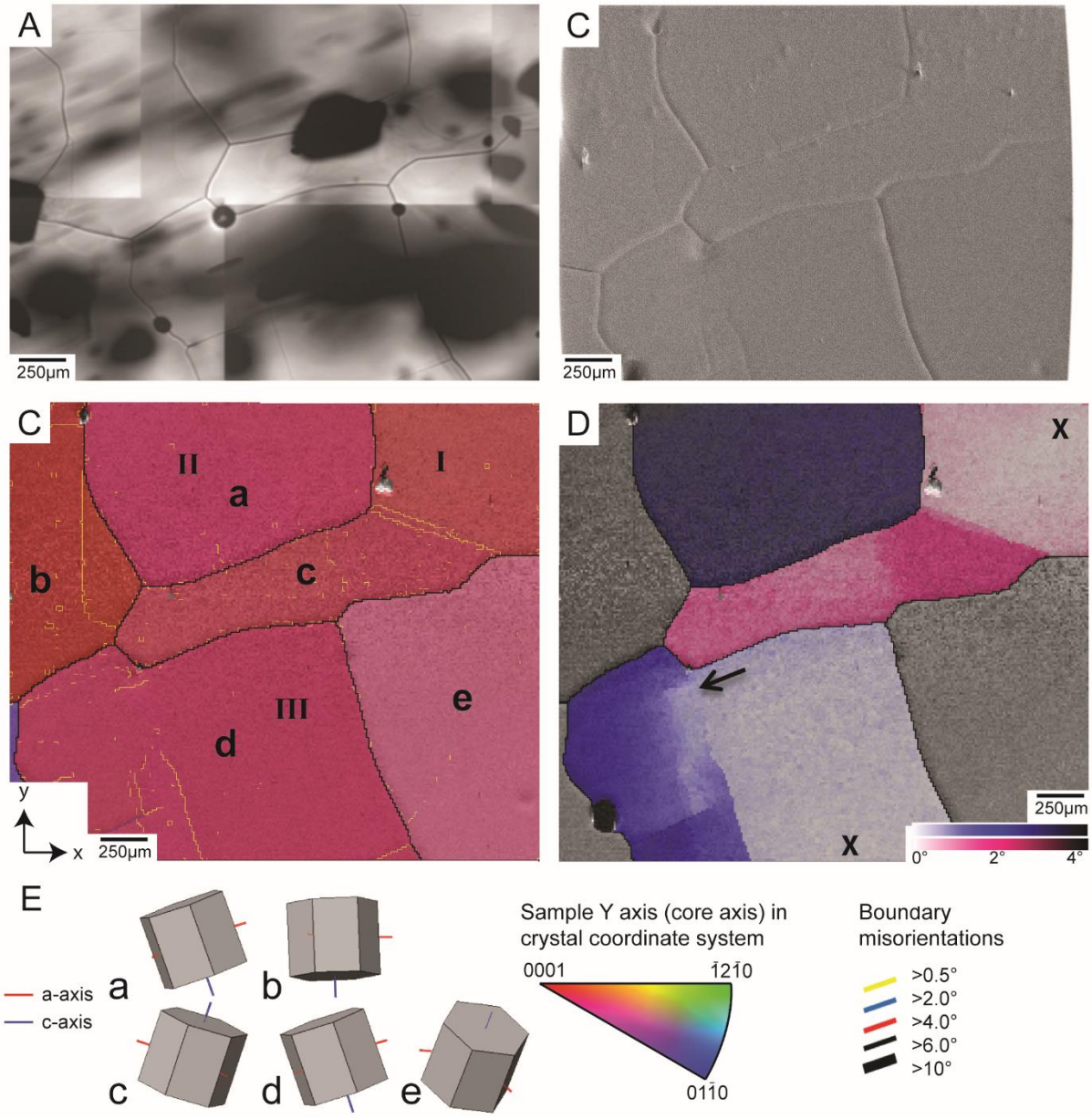

Figure 8: Optical-microscopy, SEM and EBSD maps of an ice core sample at 442.7m depth in the NEEM ice core. (A) Part of the optical-microscopy image taken just after sample preparation. (B) SEM image of the mapped part of the EBSD sample. The curved edges are a result of the beam being blocked by the electron column. (C) EBSD map, with the y-axis parallel to the (vertical) core axis. (D) Map showing the orientation difference of up to 4° relative to the two spots marked with 'X'. (E) Schematic illustration of measured full CPO (c- and a-axes) at positions (a-e), and colour codes for CPO and boundary misorientation.

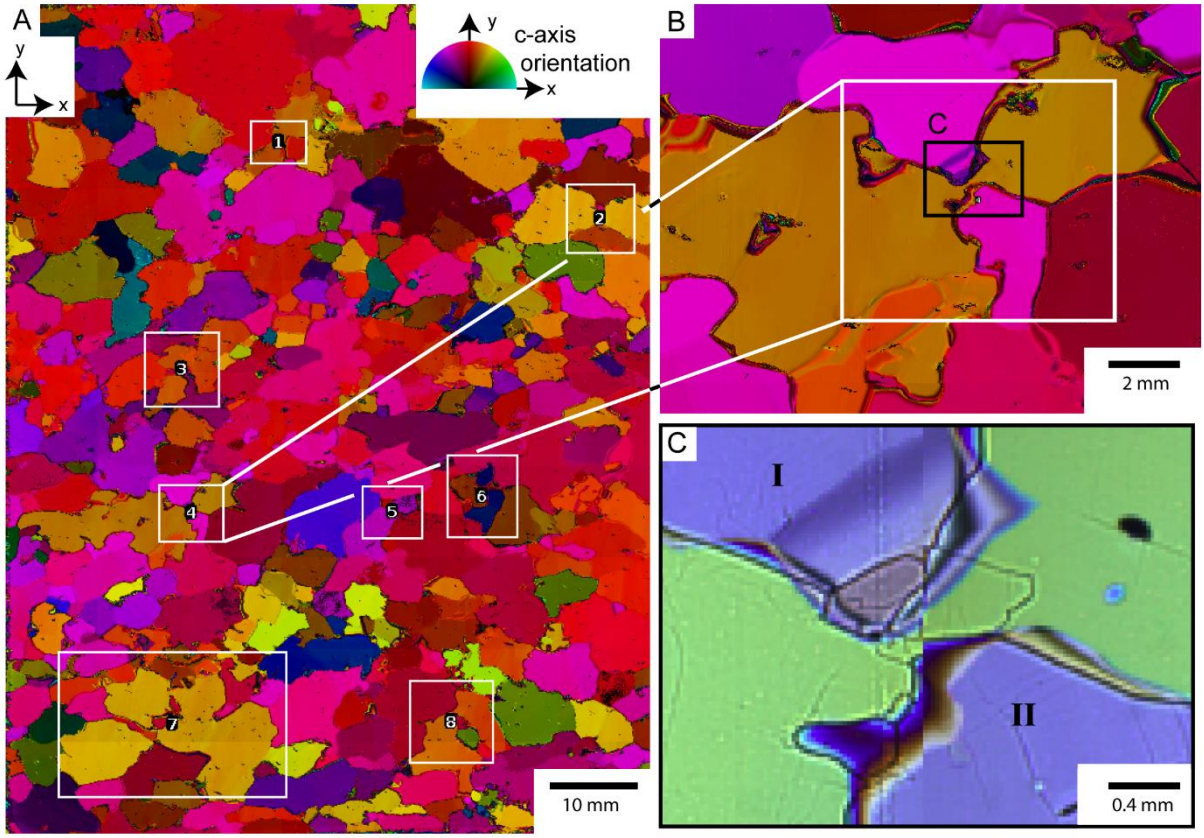

Figure 9: Grain dissection events in c-axis map, y-axis parallel to (vertical) core axis. **(A)** C-axis orientation map of a 7 x 9 cm thin section from the NEEM ice core at 1211.7 m. Colours indicate the azimuth of c-axes relative to the vertical y-axis. Imminent dissection events are marked with white rectangles. **(B)** Detail of a dissection event. Grain boundaries are highly irregular due to dynamic recrystallisation. The orange grain is almost split in two grains that are still connected through a very narrow bridge. **(C)** Photomicrograph, with cross-polarised light, of the same spot showing the connecting bridge in detail. Dark lines are grain-boundary grooves at the surface. Subgrain-boundaries develop at the thin bridge between the dissected subgrains.

samples from glacial ice, from about one per grain to one per every four grains. Counts of imminent split events observed in c-axis maps are only available for Holocene ice down to 1279 m depth. The average number of imminent split events is much about one per one hundred grains (0.010 ± 0.003). This number is much lower than split events counted in EBSD images as only imminent events are counted in the c-axis maps. The frequencies of grain dissection in c-axis maps do not show a significant trend towards higher or lower grain-dissection frequencies with depth.

4 Discussion

4.1 Time-resolved numerical microstructure evolution under the influence of grain dissection

All simulations show situations that can be identified as grain dissection in the sense of the descriptions by Urai (1987) and Means (1983; 1989) (see movies, supplementary material). The simulations provide

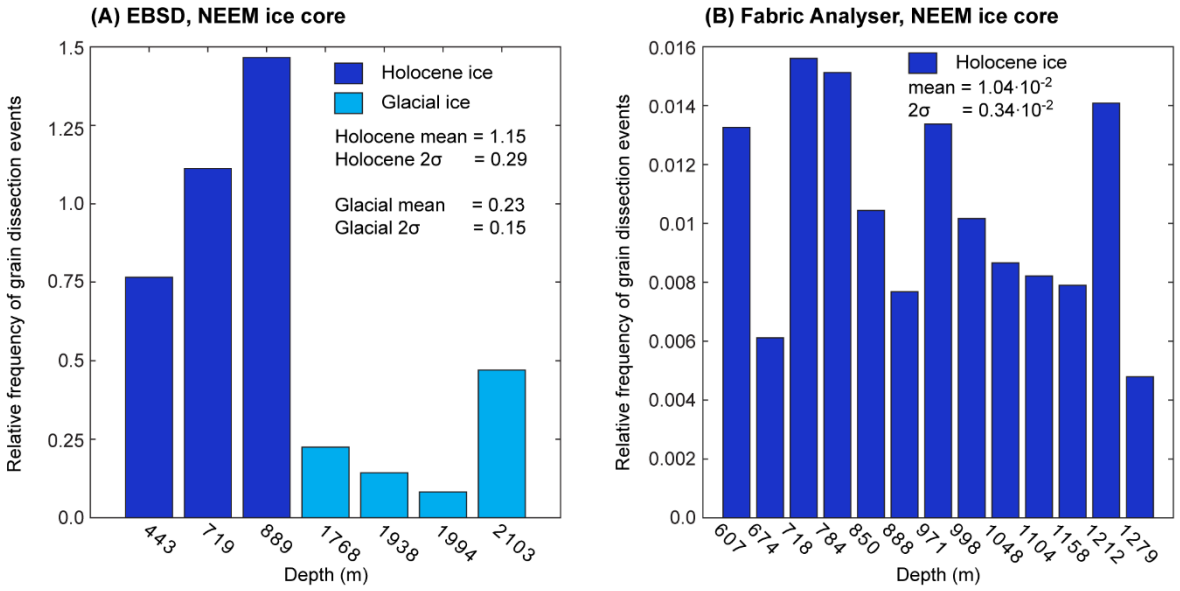

Figure 10: Frequency of grain dissection events. (A) Results obtained from EBSD maps plotted as a function of depth across the transition from Holocene to glacial ice. (B) Results from c-axis maps (Fabric Analyser). The generally lower frequencies for c-axis maps are a result of only counting imminent grain dissection events in c-axis maps and completed dissection events in EBSD maps.

a time series to study the interaction of this process with polygonisation, recovery, grain boundary migration and viscoplastic deformation and their relative contribution to microstructure evolution. The numbers of grain dissection and polygonisation events are similar (Figure 6), which indicates that both mechanisms significantly contribute to microstructure evolution. Thus, grain dissection cannot be considered as a transient or negligible effect during the simulations, which underlines the necessity to assess its importance for ice micro- to macro-dynamics. As our simulations are 2D, grain dissection cannot be sectioning effect of a 3D sample. It needs to be assessed under which conditions, grain dissection is most efficient.

High frequencies of grain dissection relative to polygonisation events can be seen in the high strain rate simulations (Figure 6A and 6C). Here, in five of eight simulations, the grain size evolution is marked by grain size decrease, which indicates the grain-size-decreasing character of grain dissection. Additionally, if the grain size does not change significantly from the start or has equilibrated to steady-state values during the second stage of grain size evolution (Figure 5A), grain dissection dominates over polygonisation (Figure 6). In particular, grain dissection is most effective during the second stage of the high strain-rate simulations (Figure 6C). The observation of efficient grain dissection at steady-state conditions is consistent with experimental results by Jessell (1986) and Urai (1987). When the mean grain size is larger than the equilibrium one and thus grain size decreases, polygonisation dominates over dissection, as is observed in the high strain-rate simulations and in rock analogue experiments by Herwegh et al. (1997).

It remains questionable how suitable mean grain areas are to assess if a steady-state microstructure is reached. Although trending towards more steady values, the final mean grain-areas still vary significantly (Figure 5A). The grain area distributions are broadened and more heterogeneous towards the end of the simulations (Figure 5B), which is expected from observations of natural ice microstructures under dynamic recrystallisation (Kipfstuhl et al., 2009). Obtaining mean grain areas from a broadened grain area distribution can be responsible for the observed variability in final grain areas. Furthermore, at low strain rates, the final number of grains is lowered, which additionally affects the mean grain-area calculation.

Compared to natural vertical strain rates at the NEEM ice core that are in the order of 10^{-12} s^{-1} (Montagnat et al, 2014a), our numerical strain rates are about an order of magnitude higher and results in larger grain sizes than observations in the NEEM ice core (Binder et al., 2014). Using lower numerical strain rates is feasible, yet even larger grain sizes are produced. The grain size depends on the effective grain boundary mobility that is an Arrhenius-type function of an intrinsic mobility, activation energy and temperature (Nasello et al., 2005). As Steinbach et al. (2016) describe, the numerical setup currently uses literature values for intrinsic grain boundary mobility and activation energy from experimental studies by Nasello et al. (2005). We suggest that the mobility and activation energy are not sufficiently constrained to reproduce realistic grain sizes at natural strain rates. In particular, dissolved impurities are suspected to reduce mobilities (Alley et al., 1986b), but are currently not taken into account in the numerical routine. Further investigations of this issue are beyond the scope of this contribution and remains part of future research.

4.2 Grain dissection along NEEM ice core

EBSD results on frequencies of grain dissection from Figure 10A imply that grain dissection in the NEEM ice core is most efficient in the Holocene ice and in particular around 700 to 900 meter depth (35 to 60% estimated finite shortening based on NEEM annual layer thicknesses by Rasmussen et al., 2013). However, whether this trend is real or a result of the limited number of processed samples is uncertain. In particular, this becomes obvious when comparing with results from c-axis maps (Figure 10B), where no evident trend in the number of imminent grain dissection events is visible.

The results in Figure 10 can be compared with mean grain-boundary curvature data from NEEM ice core presented by Binder (2014, Figures 7.1 to 7.8 therein). The study by Binder (2014) converts mean grain-boundary curvature to dislocation densities and observes highest curvatures from about 600 to 1300 m depth (30 to 75% estimated finite shortening based on Rasmussen et al., 2013). Our EBSD samples marked by highest relative numbers of grain dissection events are taken from this region of high mean grain-boundary curvature. This implies that strong grain boundary curvature may be indicative for the potential activity of grain dissection. Another characteristic of this region are stable grain sizes

(Binder, 2014). The higher efficiency of grain dissection in Holocene ice of NEEM ice core (Figure 10A) is in accordance with the observations from simulations that grain dissection is most efficient relative to polygonisation, if the microstructure is in steady state (Figure 6C).

The deformation mode in NEEM ice core is interpreted to change from vertical shortening to simple shear at about the transition from Holocene to glacial ice, when c-axes in Holocene ice trend towards a vertical single maximum (Montagnat et al., 2014a). As ice crystals in the Holocene part are mainly vertically shortened, a higher density of non-basal dislocations may be expected in Holocene ice, in particular towards the Holocene-glacial ice transition. The activation of non-basal planes is explicable with the single maximum CPO in which the basal planes are in an unfavourable orientation to accommodate vertical shortening. Alternatively, a constant non-basal activity would imply a strain rate decrease with depth as the ice becomes harder to deform. Non-basal dislocations provide higher line energies (Schulson and Duval, 2009, pp. 16-18), which in turn implies higher energy gradients driving SIBM and more grain dissection. This may be reflected in Figure 10A showing a trend towards more efficient grain dissection with depth in Holocene ice, but a significantly less grain dissection in glacial ice. Future research could further investigate, whether a change in deformation conditions from pure to simple shear during numerical simulations, will cause similar trends.

4.3 Characteristics of grain dissection in simulation and nature

Evidence that microstructures exhibit imminent or completed grain dissection events can be found in (1) a distinct distribution of orientation gradients, (2) heterogeneous strain-energy distribution leading to localised occurrence of SIBM, (3) irregular shape of grain boundaries and (4) equal orientations of next-neighbour grains, which Urai (1983) describes as equal orientation families (Figure 7, Figure 8, Figure 9). Typically, all characteristics (1) to (4) are observed together in natural samples and simulations. Another characteristic important for grain dissection could be (5) the relation of bulge width and mean grain size.

(1) Orientation differences indicate high stored strain-energies and can be observed as high densities of subgrain boundaries and orientation gradients. Both EBSD maps, c-axis maps and simulations reveal that grain dissection is accompanied by high orientation gradients (subgrain boundaries) in the dissected grain. The spatial distribution shows these high gradients as high densities of subgrain boundaries on the convex side of bulges (Figure 9C and Figure 4A, 4C). The observation of grain dissection accompanied with subgrain boundaries can be seen as an indication that grain dissection and polygonisation are not completely independent processes but rather act simultaneously, possibly strengthening each other, and cause splitting of grains with high strain-energy gradients.

(2) Dislocations induce strain energies that drive SIBM. If the dislocation-density difference between the bulging and dissected grain is high, rapid bulge migration is possible (Figure 4, supplementary

movies). The direction of grain boundary migration is indicated by locally high orientation gradients that are favourably consumed by the expanding grain (arrow in Figure 8C). In some cases, this direction could be verified using the observed migration of grain boundaries during storage of samples (see dotted line, from grain I in II, Figure 8B). SIBM causing grain dissection is a localised process as the dislocation energies can be highly heterogeneous within one grain (grain II, Figure 8, Figure 3, Figure 4A, 4B). Locally high strain energies lead to localised SIBM, which in turn causes directed bulging of grain boundaries and dissection instead of overgrowing of grains. Therefore, localised SIBM may be an essential feature of grain dissection. This assumption is consistent with simulation results, where grain dissection is observed when grain boundaries bulge in areas with locally high dislocation densities (simulation G15R10 in Figure 4). The combination of localised SIBM and grain dissection is further supported geological studies. For instance, Tullis et al. (1990) observe increased bulging and less polygonisation if the dislocation density distribution is more heterogeneous. The heterogeneous distributions of dislocations in ice are expected, considering that strain localisation is suggested to be a common mechanism in ice micro-dynamics (Jansen et al., 2016; Llorens et al., 2016a; Steinbach et al., 2016). Although these studies describe strain localisation on the scale of polycrystals, their results also show intracrystalline localisation, which is required for localised SIBM and grain dissection. Additionally, Steinbach et al. (2016) indicate that strain localisation may occur over a range of different scales.

(3) The elongated shape of some bulges is caused by strong gradients in stored strain energy and accompanied by relatively high orientation gradients. This is reflected between grain I and grain II-III in Figure 7D and detail images of simulation G60R10 results (Figure 4B). When examining natural microstructures, an irregular grain boundary network and high orientation gradients reflecting strain energy gradients may be indicative for an increased influence of grain dissection.

(4) Equal orientation of next-neighbour grains or orientation families (grains III and IV, Figure 8C) can only serve as an indication for completed grain dissection if the full CPO (a-axes as well as c-axes) is known. This is the case for EBSD measurements and numerical simulations. However, as a-axes can also align (Miyamoto et al., 2005), even in EBSD-maps, the recognition of orientation families can become difficult when the CPO is very strong. Although an orientation family is clearly observed, other indicators for grain dissection such as an irregular grain boundary network should accompany the observation. Obbard et al. (2006) observed orientation families in GISP2 (Greenland ice sheet project 2) ice core samples. Orientation families may be produced by grain dissection, rather than by polygonisation. In fact, in the misorientation distribution data shown by Obbard et al. (2006), there was no difference between the correlated and un-correlated distributions. This implies that misorientations are controlled by the strong CPO (Fliervoet et al., 1999). In addition, there is a lack of 5° to 15° misorientation boundaries, which would be expected if polygonisation was the

main grain-size-reducing mechanism (Trimby et al., 1998; 2000). The occurrence of a relatively high amount of 5° to 15° c-axis misorientations has been suggested as a signature of polygonisation in ice (Alley et al., 1995; Durand et al., 2008). However, the EBSD study of Obbard et al. (2006) shows that c-axis data can overestimate the occurrence of the 5° to 15° boundaries.

(5) The prevalence of grain dissection could be related to grain size itself. Means (1989) shows that grain dissection is most frequent when the bulge width is in the order of the mean grain size. If the grain size is significantly larger, a bulge will remain close to the position of the original boundary and does not migrate through a grain. In this situation, grain dissection is not possible. On the other hand, if the grain size is significantly smaller than the bulge width, the bulge shape itself cannot develop and the migrating boundary consumes a whole grain instead of dissecting it. NEEM ice core microstructures appear to support this dependency. In glacial ice, the grain size is smaller and grain dissection is less common than in Holocene ice (Figure 10A). On the contrary, in simulations, the frequency of grain dissection was higher for high strain rate simulations leading to smaller grain sizes (Figure 6). This does not represent a contradiction, but may illustrate the two end-members of grain size being larger or smaller than the bulge width.

Above it was argued that dissection is most important, relative to polygonisation, when the grain size is close to steady state. A steady state is only reached when deformation conditions are stable. High frequencies of dissection events can thus be regarded as indicators for relatively constant conditions. This appears to fit the observations in the NEEM ice core, where high frequencies of grain dissection are found at the base of the Holocene ice (Figure 10A). While microstructures stabilise downward in Holocene ice, both the CPO (Montagnat et al., 2014a) and the grain size (Binder, 2014) change at the transition to glacial ice. According to the recrystallisation diagram by Faria et al. (2014b), this change reflects a change in deformation conditions. In turn, this implies less grain dissection relative to polygonisation, which seems to fit our observation of low frequencies in grain dissection in glacial ice (Figure 10A).

The proposed mechanisms controlling grain sizes in ice are classically polygonisation leading to decreasing grain sizes (Alley et al., 1995, De La Chapelle et al., 1998) and boundary migration leading to a grain size increase (Duval and Castelnau, 1995; De La Chapelle et al., 1998). A mixture of both is suspected to cause steady grain sizes in the middle of ice-sheets columns. However, SIBM may provide an additional grain-size-reducing process, if grain dissection is initiated (Means et al., 1989). Therefore, equilibrium grain sizes may be achieved with only SIBM, whereas polygonisation or nucleation need additional grain-size-increasing mechanisms to achieve equilibrium.

5 Conclusions

In this study, we investigate the importance of grain dissection as a feature of strain-induced boundary migration (SIBM) in ice using numerical simulations and natural microstructures from the NEEM ice core. For the first time, we present evidence that grain dissection is a common mechanism during ice deformation. The efficiency of grain dissection is probably independent of depth and rather a function of the state of the microstructure and deformation conditions. In particular, grain dissection is most efficient in depths in the ice column where deformation conditions remained constant over time and microstructures approach steady state in terms of grain size or CPO. Here, grain dissection is an efficient mechanism in addition to polygonisation, to achieve grain size reduction and maintain a balance between grain-size-increasing and -decreasing mechanisms. In turn, this implies that SIBM not necessarily leads to grain size increase, but eventually to the dissection of grains, especially at high strain energy gradients.

Future models that describe grain-size evolution during ice deformation, should incorporate grain dissection and further investigate its frequency as a function of grain size, deformation mode, CPO or other microstructural properties. Furthermore, grain dissection should be taken into account when developing a mechanistic, grain-size sensitive flow law for ice. This is required to improve our description of small-scale, but in particular also large-scale flow if ice sheets and glaciers.

Author Contributions

Initial concept by FS and EK. FS performed numerical modelling with support from AG and PB. EK did electron backscatter diffraction analyses supported by MD and GP. JE processed the Fabric Analyser data. IW provided the glaciological input, samples and NEEM Fabric Analyser measurements. Major parts of the paper were written by FS, EK and JE with contributions of all co-authors.

Funding

We acknowledge funding by the DFG (SPP 1158) grant BO 1776/12-1 and the Helmholtz Junior Research group “The effect of deformation mechanisms for ice sheet dynamics” (VH-NG-802).

Acknowledgments

We are thankful for the support of the Elle community and the discussions with Daniela Jansen, Maria-Gema Llorens and Johanna Kerch that helped improving the manuscript. We thank Sepp Kipfstuhl for

the possibility to use microstructure images from NEEM ice core. NEEM is directed and organised by the Center of Ice and Climate at the Niels Bohr Institute and US NSF, Office of Polar Programs. It is supported by funding agencies and institutions in Belgium (FNRS-CFB and FWO), Canada (NRCan/GSC), China (CAS), Denmark (FIST), France (IPEV, CNRS/INSU, CEA and ANR), Germany (AWI), Iceland (RannIs), Japan (NIPR), Korea (KOPRI), The Netherlands (NWO/ALW), Sweden (VR), Switzerland (SNF), United Kingdom (NERC) and the USA (US NSF, Office of Polar Programs).

PAPER III

Dynamic recrystallisation during deformation of polycrystalline ice: insights from numerical simulations

Maria-Gema Llorens[1,2], Albert Griera[3], **Florian Steinbach**[1,2], Paul D. Bons[1], Enrique Gomez-Rivas[4], Daniela Jansen[2], Jens Roessiger[1], Ricardo A. Lebensohn[4] and Ilka Weikusat[1,2]

1. Department of Geosciences, Eberhard Karls University Tübingen, 72074 Tübingen, Germany
2. Alfred Wegener Institute Helmholtz Centre for Polar and Marine Research, 27568 Bremerhaven, Germany
3. Departament de Geologia, Universitat Autònoma de Barcelona, 08193 Bellaterra (Barcelona), Spain
4. School of Geosciences, University of Aberdeen, UK
5. Material Science and Technology Division. Los Alamos National Laboratory, USA

Published in *Philosophical Transactions of the Royal Society A*, 26 December 2016.

Abstract

The flow of glaciers and polar ice sheets is controlled by the highly anisotropic rheology of ice Ih that is close to its melting point. To improve our knowledge of ice sheet dynamics, it is necessary to understand how dynamic recrystallisation controls ice microstructures and rheology at different boundary conditions that range from pure shear flattening at the top to simple shear near the base of the sheets.We present a series of two-dimensional numerical simulations that couple ice deformation with dynamic recrystallisation of various intensities, paying special attention to the effect of boundary conditions. The simulations show how similar orientations of c-axis maxima with respect to the finite deformation direction develop regardless the amount of dynamic recrystallisation and applied boundary conditions. In pure shear this direction is parallel to the maximum compressional stress, while it rotates towards the shear direction in simple shear. This leads to strain hardening and increased activity of non-basal slip systems in pure shear and to strain softening in simple shear. Therefore, it is expected that ice is effectively weaker in the lower parts of the ice sheets than in the upper parts. Strain-rate localisation occurs in all simulations, especially in simple shear cases. Recrystallisation suppresses localisation, which necessitates the activation of hard, non-basal slip systems.

Keywords: ice rheology, dynamic recrystallisation, ice microstructure, non-basal activity, strain hardening

1 Introduction

Ice is one of the most common minerals found at the Earth's surface. Most of it is concentrated in polar ice sheets, formed originally from precipitation of snow. Due to its ductile behaviour, ice flows towards the ice sheet margins driven by gravity. While this behaviour is commonly described by continuum-mechanical approaches, its underlying processes are of crystallographic nature, where deformation takes place by dislocation creep (Schulson and Duval, 2009). At terrestrial conditions, single ice crystals have a hexagonal symmetry (ice Ih) and deform plastically by preferential glide of dislocations along the basal planes of the hexagonal lattice, where the slip of dislocations is almost isotropic. The stress required to activate dislocation glide along non-basal slip systems is about 60 times higher than that for the basal one (Duval et al., 1981), when subjected to similar strain rates.

Natural ice usually occurs in the form of polycrystalline aggregates, which develop a c-axis preferred orientation during deformation. This process is facilitated by recrystallisation of the ice grains, as polar ice is always at high homologous temperatures (i.e. near to the melting point). The microstructural evolution of the mineral aggregate during deformation leads to progressively anisotropic macroscopic behaviour (e.g. Faria et al., 2009). The development of a fabric or a lattice preferred orientation (LPO) due to deformation influences the response of ice layers to imposed stresses (Van der Veen and Whillans, 1994), deforming an order of magnitude faster than an equivalent isotropic polycrystal in simple shear deformation. We define LPO here as the statistically preferred orientation of the crystalline lattices of a population of grains (Faria et al., 2014b). Activation of recrystallisation processes during plastic deformation (dynamic recrystallisation, *DRX*) can enhance ice flow, modifying the microstructure (defined as the collection of all microscopic deformation-related structures and the orientation stereology of polycrystals (Faria et al., 2014b)) and lattice preferred orientations (LPO) (Duval and Castelnau, 1995; Duval et al., 2000), or activating non-basal slip systems (Llorens et al., 2016a). It is therefore critical to understand how *DRX* influences ice microstructures at different boundary conditions, because microstructural changes are related with climatic transitions in the paleoclimate record stored in ice sheets (Faria et al., 2010).

Natural ice deformation fabrics and microstructures can be studied with different techniques. Firstly, the analysis of ice microstructures measured from ice core samples provides an insight into the nature of strongly deformed natural ice. There is abundant data from the upper 100 meters of ice cores, where firn transitions into ice. However, only a limited number of datasets from deep ice cores exist. Very few

campaigns have been able to acquire deep ice samples, because they are expensive and logistically demanding (see reference 5 for an overview). Furthermore, coring sites are preferably located in very special strain environments, mainly in zones of ice divides and domes. This is because deformation in these zones mostly takes place under vertical compression (e.g. pure shear or axial compression) as the ice is buried under annual snow layers. These locations are specifically chosen to get relatively undisturbed layers to extract the clearest possible paleoclimate signals. Therefore, the deformation regimes that are subjected to high shear strain rates, which are found at the flanks or outlets of the ice sheets, are usually not prioritised for deep drilling campaigns, as this regime gives rise to folding of ice layers (Waddington et al., 2001; Alley et al., 1997; Faria et al., 2010; Bons et al., 2016). However, it is critical that we understand how ice behaves in all the parts of ice sheets and not only in ice divides and domes. Only few ice coring projects have focused to date on recovering samples with the aim of studying ice flow properties (Budd and Jacka, 1989; Etheridge, 1989). The EGRIP campaign will soon recover ice samples from the onset region of an ice stream (EGRIP Website: http://eastgrip.org/).

Experiments are another widely used technique to learn about ice rheology during deformation and recrystallisation. Samples of natural or artificial ice are deformed under controlled strain or stress boundary conditions and at a certain temperature in order to understand the processes that govern deformation and the resulting microstructures. These methods have significantly contributed to our understanding of ice rheology (Jacka, 1984; Azuma, 1994; Treverrow et al., 2012). However, experiments are limited to certain geometries and usually do not achieve high finite strains. Another disadvantage here is that experimental samples are subjected to much higher strain rates ($\dot{\varepsilon}$) than natural ice, especially in the case of slowly flowing polar ice sheets ($\dot{\varepsilon} \approx 10^{-10}$ - 10^{-13} s^{-1}; Budd and Jacka, 1989; Montagnat and Duval, 2004). As the viscosity of ice depends on the applied stress and this relation is highly non-linear, other techniques should be used in order to complement our understanding of ice rheology (Glen, 1955).

Numerical simulations provide a tool to fill in the gaps left by the study of natural and experimental ice deformation, because simulations are not limited by scale, stress or strain rate. Moreover, numerical models allow the systematic investigation of different aspects of dynamic recrystallisation on ice flow, based on the underlying physical processes (Montagnat et al., 2014a). In this way, it is possible to link processes on the dislocation scale to the behaviour of ice at the scale of the polycrystal. Additionally, by evaluating the relation between stress and strain rate from the bulk behaviour at the mesoscopic (cm – m) scale we can also establish links with the macroscopic scale. Furthermore, modelling allows the comparison of ice rheology under different boundary conditions, such as pure- and simple-shear deformation. Thus, microstructural modelling can be a valuable addition to the analysis of ice microstructures in natural ice samples and laboratory experiments.

Despite the importance of *DRX* on the behaviour of natural ice, theoretical and computational studies have been restricted mostly to the simulation of (i) ice deformation at the scale of single crystals (Castelnau et al., 1008), or (ii) deformation of polycrystalline materials using finite-element methods, whereby isotropic rheological properties are used to model crystal plasticity (Becker, 1991; Diard et al., 2005).

The full-field formulation based on fast Fourier transforms (FFT) (Moulinec and Suquet, 1994) has proven to be a successful alternative modelling tool to simulate plastic deformation of polycrystals (Lebensohn, 2001; Lebensohn et al., 2004), especially when coupled with algorithms for dynamic recrystallisation processes (Llorens et al., 2016a; Jansen et al., 2016). Viscoplastic full-field numerical modelling (in short VPFFT-modelling) of the evolution of a polycrystalline aggregate under controlled strain boundary conditions can be applied to investigate the relative importance of deformation mechanisms and recrystallisation processes on the development of ice fabrics and flow (e.g. Montagnat et al., 2014a). Here we use the VPFFT formulation inside the modelling platform ELLE (Jessell et al., 2001; Bons et al., 2008), which has been widely used to model processes in rocks and has recently been adapted to experiments on polycrystals with the characteristics of natural ice. The aim of this paper is to present the state-of-the-art of the VPFFT/ELLE modelling of ice, paying particular attention to the effect of vorticity boundary conditions (i.e. pure versus simple shear) and dynamic recrystallisation.

2 Numerical procedure

2.1 ELLE numerical platform

The software platform ELLE (Jessell et al., 2001; Bons et al., 2008) was used to perform the simulations presented in this contribution. The ELLE software is open-source and can be downloaded from the online repository (http://www.elle.ws). ELLE processes reproduce the evolution of microstructures during deformation and metamorphism, such as grain growth (Bons et al., 2001; Jessell et al., 2003; Roessiger et al., 2011), dynamic recrystallisation (Becker et al., 2008; Piazolo et al., 2002; Llorens et al., 2016), folding (Llorens et al., 2013a,b; Jansen et al., 2016; Bons et al., 2016) and rotation of rigid objects in anisotropic materials (Griera, et al., 2011; 2013).

In this contribution we compare the microstructural evolution of ice Ih during viscoplastic deformation and recrystallisation. The numerical approach is based on the coupling of (i) a full-field viscoplastic code that uses a Fast Fourier Transform approach (VPFFT; Lebensohn, 2001; Lebensohn et al., 2008)

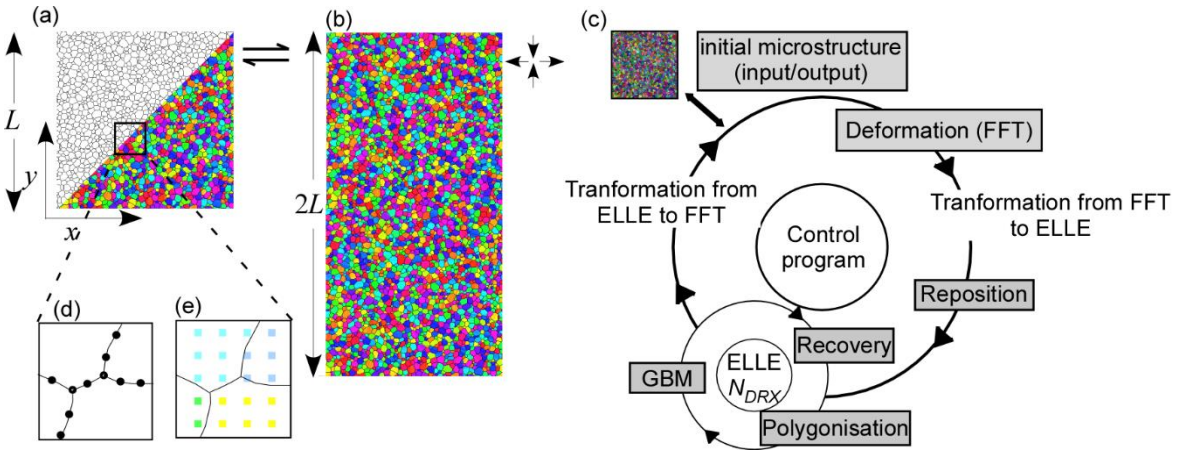

Figure 1: Initial microstructures showing the ELLE data layers and program flow. The initial microstructure in simple shear simulations is a square model defined by a side of one-unit length (*L*) (a), while in pure shear simulations the initial size of the model is duplicated vertically (2*L*) to allow better visualisation of the deformed microstructure. (d) Detail of boundary nodes (*bnodes*) defining grains and (e) detail of *unodes* or Fourier points. (c) The microstructure goes through a loop of processes every time step: deformation by small increments of dextral simple shear or vertical shortening in pure shear simulations, reposition that brings the model back into the unit cell, and a subloop of *DRX* processes (grain boundary migration - *GBM*, recovery and polygonisation).

to calculate the viscoplastic deformation of the polycrystalline aggregate, and (ii) the microstructural modelling platform ELLE for the simulation of dynamic recrystallisation processes (*DRX*).

Two main layers define the data structure of the models: (a) a contiguous set of polygons (Figure 1a-b) that are used to define grains and that are themselves defined by straight boundary segments joined at boundary nodes (*bnodes*) (Figure 1d), and (b) a high-resolution grid of unconnected nodes (*unodes*) that store physical properties within grains, such as the local lattice orientation, defined by three Euler angles, and the dislocation density (Figure 1e). These *unodes* also serve as Fourier points to simulate crystallites for the viscoplastic deformation calculations (Lebensohn, 2001). The data structure of the VPFFT and ELLE codes is fully wrapping: grains touching one side of the model continue on the other side. Two different sets of initial microstructures are used to investigate three series of simulations (Table 1): a single-phase ice polycrystalline aggregate with a cell size of *L*x*L* to be deformed in simple shear (Figure 1a), an *L*x2*L* cell to be deformed in pure shear vertical shortening (Figure 1b). A grid density of 256 x 256 *unodes* was used to define a unit cell, resulting in a total of 65,536 discrete *unodes*. Grains initially have a random lattice orientation (Figure 1a-b-c), representing a bulk isotropic material.

In our approach, each small time increment (Δt) is represented by a sequential loop of processes. For all the simulations presented, an experimental run (Figure 1f1c) consists of iterative applications of an incremental 0.02 natural strain, defined as $\ln(\frac{Lf}{Li})$, equivalent to 2% of shortening of vertical coaxial compression or an incremental shear strain of $\Delta\gamma$=0.04 in simple shear simulations. The deformation step is followed by a subloop of *DRX*, where grain boundary migration (*GBM*), recovery and polygonisation processes are activated. Since the mobility parameter of recrystallisation processes and

Table 1: Set-up of the two series of numerical simulations.

name	DRX/VPFFT ratio (N_{DRX})	ELLE process	strain rate (s^{-1})
first series (PSH N_{DRX})			
experiment PSH 0	0	GBM+recovery	-
experiment PSH 1	1	GBM+recovery	3.17×10^{-11}
experiment PSH 10	10	GBM+recovery	3.17×10^{-12}
experiment PSH 20	20	GBM+recovery	1.00×10^{-10}
experiment PSH 20_N	20	GBM+recovery+polygnization	1.00×10^{-10}
experiment PSH 25	25	GBM+recovery	1.27×10^{-12}
second series (SSH N_{DRX})			
experiment SSH 0	0	GBM+recovery	-
experiment SSH 1	1	GBM+recovery	3.17×10^{-11}
experiment SSH 1_N	1	GBM+recovery+polygonization	3.17×10^{-11}
experiment SSH 10	10	GBM+recovery	3.17×10^{-12}
experiment SSH 10_N	10	GBM+recovery	3.17×10^{-12}
experiment SSH 25	25	GBM+recovery	1.27×10^{-12}

time step are the same for all simulations, we model deformation at different strain rates by varying the ratio between the viscoplastic deformation step and the *DRX* step, activating the *DRX* subloop N_{DRX} = 0, 1, 10, 20 or 25 times per deformation time step (see values in Table 1). When *DRX* is not active is not possible to calculate the strain rate, because there is no time step defined in the model. When *DRX* is active, N_{DRX} is inversely proportional to the strain rate. Using the parameters defined further below, the N_{DRX} correspond to strain rates ranging from $3.17 \cdot 10^{-11}$ down to $1.27 \cdot 10^{-12}$ s^{-1}.

The first series of simulations (labelled by PSH N_{DRX}) models *DRX*, including *GBM* and recovery, of ice under pure-shear vertical shortening up to natural strain of 1.2. This series includes a simulation (PSH 20_N) that incorporates polygonisation. The second series (SSH N_{DRX}) simulates *DRX*, including *GBM* and recovery, of ice under dextral simple shear conditions up to a natural strain of 1.2. This series includes simulations (SSH 1_N and SSH 10_N) that incorporate polygonisation. The simulation setup is listed in Table 1. Lattice orientation data, as well as misorientation and activity of slip systems fields, were plotted using the texture analysis software MTEX (Mainprice, et al., 2011).

2.2 FFT – viscoplastic deformation by dislocation glide

Viscoplastic deformation is calculated using the Fast Fourier Transform algorithm (VPFFT) that provides a strain rate and stress field that minimises the average local work-rate under compatibility and equilibrium constraints (Lebensohn, 2001; Lebensohn et al., 2008). VPFFT is a full-field crystal plasticity formulation that explicitly resolves velocity and stress fields, assuming that deformation is accommodated by dislocation glide only. The constitutive relation between the strain rate $\dot{\varepsilon}_{ij}(\boldsymbol{x})$ and the deviatoric stress $\sigma'(x)$ at a point x of the Fourier grid is given by:

$$\dot{\varepsilon}_{ij}(\boldsymbol{x}) = \sum_{s=1}^{N_s} m_{ij}^s(\boldsymbol{x})\dot{\gamma}^s(\boldsymbol{x}) = \dot{\gamma}_0 \sum_{s=1}^{N_s} m_{ij}^s(\boldsymbol{x}) \left| \frac{m^s(\boldsymbol{x}) : \sigma'(\boldsymbol{x})}{\tau^s(\boldsymbol{x})} \right|^n sgn(m^s(\boldsymbol{x}) : \sigma'(\boldsymbol{x})) \qquad (1)$$

Where the sum runs over all (N_s) slip systems s in the crystal, m^s is the symmetric Schmid tensor, τ^s is the resistance to slip or critical resolved shear stress, $\dot{\gamma}^s$ is the shear strain rate, $\dot{\gamma}_0$ is a reference strain rate and n is the rate sensitivity or stress exponent in Glen's law (Glen, 1952). To simulate the mechanical properties of a polycrystalline aggregate of ice Ih crystals, a mineral with hexagonal symmetry and deformation accommodated by glide of dislocations along basal and non-basal slip systems (i.e., prismatic and pyramidal) is assumed. The degree of anisotropy (*A*) is defined by the ratio between the critical resolved shear stresses τ^s between the non-basal and the basal slip systems. *A* is approximately 60 according to (Duval et al., 1983), but the basal slip system is assumed to be 20 times weaker than the pyramidal and prismatic ones (*A*=20) in all the simulations presented here. This value of *A* is a compromise to avoid too long calculation time, while still maintaining an acceptable accuracy of the result (Llorens et al., 2016a). The rate sensitivity exponent is *n*=3 for all the slip systems. The resulting micromechanical fields from VPFFT are used to estimate the geometrically necessary dislocation density and deformation-induced lattice rotation, required inputs to simulate intra-crystalline recovery and grain boundary migration (*GBM*).

2.3 ELLE - recrystallisation processes

After each deformation step, recrystallisation is simulated by means of three processes: polygonisation, grain boundary migration and recovery. The polygonisation routine creates new high-angle grain boundaries (HAGB) when a cluster of *unodes* within a grain have a misorientation angle with respect to the parent grain that is higher than a critical pre-defined angle. Grain boundary migration (*GBM*) is driven by the reduction of grain boundary energy and stored strain energy, reproducing the motion or displacement of high-angle grain boundaries (Urai et al., 1986). Recovery reduces the intra-granular stored energy in a deformed crystal, simulating annihilation of dislocations and their rearrangement into low-angle subgrain boundaries (LAGB) (Borthwick et al., 2014).

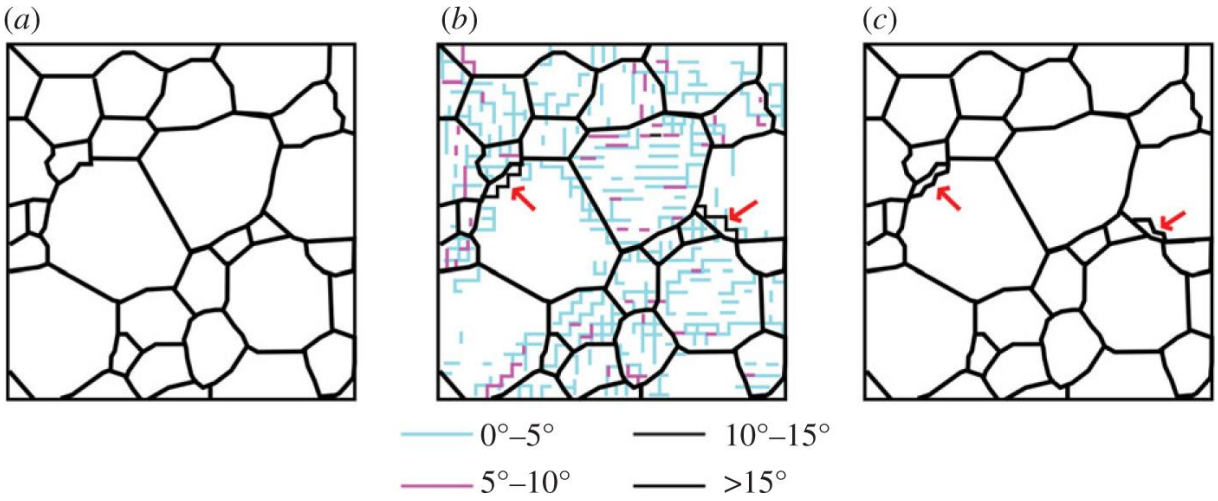

Figure 2: Example of the polygonisation routine. (a) The initial microstructure has grains with homogeneous lattice orientations inside grains (no misorientation). (b) After one step of simple shear deformation LAGB (red, green and blue lines) and new HAGB (grey lines) have developed. (c) The polygonisation routine identifies the HAGB (>15º) and updates the grain boundary network. Red arrows indicate newly nucleated grains.

2.3.1 Polygonisation

The polygonisation routine modifies the *bnodes* layer through splitting a pre-existing grain by inserting new boundary nodes. This process commences with a routine that identifies subgrains, i.e. clusters of *unodes* with misorientation values above a pre-defined threshold (HAGB > 15º; Figure 2b). Once a critical subgrain is detected, the position of its boundary is obtained using a Voronoi tessellation of the cluster of unodes clipping the boundary to the pre-existing grain. A convex hull routine is used to define the smallest convex polygon enclosing the Voronoi points and clipped boundary nodes. The use of Voronoi decomposition allows us to prevent topological errors in the network of grains.

2.3.2 Grain boundary migration

Grain boundary migration (*GBM*) is modelled according to the front tracking approach explained in more detail in Becker et al. (2008) and Llorens et al. (2016a). *GBM* is driven by a reduction of surface energy and stored strain energy. The driving stress (Δf) is derived from the internal strain energy (ΔH) and the total grain boundary surface energy, which depends on the surface energy (J) and the local radius of curvature (r) of the grain boundary:

$$\Delta f = \Delta H - \frac{2J}{r} \tag{2}$$

The velocity ($\vec{v}$) of the grain boundary is calculated from the driving stress (Δf) and grain-boundary mobility (M) such that the work done equals the change in the local energy state:

$$\vec{v} = M \Delta f \vec{n} \tag{3}$$

Here $\vec{n}$ is a unit vector in the direction of movement. The mobility is highly dependent on temperature (T) and it is calculated from the intrinsic mobility (M_0 =0.023 $m^2kg^{-1}s^{-1}$; Nasello et al., 2005), the grain boundary diffusion activation energy (Q= 40 KJ mol-1; Thorsteinsson, 2002) and the universal gas constant (R):

$$M = M_0 exp^{(-Q/RT)} \quad (4)$$

The stored energy (ΔH) is calculated from the difference in dislocation density across a grain boundary ($\Delta\rho$), the shear modulus (G, assumed to be isotropic) and the Burgers vector ($\vec{b}$):

$$\Delta H = \Delta\rho G|b|^2 \quad (5)$$

This routine picks single *bnodes* in a random order and uses four orthogonal small trial moves (parallel to the *x*- and *y*-axes, and of 1/100 of the average distance between *bnodes*) of that *bnode* to determine the direction ($\vec{n}$) with the maximum driving stress (Δf) (Becker et al., 2008). The *bnode* is then moved over a small distance, $\vec{v}\cdot\Delta t$, in the direction of $\vec{n}$ according to equation (3). In areas swept by the moving boundary, the stored strain energy (ΔH) is reduced to zero.

2.3.3 Recovery

The recovery module that simulates intra-granular reduction of the stored strain energy is applied after grain boundary migration. The recovery routine implemented in ELLE (Borthwick et al., 2014) simulates annihilation of dislocations and their rearrangement into low-angle subgrain boundaries. This process assumes that each *unode* represents a small crystallite or potential subgrain. The rotation rate of the lattice within the crystallite is proportional to the torque applied on the sides of the crystallite. This torque is calculated from the angular mismatch of the *unode* and its neighbours, which results in an effective interface energy (Randle, 1993). The algorithm, described in detail in Llorens et al. (2016a) is applied to an *unode* and its neighbours that belong to the same grain. The lattice orientation of the reference *unode* is rotated towards the value that results in the maximum reduction in interface energy calculated from trial rotations. This procedure is repeated for each *unode* in random order.

3 Results

3.1 Microstructure evolution

At the end of the simulations (natural strain of ε=1.2) differences on grain size and grain shape are observed. They reflect the different strain rates applied and the concomitant differences in the activity of dynamic recrystallisation processes (Table 2). The case of ice deformation without dynamic recrystallisation (*DRX*) is represented by Experiments PSH 0 and SSH 0, for pure and simple shear boundary conditions, respectively. In both cases viscoplastic deformation leads to the development of a

Table 2: Grain average values.

name	initial average grain area (mm²)	final number of grains	final average grain area (mm²)	Standard deviation
first series (PSH N_{DRX})				
experiment PSH 0	6.12	3321	6	4
experiment PSH 1	6.12	1949	10	8
experiment PSH 10	6.12	365	55	42
experiment PSH 20	6.12	1160	6	5
experiment PSH 20_N	6.12	1631	12	12
experiment PSH 25	6.12	145	138	105
second series (SSH N_{DRX})				
experiment SSH 0	6.12	1636	6	4
experiment SSH 1	6.12	873	12	9
experiment SSH 1_N	6.12	1943	5	6
experiment SSH 10	6.12	156	64	55
experiment SSH 10_N	10	490	20	21
experiment SSH 25	25	61	163	122

grain shape preferred orientation (SPO) by the irregular elongation of grains oriented parallel to the stretching direction (Figure 3a,e). This direction is the horizontal *x*-axis in pure shear models, while in simple shear models it rotates clockwise from 45º with respect to *x* at the beginning of the simulations towards the shear direction that is parallel to the *x*-axis. Deformation localisation in the simple shear models produces strongly elongated grains in high-strain bands, which form at low angle with respect to the shear direction (Figure 3a). In pure shear models conjugate sets of such high-strain bands are observed, but oriented symmetrically with respect to the vertical maximum shortening direction (Figure 3e). In both cases the high-strain bands are obliquely oriented with respect to the grain SPO. These bands are additionally characterised by high values of misorientations (i.e. intragranular heterogeneities calculated as the angular difference in lattice orientation between an *unode* and its neighbours), progressively developing high local misorientations and recognisable subgrains, as can be seen in the misorientation field maps (Figure 3e).

Different degrees of dynamic recrystallisation were simulated in Experiments PSH and SSH 1, 10 and 25, where the number refers to N_{DRX}, i.e. the number of recrystallisation steps per VPFFT steps in the

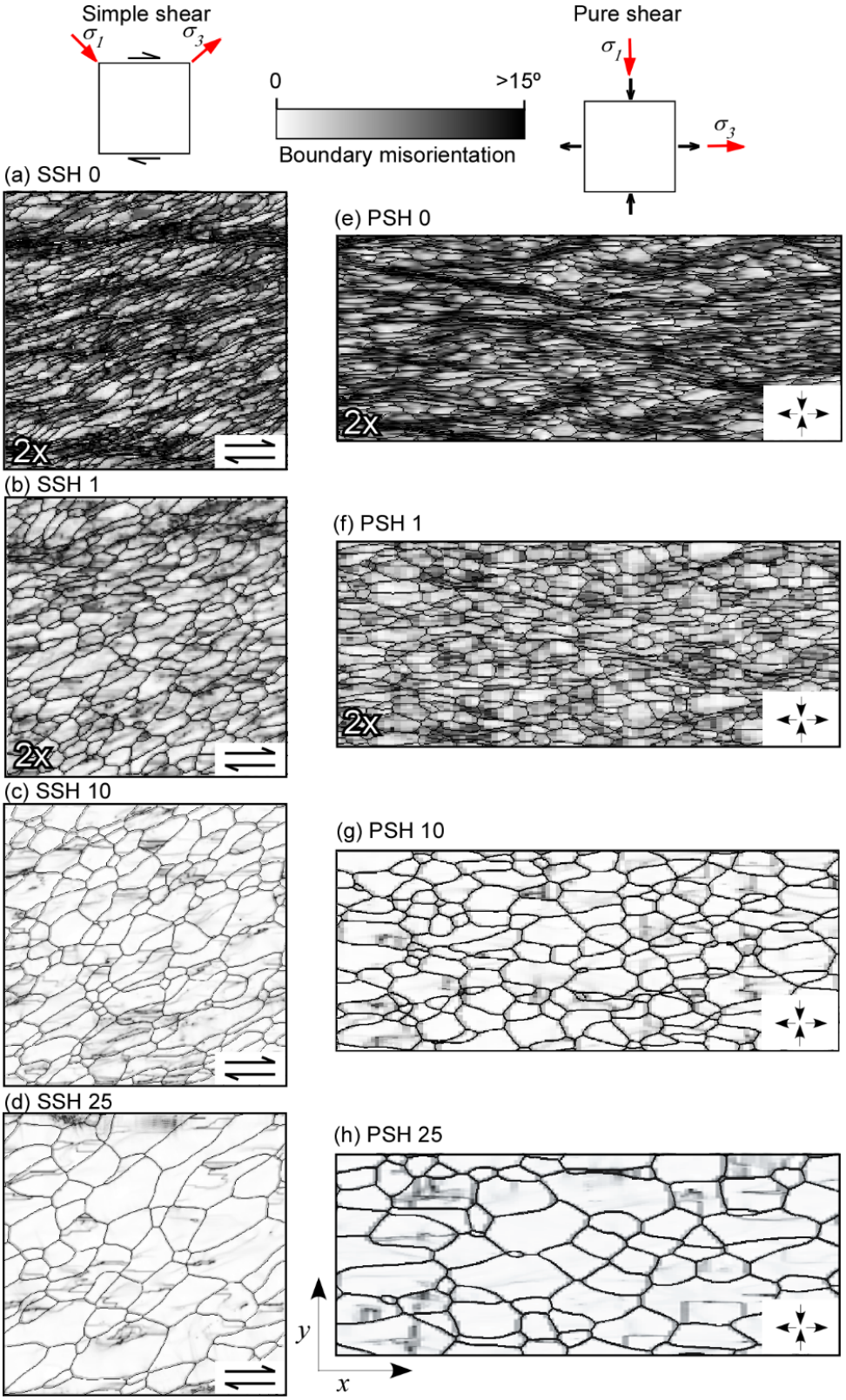

Figure 3: Comparison of the grain-boundary network and local misorientation field at a natural strain of ε=1.2 for simulations deformed in simple shear (left column) and pure shear (right column), with (a, e) no recrystallisation, (b, f) 1 step, (c, g) 10 steps, and (d, h) 25 steps of recrystallisation per deformation step, respectively, indicated by the N_{drx} suffix (or ratio DRX/VPFFT). The initial microstructure is shown in figure 1a-b. In pure shear simulations (e-h) the original image length is double than the images shown. For better visibility, figures for Experiments 0 and 1, both in simple (SSH) and pure shear (PSH), have been enlarged two times, only showing the upper left quarter of each model.

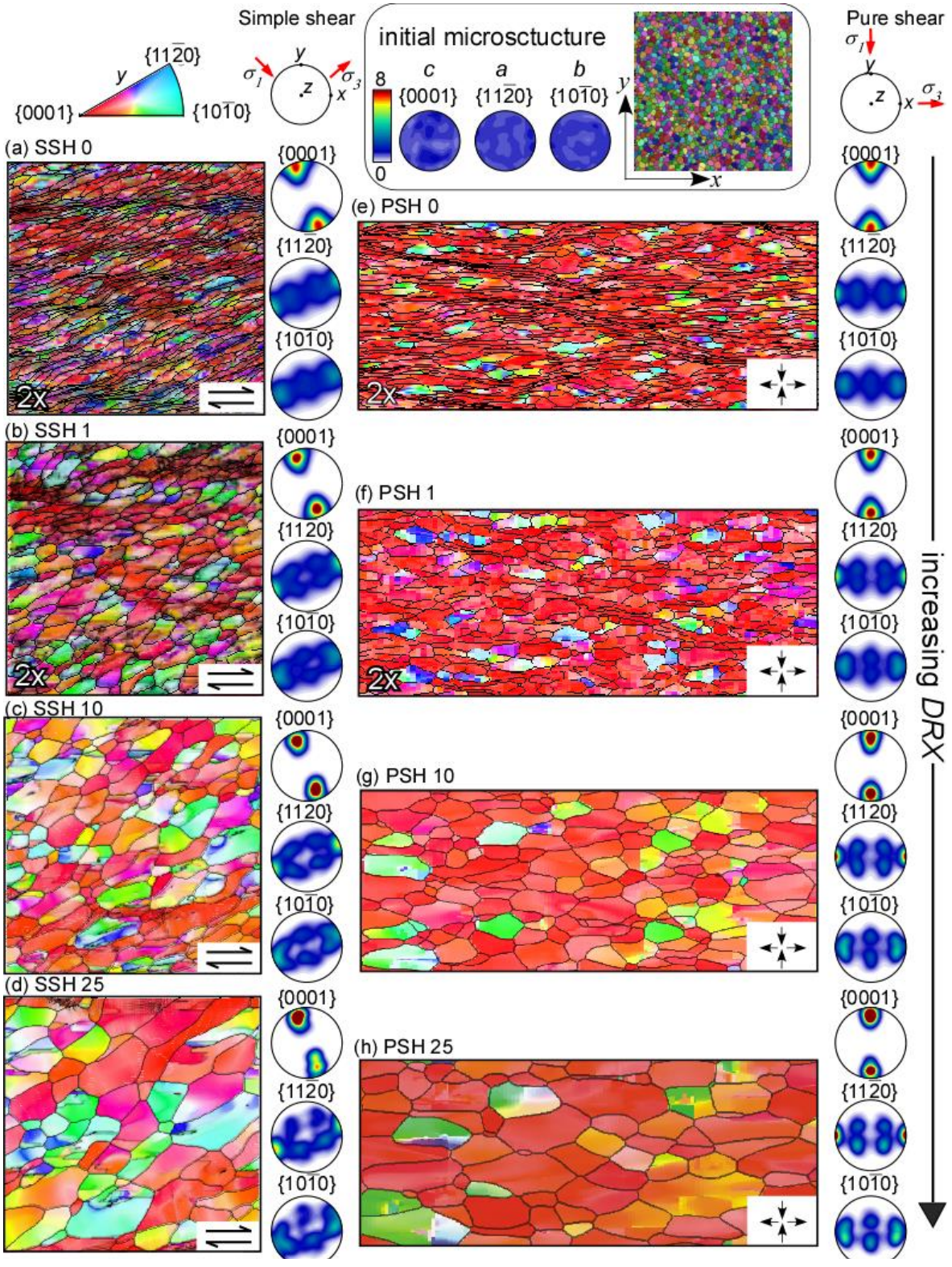

Figure 4: Lattice orientations relative to the y-direction (inverse poles) and pole figures of lattice orientation at natural strain of ε=1.2 for simulations of ice deformed in simple shear (left column) and pure shear (right column), with (a, e) no recrystallisation, (b, f) 1 step, (c, g) 10 steps, and (d, h) 25 steps of recrystallisation per deformation step, respectively. Initial random distribution of lattice orientations is shown in the upper part of the figure. In pure shear simulations (e-h) the original image length is double than the images shown. In order to allow visualisation of the microstructures, the figures of Experiments 0 and 1, in both simple (SSH) and pure shear (PSH), have been enlarged two times, only showing the upper left quarter of each model. Lattice orientation figures include misorientation map and grain network. Pole figures show orientation of unodes

loop. The activation of grain boundary migration and recovery produces a general grain size coarsening, with grains becoming more equant with decreasing strain rate (Table 2 and Figure 3b-d, 3f-h). As a result, the grain SPO qualitatively weakens, but preferred elongation of grains parallel to the stretching direction is still remains recognisable in models that have up to N_{DRX} = 25 steps per deformation increment (Figure 3b-d,f-h). A reduction of the local misorientation by the arrangement of subgrain domains results in the development of low angle boundaries and lower intragranular heterogeneities than in models with $N_{DRX}=0$. Subgrain size generally tends to increase with N_{DRX}. Contrary to what can be observed in models without recrystallisation, bands with highly stretched grains do not develop in other simulations, except in models with N_{DRX} = 1. However, these bands are small compared to those in models that only include deformation. In the models N_{DRX} = 10 and N_{DRX} = 25, these bands are not recognisable and grain size distributions are relatively uniform. In general, grain boundaries show straight to smooth geometries. Triple junctions are typically characterised by angles close to 120º with increasing N_{DRX}, but large deviations from this angle can still be qualitatively observed in the N_{DRX} = 25 cases.

3.2 Lattice orientation evolution

Orientation maps and lattice orientation distributions at a natural strain of ε=1.2 are displayed in Figure 4. Differences in lattice orientation are recognisable from colour differences according to inverse pole Figures relative to the *y* direction of the sample. All simulations present a final similar lattice preferred orientation with respect to the finite deformation directions, regardless of the applied boundary conditions (vorticity) and amount of *DRX*. The initial randomly oriented grains (initial microstructure in Figure 4) evolved towards a LPO approximately defined by c-axes (i.e. {0001} axes in Figure 4 a-d) parallel to the maximum shortening direction, or perpendicular to the foliation, while the a-axes (i.e {11-20} axes in Figure 4) tend to be parallel to the stretching direction, or parallel to the foliation.

In the case of pure shear deformation, the c-axes maxima are oriented sub-parallel to the compression axis σ_1 during all simulation time, displaying a broad single maximum for the PSH_0 case and becoming increasingly concentrated towards the *y*-axis with increasing *DRX* (see polar Figures in Figures 4 e-h and 5 e-h). In the case of simple shear deformation, c-axes are oriented obliquely to the maximum compression axis and rotate in a synthetic sense (i.e. in the same way than the imposed shear-sense) towards the normal to the shear plane (or sample y-axis) with progressive deformation. It has to be noted that this condition was not achieved at the end of the simulations (Figure 5 a-d). Apart from the orientation of the c-axis maximum with respect to σ_1, differences between pure and simple shear are remarkably subtle (Figure 5). The fabric generally tends to be slightly weaker in pure shear models and displays a more marked girdle component than in simple shear cases.

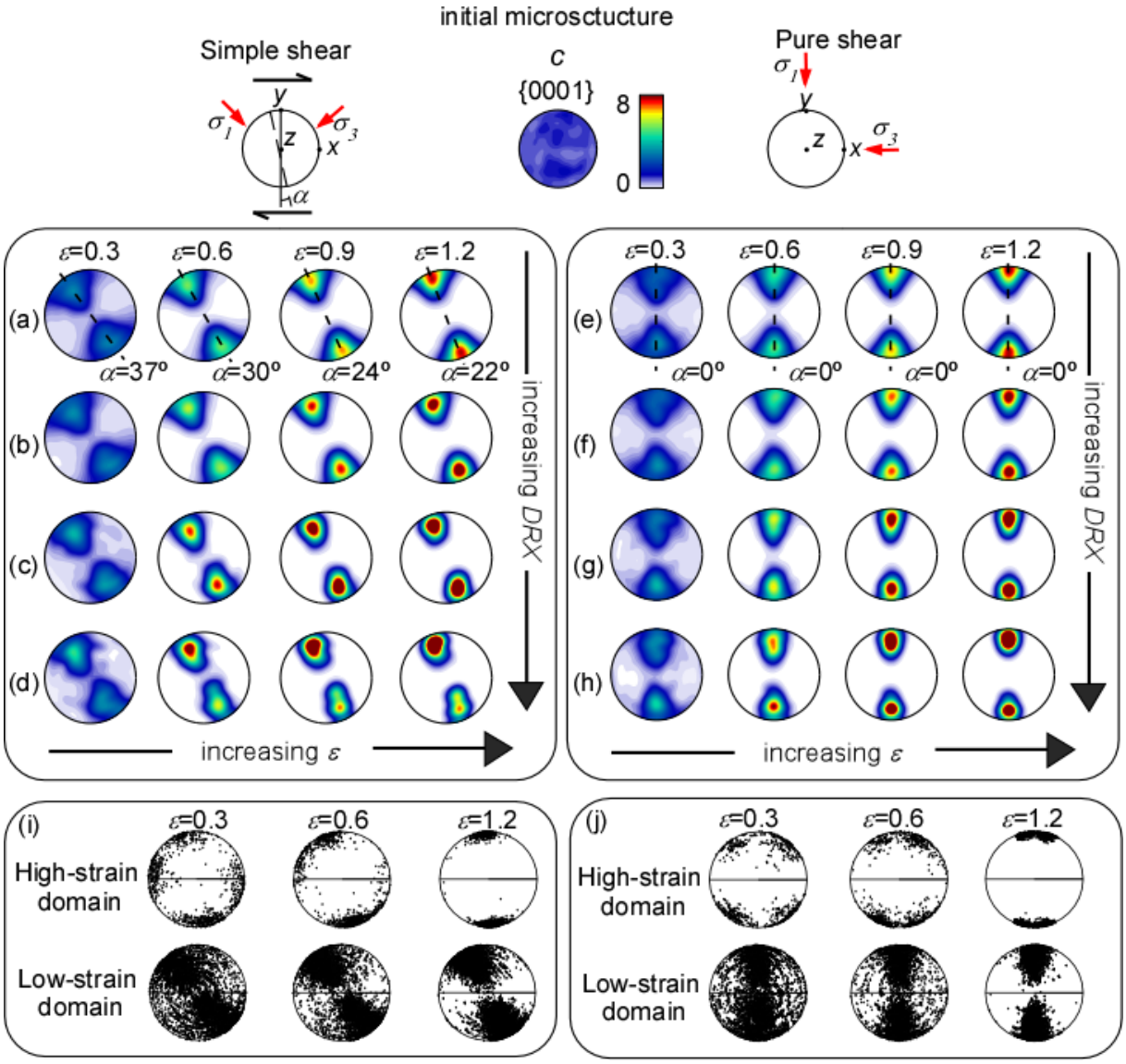

Figure 5: Pole figures of c-axes {0001} orientation at natural strains of ε=0.3, 0.6, 0.9 and the end of the simulations (ε=1.2) for simulations of ice deformed in simple shear (left side) and pure shear (right side) boundary conditions, with (a, e) no recrystallisation, (b, f) 1 step, (c, g) 10 steps, and (d, h) 25 steps of recrystallisation per deformation step, respectively. The angle α indicates the obliquity of the developed LPO with respect to the *y*-direction. The colour bar indicates the multiples of a uniform distribution. Pole figures of lattice orientation in high-strain and low-strain domains of simulations performed with no recrystallization in both pure and simple shear respectively (i, j). Pole figures show orientation of unodes.

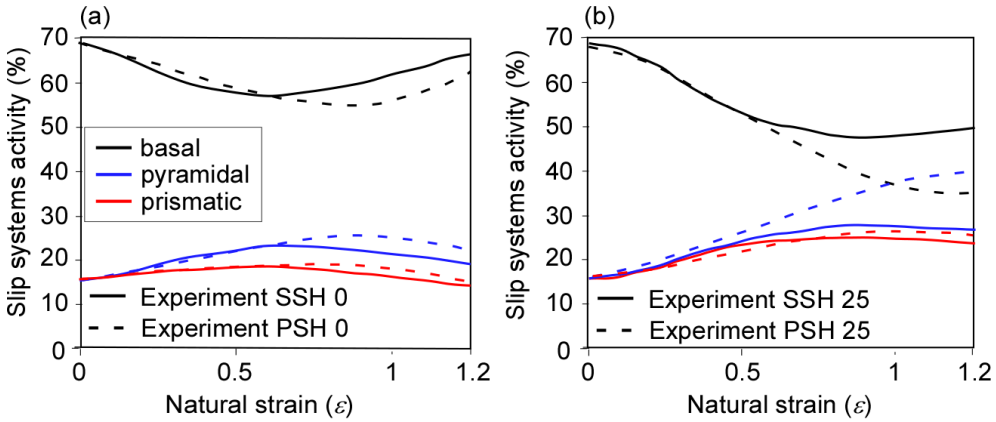

Figure 6: Evolution of the average relative slip system activity with progressive deformation for the simulations (a) without *DRX* (N_{DRX} = 0) and (b) including *DRX* (N_{DRX} = 25).

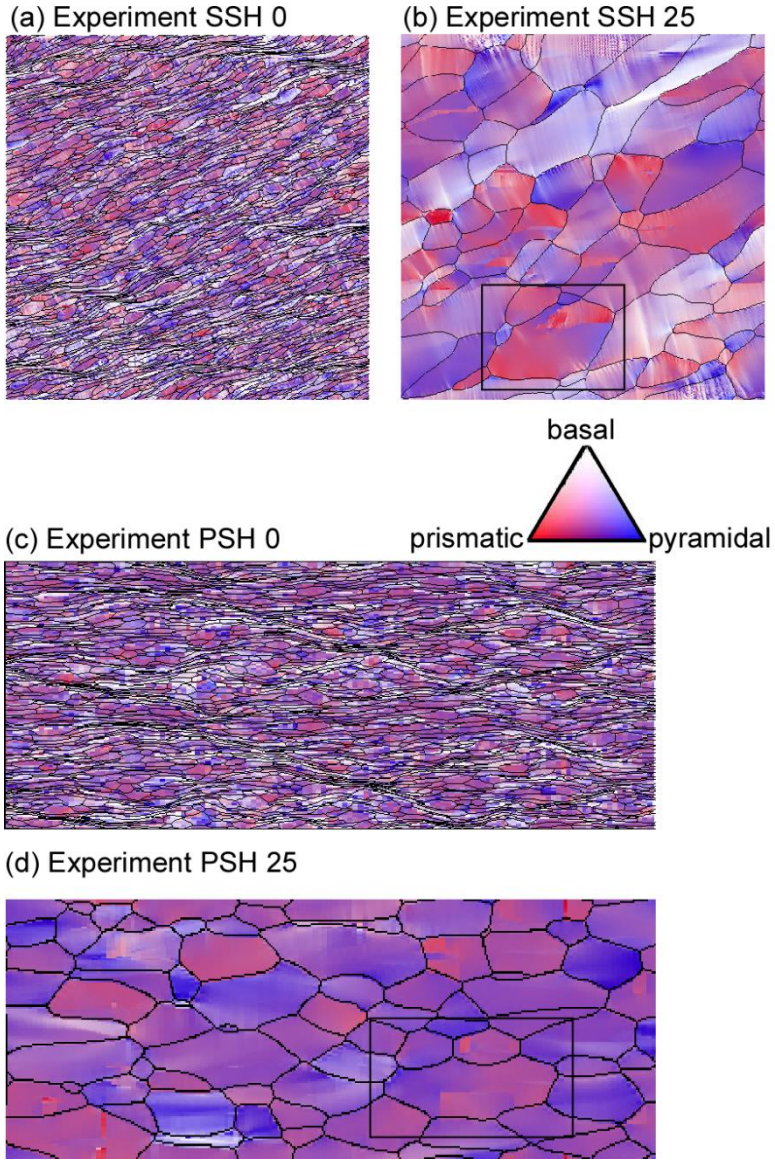

Figure 7: Maps of slip system activity for the last step of deformation (at ε=1.2) are shown for (a,b) simple shear and (c,d) pure shear simulations with N_{DRX} = 0 and N_{DRX} = 25. In pure shear simulations (c-d) the original image length is double than the images shown. Two examples of grains with subgrain boundaries developed by the activity of non-basal slip systems are marked in black squares in (b,d).

When *DRX* is active, the LPO develops faster and c-axes tend to be slightly inclined with respect to the *xy* plane in both pure and simple shear simulations (Figure 5). The effect of *DRX* is more pronounced on the distributions of a- and b-axes, since they lie on a broad great circle in models with low *DRX*, and this trend is divided in a number of distinct maxima for cases with higher *DRX*. This result is coherent with the enhancement of the LPO single maximum.

3.3 Activity of the slip systems

In the absence of *DRX* the activity of the basal slip systems is 60-70% higher than that of the non-basal slip systems in both pure and simple shear simulations (Figure 6a). The basal slip system activity is concentrated in the high strain-rate bands, oriented at low angles to the horizontal shear plane in simple shear (Figure 7a), or in conjugate bands distributed symmetrically around the vertical *y*-direction in pure shear simulations (Figure 7c). When *DRX* is active the activity of the non-basal slip systems is increased in both pure and simple shear simulations, especially in pure shear (Figure 6b). The slip system activity is not distributed in bands because they are destroyed by the *DRX*. Larger grains, produced by *GBM*, contain subgrains with different amounts of basal (tilt and twist boundaries) and non-basal activity (Figure 7b,d).

3.4 Rheology

All simulations show an increment of ≥30% in differential stress with increasing strain (*i.e.*, strain hardening) (Figure 8a). Differential stress is defined as the difference between the maximum and minimum principal stresses. Significant deviations of the stress evolution between pure and simple shear only start developing after $\varepsilon \approx 0.5$, where differential stress stabilises in simple shear models (light lines in Figure 8a) and continue increasing in the pure shear cases (dark lines in Figure 8a). A similar hardening behaviour, but followed by weakening at higher strain, was observed in simple shear deformation of polycrystalline aggregates of olivine (Hansen et al., 2016; Skemer et al., 2011) and quartz (Holyoke and Tullis, 2006), and also in numerical simulations of two phase materials (Takeda and Griera, 2006). Differences between laboratory experiments and numerical simulations are discussed further in section 4.2.

3.5 Strain localisation

The observable strain localisation in conjugate high-strain bands of strongly elongated grains (Figure 3a,e) is quantified using a slight modification of the localisation factor defined by Sornette et al. (1993) and Gomez-Rivas (2008):

$$f = 1 - \frac{1}{n_t} \frac{\left(\sum_{n_i}^{n_t} \dot{\varepsilon}_{vm}\right)^2}{\sum_{n_i}^{n_t} \dot{\varepsilon}_{vm}{}^2} \tag{6}$$

where n_t the total number of unodes and $\dot{\varepsilon}_{vm}$ is the von Mises strain rate for every *unode* n_i, defined as:

$$\dot{\varepsilon}_{vm} = \sqrt{\frac{2}{3}\dot{\varepsilon}_{ij}\dot{\varepsilon}_{ij}} \quad (6)$$

The strain localisation factor (*f*) can range from 0 to 1, where 0 represents homogeneous deformation and 1 maximum localisation.

All simulations in simple shear show an initial trend towards more homogeneous deformation, followed by a reversal when localisation strengthens again (Figure 9a). *DRX* suppresses localisation, with the reversal occurring at a higher strain in cases with higher N_{DRX}. Pure shear simulations are characterised by a steady state up to a natural strain of ε=0.3, followed by either a reduction of localisation at high N_{DRX} or an increase in localisation when N_{DRX} is low (Figure 9b). In general, *DRX* suppresses localisation of deformation, but only after about a natural strain of ε=0.3, when a distinct LPO starts to develop.

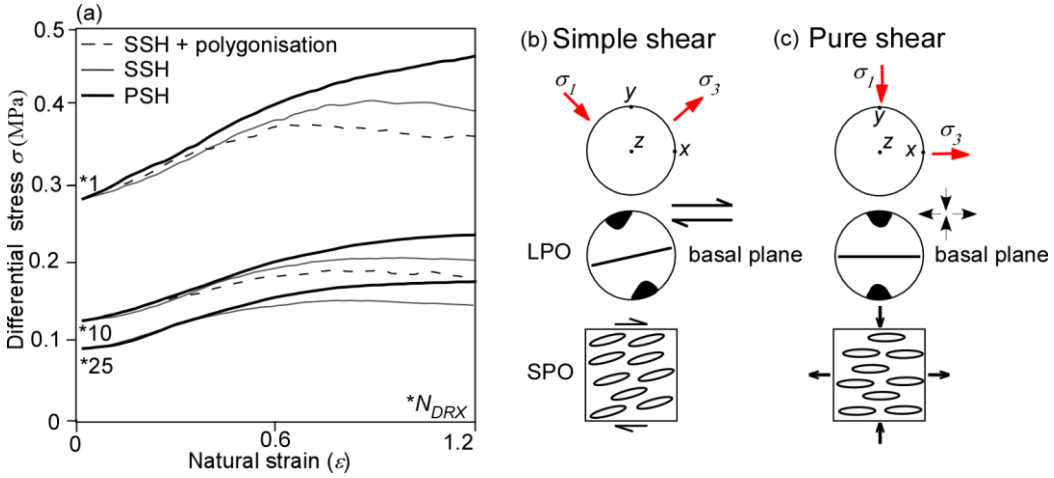

Figure 8: (a) Differential stress vs natural strain for all simulations. The ratio between *DRX* and FFT (N_{DRX}) is indicated as 1, 10 or 25. A summary of the LPO and SPO developed with respect to the principal stresses is indicated in (b) for simple shear and (c) for pure shear numerical simulations. Differential stresses were normalised using the experimental values of Duval et al. (1983).

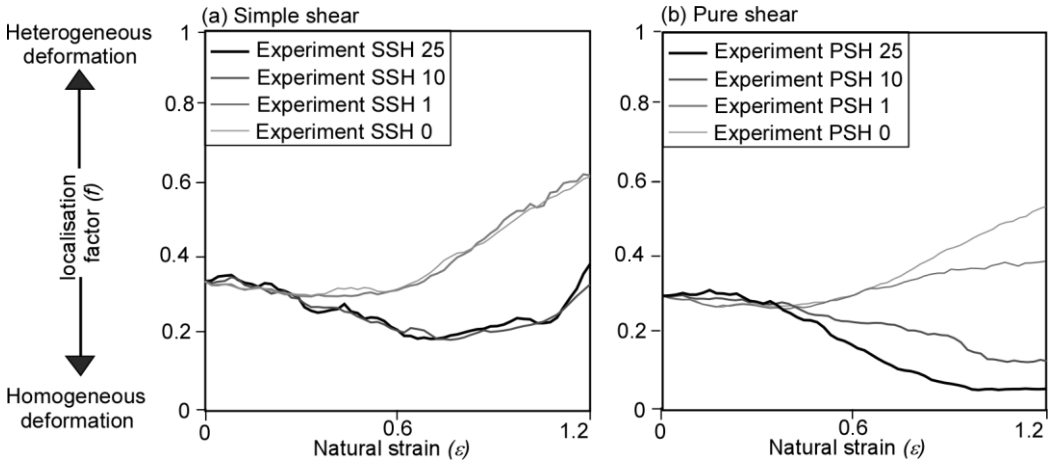

Figure 9: Localisation factor *(f)* evolution (equation 6) during deformation for simulations with N_{DRX} = 0, 1, 10 and 25 with (a) simple and (b) pure shear boundary conditions.

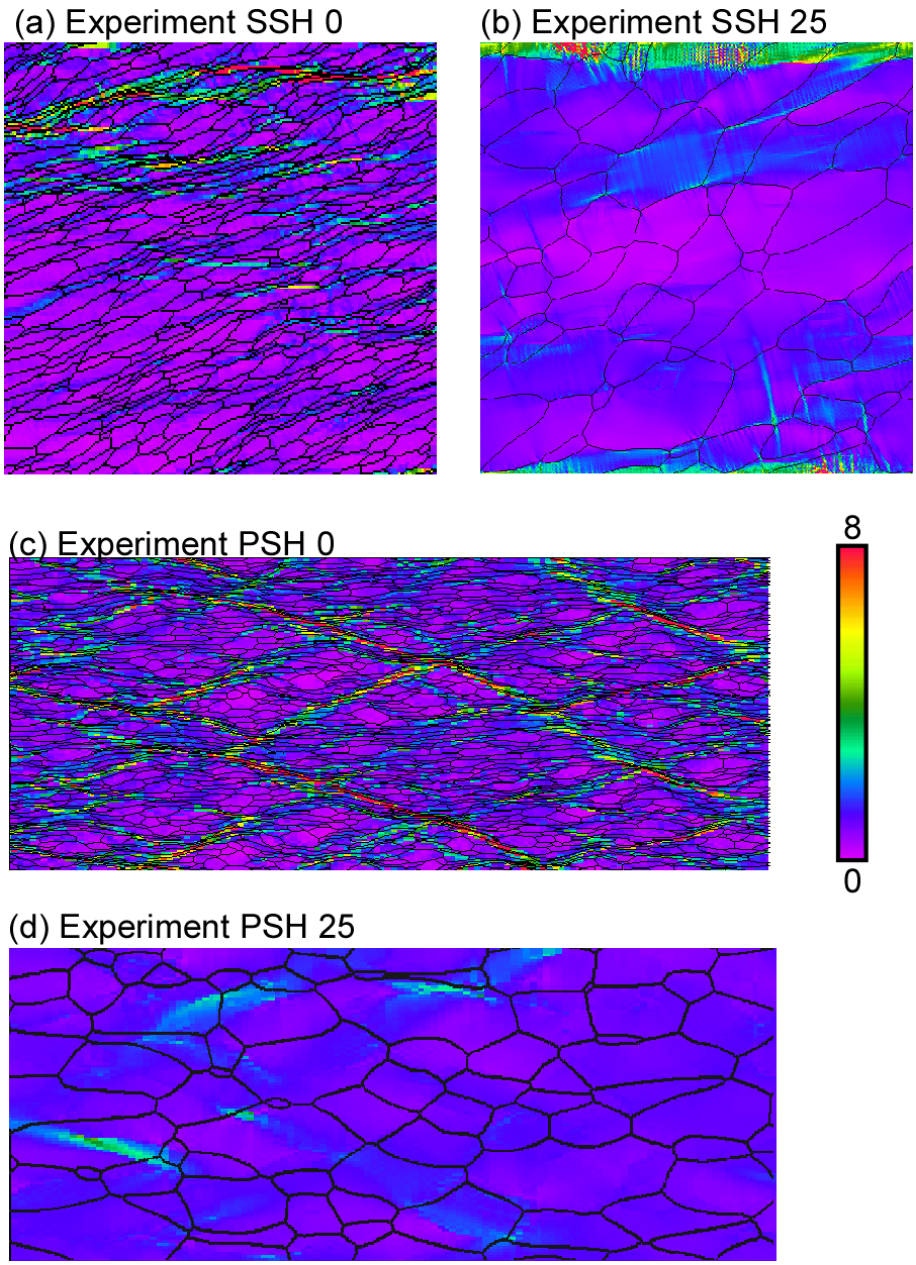

Figure 10: Maps of the von Mises strain-rate field normalised to the bulk von Mises strain rate at the final step (natural strain ε=1.2) are shown for (a,b) simple shear and (c,d) pure shear simulations with N_{DRX} =0 and 25. Colour coding is for local strain rate normalised to bulk strain rate. In pure shear simulations (c-d) the original image length is double than the images shown.

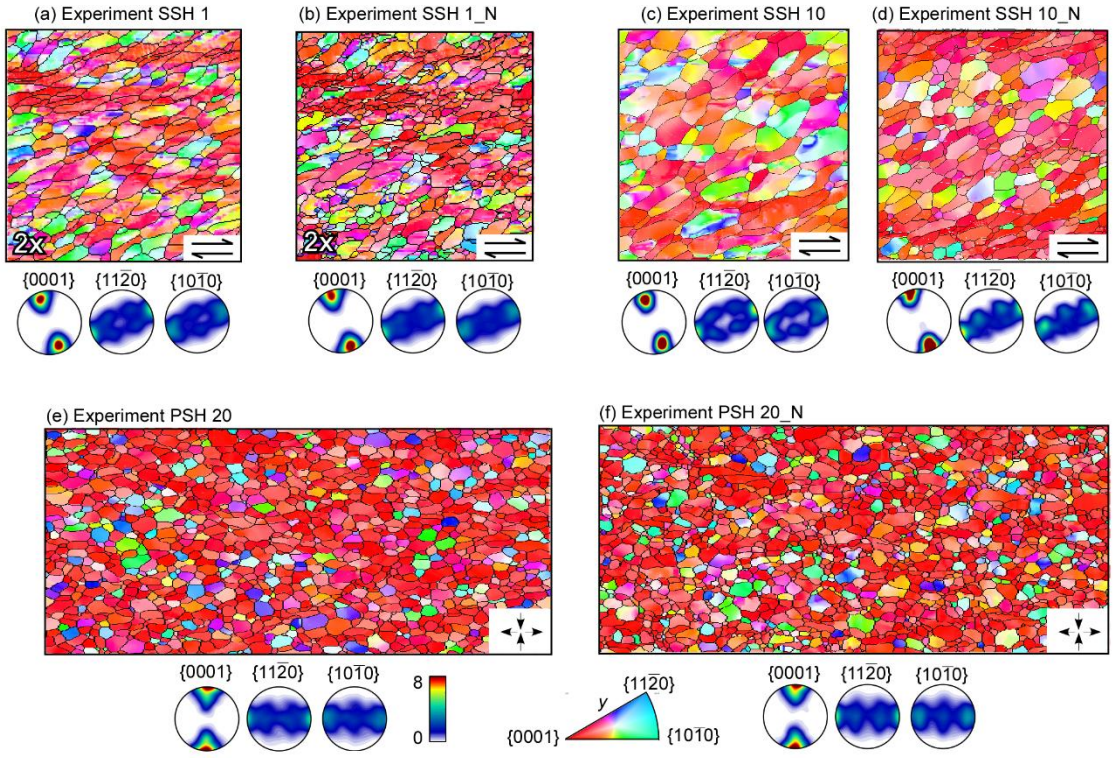

Figure 11: Lattice orientations relative to the *y*-direction (inverse poles) and pole figures of lattice orientation comparing the influence of incorporation of the polygonisation process (indicated with suffix _N). Simple shear simulations (a-b and c-d) reach a final natural strain of ε=1.2, while pure shear simulations (e-f) reach a final natural strain of ε=0.75. The final LPO is not noticeably affected by polygonisation, regardless of the amount of *DRX*: 1 (a-b), 10 (c-d) and 20 (e-f). In order to allow visualisation of the microstructures, the figures of Experiments SSH 1 and SSH 1_N, have been enlarged two times, only showing the upper left quarter of each model. Pole figures show orientation of unodes.

To show the strain rate intensity, the Von Mises strain rate is calculated as a function of the symmetric strain rate tensor (equation 7) and plotted in Figure 10. In simple shear simulations high strain-rate synthetic bands oriented at low angles to the horizontal shear plane (also called synthetic shear bands) develop (Figure 10a). In pure shear simulations, high strain-rate conjugate bands develop at angles of 66º-71º with respect to the vertical *y*-direction (Figure10c). In both simple and pure shear models the number and intensity of shear bands is reduced by dynamic recrystallisation (Experiment 25 in Figure 10b,d).

3.6 Ice simulations including polygonisation

The influence of polygonisation on the final microstructures was tested by analysing a series of simulations that include the ELLE polygonisation subloop (*i.e.*, experiments with suffix _N). These models were carried out in both pure and simple shear deformation and with different amount of recrystallisation: 1, 10 and 20 *DRX* steps per deformation step, respectively (Figure 11b,d,f). When polygonisation is active the differential stress reaches a steady-state earlier than in the case of the corresponding simulation without this routine (dashed lines in Figure 8). Polygonisation does not affect

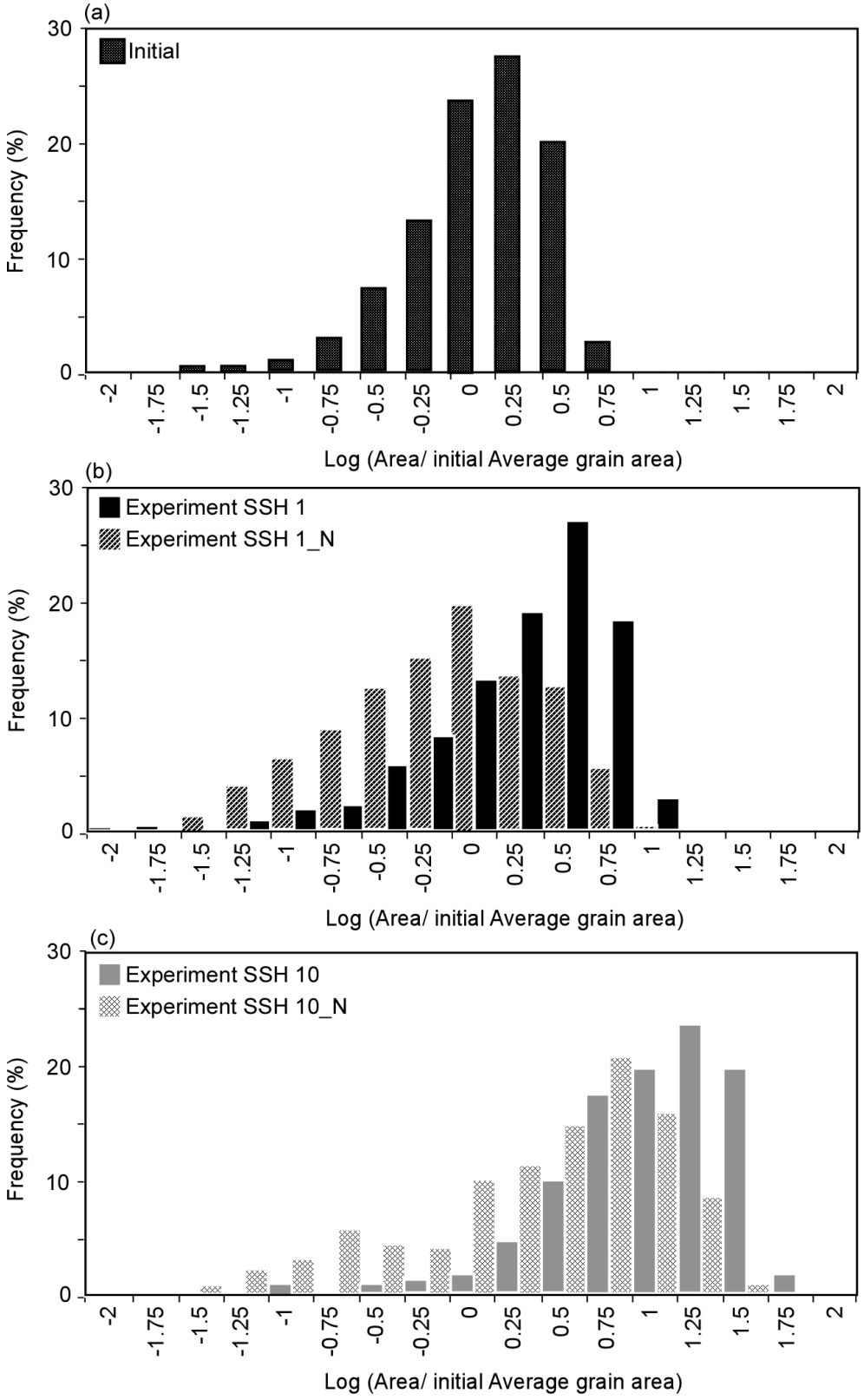

Figure 12: Comparison of the final grain area distribution normalised to the initial average grain area at the start of the simulation (a) and at the end of the simulations, performed without or with polygonisation (indicated with suffix _N), for (b) 1 step or (c) 10 steps of *DRX* per deformation. Initial distribution in (a).

the final strong LPO regardless the amount of *DRX*. This applies to both simple and pure shear cases (Figures 11a-d and 11e-f, respectively). The lack of influence of polygonisation is probably due to the fact that new grains have lattice orientations close to those of their parent grains. However, the incorporation of the polygonisation process, and therefore the development of proper high-angle grain boundaries out of tilt walls, reduces grain size compared to the cases in which this process is not included (Table 2) (Llorens et al., 2016a). Polygonisation also changes the distribution of grain sizes, reducing the skewness and, in the case of the simple-shear simulation SSH 10_N developing a bimodal distribution (Figure 12b,c).

4 Discussion

4.1 Effects of ice flow on the LPO and final microstructure

Natural deformation in glaciers and ice sheets mostly occurs under general strain conditions between the end-members pure and simple shear. In general, there is an increase in vorticity with depth, with pure shear dominating at the top and simple shear at the base (e.g. Cuffey and Paterson, 2010). It is therefore important to understand how ice behaves differently under these varying boundary conditions, especially considering the strong anisotropy (LPO) developed in ice sheets and glaciers (Faria et al., 2009; NEEM community members, 2013). The numerical results show that the boundary conditions do not significantly change the evolution of the microstructure due to viscoplastic deformation, because elongated grains and a shape-preferred orientation (SPO) parallel to the stretching direction and normal to the finite shortening direction develop in both pure and simple shear cases. Qualitatively, increasing DRX in simple shear simulations results in a SPO oriented at a high angle with respect to the shear plane. Simple shear deformation results in a rotation of the SPO towards the shear plane, according to the sense of shear (Figures 3,4). GBM in isolation leads to an increase in grain size, as long as the grain boundary energy is a significant component of the driving force (equation 2). It also reduces the grain elongation, hence masking strain localisation. Although GBM is assumed to dominate in materials close to their melting point (Humphreys and Hatherly, 2004), recovery and polygonisation probably play a significant role in ice sheets and glaciers. These counteract the GBM-induced grain growth, leading to a steady grain size where a balance is reached (Mathiesen et al., 2004; Roessiger et al., 2011). Adding polygonisation to the model indeed leads to a reduction in grain size and in grain elongation, although a steady state is not (yet) reached in our simulations (Figures 11,12). The results are consistent with the observation that GBM and polygonisation are active in large parts of ice sheets, as indicated by the absence of elongated grains in most ice core microstructures observed to date (e.g. Faria et al., 2014b; Weikusat et al., 2017a). Moreover, polygonisation has recently been found to be active too in experimental ice creep tests close to the melting point (Montagnat et al., 2015).

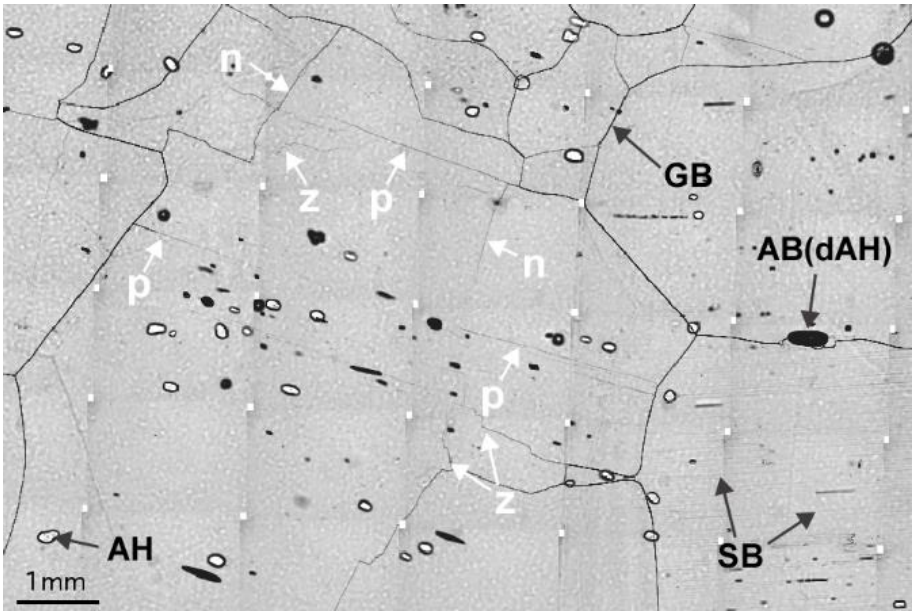

Figure 13: Example of sGB types in EDML ice core. n = normal to basal plane "Nakaya" type, p = parallel to basal plane type, z = mixed type. Further details see Weikusat et al. (2009b; 2011b).

In our simulations, a strong c-axes maximum initially develops parallel to maximum compressive direction (σ_1) at a natural strain of ε=0.3 in pure shear boundary conditions. When DRX is active this single maximum tends to shift towards being obliquely oriented with respect to σ_1 (or X axis) in the YZ plane (see Figure 5). Pure shear and uniaxial compression experiments (Jacka and Maccagnan, 1984; Piazolo et al., 2013) of polycrystalline ice result in a girdle fabric of c-axes around the direction of σ1 (compression direction). The lack of c-axes oriented parallel to σ1 in our simulations is interpreted due to the activation of recrystallisation processes, coherently with temperatures near to the melting point in the experiments (between -2 º and -7º C).

In simple shear the c-axes maximum initially develops parallel to σ_1, but rapidly tends to rotate with increasing strain towards being oblique or normal to the shear plane (Figure 5). Similar to the pure shear cases, activation of recrystallisation processes shifts the maximum to be oblique to the XY section. Ice deformation laboratory experiments revealed a similar pattern in simple shear, with the c-axes maximum oriented normal to the shear plane but also obliquely oriented with respect to σ_1 (e.g. Bouchez and Duval, 1982; Wilson and Peternell, 2012).

Once a LPO forms, it does strengthen and rotate with increasing deformation according to the sense of shear in simple shear simulations (Figures 4 and 5). The rotational evolution of ice fabrics in simple shear is typically characterised by the development of a strong single maximum approximately perpendicular to the shear direction (Bouchez and Duval, 1982). With increasing strain, the obliquely-oriented maximum disappears in experiments and only the maximum oriented perpendicular to the shear plane remains (Bouchez and Duval, 1982). This observation differs from our simulations, in which the c-axes maximum is always obliquely oriented. This rotational evolution of ice fabrics has been

recognised as vertical or near vertical single maximum LPOs in ice cores (Faria et al., 2014b; Fitzpatrick et al., 2014; Herron and Langway, 1982; Montagnat et al., 2014a; Thorsteinsson et al., 1997). The vorticity of deformation is typically close to simple shear in the deep part of ice sheets, with the shear plane generally oriented parallel to the bedrock (Weikusat et al., 2017a). Another difference between laboratory experiments and numerical simulations is that the first only consider uniaxial deformation while simulations are performed under perfect 2D plane strain (i.e. pure shear).

The statement that a single maximum LPO like observed in nature under simple shear cannot be simulated unless recrystallisation is taken into account (Van der Veen and Whillans, 1994) is not consistent with the results of our simulations, as the developing hard grains further rotate according to the sense of shear independently of the intensity of recrystallisation NDRX (Figure 5, at a natural strain of ε=1.2).

Our simulations show how such LPOs develop as a consequence of deformation, even when there is strong recrystallisation. The implementation of the polygonisation routine does not affect the developed LPO, because new grains that nucleate maintain the c-axis orientations close to that of their parental grains (Figure 11b-d-f). An additional factor controlling the development of a LPO is the degree of strain localisation, as illustrated by the difference in LPO developed in high and low strain-rate domains (e.g. Figure 5i-j). The detailed evolution of the LPOs in different scenarios of strain localisation needs to be systematically addressed in future studies.

4.2 Effects of vorticity of ice flow on rheology

All simulations present strain hardening behaviour during the first stages of deformation (Figure 8), during which the degree of deformation localisation remains relatively constant (Figure 9a-b). At a natural strain of ε=0.3 an LPO can be identified in both pure and simple shear simulations (Figure 5), which result in the development of an intrinsic anisotropy that leads to an increment of strain localisation in simulations performed at high strain rates (i.e., Experiments SSH and PSH 0 and 1) (Figure 9). Differential stress reaches a steady state in simple shear simulations (Figure 8a). This is associated with the rotation of the LPO and SPO to a more favourable position for slip, since basal planes and elongated grains progressively rotate towards the shear direction (Figure 4 a-d). However, the SPO and LPO develop in a less favourable orientation for easy glide in pure shear models, where they tend to rotate away from σ_1 (Figure 4e-h). In such cases, strain hardening keeps increasing until the end of the simulations (Figure 8a). The development of an SPO perpendicular to compression direction has been proposed as the cause of strain hardening in previous studies (Treagus and Lan, 2004; Takeda and Griera, 2006). The formation of new grain boundaries by polygonisation have a clear influence on the rheology, where the differential stress reaches a steady state earlier than the equivalent simulation without polygonisation (dashed lines Figure 8a). This steady state is achieved when an equilibrium in

grain size is reached (Jacka and Li, 1994), which that depends on the relative amount of new grains nucleated by polygonisation versus grain boundary migration (Faria et al., 2014b).

A hardening-and-softening behaviour is observed in laboratory experiments under constant stress or constant strain rate in both pure and simple shear configurations (Piazolo et al., 2013). In experiments, a stress peak is typically observed below a strain of 0.04. In our simulations the transition between hardening and softening is observed at a higher strain, at 0.30 approx. There are some remarkable differences between laboratory experiments and numerical simulations. One of them is that in our models we assume lower strain rate conditions (10^{-10}-10^{-12} s^{-1}) than those used in laboratory experiments, where higher strain-rates are utilised (10^{-5} and 10^{-7} s^{-1}). This implies that our assumption of viscoplastic behaviour of ice polycrystals is perhaps not valid for the range of strain rates used in laboratory experiments, although it is more realistic for comparisons with natural cases. In these conditions transient creep must be considered and an elastoviscous-plastic behaviour is more appropriate to describe the mechanical behaviour of the ice polycrystalline aggregate. For example, Suquet et al. (2012) used an elastovisous-plastic model to simulate transient creep from the experimental data of Weertman (1973). However, this approach is limited to very low strains (<0.05), significantly lower than those expected in natural ice sheets. Another key difference is that a hardening-and-softening behaviour is always observed in laboratory experiments regardless the stress configuration. Contrarily, this is only observed in our models in simple shear conditions. We have to take into account that the strain rate and geometry of deformation is constant during the simulation time. Only strain hardening occurs in numerical pure shear models, at least up to the end of the simulation time (ε=1.2). Our results indicate that tertiary creep is probably not steady-state, and that hardening and softening can probably occur at large strain. This would be associated with an increase of the strength of the LPO and the viscous anisotropy of the material.

Simulations performed at low strain rates do not show high-strain localisation bands (Figure 10b-d), as the deformation is more homogeneously distributed (Figure 9, Experiments SSH and PSH 10 and 25). GBM and polygonisation result in microstructures dominated by larger and more equidimensional grains, preventing the formation of strong grain elongation and masking localisation bands. In that situation and with a strong LPO, deformation cannot be accommodated by high-strain bands any more, leading to the activation of the non-basal slip systems in both pure and simple shear simulations (Figure 6b). The favourable orientation of the pyramidal plane with respect to σ_1 in pure shear models (Figure 5e-h) enables dislocations to glide along this system of planes rather than along the basal ones (Figure 6b, dashed lines). However, the pyramidal plane does not reach this favourable orientation with respect to σ_1 in simple shear simulations, due the rotation of the LPO with the sense of shear (Figure 5a-d). This results in the basal slip system remaining more active than the non-basal ones throughout the simulations (Figure 6b, solid lines). This evolution of changing slip system activity has to be investigated further, as

heir occurrence has been proposed to be a rate-limiting mechanism at high stresses (Montagnat and Duval, 2000), but also applicable to low stress conditions.

The activation of non-basal slip systems can be recognised from the rotation of the a-axes towards the maximum elongation axis while c-axes rotate towards the direction of the maximum finite shortening (Figure 4c-d,g-h). Recently, Montagnat et al. (2015) observed clustering of a-axes in a wide girdle at a high angle to the compression direction in experiments with dynamic recrystallisation analysed by EBSD. Clustering of a-axes has been previously described in the deep part of the GRIP ice core, where the slip along non-basal systems is proposed as a possible cause of the a-axis concentration (Miyamoto et al., 2005). The activation of the non-basal slip systems is related to the development of subgrain boundaries, as shown in Figure 7b,d. Subgrain boundaries composed of basal (tilt and twist boundaries) and non-basal dislocations (tilt boundaries) were described using EBSD datasets, where the non-basal dislocations play an important role in the formation of all subgrain boundaries (Weikusat et al., 2011a,b). The frequent abundance of different subgrain boundaries types (Figure 13), especially the "p-type" sGB (> 50% of all sGB in EDML, Weikusat et al., 2009b), which can be basal twist boundaries, but also non-basal tilt boundaries (more than 75% according to very first estimates, see table 2, Weikusat et al., 2011b) gives very first indications on the importance of non-basal dislocation activity. This has to be treated with care, as only recovered dislocations can be measured, forming sGB, not all dislocations involved in deformation. Clearly more high resolution full-crystal orientation measurements are needed to validate our models with respect to magnitude of recovery versus activation of different slip systems during deformation.

5 Conclusions

We present a state-of-the-art of a full-field numerical approach applied to ice. It includes simulations with and without recrystallisation under pure and simple shear boundary conditions. Although the amount of recrystallisation strongly affects the grain morphology, it has a much smaller effect on LPO development. In all cases, regardless the amount of *DRX* and ice flow, a single c-axes maximum develops that is oriented approximately perpendicular to the maximum finite shortening direction and which in simple shear rotates towards the normal to the shear plane. This leads to distinctly different behaviour in pure and simple shear. In pure shear, the LPO and SPO are increasingly unfavourable for deformation, leading to hardening and an increased activity of non-basal slip. The opposite happens in simple shear, where the vorticity causes rotation of the LPO and SPO to a favourable orientation that leads to strain softening. An increase of recrystallisation enhances the activity of the non-basal slip, due to the reduction of the localisation of the deformation. In pure shear conditions, the pyramidal slip activity is thus even more enhanced and can become higher than the basal-slip activity.

Our results further show that subgrain boundaries can be developed by the activity of the non-basal slip systems. The implementation of the polygonisation routine reduces grain size and SPO, but does not change the final LPO significantly, because newly nucleated grains approximately keep the c-axis orientations of their parental grains. However, it enables the establishment of an equilibrium in grain size, and therefore the differential stress reaches a steady-state.

Acknowledgements

We thank all the members of the ELLE development group, in particular Lynn Evans, Sandra Piazolo and Verity Borthwick for their contributions to the simulation code. We gratefully acknowledge A. Treverrow and an anonymous reviewer, whose constructive reviews greatly improved the manuscript, together with the editorial guidance of P. Sammonds. This work was carried out as part of the Helmholtz Junior Research group "The effect of deformation mechanisms for ice sheet dynamics" (VH-NG-802). F.S was funded by the DFG (SPP 1158) grant BO 1776/12-1. MGL was funded by the programme on Recruitment of Excellent Researchers of the Eberhard Karls Universität Tübingen. The Microdynamics of Ice (MicroDICE) research network, funded by the European Science Foundation, is acknowledged for funding research visits of MGL.

PAPER IV

Small-scale disturbances in the stratigraphy of the NEEM ice core: observations and numerical model simulations

Daniela Jansen[1], Maria-Gema Llorens[2,1], Julien Westhoff[2], **Florian Steinbach**[2,1], Sepp Kipfstuhl[1], Paul D. Bons[2], Albert Griera[3] and Ilka Weikusat[1,2]

1. Alfred Wegener Institute Helmholtz Centre for Polar and Marine Research, 27568 Bremerhaven, Germany
2. Department of Geosciences, Eberhard Karls University Tübingen, 72074 Tübingen, Germany
3. Departament de Geologia, Universitat Autònoma de Barcelona, 08193 Bellaterra (Barcelona), Spain

Published in *The Cryosphere*, 12 February 2016.

Abstract

Disturbances on the centimetre scale in the stratigraphy of the NEEM ice core (North Greenland) can be mapped by an optical line scanner as long as the ice does have a visual layering, such as, for example, cloudy bands. Different focal depths allow, to a certain extent, a three dimensional view of the structures. In this study we present a detailed analysis of the visible folds, discuss their characteristics and frequency and present examples of typical fold structures. We also analyse the structures with regard to the deformation boundary conditions under which they formed. The structures evolve from gentle waves at about 1500 m to overturned z-folds with increasing depth. Occasionally, the folding causes significant thickening of layers. Their similar-fold shape indicates that they are passive features and are probably not initiated by rheology differences between alternating layers. Layering is heavily disturbed and tracing of single layers is no longer possible below a depth of 2160 m. C-axes orientation distributions for the corresponding core sections were analysed, where available, in addition to visual stratigraphy. The data show axial-plane parallel strings of grains with c-axis orientations that deviate from that of the matrix, which shows a single-maximum fabric at the depth where the folding occurs.

Numerical modelling of crystal-viscoplastic deformation and dynamic recrystallisation was used to improve the understanding of the formation of the observed structures during deformation. The

modelling reproduces the development of bands of grains with a tilted lattice orientation relative to the single maximum fabric of the matrix, and also the associated local deformation. We conclude from these results that the observed folding can be explained by formation of these tilted-lattice bands.

1 Introduction

The NEEM (North Greenland Eemian Ice drilling) ice core, located at 77° 27' N 51° 3.6' W in the northwest of Greenland, has been drilled between June 2008 and July 2012. It is located on a topographic ridge, which dips towards the northwest so that the surface velocities on the ice divide have a non-negligible component of along ridge flow of about 6 m a^{-1} (NEEM community members, 2013). In July 2010 the bedrock was reached at 2537.36 m depth. The site has been chosen in order to recover an undisturbed Eemian warm-period ice layer. However, it was found later that the ice below 2200 m was heavily disturbed and probably folded on a large scale (NEEM community members, 2013).

Visual stratigraphy of the NEEM ice core revealed folding on a small scale too, with fold amplitudes varying from less than 1 cm to a few decimetres (Samyn et al., 2011). These types of folds occur well above the large scale disturbances reported by the NEEM community members (2013). Similar structures have been found in the lower parts of other deep ice cores (Alley et al., 1997; Thorsteinsson, 1996; Svensson et al., 2005; Faria et al., 2010; Fitzpatrick et al., 2014). Stratigraphy bands are visualized by an indirect light source scattering on surfaces inside the ice, mainly particles and air bubbles / hydrates (Svensson et al., 2005). High impurity content is found in ice that originates from snow accumulated during glacial periods. Changing impurity contents between ice from glacial and interglacial periods have been linked to rheological differences (e.g. Paterson, 1991) and may lead to shear localization in distinct horizontal layers.

Due to their potential influence on the integrity of the climatic record, folds have been subject to modelling studies (e.g. Waddington et al., 2001). Thorsteinsson and Waddington (2002) explored the amplification of small disturbances in the layering of ice cores for isotropic and anisotropic conditions, investigating the potential for the existence of overturned folds near ice sheet centres. Azuma and Goto-Azuma (1996) concluded from their proposed anisotropic flow law formulation that an inclined single maximum fabric could lead to vertical strain even in simple shear and thus influence the stratigraphy. They also suggested that horizontal variations in the inclinations could then cause alternating thickening and thinning of layers, leading to folding or boudinage in the stratigraphy. However, the initial formation of the disturbances is not fully understood.

Here we present a characterisation of the small-scale folding observed in the NEEM ice core. Another feature occasionally observed along with folding in deep ice cores are “fabric stripes” (Alley et al., 1997). They describe bands of deviating grain orientations with respect to the surrounding matrix, which

is essentially a single maximum fabric in regions where folding occurs. We discuss possible folding mechanisms and the link to the so-called “Alley-stripes” in the crystal fabric of grains. Microstructural modelling with ELLE reproduces similar fabrics and fold structures to the ones we observe in the NEEM ice core.

2 Methods

The data used in this study were obtained by different observational methods, which will be introduced only briefly in the following section. For technical details we recommend to check the original literature cited in the subsections.

2.1 Line scan visual stratigraphy

The visual stratigraphy of the NEEM ice core was recorded by means of an automated line scan instrument (see Svensson et al. (2005) for a detailed description of the instrument and data from the North GRIP ice core). Clear ice appears dark when illuminated by an indirect light source. Dust particles or bubbles cause scatter of light and make the ice appear bright in the line scan image. A clear correlation between backscatter and dust content has been found in the North GRIP ice core (Svensson et al., 2005). The method can be applied directly in the field and in the case of the NEEM ice core was applied continuously for the entire core, with a gap between 860 m and 1150 m, which corresponds to the brittle zone where the core quality did not allow preparation for the line scanner. For the NEEM ice core the line scan images were recorded with a standardised exposure time and three focal planes within the ice core section with a vertical distance of 1 cm (Kipfstuhl, 2010b). This allows to a certain degree a three-dimensional mapping of the visible layering in the ice core. The data are stored in high-resolution (118 pixel per centimetre) bmp images. One drawback of this method is, of course, that it only shows disturbances in the ice if scattering surfaces are present. However, it is possible to even reveal structures at low dust content by means of image processing and filtering.

2.2 Automated Fabric Analyzer

The crystal fabric orientation of discrete samples was measured using a G50 Automatic Fabric Analyzer (Australian *Russell-Head* type, see e.g. Russell-Head and Wilson, 2001; Peternell et al., 2010, data set: Weikusat and Kipfstuhl, 2010). Samples cut from the physical properties part of the NEEM core were cut to 250 µm thin sections to measure c-axis crystal lattice orientations by polarized light microscopy, where the thin section is placed between systematically varying crossed polarizers (e.g. Wilson and Russell-Head, 2003). The data coverage is much better than in previous ice cores with continuous sampling of selected core sections (bags) to investigate meter-scale variations in fabric throughout the

core. However, due to the time-consuming preparation of the samples it was not possible to produce a continuous record.

2.3 Microstructural modelling with ELLE and full field crystal plasticity

We use 2-D numerical modelling to investigate the development of strain localization in a polycrystalline aggregate. At the moment it is not possible to combine simple shear and pure shear boundary conditions. We chose simple shear boundary conditions as an approximation for the in-situ conditions in the lower part of the ice sheet where the bands of deviating grain orientation are observed, and where horizontal shear is dominant. The simulation approach couples a full field method based on the fast Fourier transform (FFT) that simulates viscoplastic deformation, with a front-tracking code that simulate dynamic recrystallisation processes (DRX), included within the open-source numerical modelling platform ELLE (http://www.elle.ws; Bons et al., 2008). ELLE has been successfully used to simulate evolution of microstructures during deformation, such as recrystallization (Piazolo et al., 2008; Roessiger et al., 2011; 2014) or strain localisation (Jessell et al., 2005; Griera et al., 2011, 2013). The full-field crystal plasticity (FFT) code (Lebensohn, 2001; Lebensohn et al., 2008; Montagnat et al., 2014b, Llorens et al., 2016a) simulates deformation by pure viscoplastic dislocation glide. An experimental run consists of iterative applications of small increments ($\Delta\gamma$=0.04) of simple shear deformation, each followed by a sub-loop of processes simulating dynamic recrystallisation (grain boundary migration and recovery). While grain boundary migration covers the motion of high-angle grain boundaries, recovery achieves a decrease in intra-crystalline heterogeneities by means of local rotation without motion of high-angle boundaries. The recrystallisation sub-loop may be called more than once to simulate the different balance between deformation and recrystallisation as a function of strain rate, since all simulations are performed with the same intrinsic mobility value (M_0) and boundary-diffusion activation energy (Q) (Roessiger et al., 2014; Llorens et al., 2016a). Exchange of data between ELLE and FFT is possible, as both use periodic boundary conditions and the physical space is discretised into a shared regular node mesh.

The ELLE data structure consists of three layers: (1) a network of nodes (boundary nodes or *bnodes*) that are connected by straight boundary segments that define the high-angle grain boundaries that enclose individual ice grains, (2) a set of unconnected nodes (*unodes*) to map lattice orientations and dislocation densities, used for the FFT calculation, and (3) a passive marker grid utilised to track finite strain. Distances between nodes are kept between $5.5\text{x}10^{-3}$ and $2.5\text{x}10^{-3}$ times the unit distance (in a 1x1 bounding box), by removing *bnodes* when their neighbours are too close or adding *bnodes* when two nodes are too far apart. The space is discretised in a mesh of 256x256 Fourier points, resulting in a unit cell defined by 65,536 discrete nodes. Each *unode* represents a small area or crystallite with a certain lattice orientation, defined by Euler angles, and a dislocation density value. The ELLE data structure

has fully wrapping boundaries. The 10x10 cm^2 initial microstructure has 1632 grains, each with a homogeneous lattice orientation, showing a c-axis preferred orientation almost perpendicular to the shear plane, in order to simulate an intrinsic anisotropic material. The misorientation between grains was set at <5° (i.e. initial noise). Dislocation glide of ice-single crystal was defined by slip on the basal {0001}{11-20}, prismatic {1-100}{11-20} and pyramidal systems {11-22}{11-23}. In these simulations, the ratio A of critical resolved shear stress (CRSS) for non-basal versus basal slip systems was set to A = 20. The same stress exponent (n = 3) is set for all slip systems. The physical values used for recrystallisation are: intrinsic mobility M_0 (0.023 $m^2kg^{-1}s$; Nasello et al., 2005), boundary-diffusion activation energy Q (40 KJ mol^{-1}; Thorsteinsson, 2002), isotropic surface energy γ_e (0.065 Jm^{-2}; Ketcham and Hobbs, 1969) and temperature was set to T=-30°C. To simulate recovery numerically, a modification of the approach proposed by Borthwick et al. (2013) was used. As the time step for the simulation of recrystallisation is smaller than necessary for the computationally expensive FFT-calculation, we modelled ten DRX steps of Δt=6.3x10^8 s for each shear strain increment of $\Delta\gamma$=0.04, giving a shear strain rate of 6.35x10^{-12} s^{-1}. Simulations with other shear strain rates were performed for comparison, but not presented here. See Llorens et al. (2016a) for a complete description of the methods.

3 Results

3.1 Stratigraphy and fold classification

The stratigraphic data were visually inspected for all parts of the ice core containing cloudy bands, in order to categorise disturbances of the visible layers. It has to be noted that this method is only appropriate where sufficient layers are visible, since clear ice may have been deformed as well. Figure 1 shows an overview of the layering structures we find in the NEEM ice core. All images shown are confined to the core sections above the major disturbances in the Eemian ice beginning at a depth of approximately 2200 m. Around this depth the ice is heavily sheared and the layering becomes more and more diffuse. Below that it is no longer possible to see fold structures in the visual stratigraphy data as the Eemian ice is mostly clear. The panels display the scans of entire core sections of about 1.10 m, which were cut into segments of 0.55 m after scanning. The top always represents the upper part of the core segment. Some segments differ in length, as the recovered core pieces are not always exactly 1.10 m long. Some of the pieces also fractured during the recovery process or during preparation, which is highlighted with red lines in Fig. 1. The images have been partly processed by applying a Gauss filter to enhance the visibility of the layering, and therefore the grey values are no absolute measure for impurity content or of other parameters that could influence the backscatter within the ice.

The upper part of the NEEM ice core shows little or no disturbances. Figure 1a shows an example from 1430 m depth with perfectly horizontal layers. The layer thickness and opacity does vary in the core

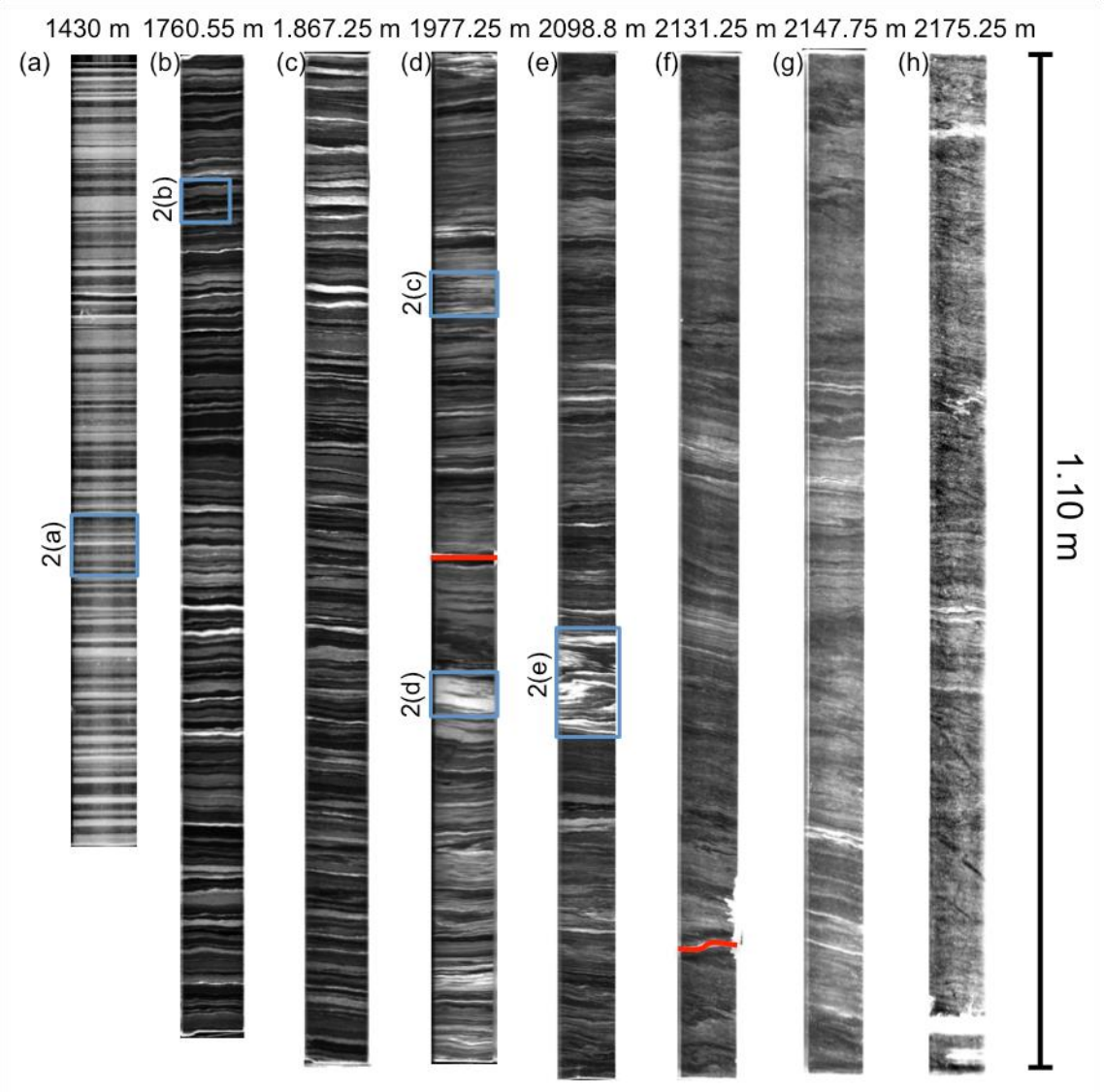

Figure 1: Visual stratigraphy overview. Line scan images of different depths. A Gauss filter was applied to images shown in panel a, d, e, f, g, and h to enhance the visibility of the layers. Red lines indicate fractures. Blue squares and associated figure codes indicate location of enlargements shown in Fig. 2. The 1.10 m line at the right indicates the scaling of the images and is also the typical length of a recovered core section.

segment, and single layers have a constant thickness throughout the 10 cm wide core section. A close-up of one of the layers shows no particular structure within it (Fig. 2a). According to the NEEM chronology published in Rasmussen et al. (2013), the annual layer thickness in this depth, which is the upper boundary of the glacial ice, is about 2 cm. Svensson et al. (2005) describe the alternating cloudy and transparent layers of ice in the NorthGRIP ice core as result of depositional events, which do not necessarily reflect annual cycles. Below a depth of about 1700 m the annual layer thickness has decreased to about 1 cm (Rasmussen et al., 2013), which is also reflected in thinner bands visible in the line scan image. In this depth the structure of the layering begins to change, as examples from depths of approximately 1760 m and 1867 m show (Fig. 1b,c). Wave-like features with cm-scale amplitudes and wavelengths in the order of the core diameter can be observed. In some parts of the core segments these

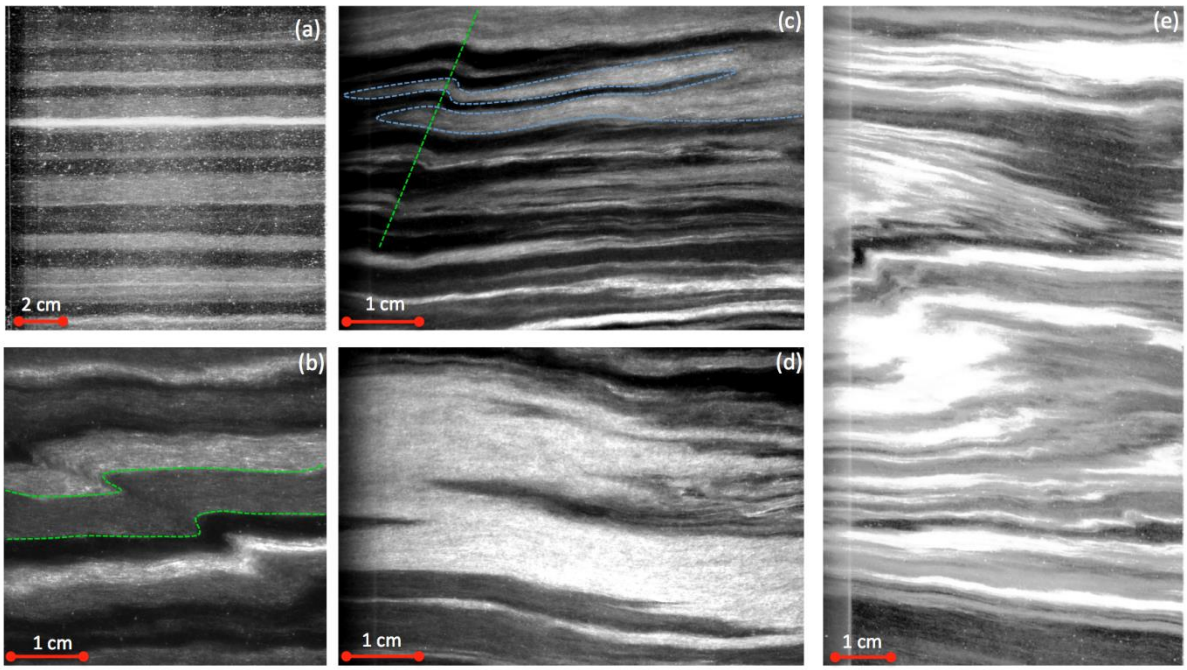

Figure 2: Close-ups from the overview Fig. 1. (a) Undisturbed layering. (b) Angular z fold consistent throughout layering. Green dashed line indicates a layer discussed in section 3.1 (c) Different generation of folds. The dashed lines indicate features discussed in section 3.1 (d) Strongly disturbed layer significantly thickened. (e) Strongly disturbed layering with different generations of folds.

disturbances can be clearly followed through several layers. Figure 2b shows an enlarged section of Fig. 1b, showing a well-developed asymmetric z-fold. Its shape indicates sinistral shear and the fold is beginning to overturn. The fold hinge is a sharp feature, which can be followed over several layers. The enlargements in Fig. 2b also show that the cloudy layers themselves appear to be laminated.

For the core sections shown in Fig. 1b,c the layers vary in thickness within the core, as can be clearly seen in Fig. 2b, where the central greyish layer (indicated with green dashed lines) nearly doubles its thickness in the centre of the image due to the folding. This shape is typical for so-called similar folds in geology (Ramsey et al., 1987). Figure 1d,e show examples from 1977 m and 2098 m depth, where the layering is significantly more disturbed. The vertical scale of the disturbances has risen to the scale of ten centimetres (Fig. 2d,e). In between the larger-scale folds the layering appears to be more regular again, however the limited width of the core sections limits our interpretation here, as the layers could be overturned folds of which the limbs became near-horizontal due to a combination of the on-going shear and vertical thinning. Fig. 2c shows a stack of flattened folds, where the doubling of layers may not be immediately obvious to the observer when focusing on the left part of the image Tracing one boundary between a clear and a cloudy band highlights that the thin layers are probably limbs of an overturned fold (indicated with a blue dashed line). There are also new generations of folds standing out through their well-defined and steeper axial planes and which are not yet overturned (Fig. 2c, on the left, fold axis indicated with a green dashed line).

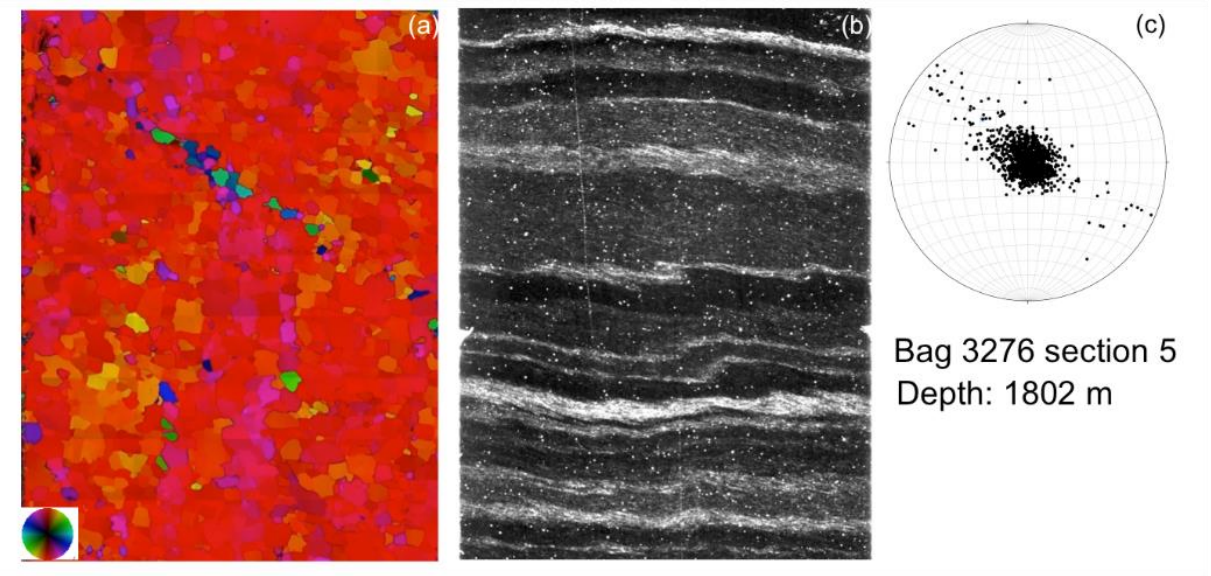

Figure 3: Comparison of fabric data and visual stratigraphy in detail, Bag 3276, approximate depth 1803 m. (a) fabric data in a vertical section, (b) linescan image in a vertical section, (c) stereoplot of c-axes orientations (horizontal plane).

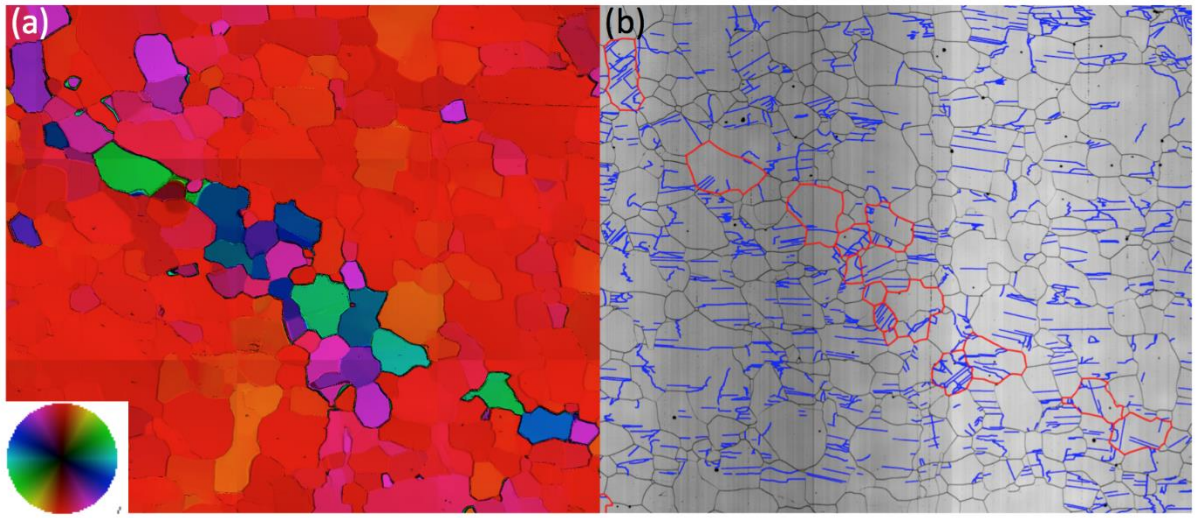

Figure 4: (a) Close-up of tilted-lattice band grains at approximately 1803 m depth (bag 3276). Inset shows the colour code for c-axes orientation (b) subgrain structures (blue) visible on LASM (Large Area Scanning Macroscope) data. Black lines indicate grain boundaries; the red outlines highlight the tilted-lattice band grains.

At even greater depth the layering becomes less distinct (Fig. 1f,g,h). In some parts of these sections the layers appear to be undisturbed but inclined, which may indicate that they are part of a larger deformation structure. The now very thin layers still show new generations of folds.

3.2 Crystal fabric orientation anomalies connected to folds

In comparison to previous deep ice cores, the amount of data gathered to analyse ice fabric is relatively high. To investigate small-scale variations entire bags of 55 cm from certain depths were processed. The general evolution of ice fabric with depth in the NEEM ice core was described in Montagnat et al.

(2014a). The c-axis orientation distribution develops more or less linearly from an isotropic fabric to a single maximum at a depth of about 1400 m, which represents the transition from the Holocene to the last glacial (Rasmussen et al., 2013). Within the well-developed single maximum fabric we found inclined bands of grains with a deviating c-axis orientation. We assume that the bands are planar features, but as the thin sections are vertical cuts through the cylindrical core section the inclination of the bands is not necessarily equal to the inclination of the planes. Similar bands were described in the GRIP ice core (Thorsteinsson, 1996) and the GISP2 ice core (Alley et al., 1997). In case of the NEEM ice core, however, significantly more fabric data are available, which enables us to follow these structures through entire core sections.

One of the first examples of such a band, shown in Fig. 3a, appears at a depth of 1800 m. The c-axis orientation of grains within the bands is tilted anti-clockwise relative to the single maximum, which is indicated by the blue-greenish colours in the colour wheel used to illustrate c-axis orientation (inset in Fig. 3a). The grain size does not differ from the average grain size of the sample. The subgrain boundary density in these grains does not differ significantly from the surrounding ones, which indicates that they are most likely not newly nucleated grains (Fig. 4). However, while the subgrain boundaries in grains with vertical c-axes are mostly parallel to the basal planes, they are mainly perpendicular to the basal plane in grains within the band, indicating the onset of rotation recrystallisation (Weikusat et al., 2009b).

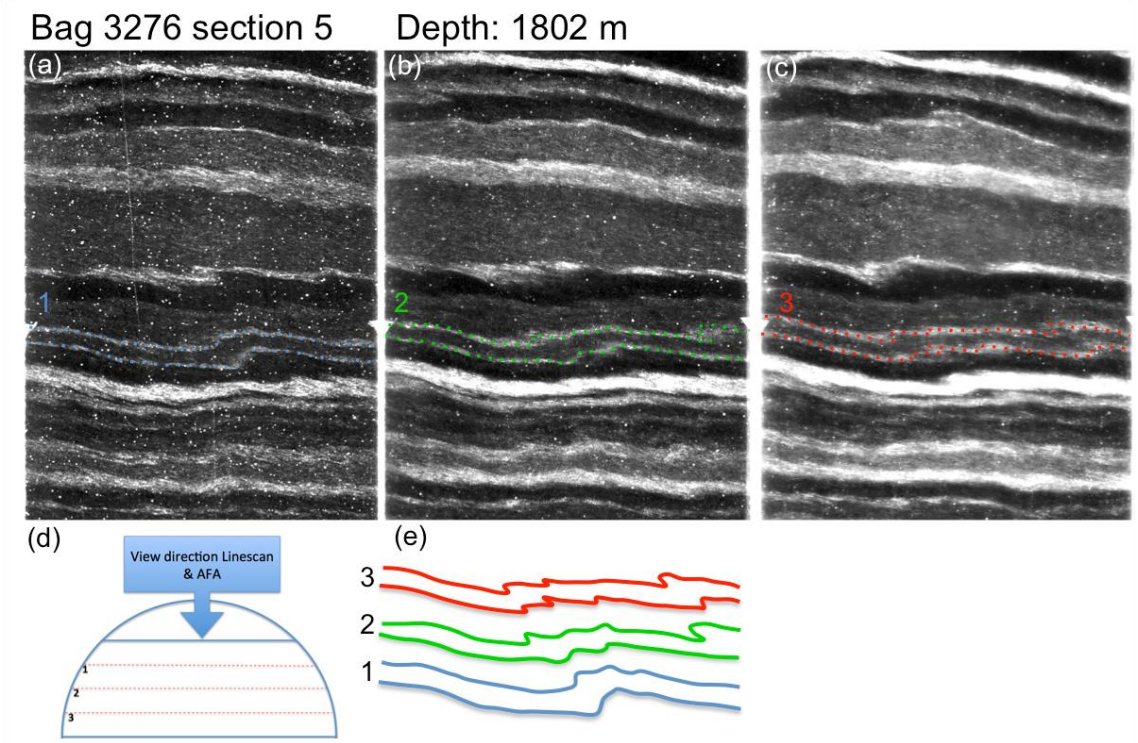

Figure 5: Linescan images from the same sample as shown in Fig. 3 from three focal depths with one highlighted layer (a) close to the surface, (b) in the centre of the core section, (c) close to the lower surface. (d) Sketch of the core sections, the upper part represents the physical properties sample, from which the thin sections are prepared. (e) Change of shape of the highlighted layer for the different foci.

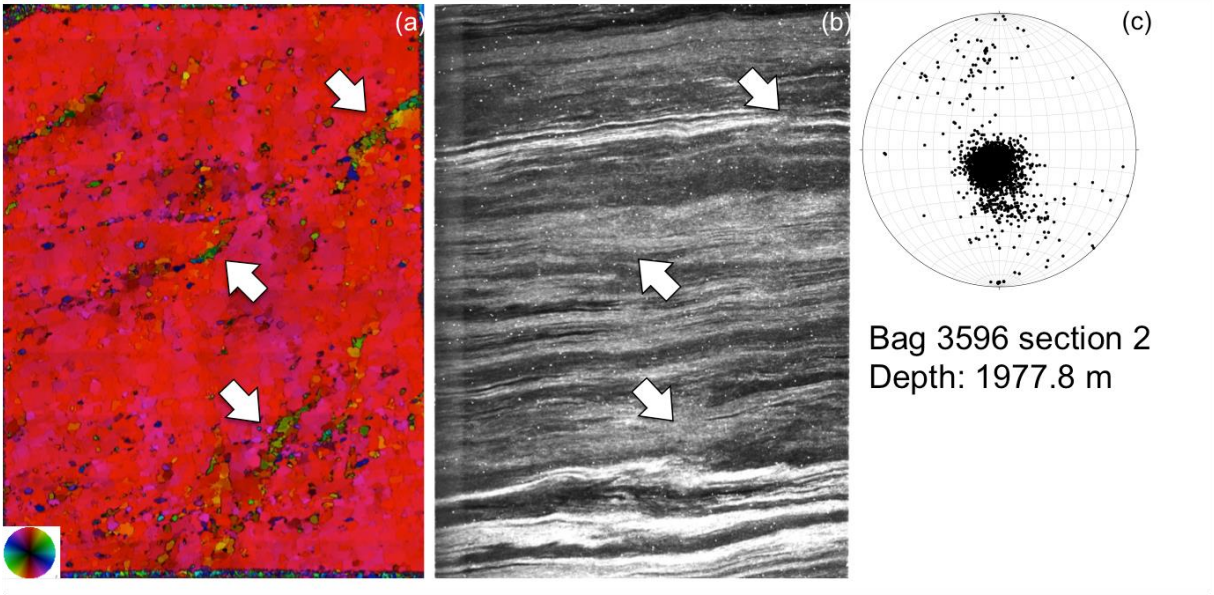

Figure 6: Comparison of fabric data and visual stratigraphy in detail, Bag 3596, approximate depth 1977.8 m. (a) fabric data in a vertical section, (b) linescan image, in a vertical section (c) stereoplot of c-axes orientations (horizontal plane).

A direct comparison of the fabric data with the line scan images (Fig. 3) reveals that these bands are connected with disturbances in the layering. The inclination is in agreement with the sense of shear that is derived from the asymmetry of the folded layers. However, layer disturbances are not always visible where fabric anomalies are found.

In Fig. 5a,b,c the three line scan images available from the different focal depths are plotted next to each other to illustrate the three-dimensional nature of the observed folding in the layering. The shape change of the highlighted layer indicates that the fold axis shifts to the left towards the centre of the core (Fig. 5e). The thin sections for the fabric analysis are prepared from the physical properties sample in the upper part. The line scan measurement is performed on the remaining part of the core with 1 cm between the different focal planes (Fig. 5d).

Figure 6 shows an example from approx. 1978 m depth where we see finely laminated layers and asymmetric folds that indicate dextral shear. The fold hinges indicated by the arrows are not very distinct, which is probably due to light diffusion caused by the distorted fine layers. The two distinct bands in the right half of Fig. 6a are relatively steep and exhibit a small tilt in the c-axes, while the feature indicated by the central arrow is more flattened and also shows a higher tilt in the c-axes. Another example can be found in the supplementary material (Fig. S1). Where several bands occur in one core section, their inclination and orientation appears to be consistent throughout (Fig. 7).

3.3 Model results

To understand the development of the observed fabric anomalies and the related disturbances in the layering, we simulated the fabric evolution under simple shear with an initially well-developed single

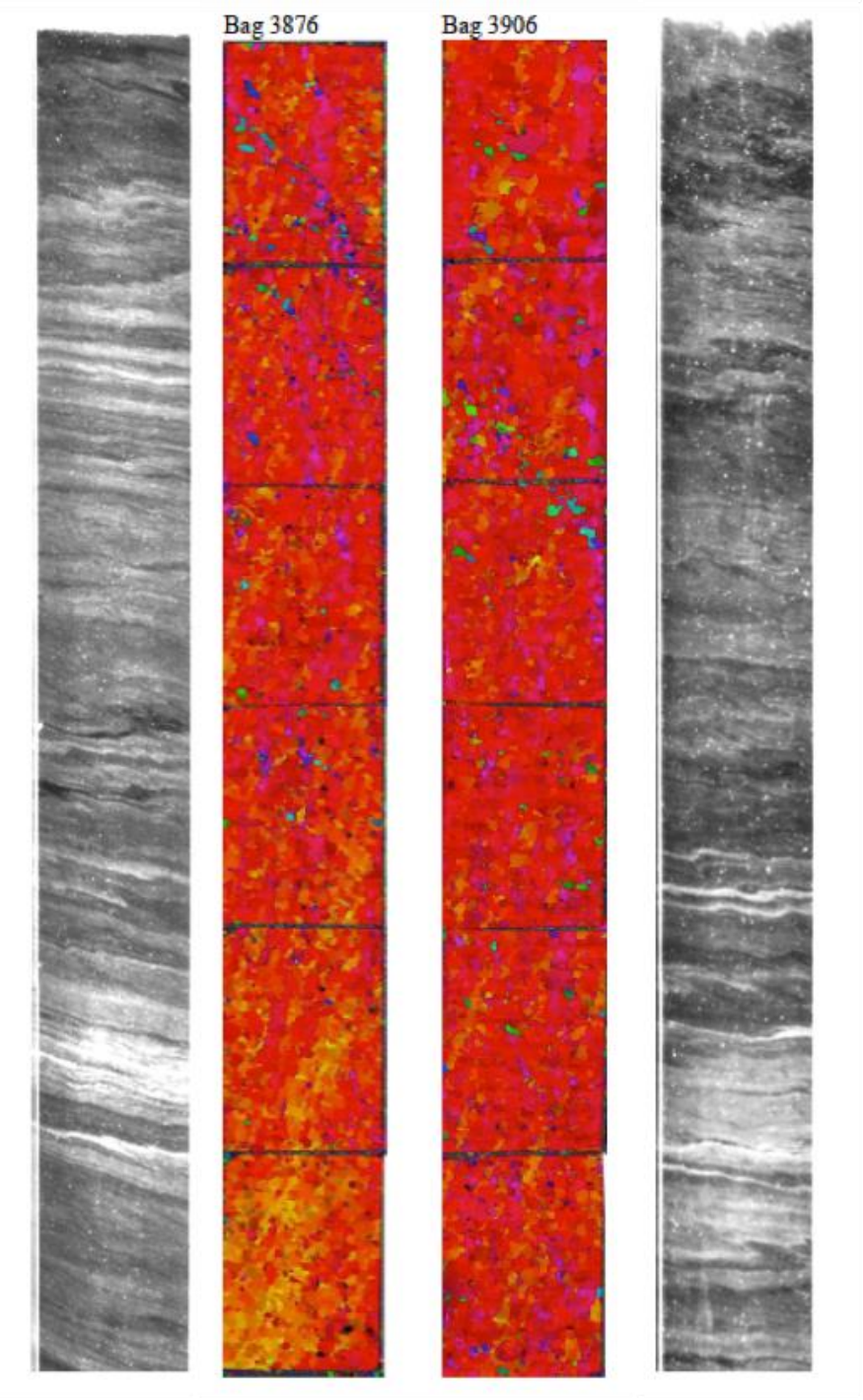

Figure 7: Comparison of entire 55 cm core sections (full bags) of linescan (a, d) and fabric data (b,c).

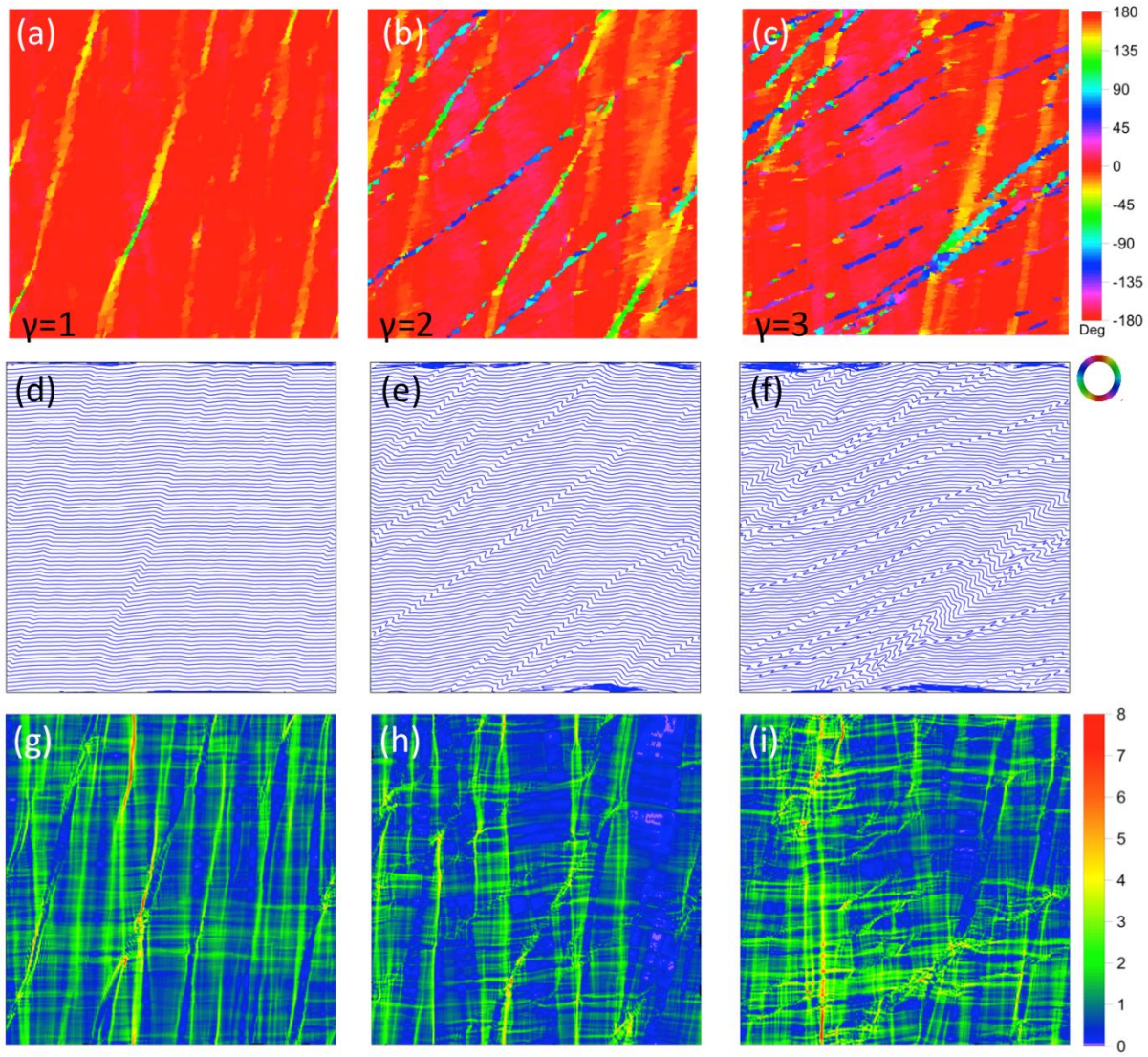

Figure 8: ELLE model results for the simple shear experiment. Panels (a), (b) and (c) show c-axes orientations for shear strains of γ=1, γ=2 and γ=3. Panels (d), (e) and (f) show the distortion of the passive grid marker. Panels (g), (h) and (i) show the equivalent von Mises strain-rate field.

maximum orientation distribution. A random noise of <5° was added to grain orientations. The setup of the simulation does not fully represent the probable kinematic boundary conditions in the region of the ice core where we observe the structures, which would be a combination of vertical compression and simple shear (Montagnat et al., 2013). We, however, model these structures in simple shear for simplicity. This approach is reasonable, since there is a significant flow along the ridge of about 6 m a^{-1} (NEEM Community Members, 2013), which gives the core location the character of a flank with relatively high shear strain rates, rather than a divide. Moreover, the choice of simple-shear boundary conditions is also justified by the fact that the bands start to appear in the lower third of the ice sheet where shear stress becomes the dominant driver for deformation (Montagnat et al., 2013). However, there might be aspects of the evolution of the folds that cannot be reproduced due to the simple shear approximation.

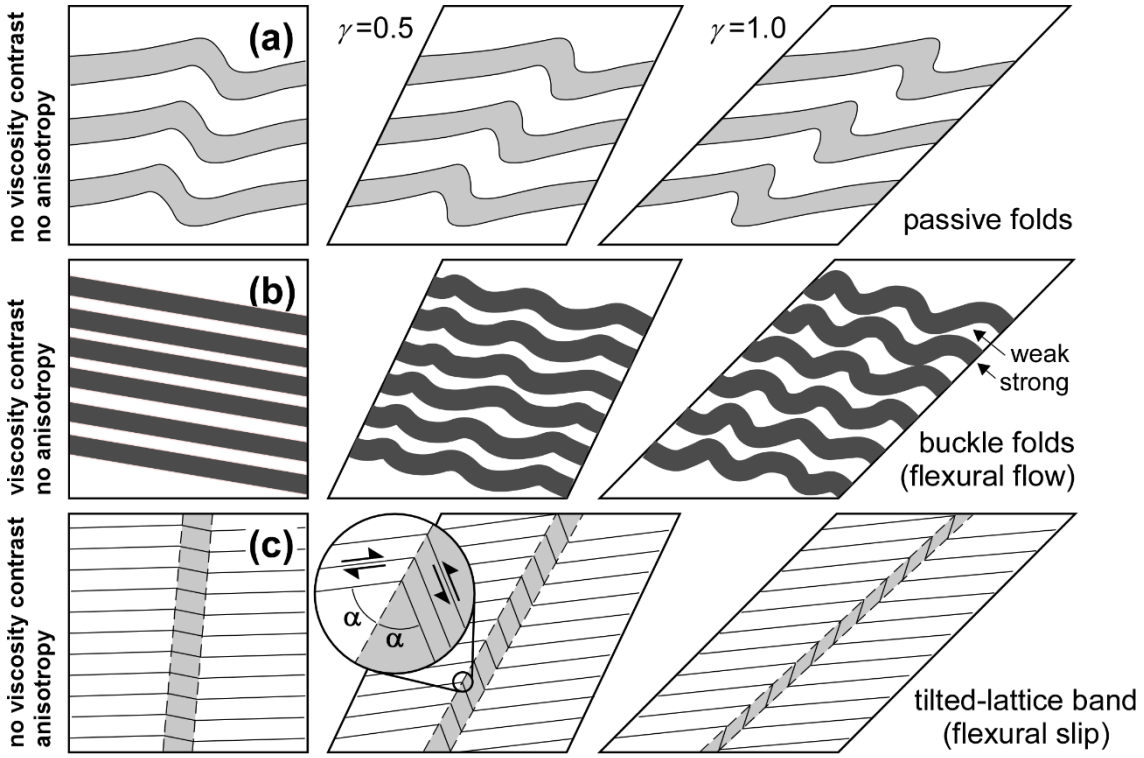

Figure 9: Basic folding mechanisms discussed in the text. (a) Passive folds form by shearing of disturbances in layering, without an active mechanical influence of that layering. Fold geometry is that of similar folds. (b) Buckle folds form by shortening of alternating strong and weak layers, in which the strong layers buckle and weak material flows into fold hinges. Fold geometry is that of parallel folds. (c) Tilted-lattice bands form in case of strong intrinsic anisotropy, but do not require viscosity contrasts between layers.

In the model simulation vertical bands similar to the ones observed in the ice core begin to stand out after a shear strain of $\gamma = 0.6$, but start to appear already after small strains (supplementary material Fig. S3). In the initial state the small deviations of the c-axes from the vertical are randomly distributed and do not show alignment (Fig. S3 a). During the first deformation steps narrow vertical bands develop with deviations from the single maximum towards the shear direction as well as broader bands with an opposite rotation of the c-axes. The rotation of c-axes in the narrow bands intensifies during the next steps and the bands begin to tilt due to the continuing shear deformation (supplementary material Fig. S2). The rotation of the c-axes is twice the inclination of the band, which is typical for flexural-slip kink bands (supplementary material Fig. S4; Dewey, 1965; Tanner, 1989). Figure 8a,b,c shows the c-axis orientations for the sample after shear strains of γ=1, γ=2 and γ=3. The bands seem to develop in different generations, which can be distinguished by their inclination as the new bands are steeper. There are areas between the bands where orientations of c-axes rotate anti-clockwise (magenta coloured), but on a larger scale and with less well-defined boundaries. In later stages of the simulation the oldest bands begin to disintegrate with the grains recrystallizing back to a vertical c-axis fabric.

Figure 8d,e,f shows the development of a passive marker grid during the simulations. The blue lines were perfectly horizontal at the beginning of the simulation and can be regarded as an analogue to the

stratigraphic layering observed in the ice core. It is apparent that the bands with abnormal grain orientation are connected with folding in the layering. At first these disturbances appear as small steps, but they develop into overturned folds with a short and steep limb with progressive deformation. They correspond to the well-developed bands in the fabric, and to a long, less inclined limb, representing the area in between the bands. The disturbances in the layering are permanent, and therefore the bands are visible in the passive grid even when they no longer exist in the orientation plot. The evolution of these bands and the corresponding folds is reminiscent to the formation of kink bands or chevron folds (Fleuty, 1964; Dewey, 1965). As these terms may have genetic connotations, referring to either single crystal processes (e.g. Wilson et al., 1986) or macroscopically strong foliated rocks under compression parallel to foliation (e. g. Cobbold et al., 1971), we use the term "tilted-lattice bands" (TLB) here to describe the bands of grains with lattice orientations that deviate from the dominant lattice preferred orientation (LPO). The rotation rate of the tilted-lattice bands in the model run is controlled by the applied overall perfect simple shear deformation. If there is an additional component of vertical shortening, as in a natural ice sheet, the rotation rate is expected to increase.

Figure 8g,h,i shows the equivalent von Mises strain-rate for the deformation steps γ=1, γ=2 and γ=3. The strain-rate appears to be localized around the margins of the bands where bending strain is the highest, which is most apparent for newer bands with steep inclinations. One also sees that strain rate localises in horizontal zones as well, which is not visible in passively deformed horizontal lines (Fig. 8d-f).

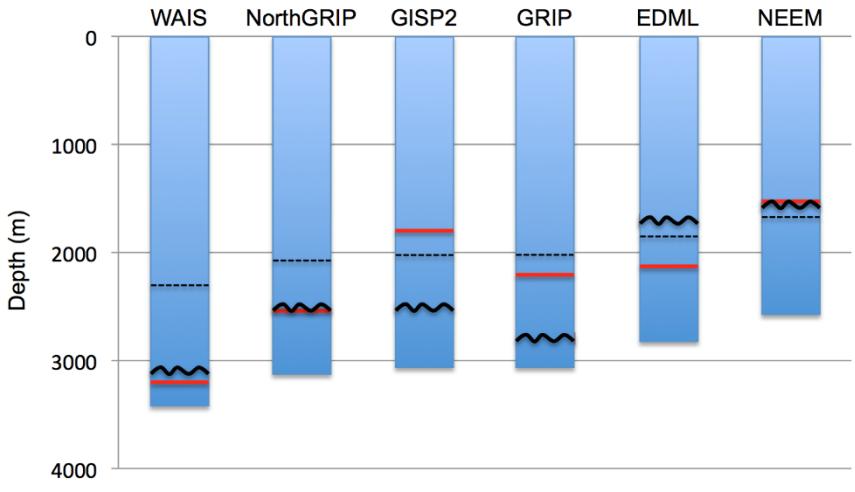

Figure 10: Comparison of the onset of visible folding in ice cores with published visual stratigraphy. The red line indicates single maximum fabric, the black line indicates onset of folding, the dashed black line indicated the lower third of the ice core. Data from Thorsteinsson, 1996 (GRIP), Alley et al., 1997; Gow et al., 1997 (GISP2), Svensson et al., 2005; Wang et al., 2006 (North GRIP), Faria et al., 2010 (EDML), Fitzpatrick et al., 2014 (WAIS).

4 Discussion

4.1 General discussion of folds

The shape of the observed folds in the NEEM ice core is typical for similar folds, as the layers are thickened in the hinge region and thinned in the fold limbs. Similar folds are passive features, where all layers of the package are deformed in a similar way (Fig. 9a). They form by passive shearing of the layering and can evolve to become overturned z-folds or even sheath folds (Quinquis et al., 1978; Bons and Urai, 1996; Alsop and Carreras, 2007). Competence or viscosity contrast between the different layers plays no or only a minor role. In contrast, buckle folds (Fig. 9b) develop when layers have different viscosities. A competence contrast with a ratio of at least about 25 between strong and weak layers is required to develop distinct folds (Llorens et al., 2013a,b). When a stack of strong and weak layers is shortened, the strong layers form folds by bending, which suppresses thickening or thinning of these layers. The weak layers accommodate this bending by ductile flow into the hinge regions, a process known as flexural flow (Donath and Parker, 1964). Strong and weak layers are thus different in shape (Fig. 9b). The fold shapes observed in the NEEM core, however, appear to be consistent across a stack of several layers (figs.1 and 2), which indicates that viscosity contrasts are very low and the folds formed by passive shearing, although there may be some differences in the flow strength of the ice between the layers due to different impurity content (Paterson, 1991).

Figure 10 gives an overview of the onset of folding (black line) and the evolution of an anisotropic fabric (red line) for several ice cores. Comparison with data from EDML (Faria et al., 2010) and WAIS (Fitzpatrick et al., 2014) in Antarctica and with GRIP (Thorsteinsson, 1996), GISP2 (Alley et al., 1997; Gow et al., 1997) and North GRIP (Svensson et al., 2005; Wang et al., 2006) from Greenland reveal that the onset of visible folding is dependent on the relation between vertical strain rates (shortening) and shear strain rates (Fig. 10). Due to the high vertical strain rates, fold structures are flattened out before they overturn, and are thus no longer visible. This has been theoretically described by Waddington (2001). Thus, the dynamical setting of the borehole location is, in addition to the anisotropy, an essential parameter for the onset of visible folding. An ice core at flanks or on divides with non-negligible flow along the ridge samples ice which experiences more shear strain than an ice core at dome positions. While the GISP 2 and North GRIP ice cores are very similar in ice thickness and accumulation rate to GRIP, the onset of folding for the latter is 300 m deeper, which may be due to its dome position and the lower surface velocity (for a comparison of ice core parameters see Faria et al., 2014a). In the region of the NEEM ice core there is an even higher along-ridge flow. A comparison of shear strain rates profiles with depth at the NEEM, GRIP and North GRIP locations can be found in Montagnat et al. (2014a). The depths of the crossing points of the curves for shear and vertical strain rate that is displayed in Montagnat et al. (2014a) corresponds approximately to the onset of folding in the cores.

The EDML ice core stands out in the comparison shown in Fig. 10, as the folding begins significantly higher than the establishment of a single maximum fabric. However, Faria et al. (2010) report that a strong girdle fabric has formed in the region of the onset of folding, thus the fabric does show some anisotropy there as well.

The scale of the disturbances found in the layering of the NEEM ice core is very similar to the ones observed at EDML (Faria et al., 2010) and North GRIP (Svensson et al., 2005), for both of which a line scan dataset of comparable quality as for the NEEM ice core is available.

The very deep onset of folding in the WAIS ice core might be due to strong basal melting at this site (Fitzpatrick et al., 2014; WAIS Divide Project Members, 2013).

4.2 Tilted-lattice bands initiate folding

Ice is a mechanically highly anisotropic mineral, as is polycrystalline ice with a strong single-maximum c-axes distribution. Our model results and the observations from the NEEM ice core show that this anisotropy and small perturbations thereof are an essential precondition for the development of folds on the cm-scale. A similar process is common in well-foliated rocks, which therefore exhibit a strong mechanical anisotropy (Hudleston and Treagus, 2010). In that context, there are basically two mechanisms for the formation of kink or chevron folds (Dewey, 1965), which may act in concert. The first is shear localisation, which occurs approximately parallel to the planes that experience the highest net shear stress. The result is a conjugate set of kink bands, originally at a high angle to each other. The second mechanism is a combination of localised bending and flexural slip. There is no thickening or thinning perpendicular to the foliation if the material can only deform by slip parallel to that foliation. A geometric necessity of this type of folding is that the axial plane must be the bisector of the interlimb angle (Fig. 9c) (Frank and Stroh, 1952; Dewey, 1965; Cobbold et al., 1971). With the interlimb angle at the beginning of folding being 180°, the bands with a slightly tilted lattice initiate at 90° to the foliation. We assume that this second mechanism can be applied to ice with strong LPO and explains the observed folding process.

Simple shear parallel to a foliation is a special case where the orientations of tilted-lattice bands formed by both mechanisms is identical: 45° to the maximum compression, which coincides with parallel and perpendicular to the foliation. Bands normal to the foliation have indeed been observed in geological simple shear experiments (Misra and Burgh, 2012; Williams and Price, 1990), and developed in our numerical model. Bands parallel to the foliation are difficult to observe in natural samples, as these would not fold the foliation. However, the numerical model shows shear-plane parallel localisation of strain rate as well (Fig. 8 g-i).

The tilted-lattice bands rotate passively, if there is a layer-parallel shear component, which does not necessarily have to be the dominant deformation component. As the band rotates by an angle α to the long limb, the short limb has to rotate by 2α, as is observed in the NEEM core and numerical simulations (Fig. 8d,e,f). The relation between the tilt of the band and the corresponding tilt of the c-axes from the model results is shown in supplementary Fig. S4. Alley et al. (1997) suggested that the rotation of the c axes of grains in the stripes lag behind the rotation of the bands themselves, while our model results indicate c-axes rotating twice as fast as the axial plane or stripe. Alley et al. 1997 explained the growth in length by the sense of shear at the perimeter of the stripe, which would cause a "spinning" to adjacent grains, causing their c-axes to rotate towards the inclination of the band and thus elongate it. In our numerical model we observe that tilted-lattice bands are seeded by individual grains and develop by linking these (Fig. S3). However, their intensification under rotation appears to propagate along their length (Fig. S2).

With progressive rotation of the tilted-lattice bands they become more distinct. Rotation of the short limb occurs by sliding parallel to the basal plane with a sense opposite to the overall shearing direction (Fig. 9c). In the case of chevron folds the features finally "lock up" when the interlimb angle reduces to about 90°, i.e. when the bands are approximately 45° to the layering (Dewey, 1965). In the numerical simulations we see that tilted-lattice bands begin to disintegrate at this stage, with recrystallization and recovery consuming the grains with deviating orientations and flow homogenizes again (see Fig. 8). However, marker lines, such as the layers in the NEEM core, will still record the tilted-lattice bands, which now continue shearing and develop into passive folds.

In summary, the model results indicate that the evolution of the observed tilted-lattice bands is a consequence of a fabric with a strong anisotropy with superimposed small random disturbances. In this way grains orientated unfavourably for basal glide are rotated by rigid body rotation, as well as shear along the basal plane with a shear sense opposite to the bulk shear strain. Thus, tilting bands appear to be an essential process in ice deformation under shear.

Azuma and Goto-Azuma (1996) suggested that horizontal variation in the single maximum direction could explain heterogeneous layer thinning or thickening of initially horizontal layers, eventually leading to folding. The development of tilted-lattice bands is a process providing such variations in the fabric.

A difficulty in comparing the results of the simulation with the observational data is that with fabric measurements we can only capture a 2-dimensional section of a 3-dimensional feature. Assuming that the tilted-lattice bands are planar features, the angle at which the cylinder of the ice core is cut relative to the inclination of the plane determines its appearance in the 2-dimensional section. Thus, the inclination of the observed bands in the plane is not sufficient to describe the full orientation of the

feature, but instead gives a minimum inclination of the plane. This also has to be taken into account when interpreting the fold structures on the line scan images.

Within one 55cm section of the ice core (bag) the cutting plane through the core is consistent and so are the samples used to prepare the thin sections for the fabric measurements. Figure 7 shows that within one bag the inclinations of the tilted-lattice bands are consistent as well, strengthening the assumption that they are connected to the local stress environment and to the sense of shear, projected onto the plane of the thin section or line scan image. A consistency between the direction of shear and the shape of z-folds in the stratigraphy has also been reported for the GRIP and GISP2 ice cores (Alley et al., 1995). In both examples displayed in Fig. 7, different generations of tilted-lattice bands can be detected, differing in inclination of the bands as the older bands have been subjected to more shear strain since their formation, and in the corresponding shift in c-axes orientation, as it is seen in the model results as well.

The connection between bands with an anomalous LPO and stratigraphic disturbances has already been discussed before (Thorsteinsson, 1986; Alley et al., 1997; Samyn et al., 2011). Together with the microstructural model results the observations can be interpreted with an improved understanding of the underlying process. The model results clearly show that tilted-lattice bands can form in simple shear conditions and that a well-developed anisotropic fabric with small perturbations is required. At the moment it is not clear why the bands sometimes appear dark in the line scan images, but from deeper parts of the core where the crystals are larger in size the line scan images give indication that the backscattering can be affected by the crystal orientation.

5 Summary and conclusions

The onset of small-scale folding can be observed at the start of the lower third of the NEEM ice core, which is similar to the fold evolution observed in EDML. Below a depth of about 2160 m it is no longer possible to track stratigraphic layers. The shape of the observed structures indicates that they are not buckle folds, which means that they are not originated by a competence contrast between alternating layers. The amounts of folding as well as the state of disturbance increase with depth.

Folding causes thickening of cloudy bands and can potentially influence the resolution of climate data extracted from the NEEM ice core. Folding causing doubling of layers was observed below a depth of about 2100 m. In some core sections the layering appears to be intact in between larger folds in the line scan data. However, within a core section, only folds and doubling of layers up to the scale of 10 cm can be delineated with certainty. It is therefore difficult to ascertain that the climate signal is not disturbed in regions with parallel layering, as these could potentially be part of larger-scale folds.

Microstructural numerical modelling results indicate that the observed folding is initiated by the formation of bands with a tilted lattice relative to the bulk LPO. The formation mechanism requires a highly anisotropic material and thus a well developed single maximum crystal orientation. Local deviations from the single maximum in the direction of shear provide the seeds for tilted-lattice bands and thus folding. Here we have shown that this process is active on the microstructural scale. Their possible link to larger scale folds still has to be investigated, but could be in line with suggestions by Azuma and Goto-Azuma (1996). Grains with inclined basal plane orientations within the tilted-lattice bands are eventually eroded through recrystallisation and recovery. However, the tilted-lattice bands formed folds in material planes that further evolve by passive folding, which is visible in the layering, but not in the c-axes patterns.

Acknowledgements

This work was carried out as part of the Helmholtz Junior Research group "The effect of deformation mechanisms for ice sheet dynamics" (VH-NG-802). F. Steinbach was funded by the DFG (SPP 1158) grant BO 1776/12-1. The NEEM Line scan data as well as the NEEM fabric data has been made available by www.pangaea.de. The Authors would like to thank Sergio H. Faria and Rüdiger Kilian for helpful discussions. The constructive and supportive comments of two anonymous reviewers and the editor J.-L. Tison helped to significantly improve the initial manuscript. We also would like to thank all members of the NEEM Community who did prepare the physical properties samples in the field.

NEEM is directed and organized by the Center of Ice and Climate at the Niels Bohr Institute and US NSF, Office of Polar Programs. It is supported by funding agencies and institutions in Belgium (FNRS-CFB and FWO), Canada (NRCan/GSC), China (CAS), Denmark (FIST), France (IPEV, CNRS/INSU, CEA and ANR), Germany (AWI), Iceland (RannIs), Japan (NIPR), Korea (KOPRI), The Netherlands (NWO/ALW), Sweden (VR), Switzerland (SNF), United Kingdom (NERC) and the USA (US NSF, Office of Polar Programs).

The Supplement related to this article is available online at doi:10.5194/tc-10-359-2016-supplement.

Bibliography

Alley, R.: Texture of polar firn for remote sensing, Annals of Glaciology, 9, 1–4, 1987.

Alley, R., Perepezko, J. and Bentley, C.: Grain growth in polar ice: I. Theory, Journal of Glaciology, 32(112), 415–424, 1986a.

Alley, R., Perepezko, J. and Bentley, C.: Grain growth in polar ice: II. Application, Journal of Glaciology, 32(112), 425–433, 1986b.

Alley, R., Gow, A. and Meese, D.: Mapping c-axis fabrics to study physical processes in ice, Journal of Glaciology, 41(137), 197–203, 1995.

Alley, R. B. and Bentley, C. R.: Ice-core analysis on the Siple Coast of West Antarctica, Annals of Glaciology, 11, 1–7, 1988.

Alley, R. B. and Fitzpatrick, J. J.: Conditions for bubble elongation in cold ice-sheet ice, Journal of Glaciology, 45(149), 147–153, doi:10.3198/1999JoG44-149-147-153, 1999.

Alley, R. B., Blankenship, D., Rooney, S. and Bentley, C.: Till beneath ice stream B: 4. A coupled ice-till flow model, Journal of Geophysical Research: Solid Earth, 92(B9), 8931–8940, 1987.

Alley, R. B., Gow, A. J., Meese, D. A., Fitzpatrick, J. J., Waddington, E. D. and Bolzan, J. F.: Grain-scale processes, folding, and stratigraphic disturbance in the GISP2 ice core, Journal of Geophysical Research: Oceans, 102(C12), 26819–26830, doi:10.1029/96JC03836, 1997.

Alley, R. B., Clark, P. U., Huybrechts, P. and Joughin, I.: Ice-sheet and sea-level changes, science, 310(5747), 456–460, doi:10.1126/science.1114613, 2005.

Alsop, G. I. and Carreras, J.: The structural evolution of sheath folds: A case study from Cap de Creus, Journal of Structural Geology, 29(12), 1915–1930, doi:10.1016/j.jsg.2007.09.010, 2007.

Anderson, D. L. and Benson, C. S.: The densification and diagenesis of snow, in Ice and Snow: Properties, Processes and Applications, MIT Press., 1963.

Arena, L., Nasello, O. and Levi, L.: Effect of bubbles on grain growth in ice, The Journal of Physical Chemistry B, 101(32), 6109–6112, 1997.

Arnaud, L., Barnola, J. M. and Duval, P.: Physical modeling of the densification of snow/firn and ice in the upper part of polar ice sheets, in Physics of Ice Core Records, pp. 285–305, Hokkaido University Press., 2000.

Arthern, R. J. and Wingham, D. J.: The Natural Fluctuations of Firn Densification and Their Effect on the Geodetic Determination of Ice Sheet Mass Balance, Climatic Change, 40(3), 605–624, doi:10.1023/A:1005320713306, 1998.

Ashby, M. F.: The deformation of plastically non-homogeneous materials, Philosophical Magazine, 21(170), 399–424, doi:10.1080/14786437008238426, 1970.

Azuma, N.: A flow law for anisotropic ice and its application to ice sheets, Earth and Planetary Science Letters, 128(3), 601–614, doi:10.1016/0012-821X(94)90173-2, 1994.

Azuma, N. and Goto-Azuma, K.: An anisotropic flow law for ice-sheet ice and its implications, Annals of Glaciology, 23(1), 202–208, doi:10.3198/1996AoG23-202-208, 1996.

Azuma, N. and Higashi, A.: Formation processes of ice fabric pattern in ice sheets, Annals of Glaciology, 6, 130–134, 1985.

Azuma, N., Miyakoshi, T., Yokoyama, S. and Takata, M.: Impeding effect of air bubbles on normal grain growth of ice, Journal of Structural Geology, 42, 184–193, doi:10.1016/j.jsg.2012.05.005, 2012.

Bachmann, F., Hielscher, R. and Schaeben, H.: Texture analysis with MTEX-free and open source software toolbox, Solid State Phenomena, 160, 63–68, 2010.

Barnola, J.-M., Pimienta, P., Raynaud, D. and Korotkevich, Y. S.: CO2-climate relationship as deduced from the Vostok ice core: a re-examination based on new measurements and on a re-evaluation of the air dating, Tellus B, 43(2), 83–90, doi:10.1034/j.1600-0889.1991.t01-1-00002.x, 1991.

Becker, J. K., Bons, P. D. and Jessell, M. W.: A new front-tracking method to model anisotropic grain and phase boundary motion in rocks, Computers & Geosciences, 34(3), 201–212, doi:10.1016/j.cageo.2007.03.013, 2008.

Becker, R.: Analysis of texture evolution in channel die compression-I. Effects of grain interaction, Acta Metallurgica et Materialia, 39(6), 1211–1230, doi:10.1016/0956-7151(91)90209-J, 1991.

Bell, R. E., Tinto, K., Das, I., Wolovick, M., Chu, W., Creyts, T. T., Frearson, N., Abdi, A. and Paden, J. D.: Deformation, warming and softening of Greenland's ice by refreezing meltwater, Nature Geosci, 7(7), 497–502, 2014.

Binder, T.: Measurements of grain boundary networks in deep polar ice cores-A digital image processing approach, Universitätsbibliothek Heidelberg., 2014.

Blackford, J. R.: Sintering and microstructure of ice: a review, Journal of Physics D: Applied Physics, 40(21), R355, doi:10.1088/0022-3727/40/21/R02, 2007.

Bons, P. D. and Urai, J. L.: An apparatus to experimentally model the dynamics of ductile shear zones, Tectonophysics, 256(1), 145–164, doi:10.1016/0040-1951(95)00161-1, 1996.

Bons, P. D., Koehn, D. and Jessell, M. W.: Microdynamics Simulation, Springer, Berlin, Heidelberg, Germany., 2008.

Bons, P. D., Jansen, D., Mundel, F., Bauer, C. C., Binder, T., Eisen, O., Jessell, M. W., Llorens, M.-G., Steinbach, F., Steinhage, D. and Weikusat, I.: Converging flow and anisotropy cause large-scale folding in Greenland's ice sheet, Nature Communications, 7, 11427, doi:10.1038/ncomms11427, 2016.

Borthwick, V. E., Piazolo, S., Evans, L., Griera, A. and Bons, P. D.: What happens to deformed rocks after deformation? A refined model for recovery based on numerical simulations, Geological Society, London, Special Publications, 394(1), 215–234, doi:10.1144/SP394.11, 2014.

Bouchez, J. and Duval, P.: The fabric of polycrystalline ice deformed in simple shear: experiments in torsion, natural deformation and geometrical interpretation, Texture, Stress, and Microstructure, 5(3), 171–190, 1982.

Breton, D. J., Baker, I. and Cole, D. M.: Microstructural evolution of polycrystalline ice during confined creep testing, Cold Regions Science and Technology, 127, 25–36, doi:10.1016/j.coldregions.2016.03.009, 2016.

Brinckmann, S., Siegmund, T. and Huang, Y.: A dislocation density based strain gradient model, International Journal of Plasticity, 22(9), 1784–1797, doi:10.1016/j.ijplas.2006.01.005, 2006.

Budd, W.: The development of crystal orientation fabrics in moving ice, Z. Gletscherkd. Glazialgeol, 8(1–2), 65–105, 1972.

Budd, W. F. and Jacka, T. H.: A review of ice rheology for ice sheet modelling, Cold Regions Science and Technology, 16(2), 107–144, doi:10.1016/0165-232X(89)90014-1, 1989.

Bunge, H. J.: Texture Analysis in Materials Science: Mathematical methods, Butterworth-Heinemann., 1982.

Calonne, N., Montagnat, M., Matzl, M. and Schneebeli, M.: The layered evolution of fabric and microstructure of snow at Point Barnola, Central East Antarctica, Earth and Planetary Science Letters, 460, 293–301, doi:10.1016/j.epsl.2016.11.041, 2017.

Castelnau, O., Th. Thorsteinsson, J. K., Duval, P. and Canova, G. R.: Modelling fabric development along the GRIP ice core, central Greenland, Annals of Glaciology, 23(1), 194–201, doi:10.3198/1996AoG23-194-201, 1996.

Castelnau, O., Duval, P., Montagnat, M. and Brenner, R.: Elastoviscoplastic micromechanical modeling of the transient creep of ice, Journal of Geophysical Research: Solid Earth, 113(B11), n/a-n/a, doi:10.1029/2008JB005751, 2008.

Church, J. A., Clark, P. U., Cazenave, A., Gregory, J. M., Jevrejeva, S., Levermann, A., Merrifield, M. A., Milne, G. A., Nerem, R. S., Nunn, P. D., Payne, A. J., Pfeffer, W. T., Stammer, D. and Unnikrishnan, A. S.: Sea Level Change, in Climate Change 2013: The Physical Science Basis. Contribution of Working Group I to the Fifth Assessment Report of the Intergovernmental Panel on Climate Change, edited by T. F. Stocker, D. Qin, G. K. Plattner, M. Tignor, S. K. Allen, J. Boschung, A. Nauels, Y. Xia, B. V, and P. M. Midgley, Cambridge University Press, Cambridge, United Kingdom and New York, NY, USA., 2013.

Cobbold, P. R., Cosgrove, J. W. and Summers, J. M.: Development of internal structures in deformed anisotropic rocks, Tectonophysics, 12(1), 23–53, doi:10.1016/0040-1951(71)90065-5, 1971.

Colbeck, S.: Theory of metamorphism of dry snow, Journal of Geophysical Research: Oceans, 88(C9), 5475–5482, 1983.

Cuffey, K. M. and Paterson, W. S. B.: The physics of glaciers, Academic Press., 2010.

Cuffey, K. M., Thorsteinsson, T. and Waddington, E. D.: A renewed argument for crystal size control of ice sheet strain rates, Journal of Geophysical Research: Solid Earth, 105(B12), 27889–27894, doi:10.1029/2000JB900270, 2000.

Cyprych, D., Brune, S., Piazolo, S. and Quinteros, J.: Strain localization in polycrystalline material with second phase particles: Numerical modeling with application to ice mixtures, Geochemistry, Geophysics, Geosystems, 17(9), 3608–3628, doi:10.1002/2016GC006471, 2016.

Dahl-Jensen, D., Albert, M., Aldahan, A., Azuma, N., Balslev-Clausen, D., Baumgartner, M., Berggren, A.-M., Bigler, M., Binder, T., Blunier, T. and others: Eemian interglacial reconstructed from a Greenland folded ice core, Nature, 493(7433), 489, 2013.

Davy, P., Hansen, A., Bonnet, E. and Zhang, S.-Z.: Localization and fault growth in layered brittle-ductile systems: Implications for deformations of the continental lithosphere, Journal of Geophysical Research: Solid Earth, 100(B4), 6281–6294, 1995.

De La Chapelle, S., Castelnau, O., Lipenkov, V. and Duval, P.: Dynamic recrystallization and texture development in ice as revealed by the study of deep ice cores in Antarctica and Greenland, Journal of Geophysical Research: Solid Earth, 103(B3), 5091–5105, doi:10.1029/97JB02621, 1998.

De Meer, S., Drury, M. R., De Bresser, J. H. P. and Pennock, G. M.: Current issues and new developments in deformation mechanisms, rheology and tectonics, Geological Society, London, Special Publications, 200(1), 1–27, doi:10.1144/GSL.SP.2001.200.01.01, 2002.

Dewey, J. F.: Nature and origin of kink-bands, Tectonophysics, 1(6), 459–494, doi:10.1016/0040-1951(65)90019-3, 1965.

Diard, O., Leclercq, S., Rousselier, G. and Cailletaud, G.: Evaluation of finite element based analysis of 3D multicrystalline aggregates plasticity: Application to crystal plasticity model identification and the study of stress and strain fields near grain boundaries, International Journal of Plasticity, 21(4), 691–722, doi:10.1016/j.ijplas.2004.05.017, 2005.

Donath, F. A. and Parker, R. B.: Folds and folding, Geological Society of America Bulletin, 75(1), 45–62, 1964.

Drury, M. R. and Urai, J. L.: Deformation-related recrystallization processes, Tectonophysics, 172(3), 235–253, doi:10.1016/0040-1951(90)90033-5, 1990.

Durand, G., Weiss, J., Lipenkov, V., Barnola, J. M., Krinner, G., Parrenin, F., Delmonte, B., Ritz, C., Duval, P., Röthlisberger, R. and Bigler, M.: Effect of impurities on grain growth in cold ice sheets, Journal of Geophysical Research: Earth Surface, 111(F1), doi:10.1029/2005JF000320, 2006.

Durand, G., Persson, A., Samyn, D. and Svensson, A.: Relation between neighbouring grains in the upper part of the NorthGRIP ice core - Implications for rotation recrystallization, Earth and Planetary Science Letters, 265(3–4), 666–671, doi:10.1016/j.epsl.2007.11.002, 2008.

Durand, G., Svensson, A., Persson, A., Gagliardini, O., Gillet-Chaulet, F., Sjolte, J., Montagnat, M. and Dahl-Jensen, D.: Evolution of the texture along the EPICA Dome C ice core, Low Temperature Science, 68(Supplement), 91–105, 2009.

Duval, P.: Anelastic Behaviour of Polycrystalline Ice, Journal of Glaciology, 21(85), 621–628, doi:10.3198/1978JoG21-85-621-628, 1978.

Duval, P.: Creep and recrystallization of polycrystalline ice, Bulletin de Mineralogie, 102(2–3), 80–85, 1979.

Duval, P.: Grain growth and mechanical behaviour of polar ice, Annals of Glaciology, 6(79), 82, 1985.

Duval, P. and Castelnau, O.: Dynamic Recrystallization of Ice in Polar Ice Sheets, Le Journal de Physique IV, 5(C3), C3-197-C3-205, doi:10.1051/jp4:1995317, 1995.

Duval, P., Ashby, M. F. and Anderman, I.: Rate-controlling processes in the creep of polycrystalline ice, The Journal of Physical Chemistry, 87(21), 4066–4074, 1983.

Duval, P., Arnaud, L., Brissaud, O., Montagnat, M. and de la Chapelle, S.: Deformation and recrystallization processes of ice from polar ice sheets, Annals of Glaciology, 30(1), 83–87, doi:10.3189/172756400781820688, 2000.

Eichler, J., Kleitz, I., Bayer, M., Jansen, D., Kipfstuhl, S., Shigeyama, W., Weikusat, C. and Weikusat, I.: Location and distribution of micro-inclusions in the EDML and NEEM ice cores using optical microscopy and in-situ Raman spectroscopy, The Cryosphere Discussions, 2016, 1–23, doi:10.5194/tc-2016-247, 2016.

Engelhardt, H. and Kamb, B.: Basal sliding of ice stream B, West Antarctica, Journal of Glaciology, 44(147), 223–230, 1998.

Etheridge, D.: Dynamics of the Law Dome ice cap, Antarctica, as found from bore-hole measurements, Annals of glaciology, 12(1), 46–50, 1989.

Evans, B., Renner, J. and Hirth, G.: A few remarks on the kinetics of static grain growth in rocks, International Journal of Earth Sciences, 90(1), 88–103, doi:10.1007/s005310000150, 2001.

Faria, S. H., Hamann, I., Kipfstuhl, S. and Miller, H.: Is Antarctica like a birthday cake?, Preprint, Max Planck Institute for Mathematics in the Sciences. [online] Available from: http://www.mis.mpg.de/de/publications/preprints/2006/prepr2006-33.html, 2006.

Faria, S. H., Kipfstuhl, S., Azuma, N., Freitag, J., Weikusat, I., Murshed, M. M. and Kuhs, W. F.: The multiscale structure of antarctica part I: Inland ice, Low Temperature Science, 68(Supplement), 39–59, 2009.

Faria, S. H., Freitag, J. and Kipfstuhl, S.: Polar ice structure and the integrity of ice-core paleoclimate records, Quaternary Science Reviews, 29(1–2), 338–351, doi:10.1016/j.quascirev.2009.10.016, 2010.

Faria, S. H., Weikusat, I. and Azuma, N.: The microstructure of polar ice. Part I: Highlights from ice core research, Journal of Structural Geology, 61, 2–20, doi:10.1016/j.jsg.2013.09.010, 2014a.

Faria, S. H., Weikusat, I. and Azuma, N.: The microstructure of polar ice. Part II: State of the art, Journal of Structural Geology, 61, 21–49, doi:10.1016/j.jsg.2013.11.003, 2014b.

Fischer, H., Behrens, M., Bock, M., Richter, U., Schmitt, J., Loulergue, L., Chappellaz, J., Spahni, R., Blunier, T., Leuenberger, M. and others: Changing boreal methane sources and constant biomass burning during the last termination, Nature, 452(7189), 864–867, 2008.

Fischer, H., Schmitt, J., Lüthi, D., Stocker, T. F., Tschumi, T., Parekh, P., Joos, F., Koehler, P., Völker, C., Gersonde, R., Barbante, C., Floch, M. L., Raynaud, D. and Wolff, E.: The role of Southern Ocean processes in orbital and millennial {CO2} variations – A synthesis, Quaternary Science Reviews, 29(1–2), 193–205, doi:10.1016/j.quascirev.2009.06.007, 2010.

Fitzpatrick, J.: Preliminary report on the physical and stratigraphic properties of the Taylor Dome ice core, Antarctic Journal of the United States, 29, 84–85, 1994.

Fitzpatrick, J. J., Voigt, D. E., Fegyveresi, J. M., Stevens, N. T., Spencer, M. K., Cole-Dai, J., Alley, R. B., Jardine, G. E., Cravens, E. D., Wilen, L. A., Fudge, T. J. and McConnell, J. R.: Physical properties of the WAIS Divide ice core, Journal of Glaciology, 60(224), 1181–1198, doi:10.3189/2014JoG14J100, 2014.

Fleuty, M. J.: The description of folds, Proceedings of the Geologists' Association, 75(4), 461–492, doi:10.1016/S0016-7878(64)80023-7, 1964.

Fliervoet, T. F., White, S. H. and Drury, M. R.: Evidence for dominant grain-boundary sliding deformation in greenschist- and amphibolite-grade polymineralic ultramylonites from the Redbank Deformed Zone, Central Australia, Journal of Structural Geology, 19(12), 1495–1520, doi:10.1016/S0191-8141(97)00076-X, 1997.

Frank, F. C. and Stroh, A. N.: On the Theory of Kinking, Proceedings of the Physical Society. Section B, 65(10), 811, 1952.

Freitag, J., Kipfstuhl, S. and Faria, S.: The connectivity of crystallite agglomerates in low-density firn at Kohnen station, Dronning Maud Land, Antarctica, Annals of Glaciology, 49(1), 114–120, 2008.

Freitag, J., Kipfstuhl, S., Laepple, T. and Wilhelms, F.: Impurity-controlled densification: a new model for stratified polar firn, Journal of Glaciology, 59(218), 1163–1169, doi:10.3189/2013JoG13J042, 2013.

Gagliardini, O., Gillel-Chaulet, F. and Montagnat, M.: A review of anisotropic polar ice models: from crystal to ice-sheet flow models, Low Temperature Science, 68(Supplement), 149–166, 2009.

Gao, X. Q. and Jacka, T. H.: The approach to similar tertiary creep rates for Antarctic core ice and laboratory prepared ice, Le Journal de Physique Colloques, 48(C1), C1-289, 1987.

Gillet-Chaulet, F., Gagliardini, O., Meyssonnier, J., Montagnat, M. and Castelnau, O.: A user-friendly anisotropic flow law for ice-sheet modelling, Journal of Glaciology, 51(172), 3–14, doi:10.3189/172756505781829584, 2005.

Gillet-Chaulet, F., Hindmarsh, R. C. A., Corr, H. F. J., King, E. C. and Jenkins, A.: In-situquantification of ice rheology and direct measurement of the Raymond Effect at Summit, Greenland using a phase-sensitive radar, Geophysical Research Letters, 38(24), doi:10.1029/2011GL049843, 2011.

Glen, J.: The flow law of ice: A discussion of the assumptions made in glacier theory, their experimental foundations and consequences, IASH Publ, 47, 171–183, 1958.

Glen, J. W.: Experiments on the Deformation of Ice, Journal of Glaciology, 2(12), 111–114, doi:10.3198/1952JoG2-12-111-114, 1952.

Glen, J. W.: The Creep of Polycrystalline Ice, Proc R Soc Lond A Math Phys Sci, 228(1175), 519, doi:10.1098/rspa.1955.0066, 1955.

Goldsby, D. and Kohlstedt, D.: Flow of ice I by dislocation, grain boundary sliding, and diffusion processes, vol. 28, p. 429., 1997.

Goldsby, D. and Kohlstedt, D.: Superplastic deformation of ice: Experimental observations, Journal of Geophysical Research, 106(B6), 11017–11030, 2001.

Goldsby, D. L.: Superplastic Flow of Ice Relevant to Glacier and Ice-Sheet Mechanics, in Glacier Science and Environmental Change, pp. 308–314, Blackwell Publishing. [online] Available from: http://dx.doi.org/10.1002/9780470750636.ch60, 2007.

Gomez-Rivas, E.: Localización de la deformación en medios dúctiles y anisótropos: estudio de campo, experimental y numérico. Trabajo doctoral, Universitat Autònoma de Barcelona, Spain., 2009.

Goodman, D. J., Frost, H. J. and Ashby, M. F.: The plasticity of polycrystalline ice, Philosophical Magazine A, 43(3), 665–695, doi:10.1080/01418618108240401, 1981.

Gottstein, G. and Mecking, H.: Recrystallization, Preferred orientation in deformed metals and rocks: An introduction to modern texture analysis, 183–218, 1985.

Gow, A. J.: On the Rates of Growth of Grains and Crystals in South Polar Firn, Journal of Glaciology, 8(53), 241–252, doi:10.3198/1969JoG8-53-241-252, 1969.

Gow, A. J., Meese, D. A., Alley, R. B., Fitzpatrick, J. J., Anandakrishnan, S., Woods, G. A. and Elder, B. C.: Physical and structural properties of the Greenland Ice Sheet Project 2 ice core: A review, Journal of Geophysical Research: Oceans, 102(C12), 26559–26575, doi:10.1029/97JC00165, 1997.

Greve, R. and Blatter, H.: Dynamics of ice sheets and glaciers, Advances in Geophysical and Environmental Mechanics and Mathematics, Springer Berlin Heidelberg, Berlin, Heidelberg, 10, 978–3, 2009.

Griera, A., Bons, P. D., Jessell, M. W., Lebensohn, R. A., Evans, L. and Gomez-Rivas, E.: Strain localization and porphyroclast rotation, Geology, 39(3), 275–278, 2011.

Griera, A., Llorens, M.-G., Gomez-Rivas, E., Bons, P. D., Jessell, M. W., Evans, L. A. and Lebensohn, R.: Numerical modelling of porphyroclast and porphyroblast rotation in anisotropic rocks, Tectonophysics, 587, 4–29, doi:10.1016/j.tecto.2012.10.008, 2013.

Hamann, I., Weikusat, C., Azuma, N. and Kipfstuhl, S.: Evolution of ice crystal microstructure during creep experiments, Journal of Glaciology, 53(182), 479–489, doi:10.3189/002214307783258341, 2007.

Hansen, L. N., Warren, J. M., Zimmerman, M. E. and Kohlstedt, D. L.: Viscous anisotropy of textured olivine aggregates, Part 1: Measurement of the magnitude and evolution of anisotropy, Earth and Planetary Science Letters, 445, 92–103, doi:10.1016/j.epsl.2016.04.008, 2016.

Herron, M. M. and Langway, C. C.: Firn densification: an empirical model, Journal of Glaciology, 25(93), 373–385, 1980.

Herron, S. L. and Langway, C. C.: A comparison of ice fabrics and textures at Camp Century, Greenland and Byrd Station, Antarctica, Annals of glaciology, 3(1), 118–124, 1982.

Herwegh, M., Handy, M. R. and Heilbronner, R.: Temperature- and strain-rate-dependent microfabric evolution in monomineralic mylonite: evidence from in situ deformation of norcamphor, Tectonophysics, 280(1), 83–106, doi:10.1016/S0040-1951(97)00139-X, 1997.

Hirth, J. and Lothe, J.: Theory of dislocations, 2nd New edition of Revised edition, Krieger Publishing Company., 1991.

Holyoke III, C. W. H. and Tullis, J.: Mechanisms of weak phase interconnection and the effects of phase strength contrast on fabric development, Journal of Structural Geology, 28(4), 621–640, doi:10.1016/j.jsg.2006.01.008, 2006.

Hondoh, T.: Nature and behavior of dislocations in ice, Physics of ice core records, 3–24, 2000.

Hondoh, T.: An overview of microphysical processes in ice sheets: Toward nanoglaciology, Low Temperature Science, 68(Supplement), 1–23, 2009.

Hooke, R.: Flow law for polycrystalline ice in glaciers: Comparison of theoretical predictions, laboratory data, and field measurements, Reviews of Geophysics, 19(4), 664–672, doi:10.1029/RG019i004p00664, 1981.

Hudleston, P. J. and Treagus, S. H.: Information from folds: A review, Journal of Structural Geology, 32(12), 2042–2071, doi:10.1016/j.jsg.2010.08.011, 2010.

Humphreys, F. J. and Hatherly, M.: Recrystallization and related annealing phenomena, Elsevier., 2004.

Huybrechts, P.: Ice sheet modeling, in Encyclopedia of the Antarctic, Routledge, New York and London, pp. 514–517., 2007.

Huybrechts, P., Rybak, O., Pattyn, F., Ruth, U. and Steinhage, D.: Ice thinning, upstream advection, and non-climatic biases for the upper 89% of the EDML ice core from a nested model of the Antarctic ice sheet, Climate of the Past, 3(4), 577–589, doi:10.5194/cp-3-577-2007, 2007.

IPCC: Summary for Policymakers, in Climate Change 2013: The Physical Science Basis. Contribution of Working Group I to the Fifth Assessment Report of the Intergovernmental Panel on Climate Change, edited by T. F. Stocker, D. Qin, G. K. Plattner, M. Tignor, S. K. Allen, J. Boschung, A. Nauels, Y. Xia, B. V, and P. M. Midgley, Cambridge University Press, Cambridge, United Kingdom and New York, NY, USA., 2013.

Jacka, T. H.: Laboratory studies on relationships between ice crystal size and flow rate, Cold Regions Science and Technology, 10(1), 31–42, doi:10.1016/0165-232X(84)90031-4, 1984.

Jacka, T. H. and Li, J.: The steady-state crystal size of deforming ice, Annals of Glaciology, 20(1), 13–18, 1994.

Jacka, T. H. and Maccagnan, M.: Ice crystallographic and strain rate changes with strain in compression and extension, Cold Regions Science and Technology, 8(3), 269–286, doi:10.1016/0165-232X(84)90058-2, 1984.

Jansen, D., Llorens, M.-G., Westhoff, J., Steinbach, F., Kipfstuhl, S., Bons, P. D., Griera, A. and Weikusat, I.: Small-scale disturbances in the stratigraphy of the NEEM ice core: observations and numerical model simulations, The Cryosphere, 10(1), 359–370, doi:10.5194/tc-10-359-2016, 2016.

Jessell, M., Bons, P., Evans, L., Barr, T. and Stüwe, K.: Elle: the numerical simulation of metamorphic and deformation microstructures, Computers & Geosciences, 27(1), 17–30, doi:10.1016/S0098-3004(00)00061-3, 2001.

Jessell, M. W.: Grain boundary migration and fabric development in experimentally deformed octachloropropane, Journal of Structural Geology, 8(5), 527–542, doi:10.1016/0191-8141(86)90003-9, 1986.

Jessell, M. W., Kostenko, O. and Jamtveit, B.: The preservation potential of microstructures during static grain growth, Journal of Metamorphic Geology, 21(5), 481–491, doi:10.1046/j.1525-1314.2003.00455.x, 2003.

Jessell, M. W., Siebert, E., Bons, P. D., Evans, L. and Piazolo, S.: A new type of numerical experiment on the spatial and temporal patterns of localization of deformation in a material

with a coupling of grain size and rheology, Earth and Planetary Science Letters, 239(3-4), 309–326, doi:10.1016/j.epsl.2005.03.030, 2005.

Jessell, M. W., Bons, P. D., Griera, A., Evans, L. A. and Wilson, C. J. L.: A tale of two viscosities, Journal of Structural Geology, 31(7), 719–736, doi:10.1016/j.jsg.2009.04.010, 2009.

Kamb, B.: Experimental Recrystallization of Ice Under Stress, in Flow and Fracture of Rocks, pp. 211–241, American Geophysical Union. [online] Available from: http://dx.doi.org/10.1029/GM016p0211, 2013.

Kerch, J.: Crystal-orientation fabric variations on the cm-scale in cold Alpine ice: Interaction with paleo-climate proxies under deformation and implications for the interpretation of seismic velocities, Universität Heidelberg., 2016.

Ketcham, W. M. and Hobbs, P. V.: An experimental determination of the surface energies of ice, Philosophical Magazine, 19(162), 1161–1173, doi:10.1080/14786436908228641, 1969.

Kipfstuhl, S.: Large area scan macroscope images from the NEEM ice core, Pangaea Data Publisher for Earth & Environmental Science, doi:10.1594/PANGAEA.743296, 2010a.

Kipfstuhl, S.: Visual stratigraphy pf the NEEM ice core with a linescanner, Pangaea Data Publisher for Earth & Environmental Science, doi:10.1594/PANGAEA.743062, 2010b.

Kipfstuhl, S., Pauer, F., Kuhs, W. F. and Shoji, H.: Air bubbles and Clathrate hydrates in the transition zone of the NGRIP Deep Ice Core, Geophysical Research Letters, 28(4), 591–594, doi:10.1029/1999GL006094, 2001.

Kipfstuhl, S., Hamann, I., Lambrecht, A., Freitag, J., Faria, S. H., Grigoriev, D. and Azuma, N.: Microstructure mapping: a new method for imaging deformation-induced microstructural features of ice on the grain scale, Journal of Glaciology, 52(178), 398–406, doi:10.3189/172756506781828647, 2006.

Kipfstuhl, S., Faria, S. H., Azuma, N., Freitag, J., Hamann, I., Kaufmann, P., Miller, H., Weiler, K. and Wilhelms, F.: Evidence of dynamic recrystallization in polar firn, Journal of Geophysical Research, 114(B5), doi:10.1029/2008JB005583, 2009.

Krischke, A., Oechsner, U. and Kipfstuhl, S.: Rapid Microstructure Analysis of Polar Ice Cores, Optik & Photonik, 10(2), 32–35, doi:10.1002/opph.201500016, 2015.

Lebensohn, R. A.: N-site modeling of a 3D viscoplastic polycrystal using Fast Fourier Transform, Acta Materialia, 49(14), 2723–2737, doi:10.1016/S1359-6454(01)00172-0, 2001.

Lebensohn, R. A., Liu, Y. and Castañeda, P. P.: Macroscopic properties and field fluctuations in model power-law polycrystals: full-field solutions versus self-consistent estimates, Proceedings of the Royal Society of London A: Mathematical, Physical and Engineering Sciences, 460(2045), 1381–1405, doi:10.1098/rspa.2003.1212, 2004.

Lebensohn, R. A., Brenner, R., Castelnau, O. and Rollett, A. D.: Orientation image-based micromechanical modelling of subgrain texture evolution in polycrystalline copper, Acta Materialia, 56(15), 3914–3926, doi:10.1016/j.actamat.2008.04.016, 2008.

Lebensohn, R. A., Montagnat, M., Mansuy, P., Duval, P., Meysonnier, J. and Philip, A.: Modeling viscoplastic behavior and heterogeneous intracrystalline deformation of columnar ice polycrystals, Acta Materialia, 57(5), 1405–1415, doi:10.1016/j.actamat.2008.10.057, 2009.

Lebensohn, R. A., Idiart, M. I., Castañeda, P. P. and Vincent, P.-G.: Dilatational viscoplasticity of polycrystalline solids with intergranular cavities, Philosophical Magazine, 91(22), 3038–3067, doi:10.1080/14786435.2011.561811, 2011.

Lebensohn, R. A., Escobedo, J. P., Cerreta, E. K., Dennis-Koller, D., Bronkhorst, C. A. and Bingert, J. F.: Modeling void growth in polycrystalline materials, Acta Materialia, 61(18), 6918–6932, doi:10.1016/j.actamat.2013.08.004, 2013.

Levi, L. and Ceppi, E. A.: Grain growth in ice, Il Nuovo Cimento C, 5(4), 445–461, doi:10.1007/BF02561650, 1982.

Li, J., Jacka, T. H. and Morgan, V.: Crystal-size and microparticle record in the ice core from Dome Summit South, Law Dome, East Antarctica, Annals of Glaciology, 27(1), 343–348, doi:10.3198/1998AoG27-1-343-348, 1998.

Ligtenberg, S. R. M., Helsen, M. M. and van den Broeke, M. R.: An improved semi-empirical model for the densification of Antarctic firn, The Cryosphere, 5(4), 809–819, doi:10.5194/tc-5-809-2011, 2011.

Lipenkov, V. Y.: Air bubbles and air-hydrate crystals in the Vostok ice core, in Physics of Ice Core Records, pp. 327–358, Hokkaido University Press., 2000.

Llorens, M.-G., Bons, P. D., Griera, A., Gomez-Rivas, E. and Evans, L. A.: Single layer folding in simple shear, Journal of Structural Geology, 50, 209–220, doi:10.1016/j.jsg.2012.04.002, 2013b.

Llorens, M.-G., Bons, P. D., Griera, A. and Gomez-Rivas, E.: When do folds unfold during progressive shear?, Geology, 41(5), 563–566, 2013a.

Llorens, M.-G., Griera, A., Bons, P. D., Roessiger, J., Lebensohn, R., Evans, L. and Weikusat, I.: Dynamic recrystallisation of ice aggregates during co-axial viscoplastic deformation: a numerical approach, Journal of Glaciology, 62(232), 359–377, doi:10.1017/jog.2016.28, 2016a.

Llorens, M.-G., Griera, A., Bons, P. D., Lebensohn, R. A., Evans, L. A., Jansen, D. and Weikusat, I.: Full-field predictions of ice dynamic recrystallisation under simple shear conditions, Earth and Planetary Science Letters, 450, 233–242, doi:10.1016/j.epsl.2016.06.045, 2016b.

Llorens, M.-G., Griera, A., Steinbach, F., Bons, P. D., Gomez-Rivas, E., Jansen, D., Roessiger, J., Lebensohn, R. A. and Weikusat, I.: Dynamic recrystallization during deformation of polycrystalline ice: insights from numerical simulations, Philosophical Transactions of the Royal Society of London A: Mathematical, Physical and Engineering Sciences, 375(2086), doi:10.1098/rsta.2015.0346, 2017.

Lüthi, D., Le Floch, M., Bereiter, B., Blunier, T., Barnola, J.-M., Siegenthaler, U., Raynaud, D., Jouzel, J., Fischer, H., Kawamura, K. and others: High-resolution carbon dioxide concentration record 650,000–800,000 years before present, Nature, 453(7193), 379–382, 2008.

MacGregor, J. A., Fahnestock, M. A., Catania, G. A., Paden, J. D., Prasad Gogineni, S., Young, S. K., Rybarski, S. C., Mabrey, A. N., Wagman, B. M. and Morlighem, M.: Radiostratigraphy and age structure of the Greenland Ice Sheet, Journal of Geophysical Research: Earth Surface, 120(2), 212–241, doi:10.1002/2014JF003215, 2015.

Maeno, N. and Ebinuma, T.: Pressure sintering of ice and its implication to the densification of snow at polar glaciers and ice sheets, The Journal of Physical Chemistry, 87(21), 4103–4110, 1983.

Mainprice, D., Hielscher, R. and Schaeben, H.: Calculating anisotropic physical properties from texture data using the MTEX open-source package, Geological Society, London, Special Publications, 360(1), 175–192, 2011.

Mangeney, A., Califano, F. and Hutter, K.: A numerical study of anisotropic, low Reynolds number, free surface flow for ice sheet modeling, Journal of Geophysical Research: Solid Earth, 102(B10), 22749–22764, doi:10.1029/97JB01697, 1997.

Mathiesen, J., Ferkinghoff-Borg, J., Jensen, M. H., Levinsen, M., Olesen, P., Dahl-Jensen, D. and Svensson, A.: Dynamics of crystal formation in the Greenland NorthGRIP ice core, Journal of Glaciology, 50(170), 325–328, doi:10.3189/172756504781829873, 2004.

Means, W.: Microstructure and micromotion in recrystallization flow of octachloropropane: a first look, Geologische Rundschau, 72(2), 511–528, 1983.

Means, W. D.: The concept of steady-state foliation, Tectonophysics, 78(1–4), 179–199, 1981.

Means, W. D.: Synkinematic microscopy of transparent polycrystals, Journal of Structural Geology, 11(1–2), 163–174, 1989.

Miller, S. L.: Clathrate hydrates of air in Antarctic ice, Science, 165(3892), 489–490, 1969.

Misra, S. and Burg, J.-P.: Mechanics of kink-bands during torsion deformation of muscovite aggregate, Tectonophysics, 548-549, 22–33, doi:10.1016/j.tecto.2012.04.014, 2012.

Miyamoto, A., Shoji, H., Hori, A., Hondoh, T., Clausen, H. B. and Watanabe, O.: Ice fabric evolution process understood from anisotropic distribution of a-axis orientation on the GRIP (Greenland) ice core, Annals of Glaciology, 42(1), 47–52, doi:10.3189/172756405781812501, 2005.

Moldovan, D., Wolf, D. and Phillpot, S. R.: Theory of diffusion-accommodated grain rotation in columnar polycrystalline microstructures, Acta Materialia, 49(17), 3521–3532, doi:10.1016/S1359-6454(01)00240-3, 2001.

Montagnat, M. and Duval, P.: Rate controlling processes in the creep of polar ice, influence of grain boundary migration associated with recrystallization, Earth and Planetary Science Letters, 183(1–2), 179–186, doi:10.1016/S0012-821X(00)00262-4, 2000.

Montagnat, M. and Duval, P.: The viscoplastic behaviour of ice in polar ice sheets: experimental results and modelling, Comptes Rendus Physique, 5(7), 699–708, doi:10.1016/j.crhy.2004.06.002, 2004.

Montagnat, M., Durand, G. and Duval, P.: Recrystallization processes in granular ice, Low Temperature Science, 68(Supplement), 81–90, 2009.

Montagnat, M., Blackford, J. R., Piazolo, S., Arnaud, L. and Lebensohn, R. A.: Measurements and full-field predictions of deformation heterogeneities in ice, Earth and Planetary Science Letters, 305(1–2), 153–160, doi:10.1016/j.epsl.2011.02.050, 2011.

Montagnat, M., Buiron, D., Arnaud, L., Broquet, A., Schlitz, P., Jacob, R. and Kipfstuhl, S.: Measurements and numerical simulation of fabric evolution along the Talos Dome ice core, Antarctica, Earth and Planetary Science Letters, 357–358, 168–178, doi:10.1016/j.epsl.2012.09.025, 2012.

Montagnat, M., Azuma, N., Dahl-Jensen, D., Eichler, J., Fujita, S., Gillet-Chaulet, F., Kipfstuhl, S., Samyn, D., Svensson, A. and Weikusat, I.: Fabric along the NEEM ice core, Greenland, and its comparison with GRIP and NGRIP ice cores, The Cryosphere, 8(4), 1129–1138, doi:10.5194/tc-8-1129-2014, 2014a.

Montagnat, M., Castelnau, O., Bons, P. D., Faria, S. H., Gagliardini, O., Gillet-Chaulet, F., Grennerat, F., Griera, A., Lebensohn, R. A., Moulinec, H., Roessiger, J. and Suquet, P.: Multiscale modeling of ice deformation behavior, Journal of Structural Geology, 61, 78–108, doi:10.1016/j.jsg.2013.05.002, 2014b.

Montagnat, M., Chauve, T., Barou, F., Tommasi, A., Beausir, B. and Fressengeas, C.: Analysis of Dynamic Recrystallization of Ice from EBSD Orientation Mapping, Frontiers in Earth Science, 3, 81, doi:10.3389/feart.2015.00081, 2015.

Moulinec, H. and Suquet, P.: A fast numerical method for computing the linear and nonlinear mechanical properties of composites, Comptes rendus de l'Académie des sciences. Série II, Mécanique, physique, chimie, astronomie, 318(11), 1417–1423, 1994.

Nasello, O., Arena, L. E. and Levi, L.: Grain growth in pure ice, effects of mobile bubbles, Physics and Chemistry of Ice (Maeno, N. and Hondoh, T. Eds). Hokkaido University Press, Hokkaido, 422–427, 1992.

Nasello, O. B., Prinzio, C. L. D. and Guzmán, P. G.: Temperature dependence of "pure" ice grain boundary mobility, Acta Materialia, 53(18), 4863–4869, doi:10.1016/j.actamat.2005.06.022, 2005.

Ng, F. and Jacka, T. H.: A model of crystal-size evolution in polar ice masses, Journal of Glaciology, 60(221), 463–477, doi:10.3189/2014JoG13J173, 2014.

Obbard, R., Baker, I. and Sieg, K.: Using electron backscatter diffraction patterns to examine recrystallization in polar ice sheets, Journal of Glaciology, 52(179), 546–557, doi:10.3189/172756506781828458, 2006.

Oerter, H., Drücker, C., Kipfstuhl, S. and Wilhelms, F.: Kohnen Station the Drilling Camp for the EPICA Deep Ice Core in Dronning Maud Land, Alfred Wegener Institute for Polar and Marine Research & German Society of Polar Research, Bremerhaven., 2009.

Ohno, H., Lipenkov, V. Y., Hondoh, T., Olgaard, D. L. and Evans, B.: Effect of Second-Phase Particles on Grain Growth in Calcite, Journal of the American Ceramic Society, 69(11), C-272–C-277, doi:10.1111/j.1151-2916.1986.tb07374.x, 20041986.

Olgaard, D. L. and Evans, B.: Grain growth in synthetic marbles with added mica and water, Contributions to Mineralogy and Petrology, 100(2), 246–260, doi:10.1007/BF00373591, 1988.

Passchier, C. W. and Trouw, R. A.: Microtectonics, Springer., 2005.

Paterson, W. S. B.: Why ice-age ice is sometimes "soft," Cold Regions Science and Technology, 20(1), 75–98, doi:10.1016/0165-232X(91)90058-O, 1991.

Pattyn, F., Perichon, L., Aschwanden, A., Breuer, B., de Smedt, B., Gagliardini, O., Gudmundsson, G. H., Hindmarsh, R. C. A., Hubbard, A., Johnson, J. V., Kleiner, T., Konovalov, Y., Martin, C., Payne, A. J., Pollard, D., Price, S., Rückamp, M., Saito, F., Souček, O., Sugiyama, S. and Zwinger, T.: Benchmark experiments for higher-order and full-Stokes ice sheet models (ISMIP–HOM), The Cryosphere, 2(2), 95–108, doi:10.5194/tc-2-95-2008, 2008.

Peternell, M., Russell-Head, D. S. and Wilson, C. J. L.: A technique for recording polycrystalline structure and orientation during in situ deformation cycles of rock analogues using an automated fabric analyser, Journal of Microscopy, 242(2), 181–188, doi:10.1111/j.1365-2818.2010.03456.x, 2011.

Petrenko, V. F. and Whitworth, R. W.: Physics of ice, Clarendon Press., 1999.

Pettit, E. C. and Waddington, E. D.: Ice flow at low deviatoric stress, Journal of Glaciology, 49(166), 359–369, doi:10.3189/172756503781830584, 2003.

Piazolo, S., Bons, P., Jessell, M., Evans, L. and Passchier, C.: Dominance of microstructural processes and their effect on microstructural development: insights from numerical modelling of dynamic recrystallization, Geological Society, London, Special Publications, 200(1), 149–170, 2002.

Piazolo, S., Jessell, M. W., Bons, P. D., Evans, L. and Becker, J. K.: Numerical simulations of microstructures using the Elle platform: a modern research and teaching tool, Journal of the Geological Society of India, 75(1), 110–127, doi:10.1007/s12594-010-0028-6, 2010.

Piazolo, S., Wilson, C. J. L., Luzin, V., Brouzet, C. and Peternell, M.: Dynamics of ice mass deformation: Linking processes to rheology, texture, and microstructure, Geochemistry, Geophysics, Geosystems, 14(10), 4185–4194, doi:10.1002/ggge.20246, 2013.

Pimienta, P. and Duval, P.: Rate controlling processes in the creep of polar glacier ice, Le Journal de Physique Colloques, 48(C1), C1-243, 1987.

Poirier, J.-P.: Creep of crystals: high-temperature deformation processes in metals, ceramics and minerals, Cambridge University Press., 1985.

Quinquis, H., Audren, C. L., Brun, J. P. and Cobbold, P. R.: Intense progressive shear in Ile de Groix blueschists and compatibility with subduction or obduction, Nature, 273(5657), 43–45, 1978.

Raj, R. and Ashby, M.: Grain boundary sliding, and the effects of particles on its rate, Metallurgical Transactions, 3(7), 1937–1942, 1972.

Ramsay, J. G. and Huber, M. I.: The techniques of modern structural geology, Academic Press, London., 1987.

Ran, H., Bons, P. D., Wang, G., Steinbach, F., Finch, M., Ran, S., Liang, X. and Zhou, J.: Numerical modelling of the evolution of conglomerate deformation up to high simple-shear strain, Journal of Structural Geology, n.d.

Randle, V.: Microtexture investigation of the relationship between strain and anomalous grain growth, Philosophical Magazine A, 67(6), 1301–1313, doi:10.1080/01418619308225356, 1993.

Rasmussen, S. O., Abbott, P. M., Blunier, T., Bourne, A. J., Brook, E., Buchardt, S. L., Buizert, C., Chappellaz, J., Clausen, H. B., Cook, E., Dahl-Jensen, D., Davies, S. M., Guillevic, M., Kipfstuhl, S., Laepple, T., Seierstad, I. K., Severinghaus, J. P., Steffensen, J. P., Stowasser, C., Svensson, A., Vallelonga, P., Vinther, B. M., Wilhelms, F. and Winstrup, M.: A first chronology for the North Greenland Eemian Ice Drilling (NEEM) ice core, Climate of the Past, 9(6), 2713–2730, doi:10.5194/cp-9-2713-2013, 2013.

Redenbach, C., Särkkä, A., Freitag, J. and Schladitz, K.: Anisotropy analysis of pressed point processes, AStA Advances in Statistical Analysis, 93(3), 237–261, 2009.

Rignot, E., Bamber, J. L., van den Broeke, M. R., Davis, C., Li, Y., van de Berg, W. J. and van Meijgaard, E.: Recent Antarctic ice mass loss from radar interferometry and regional climate modelling, Nature Geosci, 1(2), 106–110, doi:10.1038/ngeo102, 2008.

Roberts, A. P. and Garboczi, E. J.: Elastic Properties of Model Porous Ceramics, Journal of the American Ceramic Society, 83(12), 3041–3048, doi:10.1111/j.1151-2916.2000.tb01680.x, 2000.

Roessiger, J., Bons, P. D., Griera, A., Jessell, M. W., Evans, L., Montagnat, M., Kipfstuhl, S., Faria, S. H. and Weikusat, I.: Competition between grain growth and grain-size reduction in polar ice, Journal of Glaciology, 57(205), 942–948, 2011.

Roessiger, J., Bons, P. D. and Faria, S. H.: Influence of bubbles on grain growth in ice, Journal of Structural Geology, 61, 123–132, doi:10.1016/j.jsg.2012.11.003, 2014.

Russell-Head, D. and Wilson, C. J. L.: Automated fabric analyser system for quartz and ice, in Geological Society of Australia Abstracts, vol. 64, pp. 159–159, Geological Society of Australia., 2001.

Russell-Head, D. S. and Budd, W. F.: Ice-Sheet Flow Properties Derived from Bore-Hole Shear Measurements Combined With Ice-Core Studies, Journal of Glaciology, 24(90), 117–130, doi:10.3198/1979JoG24-90-117-139, 1979.

Ruth, U., Barnola, J.-M., Beer, J., Bigler, M., Blunier, T., Castellano, E., Fischer, H., Fundel, F., Huybrechts, P., Kaufmann, P., Kipfstuhl, S., Lambrecht, A., Morganti, A., Oerter, H., Parrenin, F., Rybak, O., Severi, M., Udisti, R., Wilhelms, F. and Wolff, E.: “EDML1”: a chronology for the EPICA deep ice core from Dronning Maud Land, Antarctica, over the last 150 000 years, Climate of the Past, 3(3), 475–484, doi:10.5194/cp-3-475-2007, 2007.

Samyn, D., Weikusat, I., Svensson, A., Azuma, N., Montagnat, N. and Kipfstuhl, S.: Micro-structure of the NEEM deep ice core: towards quantifying stratigraphic disturbances, EGU General Assembly, http://meetingorganizer.copernicus.org/EGU2011/EGU2011-12563-1.pdf., 2011.

Schmitt, J., Schneider, R., Elsig, J., Leuenberger, D., Lourantou, A., Chappellaz, J., Köhler, P., Joos, F., Stocker, T. F., Leuenberger, M. and Fischer, H.: Carbon Isotope Constraints on the Deglacial CO2 Rise from Ice Cores, Science, 336(6082), 711–714, doi:10.1126/science.1217161, 2012.

Schulson, E. M. and Duval, P.: Creep and fracture of ice, Cambridge University Press Cambridge., 2009.

Schwander, J. and Stauffer, B.: Age difference between polar ice and the air trapped in its bubbles, Nature, 311(5981), 45–47, doi:10.1038/311045a0, 1984.

Seddik, H., Greve, R., Placidi, L., Hamann, I. and Gagliardini, O.: Application of a continuum-mechanical model for the flow of anisotropic polar ice to the EDML core, Antarctica, Journal of Glaciology, 54(187), 631–642, doi:10.3189/002214308786570755, 2008.

Sheldon, S. G., Steffensen, J. P., Hansen, S. B., Popp, T. J. and Johnsen, S. J.: The investigation and experience of using ESTISOL 240 and COASOL for ice-core drilling, Annals of Glaciology, 55(68), 219–232, doi:10.3189/2014AoG68A036, 2014.

Shepherd, A., Ivins, E. R., A, G., Barletta, V. R., Bentley, M. J., Bettadpur, S., Briggs, K. H., Bromwich, D. H., Forsberg, R., Galin, N., Horwath, M., Jacobs, S., Joughin, I., King, M. A., Lenaerts, J. T. M., Li, J., Ligtenberg, S. R. M., Luckman, A., Luthcke, S. B., McMillan, M., Meister, R., Milne, G., Mouginot, J., Muir, A., Nicolas, J. P., Paden, J., Payne, A. J., Pritchard, H., Rignot, E., Rott, H., Sørensen, L. S., Scambos, T. A., Scheuchl, B., Schrama, E. J. O., Smith, B., Sundal, A. V., van Angelen, J. H., van de Berg, W. J., van den Broeke, M. R., Vaughan, D. G., Velicogna, I., Wahr, J., Whitehouse, P. L., Wingham, D. J., Yi, D., Young, D. and Zwally, H. J.: A Reconciled Estimate of Ice-Sheet Mass Balance, Science, 338(6111), 1183, doi:10.1126/science.1228102, 2012.

Shoji, H. and Higashi, A.: A deformation mechanism map of ice, Journal of Glaciology, 21(85), 419–427, doi:10.3198/1978JoG21-85-419-427, 1978.

Shoji, H. and Langway, C. C.: Air hydrate inclusions in fresh ice core, Nature, 298(5874), 548–550, doi:10.1038/298548a0, 1982.

Skemer, P., Sundberg, M., Hirth, G. and Cooper, R.: Torsion experiments on coarse-grained dunite: implications for microstructural evolution when diffusion creep is suppressed, Geological Society, London, Special Publications, 360(1), 211–223, 2011.

Smith, C. S.: Some elementary principles pf polycrystalline microstructure, Metallurgical Reviews, 9(1), 1–48, doi:10.1179/mtlr.1964.9.1.1, 1964.

Sornette, A., Davy, P. and Sornette, D.: Fault growth in brittle-ductile experiments and the mechanics of continental collisions, Journal of Geophysical Research: Solid Earth, 98(B7), 12111–12139, 1993.

Stauffer, B., Schwander, J. and Oeschger, H.: Enclosure Of Air During Metamorphosis Of Dry Firn To Ice, Annals of Glaciology, 6(1), 108–112, doi:10.3198/1985AoG6-1-108-112, 1985.

Steinbach, F., Bons, P. D., Griera, A., Jansen, D., Llorens, M.-G., Roessiger, J. and Weikusat, I.: Strain localization and dynamic recrystallization in the ice–air aggregate: a numerical study, The Cryosphere, 10(6), 3071–3089, doi:10.5194/tc-10-3071-2016, 2016.

Steinemann, S.: Flow and recrystallization of ice, IASH Publ, 39, 449–462, 1954.

Stephenson, P.: Some considerations of snow metamorphism in the Antarctic ice sheet in the light of ice crystal studies, Physics of Snow and Ice, 1(2), 725–740, 1967.

Suquet, P., Moulinec, H., Castelnau, O., Montagnat, M., Lahellec, N., Grennerat, F., Duval, P. and Brenner, R.: Multi-scale modeling of the mechanical behavior of polycrystalline ice under transient creep, Procedia IUTAM, 3, 76–90, doi:10.1016/j.piutam.2012.03.006, 2012.

Svensson, A., Nielsen, S. W., Kipfstuhl, S., Johnsen, S. J., Steffensen, J. P., Bigler, M., Ruth, U. and Röthlisberger, R.: Visual stratigraphy of the North Greenland Ice Core Project (NorthGRIP) ice core during the last glacial period, Journal of Geophysical Research: Atmospheres, 110(D2), n/a-n/a, doi:10.1029/2004JD005134, 2005.

Takeda, Y.-T. and Griera, A.: Rheological and kinematical responses to flow of two-phase rocks, Tectonophysics, 427(1-4), 95–113, doi:10.1016/j.tecto.2006.03.050, 2006.

Tanner, P. W. G.: The flexural-slip mechanism, Journal of Structural Geology, 11(6), 635–655, doi:10.1016/0191-8141(89)90001-1, 1989.

Theile, T., Löwe, H., Theile, T. C. and Schneebeli, M.: Simulating creep of snow based on microstructure and the anisotropic deformation of ice, Acta Materialia, 59(18), 7104–7113, doi:10.1016/j.actamat.2011.07.065, 2011.

Thorsteinsson, T.: Textures and fabrics in the GRIP ice core, in relation to climate history and ice deformation, Berichte zur Polarforschung (Reports on Polar Research), 205, 1996.

Thorsteinsson, T.: Fabric development with nearest-neighbor interaction and dynamic recrystallization, Journal of Geophysical Research: Solid Earth, 107(B1), ECV-3-1–ECV 3-13, doi:10.1029/2001JB000244, 2002.

Thorsteinsson, T. and Waddington, E. D.: Folding in strongly anisotropic layers near ice-sheet centers, Annals of Glaciology, 35(1), 480–486, doi:10.3189/172756402781816708, 2002.

Thorsteinsson, T., Kipfstuhl, J. and Miller, H.: Textures and fabrics in the GRIP ice core, Journal of Geophysical Research: Oceans, 102(C12), 26583–26599, doi:10.1029/97JC00161, 1997.

Treagus, S. H. and Lan, L.: Deformation of square objects and boudins, Journal of Structural Geology, 26(8), 1361–1376, doi:10.1016/j.jsg.2003.12.002, 2004.

Treverrow, A., Budd, W. F., Jacka, T. H. and Warner, R. C.: The tertiary creep of polycrystalline ice: experimental evidence for stress-dependent levels of strain-rate enhancement, Journal of Glaciology, 58(208), 301–314, doi:10.3189/2012JoG11J149, 2012.

Trimby, P. W., Prior, D. J. and Wheeler, J.: Grain boundary hierarchy development in a quartz mylonite, Journal of Structural Geology, 20(7), 917–935, doi:10.1016/S0191-8141(98)00026-1, 1998.

Trimby, P. W., Drury, M. R. and Spiers, C. J.: Misorientations across etched boundaries in deformed rocksalt: a study using electron backscatter diffraction, Journal of Structural Geology, 22(1), 81–89, doi:10.1016/S0191-8141(99)00126-1, 2000.

Tullis, J., Dell'Angelo', L. and Yund, R. A.: Ductile Shear Zones from Brittle Precursors in Feldspathic Rocks: the Role of Dynamic Recrystallization, in The Brittle-Ductile Transition in Rocks, pp. 67–81, American Geophysical Union. [online] Available from: http://dx.doi.org/10.1029/GM056p0067, 1990.

Uchida, T., Duval, P., Lipenkov, V. Y., Hondoh, T., Mae, S. and Shoji, H.: Brittle zone and air-hydrate formation in polar ice sheets, Memoirs of National Institute of Polar Research. Special issue, 49, 298–305, 1994.

Uchida, T., Yasuda, K., Oto, Y., Shen, R. and Ohmura, R.: Natural supersaturation conditions needed for nucleation of air-clathrate hydrates in deep ice sheets, Journal of Glaciology, 60(224), 1111–1116, doi:10.3189/2014JoG13J232, 2014.

Urai, J., Means, W. and Lister, G.: Dynamic recrystallization of minerals, Mineral and Rock Deformation: Laboratory Studies: The Paterson Volume, 161–199, doi:10.1029/GM036p0161, 1986.

Urai, J. L.: Water assisted dynamic recrystallization and weakening in polycrystalline bischofite, Tectonophysics, 96(1), 125–157, doi:10.1016/0040-1951(83)90247-0, 1983.

Urai, J. L.: Development of microstructure during deformation of carnallite and bischofite in transmitted light, Tectonophysics, 135(1–3), 251–263, 1987.

Van Der Veen, C. J. and Whillans, I.: Flow laws for glacier ice: comparison of numerical predictions and field measurements, Journal of Glaciology, 36(124), 324–339, doi:10.3189/002214390793701372, 1990.

Vaughan, D. G., Comiso, J. C., Allison, I., Carrasco, J., Kaser, G., Kwok, R., Mote, P., Murray, T., Paul, F., Ren, J., Rignot, E., Solomina, O., Steffen, K. and Zhang, T.: Observations: Cryosphere, in Climate Change 2013: The Physical Science Basis. Contribution of Working Group I to the Fifth Assessment Report of the Intergovernmental Panel on Climate Change, edited by T. F. Stocker, D. Qin, G. K. Plattner, M. Tignor, S. K. Allen, J. Boschung, A. Nauels, Y. Xia, B. V, and P. M. Midgley, Cambridge University Press, Cambridge, United Kingdom and New York, NY, USA., 2013.

Veen, C. J. van der and Whillans, I. M.: Development of fabric in ice, Cold Regions Science and Technology, 22(2), 171–195, doi:10.1016/0165-232X(94)90027-2, 1994.

Waddington, E. D., Bolzan, J. F. and Alley, R. B.: Potential for stratigraphic folding near ice-sheet centers, Journal of Glaciology, 47(159), 639–648, 2001.

WAIS Divide Project Members: Onset of deglacial warming in West Antarctica driven by local orbital forcing, Nature, 500(7463), 440–444, doi:10.1038/nature12376, 2013.

Wang, Y., Thorsteinsson, T., Kipfstuhl, J., Miller, H., Dahl-Jensen, D. and Shoji, H.: A vertical girdle fabric in the NorthGRIP deep ice core, North Greenland, Annals of Glaciology, 35(1), 515–520, doi:10.3189/172756402781817301, 2002.

Weaire, D. and Rivier, N.: Soap, cells and statistics-random patterns in two dimensions, Contemporary Physics, 25(1), 59–99, doi:10.1080/00107518408210979, 1984.

Weertman, J.: Creep of ice, Physics and chemistry of ice, 320–337, 1973.

Weikusat, I. and Kipfstuhl, S.: Crystal c-axes (fabric) of ice core samples collected from the NEEM ice core, Pangaea Data Publisher for Earth & Environmental Science, doi:10.1594/PANGAEA.744004, 2010.

Weikusat, I., Kipfstuhl, S., Azuma, N., Faria, S. H. and Miyamoto, A.: Deformation microstructures in an Antarctic ice core (EDML) and in experimentally deformed artificial ice, Low Temperature Science, 68(Supplement), 115–123, 2009a.

Weikusat, I., Kipfstuhl, S., Faria, S. H., Azuma, N. and Miyamoto, A.: Subgrain boundaries and related microstructural features in EDML (Antarctica) deep ice core, Journal of Glaciology, 55(191), 461–472, doi:10.3189/002214309788816614, 2009b.

Weikusat, I., De Winter, D. A. M., Pennock, G. M., Hayles, M., Schneijdenberg, C. T. W. M. and Drury, M. R.: Cryogenic EBSD on ice: preserving a stable surface in a low pressure SEM, Journal of Microscopy, 242(3), 295–310, doi:10.1111/j.1365-2818.2010.03471.x, 2011a.

Weikusat, I., Miyamoto, A., Faria, S. H., Kipfstuhl, S., Azuma, N. and Hondoh, T.: Subgrain boundaries in Antarctic ice quantified by X-ray Laue diffraction, Journal of Glaciology, 57(201), 111–120, doi:10.3189/002214311795306628, 2011b.

Weikusat, I., Kuiper, E.-J. N., Pennock, G. M., Kipfstuhl, S. and Drury, M. R.: EBSD in Antarctic and Greenland Ice, Solid Earth Discussions, 2017, 1–35, doi:10.5194/se-2017-12, 2017b.

Weikusat, I., Jansen, D., Binder, T., Eichler, J., Faria, S. H., Wilhelms, F., Kipfstuhl, S., Sheldon, S., Miller, H., Dahl-Jensen, D. and Kleiner, T.: Physical analysis of an Antarctic ice core-towards an integration of micro- and macrodynamics of polar ice, Philos Transact A Math Phys Eng Sci, 375(2086), doi:10.1098/rsta.2015.0347, 2017a.

White, S.: Geological significance of recovery and recrystallization processes in quartz, Tectonophysics, 39(1–3), 143–170, doi:10.1016/0040-1951(77)90093-2, 1977.

Wilkinson, D. S. and Ashby, M. F.: Pressure sintering by power law creep, Acta Metallurgica, 23(11), 1277–1285, doi:10.1016/0001-6160(75)90136-4, 1975.

Williams, P. F. and Price, G. P.: Origin of kinkbands and shear-band cleavage in shear zones: an experimental study, Journal of Structural Geology, 12(2), 145–164, doi:10.1016/0191-8141(90)90001-F, 1990.

Wilson, C. J. and Peternell, M.: Ice deformed in compression and simple shear: control of temperature and initial fabric, Journal of Glaciology, 58(207), 11–22, 2012.

Wilson, C. J., Russell-Head, D. S. and Sim, H. M.: The application of an automated fabric analyzer system to the textural evolution of folded ice layers in shear zones, Annals of Glaciology, 37(1), 7–17, 2003.

Wilson, C. J. L.: Experimental folding and fabric development in multilayered ice, Tectonophysics, 78(1), 139–159, doi:10.1016/0040-1951(81)90011-1, 1981.

Wilson, C. J. L.: Foliation and strain development in ice-mica models, Tectonophysics, 92(1), 93–122, doi:10.1016/0040-1951(83)90086-0, 1983.

Wilson, C. J. L.: Deformation induced recrystallization of ice: The application of in situ experiments, Washington DC American Geophysical Union Geophysical Monograph Series, 36, 213–232, doi:10.1029/GM036p0213, 1986.

Wilson, C. J. L., Burg, J. P. and Mitchell, J. C.: The origin of kinks in polycrystalline ice, Tectonophysics, 127(1), 27–48, doi:10.1016/0040-1951(86)90077-6, 1986.

Wolovick, M. J., Creyts, T. T., Buck, W. R. and Bell, R. E.: Traveling slippery patches produce thickness-scale folds in ice sheets, Geophysical Research Letters, 41(24), 8895–8901, doi:10.1002/2014GL062248, 2014.

Zwally, H. J. and Li, J.: Seasonal and interannual variations of firn densification and ice-sheet surface elevation at the Greenland summit, Journal of Glaciology, 48(161), 199–207, doi:10.3189/172756502781831403, 2002.

Appendix

Introduction to the appendix

Years of code development created a complex set of Elle modules and codes for modelling the dynamic interaction of various deformation and recrystallisation processes for poly- and single-phase polycrystalline aggregates such as the ice- or ice-air aggregate. In addition, numerous pre- or post-processing scripts exists apart from the ones provided by the standard Elle release. Thus, understanding the structure and handling of this complex assembly is time consuming. At this point of code evolution, there is a necessity to properly summarise the most basic parts and provide an easier start for following researchers.

This appendix is designed to highlight and explain new developments in numerical modelling of deformation and recrystallisation in poly- and single-phase polycrystalline materials such as the ice- or ice-air aggregate. Part of the new developments have been applied to the research questions of this thesis. The application of other new developments remains part of future research. Furthermore, this appendix is designed as a guideline for future researchers using the Elle / VPFFT numerical modelling approach. Additionally, a digital appendix is provided that contains codes, scripts and instructions on Elle / VPFFT used and developed in the course of this thesis. Besides, the simulation input for all simulations performed for this thesis is provided.

A.1 Summary of new developments

This thesis made several developments within the Elle / VPFFT approach for modelling deformation and recrystallisation in poly- and single-phase polycrystalline materials. All such codes are found in the digital appendix. The prefix “FS” (initials of Florian Steinbach) is used to indicate that the code has been created or at least changed in the course of this thesis. A summary of the new developments is given in the Tables below. The handling of the codes is explained in the following appendix chapters, in particular chapter A.3 that provides a tutorial for beginners in numerical modelling with the Elle / VPFFT approach. The reader is also referred to research papers by Maria-Gema Llorens, Florian Steinbach, Jens Roessiger, Albert Griera and Ricardo Lebensohn.

The most significant development can probably be summarised as the creation of a robust and working setup for numerically modelling the evolution of a polyphase aggregate (such as ice-air) under deformation and recrystallisation. This takes into account dislocation creep, grain boundary migration driven by surface- and strain energy reduction and rotation recrystallisation including the evolution from dislocation walls over subgrain boundaries to new high angle grain boundaries. In the course of this, comprehensive topology checks were necessary, which is why the new code “FS_topocheck” was

created. It is also provided as a built-in version to add to existing Elle modules. Besides, a considerable amount of code was checked for errors and debugged and further code-comments have been added.

Some developments have not yet been applied in published literature and are not as well-tested as the established ones. Examples for such developments are a suggestion for a new recovery approach, the creation of a set of modules called “strain -analysis” and an approach to assume grain boundary sliding during the simulations. Additionally, several utilities and small routines have been created, mainly to facilitate daily life, but also to allow some pre- or post-processing steps.

What follows is a set of tables summarising new developments and highlighting the basic purpose of each module or code.

Table A.1.1 Summary of new developments in VPFFT and Elle – VPFFT conversion codes

Name	Short description	What is new?
VPFFT code (Fortran)	The basic VPFFT by Ricardo Lebensohn (Lebensohn, 2001)	Possible IDs for Fourier points were set to more than 10^9 digits (allowing 1024x1024 simulations)
FS_elle2fft	Converting Elle file to input for VPFFT code. Resetting regular square grid of *unodes*.	Running without storing *flynn* information: Output file “all.out” will not contain bulk information for every *flynn*. This improves computation time
FS_fft2elle	Converting VPFFT result in Elle file again by applying incremental strain field to *bnodes* and *unodes*. Setting VPFFT output properties to *unodes* (new orientations, dislocation densities). Updating passive marker grid information in U_FINITE_STRAIN	Repaired bugs in updating passive marker grid information (no errors on box edges, also possible for pure shear) and soring the information in U_FINITE_STRAIN Detecting *unodes* that changed *flynns* and updating their properties correctly
FS_fft2elle_strainanalysis	See FS_fft2elle Compute incremental strain tensors for each *unode* and use those to update *bnode*, *unode* and passive marker positions. Store such tensors in separate text file for possible post-processing with “FS_strainanalysis” - codes	The ability to compute and use incremental strain tensors from each *unode* (see column to the left) This version is about 10-20 times faster than the old FS_fft2elle, but has not yet been used in the studies presented in this thesis

Table A.1.2 Summary of new developments in recrystallisation codes

Name	Short description	What is new?
FS_gbm_pp_fft	Polyphase grain boundary migration driven by surface- and stored strain energy reduction Based on the codes presented by Becker et al. (2008) and Roessiger et al. (2014) Using J. Roessiger's area energy term for conservation of areas / masses	Ability to use strain energy driving force for polyphase aggregates Possibility to scale dislocation line energy for non-basal activity (see line 25 in FS_gbm_pp_fft.elle.cc) Storing velocity, surface- and strain-energy gradients of each *bnode* before their movement. Stored in node attributes A, B, C. See lines 822-839 in FS_gbm_pp_fft.elle.cc). For this I added the new function "ElleGetNodeAttribute" to basecode. See "nodesP.cc" (line 1218) in "FS_ElleChanges/basecode" in digital appendix Including a full topology check after each step. See the description of "FS_topocheck" Writing a file called "UnodeOriChangeGBM.txt" that indicates which *unodes* changed their host flynn and what their previous and afterwards orientation is Various debugging
FS_recovery	Recovery code, based on misorientation minimisation. As described in Borthwick et al. (2014) or Llorens et al. (2014a). See suggestion for new recovery approach in chapter A.4.1	Possibility to exclude phases such as air or melt (phases where no recovery will happen) Error in implementation of Read-Shockley equation was repaired (line 802 in FS_recovery.elle.cc)
subgrain_unodes_alb	Step 1 of polygonisation, by Albert Griera. See chapter A.2.3.3 for more information. In each *flynn*: Detecting clusters of *unodes* within a certain misorientation	Included the possibility to exclude a phase. Polygonisation cannot happen in air or melt Everything else as in A. Griera's code, therefore no "FS" prefix
u2f_sgb_alb	Step 2 of polygonisation, by Albert Griera. See chapter A.2.3.3 for more information Using the clusters and creating a *flynn* around each cluster. Can produce duplicate *bnodes*, important to run a topology check afterwards	Phase exclusion like in "subgrain_unodes_alb". Tracking of how often a grain is split by polygonisation Everything else as in A. Griera's code, therefore no "FS" prefix

Table A.1.3 Summary of new utilities for pre- or post-processing Elle / VPFFT simulations

Name	Short description	What is new?
FS_create_plotlayer	Can create a new Elle file that is only used for plotting. This file will potentially only contain the *unodes* of a particular phase (such as ice *unodes*) and can be scaled up or down There is also the possibility to set *unode* properties of one phase (e.g. air) to a dummy value for plotting	The whole code
FS_elle2mtex	Convert an Elle file into a text file that can be read with the MATLAB toolbox MTEX. This can be useful when plotting pole figures or processing orientation data. The code needs the *unode* attributes U_VISCOSITY and U_EULER_3	The whole code
FS_euler3random	Creating an either random set of Euler angles in *flynns* or *unodes* or a single maximum distribution with a given cone angle. Contains also code to shift any set of 3 Euler angles to the interval required by VPFFT code (see comments in code's "ProcessFunction")	The whole code
FS_flynn2unode_attribute	Shifting any *flynn* attribute to the overlying *unodes*: Handy to use this after every VPFFT step to update phase properties in *unodes*	The whole code
importFFTdata_florian	Transfer information from tex.out in Elle file after using any fft2elle code	Mostly an update of the properties that are loaded, but no really new developments
FS_plot_ugrid	Plot a deformed grid in passive markers assuming either initially horizontal, vertical or diagonal lines The output is a post-script (*.ps) file	Compatible with the output of FS_fft2elle. Possible to use it with pure- or simple-shear setups Various debugging and improvements in performance Added comments to code
FS_scalefile	Scale any modelling box and all containing data structures (*bnodes*, *unodes*) by a certain factor in x- and y-direction. Also, it is possible to scale a deformed box back to 1x1.	The whole code
FS_splitflynn	Split *flynn* X along *bnodes* Y and Z. A very crude way to fix topology errors with *flynns* wrapping on both sides of a box	The whole code

Table A.1.3, continued

Name	Short description	What is new?
FS_statistics	It was not possible to use the Elle module for statistics with polyphase simulations. Therefore, this module was created containing a number of statistical or post-processing operations: Grain sizes and area fractions (bulk and individual) Reading and properly storing data from "all.out" files (stress, strain tensors and bulk slip system activities) Calculating localisation factors (see PAPER I, section 2.7.1) Calculation of perimeter ratios Slip system activities from individual *unodes* (possible to exclude air)	The whole code

FS_topocheck	Dealing with topological issues was most important when further developing codes to higher complexity. Therefore, a whole module for topology checks was created.
	This module is also available as a built-in version to use it in other Elle modules (as done with GBM code)
	The following topological checks are performed (also see function "TopologyChecks" in "FS_topocheck.elle.cc" from line 30 on):
	- Detection of island *flynns*
	- Detecting and deleting *flynns* below the resolution threshold
	- Detect and solve a situation where two *bnode* positions coincide
	- All "standard" topology checks found in elle_gg
	- "check angle": Check for "too pointy" *flynn* corners
	- Important: "CheckIfFlynnNeedSplit", line 99 in FS_topocheck.elle.cc:
	  - Checking if two non-neighbouring *bnodes* are too close together and resolving this situation by merging them and splitting the host-*flynn* into two *flynns*.
	  - This was necessary to allow grain dissection (PAPER II)
	- Updating *unodes* that changed their host *flynn* by e.g. GBM or deformation
		The whole code.
		Topology checks from elle_gg and checkangle were applied as it was. Deletion of small *flynns* was created by Jens Roessiger and further developed within this thesis

Table A.1.4 Summary of the development of a set of modules called "strain analysis" to obtain information such as strain tensors, vorticity, strain ellipse data and related properties for each *unode*. See chapter A.4.4 for more information. Applications of these codes have not yet been published.

Name	Short description	What is new?
FS_postprocess_strainanalysis	Requires a set of files containing incremental strain tensors for each *unode* from VPFFT step N to P. (N is not necessarily 1 and P is not necessarily the last step of the simulation. Uses them to calculate the finite strain tensor from step N to P and stores this data in an output Elle file It is required to run the simulation first and use FS_fft2elle_strainanalysis	The whole code
FS_plot_strainanalysis	Requires the output Elle file of FS_postprocess_strainanalysis Creates a user-defined regular square grid of *unodes*. On this grid, it will plot the properties such as strain ellipse data and vorticity calculated for every passive marker *unode*. This way, it is easier to visualise the data using showelle	The whole code
FS_plot_stretchdir	Used with the output Elle file of FS_plot_strainanalysis Plots a small line for every *unode* in the orientation of maximum stretching (long strain ellipse axis). Angles are indicated from positive x-axis, counter-clockwise. The length of the lines can be constant or depend on the strain ellipse ratio The output is a post-script (*.ps) file	The whole code

Table A.1.5 Summary of other the developments in the course of this thesis. More information can be found in chapter A.4.

Name	Short description	What is new?
FS_DDEnergyRecovery	A suggestion for a new recovery approach, created in cooperation with Paul Bons and Albert Griera. The "old" approach assumed each *unode* is a small crystallite that changes its surface energy as a function of misorientation (Read-Shockley equation). This approach did not allow scaling the rotation of a *unode* into lower energy configuration to the numerical time step. The new approach is based on strain energies from dislocation densities. Using a simple model for dislocation densities from misorientations, it calculates the strain energy gradient from rotating a *unode* and, with the help of this, its angular velocity. For this, a theoretical "rotational viscosity" is required. More information is found in chapter A.4.1.	The basic framework is from the "old" recovery code, the rest is new.
FS_getmisoriDD	Calculating dislocation densities from misorientations using the model that is also used in "FS_DDEnergyRecovery"	Based on a "misori2dd" function provided by Lynn Evans, but re-coded
FS_gg_potts and **FS_gg_potts3D**	Two- and three-dimensional Potts models for grain growth. The 3D model is not based on Elle. In particular, the 3D model can help preparing 3D VPFFT simulations in the future. The model is based on the description of Potts models in Bons et al. (2008, pp. 25).	The whole code
FS_GrainBoundarySliding	A simple approach towards assuming grain boundary sliding in a VPFFT simulation. The idea is to introduce a "boundary phase" on *unodes* and setting this phase as an isotropic, yet soft material. Actually there are two modules, one initiating and one removing the "boundary phase" from *unodes*. They are called "FS_startGBS" and "FS_endGBS". Especially the treatment of the boundary phase in "FS_endGBS" is critical and needs special care for future use.	The whole code

A.2 Handling of Elle / VPFFT related codes

A.2.1 Introducing the multi-process modelling setup

Dynamic systems such as the microstructure evolution under deformation and recrystallisation result from the interplay of various physical and potentially also chemical mechanisms. The philosophy of Elle allows modelling such multi-process systems using a standalone code for each contributing physical process. These codes are called “modules” or also “processes” in Elle. Consecutively running these processes, each for a short numerical time step effectively allows modelling a multi-process system that is impossible or inadequately complex to implement in a single governing equation or numerical modelling code. The advantage of this procedure is that certain processes can be added to- or removed from the numerical setup.

The general sequence of Elle processes performed for many simulations presented in this thesis is outlined in PAPER I (section 2.5 and Fig. 2). Additionally, conversion and pre- or post-processing processes were running together with the deformation and recrystallisation processes. In what follows, the handling of each of these codes is briefly explained. It is recommended to read about the “direct launching of experiments” in the Elle book (Bons et al., 2008, pp. 362-363). For more information on the mentioned codes, the reader is also referred to chapters A.1 and the tutorial in chapter A.3. Other codes (not used within the deformation and recrystallisation setup yet) are explained in chapter A.4. More information is also found in “readme”-files that are stored with every code found in the folder “*FS_Codes/*” in the digital appendix.

A.2.2 VPFFT and conversion processes

FS_elle2fft -i filename.elle -u A B C –n

A. *Unode Dimension (128,256 etc...)*
B. *Hardly used, do not input anything for the moment*
C. *Hardly used, do not input anything for the moment*

Explanation: Reading an Elle file, transferring its *unodes* in a regular square grid again (if necessary) and writing VPFFT input files (*make.out* indicating orientations for each *unode* or Fourier point and *temp.out* containing the initial model box size and simple shear offset). The code requires the *flynn* attribute VISCOSITY with a phase attribute ID counted from 1 to the maximum number of phases. If no Euler angles are active in *unodes*, the code first transfers *flynn* Euler angles to undoes. There is also FS_elle2fft_onlyunodes, it is working the same way, but *unode* attribute U_VISCOSITY is phase indicative and it directly reads Euler angles from *unodes*.

FS_fft2elle -i filename.elle -u A B C –n

A. *Set to 1 to add dislocation densities from tex.out, set to 0 not to add them. Default: 0*
B. *Do not update dislocation densities from phase = B, set to 0 not to use this. Default: 0 (recommended to leave at 0 as code will run quicker and option is not necessary at this stage)*
C. *Set to dimension of unodes (128, 256, etc.) to also update passive marker points stored in the unode attribute U_FINITE_STRAIN. Default: 0 (means no update*)

Explanation: Requires the output Elle file of "elle2fft" as input. Reads the output files (*.out) from the VPFFT code and writes a new Elle file with updated *unode* and *bnode* positions and updates Euler angles in *unodes*. If used switches this on, it also updates passive marker positions and dislocation densities.

FFT_vs128 and FFT_vs256: The VPFFT codes

Explanation: The VPFFT code can simply be started by typing FFT_vsXXX, where XXX denotes the dimension of *unodes* (e.g. FFT_vs128, FFT_vs256, etc.). The code needs to be re-compiled when the user wants to create a new executable for a different number of *unodes* (see explanations in "readme"-file and "*ppc.dim*" found with the codes in digital appendix). Before running the code, make sure you have created the correct input files using *FS_elle2fft* or whatever script. This code was hardly changed in the course of this thesis.

A.2.3 Recrystallisation processes

Grain boundary migration

FS_gbm_pp_fft -i filename.elle -u A B C D E –s Stages –f Frequency n (All defaults = 0)

Explanation: The polyphase GBM code is a large code that descended from the code by Jens Becker (Becker et al., 2008) and Jens Roessiger (Roessiger et al., 2014). The code requires the file "*phase_db.txt*" to be in the directory from where the code is called. Other changes can be made in the beginning of "*FS_gbm_pp_fft.elle.cc*". E.g. scaling the dislocation line energy to non-basal activity (as done for simulations in PAPER II) can be switched on by setting the Boolean variable in line 25 to "true". The GBM code automatically performs all topology checks of "*FS_topocheck*" after each time-step (see line 563 in "*FS_gbm_pp_fft.elle.cc*" and the topology-check built-in codes. This version of the GBM code produced another output file called "*UnodeOriChangeGBM.txt*" indicating which undoes changed their host *flynn* during GBM and what their previous and new orientation is.

See the code in "*FS_Codes/FS_recrystallisation/FS_gbm_pp_fft/GBM_ReduceMobInTheMiddle/*": This slightly changed GBM code is able to change the intrinsic grain-boundary mobilities in the middle 3rd of the model box by a certain factor (factor > 0 increase mobility, factor < 0 decrease mobility). This

code has another input property (-u A B C D E **F**): Set "**F**" to the desired factor. By default, *F=1* (no change in mobility).

A. *A=1: Also use diagonal trial positions, A=0: Do not use them*
B. *The "a-factor" for dislocden redistribution (never used it, always set to to 0)*
C. *Logscreen: Type 1 to switch random choice of bnodes of and to access them always in the same order (handy only for debugging)*
D. *Start Timestep: Timesteps already performed in input file (Set to > 0 if you already did some GBM to this file, if D ≠ 0 use initial_stuff.txt file!!)*
E. *ExcludePhase: Indicate any phase which inner boundaries are unimportant, e.g. air-air boundaries. Type VISCOSITY as phase ID indicator to use it, type 0 not to use it*

Recovery

FS_recovery -i filename.elle -u A B C D E –s Stages –f Frequency –n (All defaults = 0)

Explanation: The code requires the file "symmetry.symm" to be in the directory from where the code is called. It contains symmetry information for the "non-excluded" phase. There is a new suggestion for a recovery code that is scaled to a numerical time and assumes strain energy gradients as driving forces for re-orientation of *unodes*. See chapter A.4.1 for more information.

A. *Important: Set high angle grain boundary threshold angle in degrees, e.g. 15°, 5°. No recovery any more if misorientation is higher.*
B. *Set ID of phase (flynn VISC.) which should be excluded (e.g. useful for air), set 0 for no exclusion*
C. *Logscreen: Switch off random picking of flynns, unodes etc. by setting this to 1 (handy only for debugging)*
D. *Set initial rotation mobility, 0 is default but will lead to NO rotation → Usually kept at 500 as this recovery code is not properly scaled to numerical time.*
E. *Set initial start step (steps already performed in input file), 0 is default*

Polygonisation

The polygonisation process is often also called "nucleation" within some codes, scripts etc. However, the process can actually be regarded as the final step of rotation recrystallisation, where a highly misoriented subgrain evolves in a new high-angle boundary. In Elle, this means adding new *bnodes* and at least one new *flynn*. The polygonisation process is composed of two single processes:

1. Detection of *unode* clusters that are all below a certain misorientation (*subgrain_unodes_alb*)

2. Form *flynns* around the detected clusters using Voronoi decomposition (*u2f_sgb_alb*)

The codes do not have a "FS_" prefix, as in the course of this thesis, only minor changes have been made (see chapter A.1). The codes are largely in the state that was created by Albert Griera.

For both processes, it is important to use" –s 1 –f 1 –n" !

<u>IMPORTANT</u>: Every polygonisation process (composed of actually two single processes) MUST FOLLOW A STEP OF FS_topocheck in order to remove duplicate *bnodes*.

subgrain_unodes_alb -i filename.elle -u A B C D –s 1 –f 1 –n

Explanation: The 1st part of the polygonisation process is searching for subgrains by checking misorientation to neighbour undoes (if misorientation <= high angle grain boundary angle → new subgrain cluster). The subgrain ID is stored in U_ATTRIB_B and used in the following process

A. *Set unode dimension, e.g. 128, 256 etc., default is 256*
B. *Set high-anlge grain boundary angle in degrees, default is 5°*
C. *Added in the course of the thesis: Set the phase ID of the phase that should be excluded (no nucleation for this phase), default is C=0 (no phase is excluded)*
D. *Set the neighbour order for the search for kernel average misorientation, default D=1*

u2f_sgb_alb -i filename.elle -u A B C D -s 1 –f 1 –n

Explanation: The 2nd part of the polygonisation process is taking the result from the previous code and sets new *flynns* from subgrains that are stored in undoes using Voronoi tessellation. If a new *flynn* is too small or would result in topological errors (*flynn* in a *flynn*), the new *flynn* is not created. Therefore, it is useful to run the two polygonisation process for more than one step (but always use FS_topocheck after every step). Do this although actually one step should be sufficient since it is not a real "physical process". This code creates an output Elle file called "*u2f.elle*" and another one called "*u2f001.elle*", using "*u2f.elle*" is enough.

A. *Set unode dimension, e.g. 128, 256 etc., default is 256*
B. *Set minimum number of undoes in a new flynn. If there are less unodes, flynn is not created (default is 10, but by experience B=5 is better)*
C. *Set to 1 to only use the flynn id indicated in D (Only use for debugging, default: 0)*
D. *A flynn ID, see C*

A.2.4 Pre- and post-processing utilities

During this thesis, many utilities summarised under the name "*FS_utilities*" have been created. Largely, this was to facilitate daily life and provide fast and reproducible ways to analyse, post-process or create Elle files.

FS_create_plotlayer -i filename.elle -u A B C D –n

Explanation: This code can create Elle files that should only be used for plotting. They can contain no *unodes* for a desired phase or have a set attribute for those *unodes*. Also, the code can merge all *unodes* belonging to one phase (provided no island *flynns* are created because of this). In addition, the user can up- or down-scale the whole model box. This is handy when plotting a deformed pure-shear box with *showelle*, where black strips can occur if *unode* spacing is too large.

A. *UNODE DELETION: Set to X if you wish to delete all unodes with U_VISCOSITY = X, if not, set to 0 and the inputs of D and E are regarded. Set to -1 if you do not wish to use them at all. Default: -1*
B. *When set to any other value than 0, all flynn clusters with this value as phase ID are merged, so that all clusters will consist of only one flynn (maybe handy for plotting). Default: 0*
C. *Scale the whole box and all nodes (boundary and unconnected) by the factor specified in C. C should be > 1 to enlarge and < 1 to shrink the box. Setting the default value 0 means NO scaling*
D. *IF A > 0: Type the value to which all unodes will be set for the attribute defined in A. By typing 0 all values will be set to the max. value in the attribute. Default: -1 (do nothing)*
E. *IF A > 0: Specify which unode attribute to use by using this code: (default: 0)*

   E=1: *U_DISLOCDEN*

   E=2: *U_EULER_3 (so far input A only defines Euler-alpha)*

   E=3 to 4: *U_ATTRIB_A – U_ATTRIB_E*

FS_elle2mtex -i filename.elle –n

Explanation: Creating MTEX input *.txt file from Elle file, that has n rows (n=number of *unodes*) and 6 columns, which indicate: unodeX – unodeY – alpha – beta – gamma – phaseID. For that purpose, U_EULER_3 and U_VISCOSITY have to be active. If not, the user can use FS_flynn2unode_attribute to shift Euler angles and VISCOSITY from *flynns* to *unodes* before running FS_elle2mtex.

FS_euler3random -i filename.elle -u A B C D E F G H –n (all defaults = 0)

Explanation: This code can create a set of Euler angles in either *flynns* or *unodes* (depending on input parameters). The user can choose to set a random distribution or a single maximum with a certain noise. The latter is unfortunately not always very efficient in terms of computation time, depending on how small the noise is (smaller noise = longer computation time).

A. *InUnodes - If set to 1: Store angles in unodes instead of flynns. Default 0 = store in flynns*
   ATTENTION: If you only want to shift any angles (e.g. created by tidy or so) to angles used by VPFFT (ranges from alpha [-180,180], beta [0,90], gamma [-180,180] use InUnodes = 99 (use flynns) or -99 (use unodes)
B. *NoiseInFlynns - Setting it to anything higher than 0 means adding a noise = +-B° to otherwise constant LPO within one flynn, the angles are then stored in unodes and removed from flynns. For that purpose, the LPO stored in flynns is transferred to unodes to make noise possible. ATTETION: Only working if InUnodes == 0 (Even though finally LPO will be stored in unodes).*
C. *Anisotropy - If set to 1: Code will create anisotropic distribution of Euler angles (single maximum) with properties defined in the FOUR following input parameters, default: 0*
D. *AnisoAlpha - Only if C==1: Value for Euler alpha*
E. *AnisoBeta - Only if C==1: Value for Euler beta*
F. *AnisoGamma - Only if C==1: Value for Euler gamma*
G. *AnisoNoise - Only if C==1: Values for alpha, beta, gamma will have a noise of +- G°*
H. *Use anisotropy (C-G) only for the phase with phase ID ==H*

FS_flynn2unode_attribute -i filename.elle -u A B C D –n

Explanation: A small script that transfers *flynn* attributes to the relevant *unodes* within this *flynn*. Set the desired input parameters (A-D) to 1 (instead of 0) to do that (all default values = 0):

A. *VISCOSITY*
B. *EULER_3*
C. *DISLOCDEN*
D. *F_ATTRIB_A*

For clarification, an example: *(...) -u 1 0 1 0 means:* Transfer "*VISCOSITY*", do not transfer "*EULER_3*", transfer "*DISLOCDEN*" and do not transfer "*F_ATTRIB_A*".

importFFTdata_florian -i filename.elle -u A B C D E –n (NOTE: There is no "FS_" as prefix)

Explanation: Transferring data from *tex.out* to *unode* attribute. As input for A, B, C etc., type the column in *tex.out* you wish to transfer to the relevant attribute (start counting from 0!!), type "12" if you do not want to transfer anything to the attribute. The attribute *U_ATTRIB_C* is not implemented, since it should always store the corresponding *flynn* ID.

A. *Transfer column number "A" to U_ATTRIB_A*
B. *Transfer column number "B" to to U_ATTRIB_B*
C. *Transfer column number "C" to to U_ATTRIB_D*
D. *Transfer column number "D" to to U_ATTRIB_E*
E. *Transfer column number "E" to to U_ATTRIB_F*

FS_plot_ugrid –i filename.elle –u A B C D E –n

Explanation: This utility creates a post-script (*.ps) file from an Elle file. The file will show the passive marker *unodes* (have to be stored in *U_FINITE_STRAIN*, see input for *FS_fft2elle*). The code connects passive marker *unodes* with lines that have been in one row, column or diagonal line in the starting regular square grid. This means, the code can plot a deformed grid (Lagrangian deformation field) of initially either horizontal, vertical, both or diagonal lines.

A. *Initial orientation of lines (0 =horizontal, 1 = vertical, 2 = diagonal, 3 = horizontal and diagonal (horizontal ones plotted in blue colours). Default: 0*
B. *Spacing of lines (use integer value as this is actually plotting every B-th unode). Default: 1 (plot every unode)*
C. *Scaling factor for the plotted box. In particular, this is helpful if box size changed during a pure-shear simulation. Default: 7 (if box size stays 1x1). Set to approximately 5 for pure-shear simulations starting with a 1x2 box and going to 50% shortening.*
D. *Threshold distance: Any pair of neighbouring unodes with a separation higher than this will not be connected by a grid line. The value D = 0.15 is default and usually works well.*
E. *Exclude the phase with phase ID = E from being drawn in the grid. Default: 0 (no exclusion). This can cause longer computation times.*

FS_scalefile –i filename.elle –u A B –n

Explanation: Up- or downscaling the Elle model box and all containing structures (*unodes*, *bnodes*) by a user-defined factor in x- and y-direction. Keep the two values the same to avoid changing the aspect ratio of the box. Handy to create Elle files that can easily be plotted with *showelle* without black stripes

between *unodes* with too high spacing. Some special operations are possible (see below). By default, all values are = 1 (no scaling).

A. *Scaling factor in x-direction (A>1: upscale, A<1 downscale).*
B. *Scaling factor in y-direction*

Specialities: If user chooses *A< -1000*, the code will scale any model box back to aspect ratio = 1 (1x1 box). The second input (B) will then control how large the box is: B = 1 means 1x1 box, B = 2 means 2x2 box etc.

FS_splitflynn –i filename.elle –u A B C –n

Explanation: Splits a *flynn* along two user defined *bnodes*. This is useful to resolve an otherwise too complex topology problem such as a grain wrapping around the whole model box (e.g. at high strains).

ATTENTION: Handle with care as can ruin your grain size statistics. The new boundary is assumed "real" boundary when using GBM or other processes. Only handy for pure VPFFT simulations to high strains.

A. *Bnode 1*
B. *Bnode 2*
C. *Flynn that user wants to split*

FS_statistics -i filename.elle -u A B –n

Explanation: This utility is able to do a variety of statistical operations on the Elle file or other output files. It has been created to mainly process the VPFFT output and Elle files with more than one phase. If you have more than one phase, remember that phase counting starts with 1 and no gaps in numbering should exist: A file with phase IDs 1, 2, 4 = 3 phases is forbidden, the phase IDs should then be 1, 2, 3!!

For more information, see instructions below:

A. *Determines which kind of statistics are extracted, default=0:*

   A = 0: Writes a text file (or appends it to an existing one) with various area and phase fraction statistics for flynns

   A = 1: Read data from file "all.out" stored with the Elle file (actually, the Elle file is not necessary for this part you can use a dummy Elle file only containing the word "UNODES" in line 1. Just make sure, that "all.out" is in the directory from where you call FS_statistics). INFO: Set B=1 when A=1, otherwise no output text file is created.

A = 2: Writes mean grain size and shape statistics for the phase with phase ID==B. Outputs an "info" text file and a file with the actual data (or appends data to an existing file)

A = 3: Get slip system activities from undoes. Basal activity needs to be stored in U_ATTRIB_D and prismatic in U_ATTRIB_E, pyramidal is calculated accordingly. You can use "importFFTdata_florian" to extract this information from "tex.out". Activities belonging to phase ID = 2 are not used: It is assumed they belong to bubbles. Change this in line 84 column 36 in FS_statistics.cc to be more flexible

A = 4: Something else, defined in user input "B"

B. *More options for the statistics mode, default=0:*
   - *If A = 0: No options implemented so far, only outputs a text file with area statistics (or appends it to an existing file)*
   - *If A = 1:*

     B = 0: Not recommended as this just extract the data, but do not write an output text file

     B = 1: Save file "AllOutData.txt" containing the summarised contents of "all.out". If file exists, new data is added at the last line.
   - *If A = 2: B should be the ID of the phase for which you want to calculate grain statistics*
   - *If A = 3: B = 1: Write output file, B = 0: Do not write an output file (not recommended)*

   Now the most important bit:
   - *If A = 4:*
     - *B < 0: Normalise driving forces for GBM (stored in bnode attributes after running FS_gbm_pp_fft) to mean surface energy and create Elle file*
     - *B = 1: Calculate perimeter-ratios for all flynns and write them in text file. Attention: This uses all flynns, also air-flynns*
     - *B > 0 and B ≠ 1: Calculate localisation factors for unodes with phase ID ≠ 2 (assumed air bubble) and write to text file. See PAPER I section 2.7.1 for details.*

FS_topocheck -i filename.elle –n

Explanation: This is probably the most important utility. Perform a comprehensive topology check, most topology checks are actually new or updated according to the requirements of the recrystallisation and deformation codes. Below, find a list of the topology checks that are performed. You can also follow this list by browsing through the "*ProcessFunction*" starting at line 30 in "*FS_topocheck.elle.cc*". The code writes many "log-files" to indicate what changes have been made in order to avoid topological errors.

The following topological checks are performed in the indicated order (the order appears important for a correct topological check):

1. *Check for island flynns (flynn inside a flynn). Exit the process if such a flynn is found with a corresponding user message: This issue cannot be resolved by any of the topology checks.*
2. *Update unodes and their attributes (checking if unodes changed host flynns) if the Boolean variable in line 44 (FS_topocheck.elle.cc) is set to "true"*
3. *Delete small flynns if:*
    a. *they have too less bnodes or*
    b. *if unodes are active: no unodes are inside the flynn or*
    c. *the area is smaller than the area between 4 unodes in square grid or*
    d. *if they are "dangling", meaning they have: only 2 neighbour flynns, only 2 triply junctions and those two triple junctions are neighbours. In such situations, the creation of an island flynn is imminent, which could not be resolved with topology checks, therefore delete the flynn "before it is too late". To switch off this option, delete the if-loop starting in line 443 in FS_topocheck.elle.cc*

    Try to delete small flynn by merging it with a neighbour of the same phase. If there is no neighbour of the same phase, merge it with any neighbour. A logfile containing information about deleted flynns will be created.
4. *Add double bnodes where necessary*
5. *Check if two bnodes have exactly the same position (which would be bad), if yes: Perform step 2) again and hope it finally solves the problem*
6. *Perform all standard topology checks, that are used in "elle_gg"*
7. *"checkangle" (an Elle utility) with minimum angle = 20°, removing "pointy" triple junctions*

Check if a flynns needs splitting because two of its boundaries are too close to each other's (and no TJ is involved): This condition effectively allows grain dissection (PAPER II).

A.3 Tutorial on Elle / VPFFT simulations

Welcome to the tutorial on Elle / VPFFT simulations. This tutorial will guide you through the steps of performing low resolution pure-shear simulation including preparations, running the simulation and post-processing the results. Before starting the tutorial, it may be advisable to browse through chapter A.2 or the "readme" files in *FS_Codes*, as the handling of every single required Elle module is not explained within this tutorial. To perform the tutorial, find the required data in the digital appendix of the thesis. The tutorial requires the data in the folder *FS_SimulationTutorial.* In addition, make sure you have access to the folder *FS_Codes a*nd the changed Elle basecode-files stored in the folder *FS_ElleChanges.* To familiarize yourself with the use of Elle modules in general, see the Elle book (Bons et al., 2008) on pages 349-360, 362 (section D.3) and 391-400.

A.3.1 Installation of Elle/VPFFT processes and utilities

Before starting simulations or even preparing *.elle files, you will have to install Elle and the required codes that are not included in the Elle release yet (referring to the available Elle release in March, 2017). The first and most important step is to install Elle itself. This tutorial is optimized for Ubuntu 14.04 or for other Debian-based Linux distributions apart from Ubuntu 16 or newer. It is recommended that you follow these instructions reading a PDF file on your computer, as you may want to copy and paste the commands instead of typing them. You can find a similar instruction on www.elle.ws.

Step 1:

Install the following packages in the terminal

Open a terminal from anywhere and type this as one command line:

sudo apt-get install gfortran gcc mesa-common-dev libgl1-mesa-dev libglu1-mesa-dev libgtk2.0-0 zlibc zlib1g make build-essential xorg-dev libmotif4 libmotif-dev xutils-dev libgtk2.0-dev cvs xutils libx11-dev libXt-dev libxpm-dev x11proto-print-dev x11proto-xext-dev libxext-dev

Step 2:

Download wxwidgets (http://www.wxwidgets.org/)

Make sure NOT to download the latest version (3.xx), but the previous stable release (2.8.12). You can find it under Downloads -> Previous Stable Release 2.8.12 -> Source Code (wxAll ZIP version). Unzip, open in terminal and type:

./configure

make

sudo make install

sudo ldconfig

Now, the zip folder and the extracted folder may be deleted

Step 3:

Download Elle by opening the terminal and typing:

cvs -z3 -d:pserver:anonymous@elle.cvs.sourceforge.net:/cvsroot/elle co -P elle

Step 4:

Copy the *elle* folder to *home/your_username/programs/*

Change "your_username" according to your user-name. It is highly recommended that you use this directory. You can use a different directory, of course, but all codes in this tutorial are optimized for installation into in this directory. Changing the directory means a lot of additional steps that are not explained here.

Step 5:

Add necessary changes to Elle main-codes and install Elle

Open *home/your_username/programs/* and find the data in *FS_ElleChanges.* Copy the files found in *FS_ElleChanges/basecode* to elle/elle/basecode (replaces some old files). Replace the folders "*tidy"* and *"view"* in *elle/elle/utilities* with the folders found in *FS_ElleChanges/utilities.*

Open *home/your_username/programs/elle/elle* in a terminal and type "*chmod +x ./install.sh*", afterwards run the installation bash script typing:

./install.sh wx

Please wait, you will get some warnings, but hopefully no errors. Type *make clean* when installation is finished.

Step 6:

Add Elle path to .bashrc

Open the file "*.bashr*c" from your home directory (e.g. type *gedit ~/.bashrc*) and add the following lines at the bottom (replace *your_username* with the correct user-name). Afterwards save and close the file.

export PATH=$PATH:/home/your_username/programs/elle/elle/binwx

export LD_LIBRARY_PATH=/lib:/usr/lib:/usr/local/lib

export ELLEPATH=/home/your_username/programs/elle/elle/binwx

export BASILPATH=/home/your_username/programs/basil/bin

export PATH=${PATH}:$ELLEPATH:$BASILPATH:

Step 7:

Checking if Elle is installed

Now close all terminal windows, open a new terminal and type *showelle*. If the graphical user interface "*showelle*" is opening, you successfully installed Elle, congratulations. You can add "*showelle*" as an "open with" option, to quickly visualise Elle files. Find the instructions under www.elle.ws → Installation (step 8).

Step 8:

Install the remaining Elle/VPFFT codes

To run an Elle/VPFFT simulation, you need to install additional Elle modules. All of these modules and codes are found in *FS_Codes* (digital appendix). This folder contains all recrystallisation and VPFFT codes and some other utilities that are helpful to pre- or post-process the simulations. Copy this folder to *home/your_username/programs/elle/elle*, you can rename it, if you like. Open a terminal from *elle/elle/FS_Codes* and type:

```
chmod +x FS_install.sh

FS_install.sh
```

Wait until the installation is finished. You may see some warnings again, but hopefully no errors.

A.3.2 Preparations

To prepare a simulation, the most important steps are to prepare a suitable initial Elle file (*.elle) and decide on input parameters. This tutorial will guide you through some basic options to create Elle files and help you to decide on a suitable strain rate and partitioning of recrystallisation mechanisms for your simulation. The way outlined below is just one way to create a suitable input file, of course there are many alternative approaches. To use Elle/VPFFT, it is only required that Elle files are in the same state than at the result of this preparation. To start the preparation, find the folder *01Preparations* in *FS_SimulationTutorial*.

To create an initial Elle file with a set of *flynns* representing a certain grain size in a foam texture, we have two options: (1) Create a *.ppm colour-indexed image and open it with *-n*. Make sure the image aspect ratio is 1 and the image size does not exceed approximately 600 pixels in width and height. Afterwards, run *tidy -i file.elle -u SD -n* to achieve a desired switch distance (replace SD with any number). (2) The other option is explained in this tutorial: Usually we already have another Elle file which we can use to create the desired foam texture. The procedure is to split the *flynns* in this Elle file until we have a structure that has a very high amount of *flynns* (i.e. low grain size) and subsequently growing grains again to achieve the desired grain size.

It is recommended to use a switch distance in the order of the *unode* spacing. That means, for 128x128 *unode* files use a switch distance around 0.01 or for 256x256 *unode* files a switch distance around 0.005. The Elle file *start_preparation.elle* already has a suitable switch distance. The switch distance can be changed using the first user input of *tidy* can alter the switch distance.

A.3.2.1 Create a suitable input Elle file

Find the file *start_preparation.elle* in *01prepare_elle_file* folder. Imagine, we want to create an Elle file that has only ice grains at a mean grain size of 40 mm² and should deform under pure-shear conditions at -30°C. We want to use a resolution of 128x128 *unodes* and a random initial CPO. The switch distance in the provided Elle file is already set to 0.01, which is suitable for this resolution of *unodes*. We will assume that one unit in the model box is 10 cm in nature (unit length = 0.1), i.e. we need an Elle file with 500 *flynns* to achieve a mean grain size of 40 mm².

This tutorial is for a single phase material (only ice). The provided input files are also suitable to use a file with air bubbles. Check step 1.7 for an explanation on how to add bubbles to your Elle file or the file *PreparedInputFileBubbles.elle* provided in *prepared_files.zip* (keep the file *initial_stuff.txt* with it whenever using *FS_gbm_pp_fft*).

Step 1.1

First, we scale the file to the desired box-size. For pure-shear simulations, you may want to start with a 1x2 box instead of 1x1. See the input of *FS_scalefile* to understand how to scale the box in x- and y-direction. To scale the file type:

FS_scalefile -i start_preparation.elle -u 1 2 –n

Step 1.2

Next, use Jens Roessiger's code "*jr_gg_split*" to split the *flynns* and achieve a very low grain size. For an explanation on the user input, see Jens Roessiger's PhD thesis (therein: appendix 4, section 1.3). If you are searching for an Elle file that already has a low grain size, check out the file *fine_gsf.elle* in *elle/extras/elle_files*. Jens Roessiger's script will run for ten time steps. Afterwards, you can delete the file *log.txt* and open *gg_split010.elle* with *showelle* to see the result, if you like. Now, type the following command to decrease the grain size:

jr_gg_split -i scaled_file.elle -u 2 1 0 0 1e-5 -s 10 -f 10 -n

Step 1.3

Now, we grow the *flynns* again using *elle_gg* to reach a number of 500 *flynns*, i.e. the desired mean grain size of 40 mm². From experience, I recommend to do 700 steps of *elle_gg* to, in a first step, approximate 500 *flynns*:

elle_gg -i gg_split010.elle -s 700 -f 700 -n

Now the file will contain something close to 500 *flynns*. In a following step we perform *elle_gg* again on the result file, but save every output step:

elle_gg -i growth700.elle -s 200 -f 1 -n

From all of these 200 output files (*growth001.elle* to *growth200.elle*), find the one that has approximately 500 *flynns* and store it. Afterwards, you can delete the remaining output files, by typing *rm growth**. To quickly check the number of *flynns*, open an Elle file in *showelle* and click on "Data → *Flynns*". Scroll down and check the highest number in the very left hand column that is still followed by a *flynn* ID. This is the number of *flynns* in the file. Alternatively, add the following C++ code in an empty Elle "ProcessFunction" and apply this small Elle script on the Elle file (see output in terminal window). You can use the empty Elle process found in *FS_Codes/FS_other* for that.

```
int count=0;
for (int i=0;i<ElleMaxFlynns();i++) if (ElleFlynnIsActive(i)) count++;
printf("Number of flynns: %u\n",count);
```

If you want to spare you this time consuming work, you can now go on with the provided file called *500flynns.elle* (already containing 500 *flynns*).

Step 1.4

Go on with your own Elle file or with the provided file called *500flynns.elle.* Open the file in any text editor of your choice. You can delete the *flynn* attributes F_ATTRIB_A and SPLIT, we do not need them any more (they are already deleted in 5*00flynns.elle*). Before the "LOCALTION" block, add the following lines (see further description below):

```
MINERAL
Default ICE
VISCOSITY
Default 1
```

This adds the "MINERAL" attribute necessary for e.g. the recovery-code and introduces the attribute "VISCOSITY", which is used as phase indicator (start counting phases with 1). It is sufficient to leave ice as the default mineral in MINERAL for ice-air aggregate simulations. However, adding *flynns* with VISCOSITY = 2 will be inevitable for such simulations.

Step 1.5

Now, add a random CPO to *flynns* using the script *FS_euler3random*:

FS_euler3random -i 500flynns.elle -n

You can plot the resulting c-axes azimuths with *showelle* by selecting EULER_ALPHA in *flynn* properties (plot ranges -180° to 180°) and choosing the colour-map "azimuth_florian", which is provided in *FS_Codes/additional_data* (digital appendix). When you do your first simulation step, the fft2elle routine will automatically transfer the orientations (EULER_3 attribute) from *flynns* to *unodes* if there is no U_EULER_3 attribute yet.

Step 1.6

If we would like to add second phases such as air bubbles, we would have to do the things decribed in step 1.7. But to keep the tutorial shorter, we restrict ourselves to a single phase simulation. The last step is now to add *unodes* in a regular square grid, this can be done with *tidy* (see Elle book (Bons et al., 2008) for further description on how to use *tidy*. Now, type:

tidy -i FS_euler3random.elle -u 0 0 0 0 128 1 -s 1 -f 1 -n

mv tidy001.elle MyIceInput.elle (Or use any other filename for your file)

Congratulations, you are finished with preparing a single phase Elle file. You can either go on with this file or with the file *PreparedInputFile.elle* (do NOT keep the file *initial_stuff.txt* with this Elle file as it does not contain bubbles).

Step 1.7 (optional)
How to add air bubbles

To add air bubbles, we would have to decide on some *flynns* to set to air, meaning setting their attribute "VISCOSITY" to 2. At best, do this before adding *unodes*. You can simply decide these *flynn* IDs by opening the Elle file in *showelle* and displaying the IDs or write a short script or use a spreadsheet to set a controlled number of *flynns* to air. As these *flynns* will not have circular shapes with dihedral angles close to 180°, we will afterwards have to run *FS_gbm_pp_fft* for a few steps until the air bubbles adopt circular shapes:

FS_gbm_pp_fft anyfile.elle -s 1000 -f 1 -n

Choose the file of the thousand output files where the mean area fraction of the air phase does not change significantly any more by plotting number of steps against relative area fraction changes. To do this, you can use the output file *PhaseAreaHistory.txt*, where each row indicates one GBM step. The 1st column represents the numer of steps and the values in the 2nd column represent the ice area in that step. Plot the 1st against the 2nd column to see when the ice area (i.e. also the air area) reaches stable values. For the tutorial Elle file you will probably need approximately 1000 steps of *FS_gbm_pp_fft* to reach round air bubbles and an equilibrium of involved energies.

Careful with the time-step in the Elle file: Air-ice and air-air *bnodes* tend to move faster than ice-ice *bnodes*. After every step, the GBM code will output the number of *bnodes* with

migration velocities too high to the set time step. You should search for a compromise between a low number of "too fast" *bnodes* and computation time. For more information on how to set a proper time step for the GBM code, see Becker et al. (2008). The time step that is pre-defined in the tutorial Elle file should work without problems.

The *phase_db.txt* file in *FS_Codes/additional_data* should serve as a suitable phase database for the ice-air aggregate. To for instance assume a wetting angle of 30°, change the 4th value in line 51 to 0.03365. Always keep *phase_db.txt* in the same folder from which you run *FS_gbm_pp_fft*.

Once finished with developing roundish air bubbles, keep the file "*initial_stuff.txt*" (created by *FS_gbm_pp_fft*) with the resulting Elle file whenever starting *FS_gbm_pp_fft* again. It allows you to keep the energy balance between surface and area energies. For further detail see Jens Roessiger's PhD thesis, Roessiger et al. (2014) or PAPER I of this thesis (Steinbach et al., 2016). If you would like to spare you the work of adding air bubbles, you could use the provided file *PreparedInputFileBubbles.elle* found in *prepared_files.zip* (keep the provided file *initial_stuff.txt* with it).

A.3.2.2 Decide on most important input parameters

Too keep this tutorial simple, this section only describes how to set the most crucial input parameters. Other parameters such as the critical resolved shear stresses, grain boundary mobilities, activation energies or surface energies we will keep in accordance to the simulations presented in this thesis. See other instructions, readme-files or cited literature for information about these parameters.

Prepared input files are found in *FS_SimulationTutorial/01Preparations/input_files* (digital appendix). All these files have to be with the input Elle file when starting the simulation. They are ready and suitable for 2-phase simulations, too, but will equally well work with our single phase Elle file. Please familiarize yourself with the input files of VPFFT using the file *InputFiles_FFT_Elle.pdf* (digital appendix) and with the comments between lines 8 and 92 in the bash script that controls the simulation (*launch_simulation.sh*).

Step 2.1

Basic deformation conditions

The most basic input parameters to decide on are already within the Elle file. Those are temperature, distribution, size and shape of phases and grains and, of course, the resolution. Furthermore, you should

decide on the deformation mode, i.e. whether to use simple- or pure-shear. For this example, we will use a pure-shear setup. As the model box itself gets deformed in pure-shear, we cannot go to very high strains. When starting with a 1x2 box, it is recommended to deform to vertical shortening $\varepsilon_{yy} \approx 0.5$ (50%), which creates a 2x1 box. This shortening is the result of *N* simulation steps, each with a time step Δt, each with an incremental shortening of $\Delta\varepsilon_{yy}$. From this, you can calculate the vertical strain rate $\dot{\varepsilon}_{yy}$ and vertical shortening ε_{yy}:

$$\dot{\varepsilon}_{yy} = \frac{\Delta\varepsilon_{yy}}{\Delta t} \tag{A.3.1}$$

$$\varepsilon_{yy} = 1 - \left(1 - \Delta\varepsilon_{yy}\right)^{N} \tag{A.3.2}$$

Step 2.2

Decide on and set incremental shortening (the *ppc.in* file)

The best approach to decide on these parameters, is first deciding on an incremental shortening ($\Delta\varepsilon_{yy}$). This should not be too large as the incremental effects of the multiple processes affecting the microstructure (deformation and recrystallisation) should be small to reduce errors. For this tutorial, we decide on $\Delta\varepsilon_{yy}$ = 0.01. With this, we can easily decide on the number of time steps *N* as we will reach the desired vertical shortening of $\varepsilon_{yy} \approx 0.5$ with *N*=70.

The incremental shortening ($\Delta\varepsilon_{yy}$) is set in the VPFFT input file *ppc.in*. It results from multiplying velocity gradient tensor $\dot{\boldsymbol{u}}$ (lines 24 to 26) with the set time step for VPFFT (line 36). As VPFFT uses dimensionless parameters, it is sufficient to set the elements in the velocity gradient tensor $\dot{\boldsymbol{u}}$ to the incremental shortening and stretching and the time step to 1. See the provided *ppc.in* to understand how this is done to achieve pure-shear. Remember that the velocity gradient tensor $\dot{\boldsymbol{u}}$ is non-symmetric. This implies that when setting a shear strain parallel to the x-axis, only the 2nd number in line 24 needs changing and not the diagonal element (see *ppc_simpleshear_demo.in*). To calculate the strain rate tensor $\dot{\boldsymbol{\varepsilon}}$ from the velocity gradient tensor $\dot{\boldsymbol{u}}$ use:

$$\dot{\varepsilon}_{ij} = \frac{1}{2}\left(\dot{u}_{ij} + \dot{u}_{ji}\right) = \begin{pmatrix} \dot{u}_{11} & \frac{1}{2}(\dot{u}_{12} + \dot{u}_{21}) \\ \frac{1}{2}(\dot{u}_{21} + \dot{u}_{12}) & \dot{u}_{22} \end{pmatrix} \tag{A.3.3}$$

The file *ppc.in* also contains the crystal file names (*.sx) that contain crystallography and critical resolved shear stresses of the phases (lines 8 and 15) and the number of *unodes* (has to be indicated for each phase, but always use total number, see lines 4 and 11). Line 41 of *ppc.in* indicates how many iterations the VPFFT process will run to iteratively solve for the mechanical (stress, strain rate) fields (for details see related papers by Ricardo Lebensohn or Albert Griera). In this tutorial, we will use 100 iterations, however to reduce numerical errors, you should consider increasing the number of iterations

to 200 or 400, in particular in a polyphase simulation setup or whenever critical resolved shear stress contrasts are high.

Step 2.3

Decide on real strain rate and number of recrystallisation steps

As VPFFT is dimensionless, but Elle uses a time step in seconds (Δt_{Elle}), we still need to decide on or calculate the actual strain rate $\dot{\varepsilon}_{yy}$ under which we will do the simulation. If we would do one recrystallisation step per VPFFT step, the effective time per step in the simulation (Δt) would be equal to the one set in the Elle file. However, this would lead to a comparatively high strain rate as this time step for the GBM code needs to be sufficiently low (Becker et al., 2008). Therefore, the user has the option to increase the number of recrystallisation steps to increase the effective time per simulation step. This is done by performing a number of sub-loops of the recrystallisation sequence (e.g. recovery, polygonisation, grain boundary migration). The effective time (Δt) results from multiplying the number of these sub-loops N_{SL} with the number of steps N_M each recrystallisation module is running, which in turn controls the strain rate, from equation A.3.1 we get:

$$\dot{\varepsilon}_{yy} = \frac{\varepsilon_{yy}}{N_{SL} N_M \Delta t_{Elle}} \tag{A.3.4}$$

It is recommended to set the number of steps per module (N_M) to 2 and further control the strain rate by varying the number of sub-loops (N_{SL}). These numbers are set in the bash script that controls the simulation, the script "*launch_simulation.sh*" is found in *01Preparations/input_files*. See how the numbers are set in lines 65, 68, 70 and 71. Also see the remaining input parameters such as the total number of simulation steps, which is set in line 37 and familiarize yourself with the input-block in the bash script.

In this tutorial, both the number of sub-loops and the steps per module are set to 2, resulting in 4 recrystallisation steps per VPFFT step. As the time in the Elle file was set to $5 \cdot 10^6 s$ and $\Delta\varepsilon_{yy}$ = 0.01, the effective strain rate for our simulation is $\dot{\varepsilon}_{yy} = 5 \cdot 10^{-10} s^{-1}$. At this state of code development, it is recommended to keep the Elle time step (Δt_{Elle}) constant, but vary the number of recrystallisation steps to change the strain rate. The strain rates used in Elle/VPFFT are still high compared to natural ice sheet strain rates, but currently smaller strain rates predict way to large grain sizes and are computationally too expensive as they require high numbers of recrystallisation steps (also see discussions in PAPER I and PAPER II of this thesis).

Step 2.4

The controlling bash script (*launch_simulation.sh*)

It makes sense to take a look at the most important input parameter in the script controlling and running the simulation called *launch_simulation.sh*. We already know how to set the number of recrystallisation

steps. Other basic input properties are listed below. For the tutorial, you can leave all parameters as they are.

line 34: *INROOT=PreparedInputFile* *# Input Elle file, do not type file extension (.elle)*

line 36: *OUTROOT=output* *# Root of the names of output Elle files, the*
 # ending "_stepXXX.elle" is added and XXX
 # will be the number of the corres ponding simulation
 # step

line 37: *TOTALSTEPS=70* *# The total number of steps you want to perform from*
 # now on. Remember that when restarting a simulation
 # at e.g. step 10 and you want to go until step 15, you
 # should type "5" here, not "15"

line 42: *DIMENSIONS=128* *# The number of unodes in x- and y-direction, it is*
 # important to indicate the correct number in the input
 # file

line 43: *EXCLUDEDPHASE=0* *# Phase ID excluded from recovery, polygonisation*
 # etc., usually this is air or melt.
 # Set to 0 not to use this option and to exclude NO
 # phase (e.g. in single phase simulations like in this
 # tutorial)

line 46: *REPOSITION=0* *# Set to 1 if repositioning is needed (simple-shear),*
 # otherwise set to 0

line 53: *MAKEPLOTFILE=1* *# Sometimes it is handy to use "plotfiles", which are*
 # Elle files only used for plotting with showelle. If this
 # option is set to 1, the following is done:
#
 # a) Deletion of all unodes belonging to the excluded
 # phase (cf. line 43)
 # b) Merging all flynns belonging to excluded phase

	# c) Scaling the whole model box by the factor *# indicated in line 57* *#* *# Set MAKEPLOTFILE=0 not to use this option. If* *# you use it, an additional output folder is created* *# containing the Elle files for plotting*
line 57: *SCALE=0.4*	*# cf. Descriptions for line 53. This is done to remove 2nd* *# black stripes between unodes when plotting with* *# showelle: Handy if resolution in low or unode* *# pacing in x- and y-direction differs.*

Step 2.5

Remaining simulation input

The folder *01Preparations/input_files* contains all necessary input files to run a simulation, apart from the initial Elle file. Please familiarize yourself with the comments in the bash script *launch_simulation.sh* and *InputFiles_FFT_Elle.pdf* (digital appendix). Please make sure, the name of the input Elle file is correctly indicated in line 34 in *launch_simulation.sh* as well as all other parameters such as the total number of steps. It is beyond the scope of this tutorial to guide you through all input parameters. It is important to keep the files *ppc.in* and **.sx* in the folder from where you start the simulation. Please note that the *.sx files are listed again in *ppc.in*, the first file listed will correspond to the phase defined by *flynn* VISCOSITY = 1, the second one listed to VISCOSITY = 2 and so on.

Other simulation input files that you should keep there as well are *phase_db.txt* and *symmetry.symm*. These files either indicate symmetry properties of the crystal defined in the Elle file by VISCOSITY = 1 (*symmetry.symm*, here for ice Ih) or contain phase and phase boundary properties for GBM (*phase_db.txt*). The latter file contains information that is not used any more by the GBM code, these properties are marked with the word "OUTDATED". See further comments in *phase_db.txt* for more information.

The folder *01Preparations/input_files* also contains the zip-file *defaults.zip*, which defines default plot properties for any Elle file opened from this folder using *showelle*. By default, the grain boundaries and bubbles (*flynn* VISCOSITY = 2) will be plotted in black and ice grains in white. If you would like to create another defaults-file, just open an Elle file with *showelle*, adjust the properties as you like and save the Elle file (File → Save). Rename the created *.zip file to *defaults.zip* and delete the files "*runopts.txt* and *userdata.txt*" within the zip-file.

A.3.3 Setting up and running the simulation

To run a simulation, it is recommended to create a new folder such as "*02RunningTheSimulation/*" found in "*FS_SimulationTutorial/*" (digital appendix). It is necessary to keep the following files in this folder before starting the simulation using a controlling bash script:

- *.sx file for each phase (e.g. *air.sx* and *ice3d.sx*) as indicated in *ppc.in*
- *ppc.in* (the input properties for VPFFT)
- *phase_db.txt* for the GBM code
- *symmetry.symm* for phase with *flynn* VISCOSITY = 1 for recovery and polygonisation (At the moment, both work only with one crystalline phase and with up to one excluded phase)
- *launch_simulation.sh* (bash script controlling the simulation)
- An Elle file serving as the initial state

Before running a simulation, make sure you have sufficient memory available on your hard drive, especially 256x256 *unodes* simulation can take up ten or more Gbytes. Also, make sure you have at least one physical core available on your CPU. Any amount of modern working memories (meaning approximately >2GB) should be sufficient for the simulation.

Step 3.1
Copy the input files to the simulation folder

As a first step, please copy all input files listed above and prepared as indicated in A.3.2.2 in the folder "*FS_SimulationTutorial/02RunningTheSimulation/*". Also, please add the prepared Elle file and, if using a polyphase setup, the *initial_stuff.txt* that resulted from equilibrating the phase boundaries and involved energies (see step 1.7 in section A.3.2.1). If you like, you can alternatively unzip the file "*input_files.zip*", which also contains all the necessary input.

Step 3.2 (optional)
Create a virtual terminal session using the software "screen"

Some simulations can take up to days or weeks. Usually, you may not want to keep a terminal window open all the time or will not run them on your local machine. In these cases, it is helpful to start the simulation in a virtual terminal session that allows you to close the terminal and will run in the background. For this purpose, install "screen" on your system:

sudo apt-get install screen

Screen is a software that allows virtual terminal sessions. For more information, see *help.ubuntu.com/community/Screen*. To open a new virtual terminal window called *MySimulation*, first open a "real" terminal window and type:

screen -S MySimulation

A new virtual terminal session starts from the present working directory, it is "attached". To "detach" the virtual session, press *Ctrl(left)+A* and afterwards just press "d". The session is now still running in the background, which you can check with the *screen -ls* command. To attach the virtual session again type:

screen -r MySimulation

You are now in the virtual session again and could close it with "*exit*". However, do NOT close the session yet, but change directory to the folder from where you intend to run the simulation.

Step 3.3

Start the bash script controlling the simulation

This step is rather simple. You should have a terminal window open (or virtual session attached) and change directory the folder from where you want to start the simulation. Now, make the controlling bash script an executable by typing:

chmod +x launch_simulation.sh

and start the simulation with running the bash script (type its name, hit enter):

launch_simulation.sh

If you like, you could also comment line 22 and uncomment line 23 in *launch_simulation.sh* and run it like this in "debug-mode": This way, the terminal window will only display the commands but not really perform them.

A lot of things should after starting the simulation, with our low resolution (128x128 *unodes*) simulation, the preparations and *FS_elle2fft* should be finished quickly and you should see the iterative solver of the VPFFT code running for as many iterations as you set in line 41 in *ppc.in*. In summary, the code is performing the following operations, check *launch_simulation.sh* to see how this is done in detail:

1. Prepare output folders and again zip up all input files
2. FS_elle2fft
3. FFT_vs128 (the VPFFT code)
4. FS_fft2elle_strainanalysis (New: Storing incremental deformation tensors for each *unode*)
5. reposition (only if you choose to do a simple-shear simulation, not the case during this tutorial)
6. importFFTdata_florian (store additional data from VPFFT output in undoes)
7. FS_flynn2unode_attribute (to shift *flynn* VISCOSITY to *unode* U_VISCOSITY)
8. FS_topocheck (a comprehensive topology check)
9. Initialise the sub-loops for recrystallisation

10. FS_recovery

11. subgrain_unodes_alb (find subgrains that should be a new grain or *flynn*)

12. u2f_sgb_alb (add new *bnodes* and *flynn* boundaries)

13. FS_topocheck (necessary after 11+12, which are polygonisation)

14. FS_gbm_pp_fft (code includes all topology checks from FS_topocheck after each step)

16. End sub-loops for recrystallisation

15. FS_flynn2unode_attribute (again on VISCOSITY, the attributes may have changed)

16. FS_scalefile (if user wants to: scale the file up or down to facilitate plotting with *showelle*)

17. If user wants to: Read data from all.out (bulk stress, strain output) and store in separate *.txt file

18. Store resulting Elle file in the output folder, zip up additional data to save memory

19. If all steps are done: zip up the whole output folder, delete temporary files and finish

While the simulation is running, please keep the terminal window open if not using screen (step 3.2). Otherwise, you can now detach the virtual terminal session with *Ctrl(left)+A* and subsequently pressing "d". When the simulation is finished, the terminal will display:

~~~~~~~~~~~~~~~~~ FINISHED ~~~~~~~~~~~~~~~~~

Now, you can close the window or virtual session by typing "*exit*". Congratulations, the simulation finished successfully.

A.3.4 Post-processing the simulation

If the simulation is finished, the newly created "*results/*" folder should contain as many Elle files as steps were performed, a *.zip file for every simulation step containing additional data and some sub-folders. Additionally, all data in "*results/*" is zipped up in *ALL_RESULTS.zip*. The sub-folder called "*incr_deformation_tensors/*" is containing the incremental deformation tensors for each simulation step. See chapter A.4.4 for further information on how to post-process these data. The sub-folder "*plotfiles/*" is only created when the option to scale Elle files for plotting was switched on in "*launch_simulation.sh*" (lines 53-56). It contains the scaled Elle files that are more suitable for straightforward plotting with *showelle* as they are scaled down so that no black space is visible between *unodes*. For more advanced plotting see the MATLAB scripts explained in chapter A.4.5. The last sub-folder is called "*additional_files/*" only contains the "*initial_stuff.txt*" created by *FS_gbm_pp_fft*. It is necessary to copy this file to the working directory whenever restarting the simulation. Finally, you will also find the file
~~~~~~~~~~~~~~~~~

"*AllOutData.txt*" in "*results/*". It contains the summarized content of all "*all.out*" files which are an output of every VPFFT step and indicate bulk strains and stresses and slip plane activities for the ice Ih crystal.

In summary, the Elle file will store the following properties in *flynns*, *bnodes* and *unodes*:

Stored in *bnodes*:

N_ATTRIB_B:	Actual surface energy for this node
N_ATTRIB_C:	Actual strain energy resulting from surrounding dislocation density for this node

Stored in *unodes*:

U_DISLOCDEN:	Dislocation densities
U_EULER_3:	Euler angles following the Bunge convention. Plot EULER_ALPHA from -180 to 180° for c-axes azimuths.
U_DENSITY:	Only temporary attribute for polygonisation
U_ATTRIB_A:	Normalised von Mises strain rates (normalised to bulk value)
U_ATTRIB_B:	Only temporary attribute for polygonisation
U_ATTRIB_C:	*Flynn* ID of the *flynn* that contains this *unode*
U_ATTRIB_D, E:	Basal and non-basal activity between 0-1
U_ATTRIB_F:	Kernel average misorientation (degrees)
U_FINITE_STRAIN:	Six values indicating x,y positions of initial, previous and current position of passive markers (to be plotted with *FS_plot_ugrid* or similar scripts)

Step 4.1

Prepare folder to visualise simulation results

Find the directory *FS_SimulationTutorial/03Postprocessing/* and unzip the file "*visualisation.zip*". The contained bash script "*prepare_visu.sh*" will help you copying all necessary files in the visualisation folders and perform the post-processing. After you are done with post-processing, the other folders will contain images of microstructural properties for each simulation step. Each folder already contains a "*defaults.zip*" file that automatically plots the Elle file in the desired way using *showelle*. Please remember: If not choosing to use "plotfiles" in "*prepare_visu.sh*", this plots all *unodes*, including *unodes* belonging to the air phase, which you may not want. Certainly you should not use these files for plotting

pole-figures or “stereos”. Set “USE_PLOTFILES=1” to use the plotfiles that exclude air *unodes*. Of course, this only works if you switched their creation on before starting the simulation. If you would like to remove air *unodes* after the simulation, use *FS_create_plotlayer -i file.elle -u 2 2 -n*, which can create a layer of only ice *unodes*.

After post-processing, the folder “*other_data/*” will contain additional data on grain size evolution, localisation factors (see PAPER I), perimeter ratios of ice *flynns* and slip system activities. In addition, you have the option to generate normalised driving forces on *bnodes* using the script *bash4drivforce_normalisation.sh*. However, this script is not automatically called by *prepare_visu.sh*. Please check all the bash scripts (or the corresponding codes in FS_Codes/*FS_utilities/* to understand how the post-processing is done in detail.

Now, open a terminal window in and make *prepare_visu.sh* an executable:

chmod +x prepare_visu.sh

Open *prepare_visu.sh* and check the following input parameters suit your simulation:

SIMULATIONDIR	Important: Set the correct path (relative or absolute) to the directory where you did the simulation
FILEROOT	The root of the name of your output Elle files in “results/”, without “_stepXXX.elle” at the end
STARTSTEP=1	The step from where you started the simulation (usually 1, if you did not restart an older simulation)
STEPS=70	The total number of simulation steps performed (NOT minus STARTSTEP)
INCREMENT=1	Usually = 1. If you did only save every N-th simulation step, then type N
USE_PLOTFILES=1	If you want to plot images from scaled “*plotfiles*”, type 1, if not type 0. This is usually 1 for pure-shear and 0 for simple-shear simulations as the latter do not need scaling to remove black spaces between *unodes* (*unode* spacing in simple-shear simulations stays the same in x- and y-direction)

Again you can comment line 7 and uncomment line 8 to run the script in “debug-mode”.

Step 4.2

Install imagemagick

The software “imagemagick” is a command-line based software for image processing purposes. Some of the post-processing bash scripts use imagemagick, therefore it is recommended to install it typing:

sudo apt-get install imagemagick

Step 4.3

Run post-processing scripts

Now run the script *prepare_visu.sh* by typing in terminal:

prepare_visu.sh

You will get some information about what is going on in the terminal. Especially for higher resolution simulations, this might take a while. Please note that additional Elle files are created in almost every folder in “”, which implies you will temporarily need additional memory on your hard drive.

All the scripts in “*other_data/*” will run automatically as well as the scripts creating pole-figures or “*stereos*” and unconnected passive marker grids (*ugrids*). Remember that for pole-figures you should exclude the air phase *unodes* when doing a polyphase simulation.

Step 4.4

Plotting

Once the script *prepare_visu.sh* is finished, the folder “*ugrids/*” and “*stereos/*” will contain the corresponding images. The folder “*other_data/*” will contain text files storing additional information on the evolution of grain sizes, slip system activities, bulk stress and strain, perimeter ratios and localisation factors (according to PAPER I). Additionally, you will find Elle files in most of the visualisation folders.

To plot images (i.e. maps for: dislocation density, strain rate, LPO etc.), open a terminal window in the relevant folder and open *showelle* with one of the contained Elle files. Now click on Graphics → Save → Save whole run. A window showing all Elle files in this folder should pop up. Just double-click on one of these Elle files. Now, *showelle* will ask you if you really wish to plot pictures from these Elle files (the indicated number should equal the real number of Elle files in the folder). Click “Yes” and *showelle* will start producing the images. Once finished, you can close *showelle* and delete all Elle files in this folder. Do the same for every folder that still contains Elle files and you will produce all sets of images for the several microstructural properties. You could make your own videos with these images using tools like ImageJ or the MATLAB script provided in chapter A.4.5.

There are more elegant ways to plot the images, especially for polyphase setups. For instance, you could overlay images only plotting *unodes* (no boundaries) with only the boundaries and bubbles coloured in black or the passive marker lines. Use the image processing tool of your choice to do these things or

find the description of some MATLAB scripts for that in chapter A.4.5. In this chapter (A.4.5), you will also find descriptions on MATLAB scripts that are capable of plotting some of the data that is now stored in *.txt files in the folder "*other_data/*".

Step 4.5

Almost finished

Now you produced the most important simulation images and post-processed the data. The last recommended step is to check for unnecessary Elle files in the post-processing folders and delete them. Also you could now store the resulting zip-file in "*results/*" called "*ALL_RESULTS.zip*" somewhere else and delete "*results/*" to save memory.

Congratulations, you successfully performed an Elle/VPFFT simulation.

A.4 Further developments

A.4.1 Strain-energy-driven recovery

The recovery routine used in the research conducted for this thesis and related papers is based on the methodology presented by Borthwick et al. (2014). The code works well and is robust, however, not properly scaled to a numerical time-step. Therefore, it is difficult to quantify the amount of recovery in a simulation. An updated routine was created in the course of this thesis, but has not been completely tested and applied yet. This section will briefly explain the methodology and outline the handling of the updated code. The code itself is found in the digital-appendix folder "*FS_DDEnergyRecovery/*" under "*FS_codes/FS_other/*". This approach should be regarded as a suggestion. Probably debugging and coding work is still necessary to improve and apply this approach.

The general principle of the new approach is the same than in Borthwick et al. (2014): A *unode* is rotated in trial rotations around several crystallographic axes by a very small angle. From every trial we determine the change in kernel average misorientation $d\theta$ and the resulting change in surface energy $d\gamma$ (using the Read-Shockley equation, see e.g. Borthwick et al., 2014). We search for the rotation direction leading to the highest energy decrease, similar to the energy minimising system used for the GBM code. From that we still need to know the amount rotation we want. In other words: We now know in which direction to rotate, but not by how much. In the old code rotation itself (ω) was determined using the rotation mobility M:

$$\omega = M \frac{d\gamma(\theta)}{d\theta} \tag{A.4.1}$$

The issue was that in this description there is no good way to scale the rotation to a certain time step, i.e. derive the rotation rate $\dot{\omega}$ (like we do in GBM, where boundary velocities instead of migration distances are calculated): An option to solve this would involve a more complex description of M that depends on several material properties such as the diffusion coefficient or type of diffusion (boundary- or lattice-diffusion) as the approach assumes re-orientation is achieved by diffusion (Moldovan et al., 2001). Therefore, the new approach described here is more practical to implement.

The new approach is based on assuming we know how the strain energy E_{strain} and with that the dislocation density ρ_{DD} relates to the kernel-average lattice-misorientation Φ_{KAM}. According to Ashby (1970), we can approximate the density of dislocations with Burgers vector length b over a distance of curved lattice using:

$$\rho_{DD} = \frac{\phi_{KAM}}{b \cdot l_m} \tag{A.4.2}$$

$$E_{strain} = \rho_{DD}(\phi_{KAM}) \cdot E_{line} \tag{A.4.3}$$

Here, l_m is the mean distance between datum *unode* and its neighbours used to determine Φ_{KAM}. The resulting energy E_{strain} then depends on the dislocation density at a certain kernel-average lattice-misorientation and the energy per line of this type of dislocation (E_{line}). Accordingly, from this we also know how energy changes with misorientation. Finding an adequate model for determining the dislocation density from misorientations (Eq. A.4.2) is one of the crucial and critical points in further improving and using the whole method.

The new approach is not calculating the rotation, but the rotation rate ($\dot{\omega}$, unit: rad/s^{-1}) and therefore allows scaling to the Elle time step Δt as the actual rotation results from the multiplication $\omega = \dot{\omega} \cdot \Delta t$. It describes the rotation to be equivalent to simple shearing the *unode* over a small increment, using a simple flow law, were the unit of A is $(Pas)^{-1}$ and α is the misorientation resulting from a trial rotation. We set the stress exponent to $n=3$ for now:

$$\dot{\varepsilon} = \frac{1}{2}\dot{\gamma} = \dot{\omega} = \dot{\alpha} = A\sigma^{n=3} \tag{A.4.4}$$

The shear strain rate is half the rotation rate and the shear stress can be described assuming a force acting on the lateral surface area of the crystallite with edge length L (will be the *unode* spacing). From the product of stress and strain (or rotation) rate, we know the work rate over a volume $V = L^2$ (in 2D, assuming unity in 3rd dimension):

$$\frac{dW}{dt} = V\dot{\varepsilon}\sigma = V\dot{\alpha}\sigma = V\frac{d\alpha}{dt}\sigma \tag{A.4.5}$$

$$\dot{\alpha} = A\sigma^3 \leftrightarrow \sigma = \left(\frac{1}{A}\right)^{\frac{1}{3}}\left(\frac{d\alpha}{dt}\right)^{\frac{1}{3}} \tag{A.4.6}$$

Combining Eq. (A.4.5) and Eq. (A.4.6) yields:

$$\frac{dW}{dt} = V\left(\frac{1}{A}\right)^{\frac{1}{3}}\left(\frac{d\alpha}{dt}\right)^{\frac{4}{3}} \tag{A.4.7}$$

Now, we equal the work rate (dW/dt) with the energy mismatch due to a change in lattice misorientation ($dE/d\alpha$) by multiplying with $dt/d\alpha$. We know $dE/d\alpha$ over volume V, from using Eq. (A.4.3):

$$\frac{dE}{d\alpha} = \frac{dW}{d\alpha} = \frac{dW}{dt}\frac{dt}{d\alpha} \tag{A.4.8}$$

$$\frac{dE}{d\alpha} = \frac{dE_{strain}}{d\alpha}V \tag{A.4.9}$$

Combining and re-arranging Eq. (A.4.7), (A.4.8) and (A.4.9) gives an expression for $d\alpha/dt = \dot{\alpha}$. Note that we can cancel out the volume occupied by the crystallite, which is important to make the approach scale independent:

$$\frac{dE}{d\alpha} = \frac{dW}{dt}\frac{dt}{d\alpha} = V\left(\frac{1}{A}\right)^{\frac{1}{3}}\left(\frac{d\alpha}{dt}\right)^{\frac{4}{3}}\frac{dt}{d\alpha} \tag{A.4.10}$$

$$\boldsymbol{\dot{\alpha} = \frac{d\alpha}{dt} = A\left(\frac{dE_{strain}}{d\alpha}\right)^{3}} \tag{A.4.11}$$

We know E_{strain} from Eq. (A.4.3) and $d\alpha$ is known from determining the misorientation change from the applied trial rotations. The parameter A remains critical and can be called the "inverse rotation viscosity" or "rotation resistance" since its unit is $(Pas)^{-1}$. Similar to the rotation mobility, it is not well-constrained yet, which remains part of future work. The provided code "*FS_DDEnergyRecovery*" uses this approach, its handling is similar to the "old" recovery code:

FS_DDEnergyRecovery –i filename.elle –u A B C D E –n (All defaults (apart from A)=0)

A. *Important: Set high angle grain boundary threshold angle in degrees, e.g. 15°, 5°. No recovery any more if misorientation is higher. Default: 5°*
B. *Set ID of phase (flynn VISC.) which should be excluded (e.g. useful for air), set 0 for no exclusion*
C. *Logscreen: Switch off random picking of flynns, unodes etc. by setting this to 1 (handy only for debugging)*
D. *Set the factor "A", the "inverse rotation viscosity" or "rotation resistance". Values around 10^{20} appear reasonable, but the effects of this value have not properly been tested yet.*
E. *Set initial start step (steps already performed in input file), 0 is default*

A.4.2 Grain boundary sliding

A simple approach was implemented to assume grain boundary sliding during a VPFFT simulation. It is not fully tested yet and probably needs refinement. The related codes are found in the digital appendix under "*FS_Codes/FS_other/FS_GBS*". The approach is based on setting certain *unodes* to a second phase, which has "grain boundary" properties. The critical resolved shear stresses of this second phase will be equal (isotropic) and should presumably be lower than for the ice Ih basal plane. Such boundary *unodes* are simply created by searching nearest *unodes* in a region of interest around each *bnode*. This region of interest shall by default be the mean *unode* spacing. In order to improve the description of the boundary phase, the user has the option to temporarily decrease the switch distance. This (temporarily) increases the number of *bnodes*.

The first step or the "start" of assuming grain boundary sliding needs to run before the "*elle2fft*" routine. Its handling is outlined below:

FS_startGBS –i filename.elle –u A B C D –n

A. *The phase ID of the boundary phase (U_VISCOSITY is set to this value). Default = 2*
B. *A factor by which the region of interest radius around bnodes is increased. Default = 1 (radius is mean unode spacing)*
C. *Temporarily use this switch distance to increase the number of bnodes and achieve a better description of boundary phase in unodes. Default: 0 (switched off)*
D. *Set to 1 to store boundary-phase unode-properties in output file "TempGBunodesProps.txt". Default = 0 (do not create this file)*

The second step or "end" of the grain boundary phase should run either before or after the "*fft2elle*" routine (remains part of future testing). Depending on the user's choice, it re-assigns ice (or 1st phase) properties to the former boundary-phase *unodes* by either searching for the property of the nearest *unode* in the same *flynn* or setting the properties to the properties stored before the VPFFT code was running. Its handling is outlined below:

FS_endGBS –i filename.elle –u A B –n

A. *The phase ID of the boundary phase (U_VISCOSITY). Default = 2*
B. *Set to 1 to read properties from file "TempGBunodesProps.txt" (needs to be created before by FS_startGBS) or set to 0 to use nearest unode properties. Default = 0*

A.4.3 Two- and three-dimensional Potts model for grain growth

In order to create simple input foam textures for VPFFT simulations, Potts models for grain growth are a suitable solution. The basic principles of Potts models are outlined in the Elle book (Bons et al., 2008, pp. 21-27). Potts models are simple applications of Monte Carlo models. A probability function is implemented that decides whether a point (or *unode*) of one grain changes its "state" to the one of a neighbour grain, i.e. whether a grain grows or not. The probability function depends on the energy mismatch between the two points and calculates the probability for the point to flip grains (see details in Bons et al. (2008, pp. 21-27):

$$if\ dE > 0: \quad P_{flip} = P_0 * e^{-(c\,dE/k\,T)}$$

$$if\ dE \leq 0: \quad P_{flip} = P_0 \qquad \text{(A.4.12)}$$

A random number generator will create a number between zero and one and depending on if this number is larger or smaller than P_{flip}, the point (or in 2D *unode*) will change its grain. The implemented Potts models are optimised for grain growth in ice.

See the data stored in the digital appendix under "*FS_Codes/FS_other/*" and find the 2D and 3D versions of the code together with MATLAB scripts that help creating initial files and visualise 3D results. Check the "*readme*" files for further instructions.

FS_gg_potts –i filename.elle –u A B C –s Stages –f SaveFrequency –n (all defaults = 0)

Explanation: The 2D code requires a NxN set of *unodes* in an Elle file. The attribute U_ATTRIB_A should be active and indicate the state (grain) of the *unode*. To create the data for U_ATTRIB_A, the provided MATLAB script "*MATLAB_create_initial_states.m*" can be used. It will produce a text file, whose contents can be copied below the U_ATTRIB_A in an Elle file.

A. *Set P_0, by default $P_0 = 0.1$*
B. *Set sensitivity factor c, by default c is the Boltzmann constant k*
C. *Set to 1 to switch off random access of unodes, default: 0*

FS_gg_potts filename.txt A B C D E F G

Explanation: Note that the 3D version is not written with help of the Elle framework and is called in a slightly different way. A pre-compiled executable is provided in the digital appendix. An input file has N^3 lines of a NxNxN box of points in a regular square grid. Each point has an ID followed by a state or grain. A demo input file is provided in the digital appendix.

A. *Set P_0, by default $P_0 = 0.1$*
B. *Set sensitivity factor c, by default c is the Boltzmann constant k*
C. *Temperature in °C, by default temperature is -30 °C*
D. *Dimension, i.e. number of points in x, y and z direction*
E. *Number of stages over which you want to run the simulation*
F. *Set to 1 to switch off random access of points, default: 0*
G. *If you already did some 3D grain growth, the number of steps already performed in the input file (only for naming of the output file)*

A.4.4 Strain analysis

The "strain-analysis" module has been created within this thesis to track and store incremental strain tensors from each simulation step, calculate the finite strain tensors and obtain information on strain ellipse properties or vorticity. The related codes in the digital appendix can be found under "*FS_Codes/FS_utilities/FS_strainanalysis/"* and "*FS_Codes/FS_fft2elle_strainanalysis/".* Performing such a strain-analysis consists of three steps: (1) Running the simulation using *FS_fft2elle_strainanalysis* as the fft2elle-module, this stores the incremental strain tensor for each step and each *unode* in the simulation in a separate text file, but in principle does the same than *FS_fft2elle* (see chapter A.2.2). (2) After the simulation, using *FS_postprocess_strainanalysis* allows the user to

obtain the finite strain tensor from the incremental tensor files from step A to B (does not have to be from the first to the last simulation step). The code should run with the resulting Elle file from step B. (3) Running *FS_plot_strainanalysis* with the resulting Elle file of *FS_postprocess_strainanalysis*. This code computes a regular square grid with a user-defined number of *unodes* and calculates and plots the strain ellipse properties, vorticity and related data from the passive marker grid onto this new grid. The resulting Elle file of *FS_plot_strainanalysis* can be visualised using *showelle*. In addition, there is a code called *FS_plot_stretchdir*, which plots the maximum stretching direction as small lines for each unode. The length of the lines can depend on the strain ellipse ratio. A short tutorial on using the strain-analysis module is provided in the digital appendix under "*FS_strainanalysisExample/*".

In what follows, the processes are explained in a little more detail:

FS_fft2elle_strainanalysis –i filename.elle –u A B -n

A. *Import dislocation densities from "tex.out": 1=yes, 0=no, default: 0*
B. *Write file "PosGradTensor.txt" for passive markers: 1=yes, 0=no, default: 0*

Explanation: This process is similar to the "other" fft2elle-modules, it is also called with the previous "elle2fft"-file. The main difference is in the calculation of deformed passive-marker *unode* and *bnode* positions: For this purpose, the incremental strain tensor $\boldsymbol{F}$ and rigid body translations in x- and y-direction (dx,dy) from the previous to this step is calculated from the new and old *unode* positions. The three nearest *unodes* to the datum passive-maker *unode* or *bnode* are determined. For those three unodes, the positions before and after this strain increment (from step n to n+1) are known and we can derive a set of six equations, two for each point that are of the following kind:

$$\begin{pmatrix} x_{n+1} \\ y_{n+1} \end{pmatrix} = \begin{pmatrix} dx + F_{11}x_n + F_{12}y_n \\ dy + F_{21}x_n + F_{22}y_n \end{pmatrix} \tag{A.4.13}$$

Solving this set of equations yields $\boldsymbol{F}$ and (dx,dy) for each *bnode* or passive-marker point. The data for the passive-marker points is stored in a separate text file called "*PosGradTensor.txt*" that should be stored separately and renamed "*PosGradTensorXXX.txt*", where XXX denotes the three-digit simulation step number (e.g. for step 1: 001). Using the simulation bash script mentioned in chapter A.3 (tutorial), this is done automatically. Note that using *FS_fft2elle_strainanalysis*, the computation time of is about one to two orders of magnitude faster than with *FS_fft2elle*.

FS_postprocess_strainanalysis –i filename.elle –u A B C D –n

A. *Start-step for determining the finite strain tensor (must not be initial step, initial step would be A=1), default: 1*
B. *End-step for determining the finite strain tensor (must not be the last step, but larger than A), default: 2*
C. *Write one text file with finite strain tensor data: 1=yes, 0=no, default: 0*

D. *Write one Elle file for each step containing not the finite data, but the incremental data for this step: 1=yes, 0=no, default: 0 (These Elle files can be further processed in the same manner than the main output Elle file of this code)*

Explanation: This code calculates the finite strain tensor and rigid body translation from step A to B, note that A does not have to be the first and B does not have to be the last simulation step. It runs with the output Elle file from step B. Furthermore, it requires all incremental strain tensor text files produced by *FS_fft2elle_strainanalysis* to be in the directory from where you call the code. They have to be consistently named like: "*PosGradTensorXXX.txt*", where XXX denotes the three-digit simulation step number (e.g. for step 1: 001). The code calculates the finite tensors by stepwise adding the incremental tensor data. Hence, the finite tensor $\boldsymbol{F'}$ at step *n* is calculated using the previous finite tensor $\boldsymbol{F}$ until step *n-1* and the incremental tensor $\boldsymbol{I}$ to go from step *n-1* to *n*. The same principle applies to calculating the finite rigid body translation dx' and dx' at step *n* using the incremental translations dx_i, dy_i and the finite ones from step *n-1* to *n* denoted dx, dy.

$$\boldsymbol{F'} = \boldsymbol{I} \otimes \boldsymbol{F} = \begin{pmatrix} I_{11}F_{11} + I_{12}F_{21} & I_{11}F_{12} + I_{12}F_{22} \\ I_{21}F_{11} + I_{22}F_{21} & I_{21}F_{12} + I_{22}F_{22} \end{pmatrix} \tag{A.4.14}$$

$$\begin{pmatrix} dx' \\ dy' \end{pmatrix} = \begin{pmatrix} dx_i \\ dy_i \end{pmatrix} + \boldsymbol{I} \begin{pmatrix} dx \\ dy \end{pmatrix} = \begin{pmatrix} dx_i + I_{11}dx + I_{12}dy \\ dy_i + I_{21}dx + I_{22}dy \end{pmatrix} \tag{A.4.15}$$

When finished, the code stores the finite tensor and rigid body translations in six *unode* attributes from *U_ATTRIB_A* to *F* and transfers the passive marker positions from the last processed step to actual *unode* positions in the output Elle file (pushed back into the model box). This output Elle file can now be used for further processing and creation of a "plotting Elle file" with the help of "*FS_plot_strainanalysis*". It is recommended not to process over a too large finite strain: For instance, obtaining finite strain tensors over a simple-shear strain of 10 or 20 (usually simulations with hundreds of steps) presumably leads to high numerical errors. In this case, it is less practical to process over all simulation steps, but only the last 50 or 100 steps.

FS_plot_strainanalysis –i filename.elle –u A B -n

A. *Unode resolution of new regular square grid. The code creates a new regular square grid to plot the results on as the passive marker grid is less handy to plot images (very variable unode distances). The new regular square grid will be AxA if the box aspect ratio is 1 (square box), if not unodes in either x- or y-direction will be added to allow an equal spacing of unodes throughout the new grid. It is recommended to keep A around the unode dimension (i.e. 128, 256, etc.) of the input Elle file. Default: 0 (needs changing!)*
B. *Additionally, write result data to text file. 1=yes, 0=no, default: 0*

Explanation: The plotting script creates an output Elle file that stores the following information:

U_ATTRIB_A: Vorticity

U_ATTRIB_B: Vorticity number

U_ATTRIB_C: Minimum strain (≈ short strain ellipse axis)

U_ATTRIB_D: Maximum strain (≈ long strain ellipse axis)

U_ATTRIB_E: Maximum stretching direction (degrees from x-axis, counter-clockwise)

U_ATTRIB_F: Ratio of strain ellipse (long/short axis)

U_VISCOSITY: Dilation, estimate for error, should remain 1 in area conservative deformation

The unodes in the resulting Elle file are in a regular square grid again that has a user-defined size (see explanation for user-input "A"). This Elle file is ready to be plotted with *showelle* or further processed with *FS_plot_stretchdir*.

FS_plot_stretchdir –i filename.elle –u A B C –n

A. *Spacing of unodes: E.g. type 1 to plot every, 2 to plot every 2nd unode's data. Default: 1.*
B. *Maximum length of a line (for 1x1 box simple shear approximately 0.01-0.02 seems fine)*
C. *Min. strain ellipse ratio (will have line length = 0) Default 1 (this option is switched off)*
D. *Max. strain ellipse ratio (will have line length = B (max. line length)) Default 1*
E. *Scale the file by a certain factor, useful to fit pure shear box on canvas. Default: 7 (which is useful for simple shear, 5 for pure shear). This is the same than the corresponding input for FS_plot_ugrid*

HINT: If C and D are the same or C<D, the line lengths are always set to maximum length (which is the case using default input)

Explanation: The code creates a post script (*.ps) file that plots a line for every unode (depending on the set unode spacing). This line will be in the direction of maximum stretching (from x-axis, counter-clockwise). The line length can either be set to a constant length or scaled to the strain ellipse ratio (ratio of 1 means a small length; higher ratios produce higher lengths).

A.4.5 MATLAB scripts

A number of MATLAB scripts has been created to facilitate plotting different properties or allow fast creation of videos from a set of images. The MATLAB-scripts is provided in the digital appendix under "*MATALB_scripts/*". The folder "*plot_data/*" contains various scripts that plot grain size-, slip-system activity- or stress-evolution. Besides, scripts using MTEX (Bachmann et al., 2010, Mainprice et al., 2011) to generate eigenvalues or pole-figures from a *.txt file that has been prepared using "*FS_elle2mtex*" on an Elle file (see chapter A.2.4). The user is instructed to follow the instructions in the MATLAB scripts and use them with the provided "*DemoModel*" – files containing exemplary data for plotting.

The provided folder "*make_showelle_images_beautiful/*" is containing MATLAB scripts to process images created with showelle. As the name implies, it is possible to process and improve images that have been created with *showelle*. It is particular handy to improve image qualities for simulation images with either changing box size (pure shear) or containing second phases such as air. In pure shear simulations, the actual area occupied by a unode is changing and plotting with "only" showelle eventually means plotting *unodes* above each other's, which we want to avoid. With poly-phase materials such as bubbles, the user may want to additionally plot grain boundaries and bubbles above the *unode*-image without *showelle* as unodes likely "reach in" bubbles, which is of course incorrect. Below, a short guide on how to use this MATLAB script is provided, the "readme" file in the digital appendix will also guide the user through the input of the script:

1. *Find the prepared images in the sub-folders. Of course, the "final_images" folder is still empty. The images belong to simulation F20 (PAPER I), i.e. a pure shear simulation with air inclusions. There are three types of images of the same microstructures:*
    a. *The images only plotting c-axes azimuths on unodes scaled back to a 1x1 box (folder: images_unodes). It is visible, that also "air-c-axes azimuths" are plotted, which are not meaningful to show.*
    b. *The images only plotting grain boundaries and bubbles in black (folder: images_gbs_bubbles), also scaled back to a 2x2 box (larger box to increase quality when plotting with showelle, this is possible as only flynn boundaries and flynns are plotted)*
    c. *The images with the "real" desired image size according to the pure-shear box. It is not important what the images are showing, only their size (width x height) should be the desired final image size. (folder: native_sized_images)*
2. *Now run the MATLAB script with the pre-defined input parameters. Take a look at the output. Familiarise yourself with the input parameters and the relevant comments in the code to understand how the script is working. Proper adjustment is necessary to achieve the best image quality. Remember that whenever you start the script, all images in final_images/ are deleted before new ones are added.*

The last MATLAB script that is provided with the digital appendix is capable of creating *.avi movies from a set of images. The script is particularly handy when images from a pure shear simulation should be transferred to a movie as their image size is not constant. The script is provided in the folder "*images2avi/*". As an example, one can use the images provided in "*images2avi/input_images/*". Browse through the input of the script to understand how it is working. For now, all input parameters can stay as they are.

A.5 Comparison of numerical and analytical solution for grain boundary migration

To validate the grain boundary migration code that has been updated in the course of this thesis, a comparison to analytical solutions for the grain boundary velocity of a circular grain was performed. The comparison is based on the analytical solution presented by Becker et al. (2008). As the new grain boundary migration code assumes the minimisation of both surface- and strain-energy as driving forces, two end-member solutions were used in isolation: (1) Grain boundary migration driven by only surface-energy reduction and (2) grain boundary migration driven by only strain-energy reduction. For both comparisons, a simple setup using a circular grain is employed, as the analytical solution is only valid for a circular grain. The circular grain will shrink according to the pre-set surface- and strain-energy conditions. The basic setup is illustrated in Fig. A.1. With low areas, the circular grain would be defined by only a few *bnodes*, which causes the numerical and in particular the analytical solution to fail. To exclude this situation, the grain boundary migration is only performed over a comparatively short time to keep a sufficient number of *bnodes*. For the numerical solution, the initial area and radius of the circular grain are known and can be re-calculated at any step of the simulation. With this, the rate of radius change (dr/dt), which equals the shrinking velocity (V), is known. Differences in analytical solutions exist between assuming surface- or strain-energy minimisation. For both end-members, the same grain boundary mobility (M) was used (Eq. A.5.1), which is a function of temperature ($T = -32°C$), intrinsic mobility ($M_0 = 0.023 m^2 s\, kg^{-1}$, Nasello et al., 2005), activation energy ($Q = 5.11 \cdot 10^4\, J\, mol^{-1}$, Nasello et al., 2005) and the universal gar constant ($R = 8.3145\, J\, mol^{-1}\, K^{-1}$).

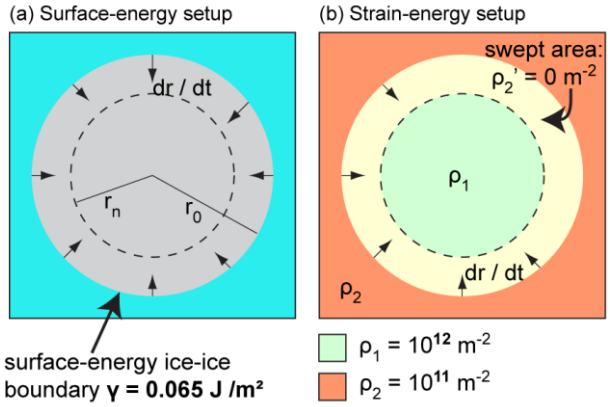

Figure A.1 The simulation setup for the comparison of the grain boundary migration code with an analytical solution comprises a circular grain in a surrounding material. The setups assumed (a) surface-energy and (b) strain-energy minimisation as driving forces. The surface-energy per area for ice-ice boundaries was used. For the strain-energy setup, the simulation will leave behind a dislocation free area once the circular grain starts to migrate inwards. This needs to be considered when comparing to the analytical solution, which does not assume a change in the difference in dislocation density.

$$M = M_0 \cdot e^{-Q/RT} \qquad \text{(A.5.1)}$$

A summary of the data obtained from comparing analytical and numerical solutions is provided in the spreadsheet "*SummaryGBMComparison.xlsx*" in the digital appendix.

A.5.1 Surface-energy minimisation

The analytical solution for grain boundary migration of a circular grain minimising its surface energy is based on the employed surface-energy per area for ice-ice boundaries ($\gamma = 0.065\ J\ m^{-2}$). In the analytical solution, the rate of radius change (dr/dt) is calculated using the actual radius of a previous state (r_{n-1}) according to Eq. A.5.2. Hence, the new radius at a following state (r_n) and the resulting grain area can be calculated analytically after some amount of time (dt).

$$\frac{dr}{dt} = M\frac{\gamma}{r_{n-1}} \quad \Leftrightarrow \quad r_n = r_{n-1} - dt \cdot M \cdot \frac{\gamma}{r_{n-1}} \qquad \text{(A.5.2)}$$

Two time-steps were employed for comparison and kept constant during each of the two simulations ($dt_1 = 10^9 s$, $dt_2 = 10^9 s$). The simulations used 100 steps using a grain with an initial radius of $r_0 = 0.45\ m$ (the Elle unit length was set to 1, for simplicity). Along with the simulations, also the analytical solution determined the shrinking velocity (dr/dt) and area of the circular grain.

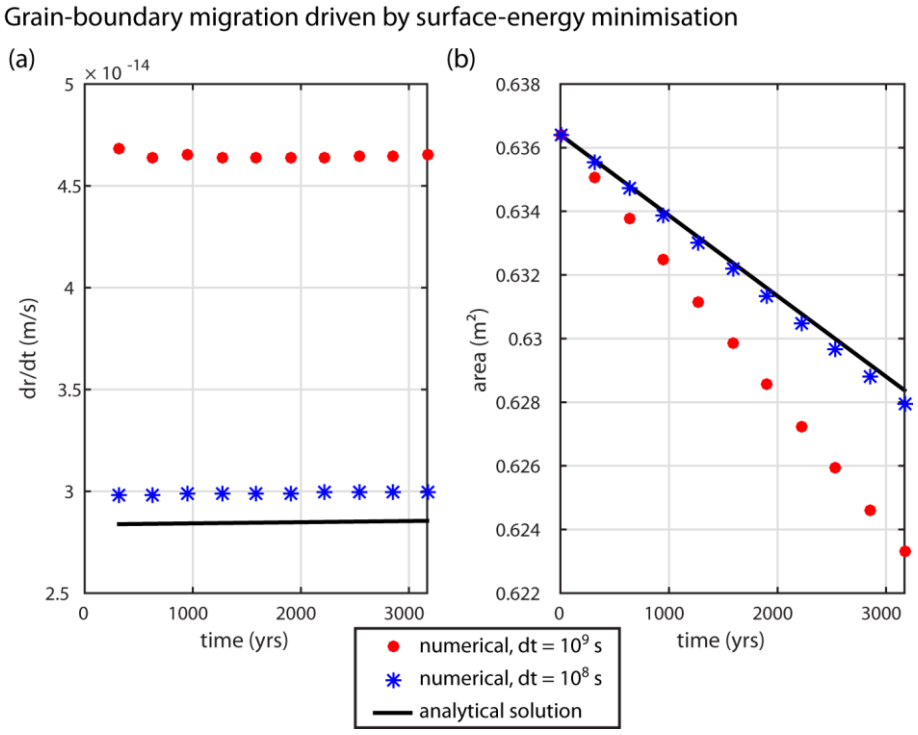

Figure A.2 Results of comparing numerical approach and analytical solution for surface-energy-driven grain boundary migration. (a) Grain boundary velocity. The velocity should increase with time, which is slightly visible, however, not well resolved as the area of the circular grain only varies slightly. (b) Area evolution of the circular grain over time.

The results are illustrated in Fig. A.2. As expected, the shrinking velocity (dr/dt) slightly increases, but it is almost constant as the applied amount of radius-change is low. Hence, the area reduction of the circular grain is almost linear over time. In addition, the difference in numerical and analytical solution is lower for the lower numerical time-step, which is expected. Furthermore, this difference increases with more time passed during the simulation (Fig. A.2b). The results illustrate that in general the numerical approach for grain boundary migration driven by surface-energy reduction is valid, however, the numerical time-steps should be kept as low as possible to approach the analytical solution, in particular, if the simulation ranges over a long total time.

A.5.2 Strain-energy minimisation

The strain-energy in a grain results from its dislocation density (ρ) and the energy per line of this dislocation type (E_{line}). For simplicity, the comparison assumed only basal-plane dislocations in ice Ih, whose line energy can be calculated from the Burgers vector length and the shear modulus (see Humphreys and Hatherly, 2004, pp. 17-18 for equations; see Schulson and Duval, 2009 for parameters for ice Ih basal-plane). The line energy for ice Ih basal-plane dislocations is $E_{line} = 3.6 \cdot 10^{-10} J\, m^{-1}$. The setup used for the comparison is illustrated in Fig. A.1b. The circular grain has initially a higher dislocation density (ρ_1) than the surrounding (ρ_2), which causes grain boundaries to migrate inside the

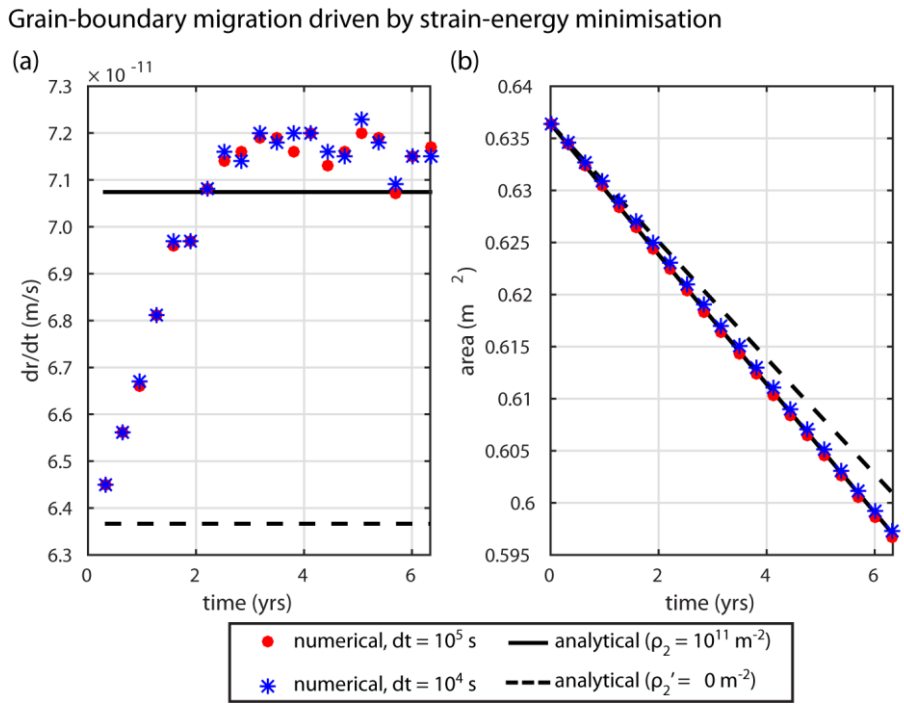

Figure A.3 Results of comparing numerical approach and analytical solution for strain-energy-driven grain boundary migration. (a) Grain boundary velocity. The numerical velocity changes from an initial situation where the surrounding dislocation density is relatively high to the velocity expected, if the surrounding has zero dislocation-density. This is related to the simulations leaving behind a dislocation free area when the circular grain migrates inwards. (b) Area evolution of the circular grain over time.

grain. Initially, the dislocation densities within the grain and the surrounding were assumed constant. Therefore, their strain-energy difference (ΔE_{strain}) can be calculated according to Eq. A.5.3.

$$\Delta E_{strain} = E_{strain,1} - E_{strain,2} = E_{line}\rho_1 - E_{line}\rho_2 \tag{A.5.3}$$

Analytically, the rate of radius change over time (dr/dt) is simply the multiplication of the strain-energy difference (ΔE_{strain}) with the grain boundary mobility, which allows also the analytical calculation of the new radius (r_n) as a function of the passed time (Eq. A.5.4).

$$\frac{dr}{dt} = M \cdot \Delta E_{strain} \;\Leftrightarrow\; r_n = r_{n-1} - dt \cdot M \cdot \Delta E_{strain} \tag{A.5.4}$$

During the numerical simulation, the grain boundaries migrate towards the higher dislocation-density area, leaving behind a dislocation-free region (Fig. A.1b). Therefore, in the simulation, the reference dislocation density of the matrix surrounding the circular grain will change from $\rho_2 = 10^{11} m^{-2}$ to $\rho_2{}' = 0 m^{-2}$, therefore the rate of radius change (grain boundary velocity) will increase after the initial stages of the simulation. In order to take this change in dislocation-density difference between circular grain and surrounding into account, two analytical calculations were performed, one assumed the surrounding dislocation density to be ρ_2, the other one assumes zero dislocation density for the surrounding ($\rho_2{}'$). The two numerical simulations use two different time-steps ($dt_1 = 10^5 s$, $dt_2 = 10^4 s$) and ran over 20,000 steps. Like in the comparison for surface-energy-driven grain boundary migration, the initial circular grain radius was $r_0 = 0.45\ m$.

The results of comparing analytical and numerical solution of strain-energy-driven grain boundary migration, are illustrated in Fig. A.3. For strain-energy-driven grain boundary migration, the shrinking velocity (dr/dt) is constant over time if the dislocation-density difference stays constant, which is not the case during the simulations. As expected, in the initial stage of the simulation, the rate of radius change is similar to the analytical solution assuming the initial surrounding dislocation density ($\rho_2 = 10^{11} m^{-2}$). However, with time, the numerical rate of radius change increases towards the analytical solution assuming zero dislocation density in the surrounding ($\rho_2{}' = 0 m^{-2}$, Fig. A.1b, Fig. A.3.a). Similar to the comparison of surface-energy-driven grain boundary migration, the difference in analytical and numerical solution is better, if lower numerical time-steps are used. However, this is not significantly reflected in the results as both numerical time-steps were already sufficiently low. The numerical results are slightly higher than the analytically predicted rate of radius change when the surrounding has zero dislocation-density. The results in the area-evolution of the circular grain (Fig. A.3.b) show that numerical and analytical solutions are close for both numerical strain rates. With increasing simulation time, the numerical solution trends towards the analytical solution assuming zero dislocation density in the surrounding. The results validate the expectations and show the general correctness of the strain-energy-driven grain-boundary migration code.

A.6 Contents of the digital appendix

Folders:

FS_Codes

- Elle/VPFFT codes used and developed in the course of this thesis. Including “readme” files for every code and on installation
- MATLAB codes developed for post-processing
- Additionally input files necessary to use the codes such as “symmetry.symm”, “phase_db.txt” and *.in and *.sx input files for VPFFT

FS_SimulationTutorial

- The data for the tutorial explained in section A.3. Follow the instructions in “readme” and section A.3

FS_StrainanalysisExample

- An example for the strain analysis code described in section A.4.4. See “readme” file for more information

FS_ElleChanges

- Some changes in the Elle basecode are necessary to use the codes in “FS_Codes”. This folder contains the new files that can be copied in an existing Elle installation

FS_SimulationInput

- The input files that have been used for the simulations in the publications in this thesis together with the state of the codes at the time when the simulations were performed. ATTENTION: These data are only provided to allow reproducibility. The state of the codes when the simulations presented in the papers were running was restored. Do not use these codes for any other simulation.

Other files

- PDF of this thesis
- Getting_Started.pdf → Read this file when starting to work with Elle/VPFFT
- Elle_Installation_instructions.pdf
- InputFiles_FFT_Elle.pdf → Structure of VPFFT input files with annotations

Acknowledgements

Three years have passed rapidly and I want to express my gratitude to anyone involved in bringing this project to a successful ending. Thanks a lot (and also sorry) to everyone I forgot in what follows. First of all, I want to thank my supervisors Ilka Weikusat and Paul Bons. Thank you for everything, all the opportunities you gave me, for teaching me and for your guidance and trust. Especially, thank you for an always friendly environment. A big "thank you" to all my colleagues in Tübingen: Melanie Finch, who carefully proof read this thesis, Enrique Gomez-Rivas, Maria-Gema Llorens, who taught me the art of Elle, Hao Ran, Tamara de Riese, Till Sachau and Zhongbao Zhao and in Ilka's group of young researchers: Tobias Binder, Jan Eichler, Daniela Jansen, Johanna Kerch, Ina Kleitz and Ernst Kuiper. Thank you all for your support and help, for any discussion or fun we had. Additionally, I am deeply grateful to Albert Griera and Jens Rößiger for teaching me and helping me to tame Elle. I thank the people at AWI for their support, in particular Johannes Freitag and Sepp Kipfstuhl. Although we never met, thanks to Ricardo Lebensohn for a fantastic code. Thanks to the Elle community, in particular Lynn Evans. Thank you, Adam Treverrow, for a friendly welcome in Hobart and teaching me about your research. Thanks to Martyn Drury and Gill Pennock for all discussions and support. Thanks to Todd Ehlers and Olaf Eisen for willing to join the committee of my PhD defence. Special thanks to Olaf for a great time on Vernagt-glacier. I am thankful for the support of my family and friends. In particular, I am thankful to my father and sister, their care and support guided me until this point in life and I thank my mother, who taught me in my younger years that I can achieve anything. Most importantly, Jessica Starke, I am deeply thankful for your love, for putting up with me, for being my fellow science nerd, for standing by me in beautiful and miserable moments and for being my partner in life.

I acknowledge funding by DFG (SPP 1158) grant BO 1776/12-1 and the Helmholtz Junior Research group "The effect of deformation mechanisms for ice sheet dynamics" (VH-NG-802). I thank the ESF research networking programme MicroDICE and the EPICA Descartes travel prize for travel support. Thanks to the Helmholtz Graduate School POLMAR for travel funds and excellent courses.